MSc Thesis

Estuarine Sand Dunes as a Nature-Based Solution Against Salt Intrusion

An idealised morphostatic model approach

Sem J. Geerts

Graduation committee:	Role:
prof. dr. ir. B.J. Geurts	Head graduation committee AM
dr. ir. P.C. Roos	Head graduation committee CEM
ir. W.M. van der Sande	Daily supervisor
prof. dr. S.J.M.H. Hulscher	Graduation committee member CEM
dr. ir. T.M. Tyranowski	Graduation committee member AM

December 14, 2023

Department of Applied Mathematics
Faculty of Electrical Engineering, Mathematics and Computer Science

Department of Civil Engineering & Management
Faculty of Engineering Technology

UNIVERSITY OF TWENTE.

Preface

This thesis is written as a finalisation of my combined Master's in Applied Mathematics and Civil Engineering & Management. Not only does it show my efforts from the first Monday to the last Thursday of 2023, but also represents the culmination and the end of a seven-year journey as a student at the University of Twente. It was great to not only perform the research, but also act as my own project manager, making it feel like a collaborative project and bringing the worlds of mathematics and civil engineering closer together. The two topics can often overlap, but at the university, they are quite well-separated and many bridges are still to be built. I have not walked this final stage alone and cannot end without thanking some people.

Firstly, I want to express my appreciation to the entire committee for the flexibility provided during the research process, which allowed me to explore my creativity and try out things that eventually failed. Thanks Wessel for your practical insights, in-depth discussions and down-to-earth small talk. It's great to know that you, too, recognise the importance of nice figures. Pieter, you showed me the vast landscape of knowledge still waiting to be explored and your belief in my independence has been encouraging. Thank you for pushing me to make my own decisions. Bernard, I enjoyed your critical thinking, thought-provoking questions, and the theoretical approach you bring. The freedom to walk my own path and be my version of a mathematician is greatly valued. Suzanne, your ability to connect the findings with other research has been invaluable. I appreciate your enthusiasm, the time you dedicated, and for giving me the opportunity to further this work.

I extend my thanks to the people behind SALTISolutions for their open arms by involving me in the user meetings. Special gratitude to Rutger for engaging in meaningful discussions and always having your door open to exchange ideas, even when they initially seemed crazy. Thanks to the people of 3MS for making me feel like a colleague and keeping me caffeinated.

To my friends, housemates and family, who reminded me why I was doing this work and why it matters. Explaining the topic to you provided me with the relevance and the main thread throughout this report. Most of all, thank you for your steadfast personal support, your many hugs, your understanding and your ability to cope with me this year.

Enjoy the read and figures.

Sem Geerts
December 14$^{\text{th}}$, 2023

Estuarine Sand Dunes as a Nature-Based Solution Against Salt Intrusion

An idealised morphostatic model approach

By S.J. Geerts
December 14, 2023

Abstract

Saltwater intrusion in estuaries can pose a critical issue with significant implications for human activities such as industry, agriculture and drinking water extraction, and can be unfavourable to environmental sustainability. This phenomenon arises when saline water infiltrates the estuarine system, potentially leading to a shortage of freshwater. The intensity of salinity intrusion and the salt intrusion length are influenced by various factors, of which freshwater river flushing and the amount of vertical transport are key predictors.

This study investigates the impact of estuarine bedforms on the salt intrusion length within estuaries. Estuarine sand dunes introduce additional roughness to the flow, resulting in reduced flow velocities and elevated mean water levels. These dunes can cause large-scale turbulence that may extend from the bed to the water surface. Resonant internal waves can form over these bed forms when stratification and large horizontal flow velocities are present, which can increase vertical mixing when breaking. In addition to these non-hydrostatic processes, estuarine sand dunes induce tide-averaged spatially periodic re-circulation cells over the bedforms. Altogether, these effects potentially increase the net vertical flux and, as such, reduce the salt intrusion length. We investigate the complex dynamics of estuarine salt transport and determine the potential of estuarine sand dunes as a nature-based solution against salt intrusion.

Given the complexity of the multi-dimensional parameter space affecting salt intrusion length, we investigate this using an idealised hydrostatic model with 2DV geometry. This enables us to specifically study the effect of vertical flow behaviour without possible interference of other parameters. Our model is designed to be adaptable for the investigation of other estuarine systems that can be approximated as a single-channel estuary with relatively uniform geometry. Current model settings are based on the Rotterdam Waterway (RWW), the Netherlands, during low river flow velocities representative of summertime conditions when salt intrusion is most detrimental. We determine the influence of dune characteristics (such as height, length and asymmetry) as well as the effects of dumping and dredging interventions on the salt intrusion length.

A numerical convergence study of the flow and salt transport is performed, and the model shows robust numerical convergence. With subsequent grid refinement, a negligible accuracy improvement of the model output is achieved. Furthermore, the discretisation and model parameters effectively capture most of the hydrostatic flow and salt transport behaviour representative of the RWW.

We show that the presence of estuarine sand dunes does not qualitatively change the dominant transport mechanisms and degree of stratification in the estuary, although quantitatively a different salt intrusion length may form by a changing balance of transport components. Changes in dune geometry and characteristics impact the salt intrusion length, which is most sensitive to a change in dune height. An increase in dune height enhances vertical advective transport, bringing more saline water upwards through the water column and thus reducing stratification. Similarly, a decrease in dune length increases the dune slope and enhances the vertical exchange. Dune asymmetry has a negligible influence on our model results.

Manipulation of an existing sand dune field affects the salt intrusion length. For example, dredging of sediment reduces the main outward-flowing river transport and decreases the amount of vertical mixing, both contributing to an increase in the salt intrusion length. The volume of sediment dredged is linearly related to the change in salt intrusion length. The influence of dumping depends on the strategy employed. When topography is preserved, and dumping is performed uniformly in space, it decreases the salt intrusion length proportionally to the volume of sediment dumped. However, when the bed is levelled by dumping of sediment, vertical mixing is reduced and this measure is only effective in mitigating salt intrusion when the volume used is sufficient to decrease the mean water depth significantly. None of the interventions changes the estuarine-sized vertical flux qualitatively over the intervention interval. Response of the salt intrusion length mostly follows from changes of the vertical at the boundaries of the intervention and changes in the relative balance of horizontal transport components.

Dredging of artificial sand dunes in a flat bed can serve as a mitigation tool against salt intrusion. If dredged sufficiently deep, dredged dunes generate sufficient vertical mixing to counteract the adverse effects of deepening the channel, maintaining estuary navigability while enhancing vertical mixing with local topography. In this way, estuarine sand dunes can serve as a nature-based solution against salt intrusion without changing accessibility to seaports.

Contents

Chapter 1

Introduction

In this chapter, we first outline the framework concerning estuarine salt intrusion and sand dunes. This leads to the study's overarching objectives and methodology. A more in-depth analysis, provided by a literature review, follows in the subsequent sections.

1.1 Research Framework and Objective

Estuaries are semi-enclosed embayments of the coast where tidal waves run through a channel or system of channels, leading to the mixing of salt ocean water and freshwater runoff (Valle-Levinson, 2010). Within the estuary, the area influenced by tidal motion is commonly referred to as the tidal river. The collision of saline and freshwater generally results in denser seawater intruding beneath the outflowing riverine freshwater. The distance with which a pre-determined significant salt concentration can penetrate inland is referred to as the salt intrusion length, usually a maximum concentration of 1 ppt (parts per thousand).

Estuaries are among the most important environments in the coastal zone, both biologically and socioeconomically and some of the largest cities around the world have been built around estuaries (Lotze, 2010). Historically, estuaries have formed natural harbours with the intricate interaction of fresh and saltwater providing good ecological conditions for many life forms, making ideal places to settle (Limburg, 1999). To human industries they offer good navigability, connect the major sea routes to inland waterways, and serve as an ideal location for large seaports (Paturej, 2008). The Rotterdam Waterway in the Netherlands is an example of such a highly industrialised estuary. Human settlements were boosted by a large fishing industry in the area. With an open connection to the river Rhine, it quickly became the largest seaport of Europe (Kirichek et al., 2018). To ensure navigability for the vessels with the largest draft, and to counteract sedimentation, the main channel is constantly dredged, deepening the channel and flattening the bed to ensure a minimum water depth. Dredging activities have increased from 4 million m^3 annually in the 90s to more than 10 million m^3 in 2016 (de Bruijn, 2018).

Saltwater intrusion in estuaries is a critical issue with significant implications for both environmental sustainability and human activities. This phenomenon arises when saline water infiltrates the estuarine system, potentially leading to a shortage of fresh water, thus affecting industries, agriculture, and the accessibility of drinking water, in addition to posing ecological challenges by creating biochemical changes (Tully et al., 2019; Miah et al., 2020). The increasing global significance of this issue is particularly pronounced in coastal regions (Wada et al., 2011), where the precarious balance between freshwater and saltwater is vulnerable to the multifaceted impacts of climate change, including rising sea levels and heightened drought occurrences (Veldkamp et al., 2015).

The intensity of salinity intrusion and the salt intrusion length are influenced by various factors, of which freshwater river flushing is an evident key predictor. Moreover, an increase in vertical mixing leads to a reduction in the salt intrusion length, as it facilitates the transport of salt upwards towards the outflowing freshwater river discharge. Studies have shown that for highly stratified estuaries, the dominant mechanism responsible for removing salt during each tidal cycle is the vertical salt flux, rather than the seaward advection of high-salinity fluid (MacDonald & Horner-Devine, 2008). Consequently, geometric features such as bottom roughness and reduced water depth have been identified as factors contributing to a decrease in the salt intrusion length (Hendrickx et al., 2023b).

Process-based models are models where physically derived equations are solved over a spatial and temporal domain. They serve as a tool to support the effects of mitigation measures. Stratification greatly reduces the eddy viscosity, mainly by limiting the vertical length scale of turbulent eddies. Hence, we argue that this stratification and its influence on turbulence should be modelled carefully. Reversely, turbulent effects often increase the vertical salt flux. These effects are usually parametrised in models by the eddy viscosity and diffusivity. Determining appropriate values is difficult and the variability of the eddy viscosity is the crux of the problem of quantifying the estuarine circulation (Geyer & MacCready, 2014).

This study investigates the impact of bottom topography, specifically estuarine bed forms, on the salt intrusion length within estuaries. Estuaries, due to their dynamic nature, exhibit unique physical processes that influence the development of these bedforms (Paarlberg et al., 2009; van der Sande et al., 2023). Among them, sand dunes represent a distinctive estuarine bed form, analogous to tidal sand waves in marine environments and river dunes in riverine settings (Hulscher & Dohmen-Janssen, 2005). However, the presence of stratification in estuaries introduces different mechanisms to the behaviour of sand dunes (van der Sande et al., 2021).

Estuarine sand dunes introduce additional roughness to the flow, known as form roughness (Zanke et al., 2022), causing decelerating of the flow field resulting in elevated mean water levels (Maddux et al., 2003). They can cause large-scale turbulence that may extend from the bed to the water surface (Best et al., 2001) and asymmetric dune shapes have been observed to amplify these processes (Bradley et al., 2013). Moreover, under certain conditions, such as high river flow velocities, they can generate resonant internal waves in a stratified environment (Kostaschuk et al., 2010). These waves can promote vertical mixing, causing saline water to rise to the surface while impeding the dominant horizontal flow (Wegman, 2021). In addition to these turbulent processes, estuarine sand dunes induce spatially periodic re-circulation cells over the bedforms, potentially increasing the net vertical flux and, as such, reducing the salt intrusion length.

This research focuses on the influence of sand dunes on estuarine salt intrusion, and the development of effective mitigation strategies requires a solid understanding of its underlying mechanisms. Traditional hydraulic structures can alleviate salt intrusion by preventing saline water from entering. However, this approach can introduce adverse effects on the shipping industry, ecological disruption, and interference with river flow and sediment transport. Therefore, research endeavours are currently directed toward innovative intervention strategies that mitigate saltwater intrusion's adverse impacts while sustaining a freshwater supply (Hendrickx et al., 2023b). This Building-with-Nature approach starts from the existing natural system and makes use of the natural dynamics to account for society's needs while creating room for nature-development (de Vriend et al., 2015). Solutions that employ this philosophy are referred to as nature-based solutions. By using natural dynamics, they often have lower costs than traditional engineering solutions on a life-cycle basis (Borsje et al., 2011). We investigate the complex dynamics of estuarine salt transport and determine the potential of estuarine sand dunes to decrease stratification and salt intrusion.

Analytic salt intrusion models have played a significant role in exploring the dominant processes responsible for mixing in estuaries. However, these models often do not incorporate features such as estuarine sand dunes and frequently rely on the rigid-lid approximation, which increases the tidally and depth-averaged flow velocity along the estuary (Dijkstra et al., 2022; Jongbloed et al., 2022). On the other hand, numerical models have been developed to provide a more detailed assessment of salt intrusion at the scale of entire estuaries, considering the influence of geomorphological characteristics (Wei et al., 2022; Hendrickx et al., 2023b; Siemes et al., 2023). Notably, these models have largely neglected the presence and impact of estuarine sand dunes.

Numerical models have aimed to account for sand dunes, but they often focus on specific aspects. For instance, some models neglect salinity (Lefebvre, 2019), while other diagnostic[1] models introduce a density stratification at the boundary, preventing the natural development of a salinity gradient (Wegman, 2021). The potential of sand dunes to decrease stratification has been investigated by Groenenboom et al. (2019), but they mainly focus on internal waves over two dunes, rather than the advective effects over a full dune field. Therefore, a crucial gap in the current research landscape lies in the absence of a comprehensive model that explicitly considers the influence of estuarine sand dunes on salt intrusion at the scale of the entire estuary in a prognostic approach. In response to this gap, we will develop a hydrodynamic numerical model that allows for the explicit implementation of sand dunes across the entirety of an estuary.

In this research, we aim to understand how estuarine sand dune geometry influences estuarine salt transport mechanisms. While flow over marine and riverine equivalents of sand dunes are well-understood, the precise influence of these estuarine sand dunes on flow dynamics and, specifically, on salt dynamics at a full estuarine scale, remains relatively unexplored. Therefore, this study aims to address the central research question:

What is the influence of estuarine sand dunes on salt intrusion?

Specifically, we ask:

- What processes govern the salt dynamics and what role do sand dunes play?
- What is the influence of sand dune characteristics such as height, length and asymmetry, on salt transport and the salt intrusion length?
- How does dredging and dumping of sediment in a sand dune pattern influence the salt intrusion length?
- How can artificially created sand dunes reduce salt intrusion in an estuary previously depth-maintained?

Given the complexity of the multi-dimensional parameter space affecting salt intrusion length, we focus our computational modelling efforts on a single specific case; the Rotterdam Waterway (RWW), the Netherlands, during summertime conditions, a period when salt intrusion is most critical. Our model is designed to be adaptable for the investigation of other estuarine systems that can be approximated as a single-channel estuary with relatively uniform geometry. The overarching goal is to assess whether sand dunes can serve as a nature-based solution to mitigate salt intrusion. To identify the most effective strategies, we model and analyse various dune dimensions and intervention approaches.

In the remainder of this introductory Chapter 1, the basic background information surrounding salinity, estuaries, the RWW and sand dunes will be introduced. This gives the theoretical framework available in literature and allows us to identify which processes should be taken into account in the

[1]We refer to diagnostic models as models where our variable of interest is explicitly implemented in the model. In this case, density gradients are imposed and the flow follows from it. Prognostic models are the opposite, where salinity gradients naturally develop throughout the estuary, allowing for the natural evolution of a certain salinity profile.

model. In Chapter 2 the theoretical framework of salt intrusion is explained. This gives the basic set of equations and introduces the basic variables and parameters that characterise an estuary. In Chapter 3 the specific implementation of model equations and model development of the RWW are described. Furthermore, we show the numerical stability and convergence of the output. Chapter 4 shows the model validation and verification, which indicates that the idealised model can represent the RWW well. The model results, specifically the influence of general sand dune dimensions, the influence of dredging and dumping of sediment, and the influence of dredging artificial dunes are all described in Chapter 5. Finally, conclusions are drawn in Chapter 6.

1.2 Salinity: Units and Physics

Salinity, the measure of all non-carbonate salt dissolved in seawater, can be expressed using different units of measurement. Two common non-dimensional units used in oceanography and marine biology are parts per thousand (ppt) and practical salinity units (psu) (IAPSO, 1985). While both units measure salinity and are numerically similar, they have different scales and are used in different contexts. The unit ppt represents the mass of dissolved salt (in grams) per kilogram of seawater and is commonly used to express salinity. Seawater with a salinity of 35 ppt contains 35 grams of salt per kilogram of seawater (including the dissolved salt itself). In contrast, psu is a measure of the conductivity of seawater and is based on measurements of the electrical conductivity of seawater. Seawater with a salinity of 35 psu has a salt concentration equivalent to seawater with a salinity of 35.165 ppt, and this relationship is nearly linear. Throughout this research, we will use the ppt unit.

The salinity of drinking water in the Netherlands is measured in terms of chlorinity (the measure of chloride Cl^- content) and an annual average of 150 mg/L Cl^- is allowed (Bijlage A Drinkwaterbesluit, 2023). Even though there are smaller quantities of other ions in seawater (e.g., K^+, Mg^{2+}, or SO_4^{2-}), sodium and chloride ions (from NaCl) represent about 91% of all seawater ions, meaning that chlorinity can be used as a proxy for overall salinity. Seawater has a chloride concentration of approximately 19400 mg/L Cl^-, meaning that the drinking water measure of 150 mg/L Cl^- converts to approximately 0.25 ppt, but this conversion is not exact (Millero et al., 2008).

The density of a fluid depends on dissolved quantities and temperature and is described by an equation of state. Eckart's formula is often used for water (Eckart, 1958), which describes the water density ρ as a function of pressure p, salinity s and temperature T, with

$$\rho(p, s, T) = \frac{p + p_0}{\lambda + \alpha_0(p + p_0)}. \tag{1.1}$$

where p_0, α_0, λ are functions of (s, T). Wright (1997) improved the fit of these functions and described them as third-order polynomials of (s, T) and called in the *revised Eckart's formula*. Under the assumption of an incompressible flow (density ρ does not depend on pressure) and constant temperature $T = 15$ °C, these expressions simplify to linear functions of s. In turn, this newly fitted revised Eckart's formula can be simplified to the linear approximation with

$$\rho_{\text{Eck}}(s) = \rho_0(1 + \beta s), \tag{1.2}$$

with $\rho_0 = 999.1$ kg/m^3 and $\beta = 7.671 \cdot 10^{-4}$ ppt^{-1} (derived in MATLAB using the revised coefficients of Wright (1997)).

The change from saline water to fresh water throughout the estuary results in horizontal and vertical density gradients, where the latter are referred to as stratification. Isohalines are contour lines that join points of equal salinity in the estuary. In case of constant temperature and incompressible flow, these align with isopycnals, lines of constant density. The pycnocline is the isopycnal that separates two fluid layers of the largest density difference.

1.3 Estuaries and Salt Intrusion Processes

We define estuaries as semi-enclosed embayments of the coast where tidal waves run through a channel or system of channels. Estuaries exist in all kinds of shapes and sizes, and subsequently, classification occurs in many aspects. As we are mainly interested in the salt intrusion itself, regardless of the geomorphology and hydrodynamics of the system, we use a classification based on the observable salinity structure and related to the amount of mixing and the vertical structure of salinity. Pritchard (1952) identifies four different *stratification regimes* (see Figure 1.1):

Salt wedge: Very strong horizontal and vertical stratification with barely any (turbulent) mixing across the pycnoclines. There is a clear freshwater riverine flow on top and a more dense saline water flow on the bed moving back and forth with the tide.

Strongly stratified: Horizontally and vertically stratified throughout the whole tidal cycle. The freshwater outflow does mix more horizontally at the top of the water column compared to a salt wedge.

Partially stratified: Strong horizontal stratification but weak vertical stratification. The stratification dampens turbulent mixing, but the vertical stratification is only stable during part of the tidal cycle.

Well-mixed: Only horizontal stratification. Vertical turbulent mixing is strong and hardly influenced by vertical stratification.

This classification has been extended theoretically by Geyer and MacCready (2014) to seven stratification regimes, which allows for the prediction of a regime given some flow- and mixing parameters.

Estuarine salt intrusion results from a continuous competition between inflowing and outflowing transport mechanisms of salt. These mechanisms are often split into subtidal components; processes that are not correlated to the tidal time scale but occur over various tidal cycles, and tidal components; processes introduced by tidally varying flow velocities and varying water levels. Hence, estuary classification can also be based on the relative magnitude of transport components. In this study, next to the stratification regimes, we also refer to the *transport regimes* by Dijkstra et al. (2022). In their study, regime classification of estuaries is based on non-dimensional parameters that determine the balance of transport components and they identify seven different types of transport regimes. This classification shows the influence and relative importance of the various transport mechanisms using an idealised 2DV model setting. More detailed information on these two classifications is given in Sections 2.3.2 and 2.3.3. Next, we describe some of these transport mechanisms.

The main outflowing transport is a result of the flushing through **river discharge**, which advects salt seaward and is increased by vertical mixing, which can be considered a subtidal process.

The main mechanism in the subtidal shear processes is **gravitational circulation**, a flow that results from a horizontal pressure gradient due to a horizontal salinity gradient in the estuary (Hansen & Rattray Jr., 1966). The baroclinic pressure gradient induces a component in the exchange flow. It has a depth-averaged velocity of zero and is directed landward near the bed and seaward near the top, generating a flow pattern that enhances vertical stratification. Moreover, as the flux of salt is the product of flow velocity and concentration, the salt flux itself is not necessarily zero over the water column and can be transported inland (Dijkstra, 2014). Larger tidal forcing causes an increase in vertical mixing and shear stress, which decreases stratification (Lerczak et al., 2009).

Tidal mechanisms of salt transport are often dependent on the geomorphology of the system. An example of this is **tidal trapping**, where salt is temporarily stored during ebb in side-embayments or tidal flats. The timing of inflow and outflow occurs asymmetrically, leading to a net influx of salt (Garcia et al., 2022). **Tidal pumping** results from the barotropic pressure gradient, where horizontal

density differences occur due to gradients in water elevation and can lead to a net influx due to tidal asymmetry (Yu et al., 2014). It is mainly dominant in macrotidal estuaries that are well-mixed vertically.

Another external process is transport due to wind; onshore winds can introduce storm surges that increase the mean water level and in turn, increase salt intrusion. Moreover, the wind itself in the estuary can change the estuarine salinity structure by several mechanisms, such as shear with the free surface and wind-induced mixing (Jongbloed et al., 2022). In turn, stratification interferes with the production and dissipation of turbulence, however, this interaction is difficult to model (Caulfield, 2021).

All in all, these processes result in salt intrusion, often quantified by the salt intrusion length, which we define[2] as the distance from the mouth to the point where the maximum salinity equals 1 ppt. The relative contribution of the transport processes largely depends on the existing hydrodynamic forcing conditions and estuarine geomorphology. Large river flows increase the outflowing transport, whereas an increase in tidal activity and asymmetry can increase the inflowing transport. In the end, the balance between all forcing terms determines the salt intrusion length, and the geomorphology modifies the boundaries in which this balance is determined (Hendrickx et al., 2023b).

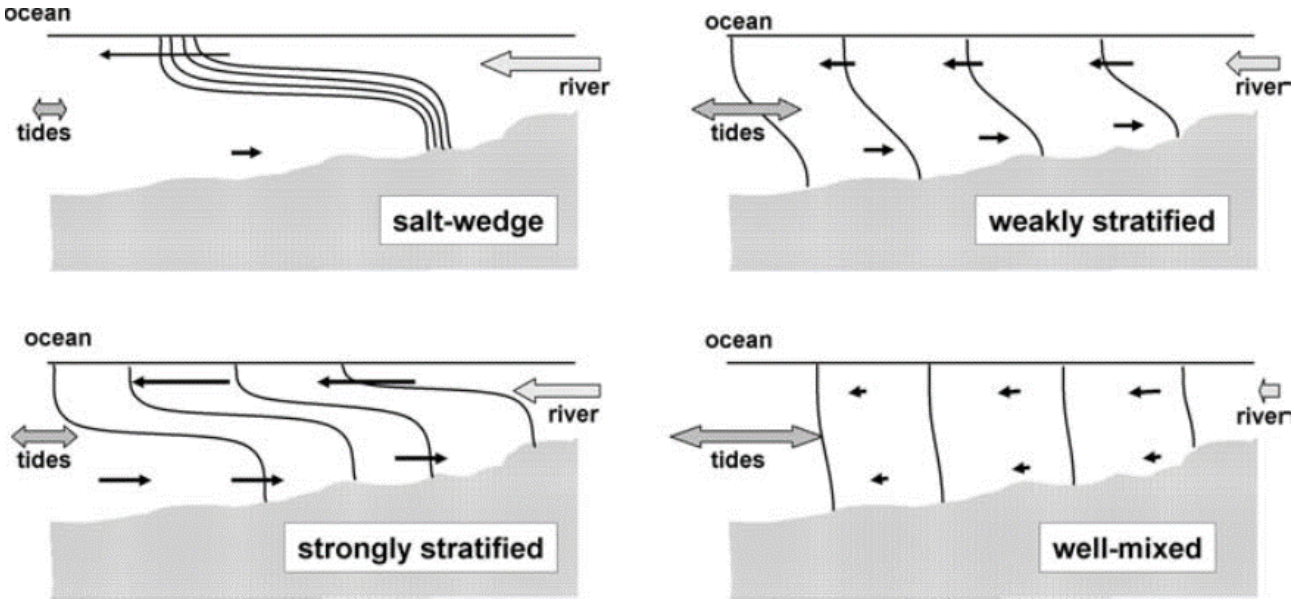

Figure 1.1: Schematisation of the estuary stratification regimes as in Pritchard (1952). Note that the arrows represent the relative magnitude of the flow velocities of the river and the tide.

1.4 The Rotterdam Waterway (RWW)

The Rotterdam Waterway (RWW) estuary is a complex system of the Rhine-Meuse delta in the West of the Netherlands (see Figure 1.2) that contains a main channel with multiple smaller branches, side basins, and harbours. The river Rhine enters the Netherlands in Lobith and forms the main source of freshwater discharge through the system. Due to the many branches and diversions of water, the overall river discharge is usually measured at Lobith. In this study, we consider the RWW estuary as the main channel of the Nieuwe Waterweg (E), the Scheur (C) and Nieuwe Maas (B) as shown in Figure 1.2. As inflowing freshwater discharge, we combine the flow of the Lek (A) and Noord (B). We assume the contribution to the flow by the Oude Maas (dashed lines) can be neglected, in line

[2]This definition is further formalised in Subsection 2.2.2 and the influence on the results is discussed in Section 4.2.

with Hamilton (1975). Moreover, the influence of salt transport over channel junctions as described by Biemond et al. (2023) is neglected. Figure 1.2 shows how this system is approximately 50 km long as we assume that all salt dynamics can be captured over this length and the influence of tidal flow velocities is minimal at the landward end.

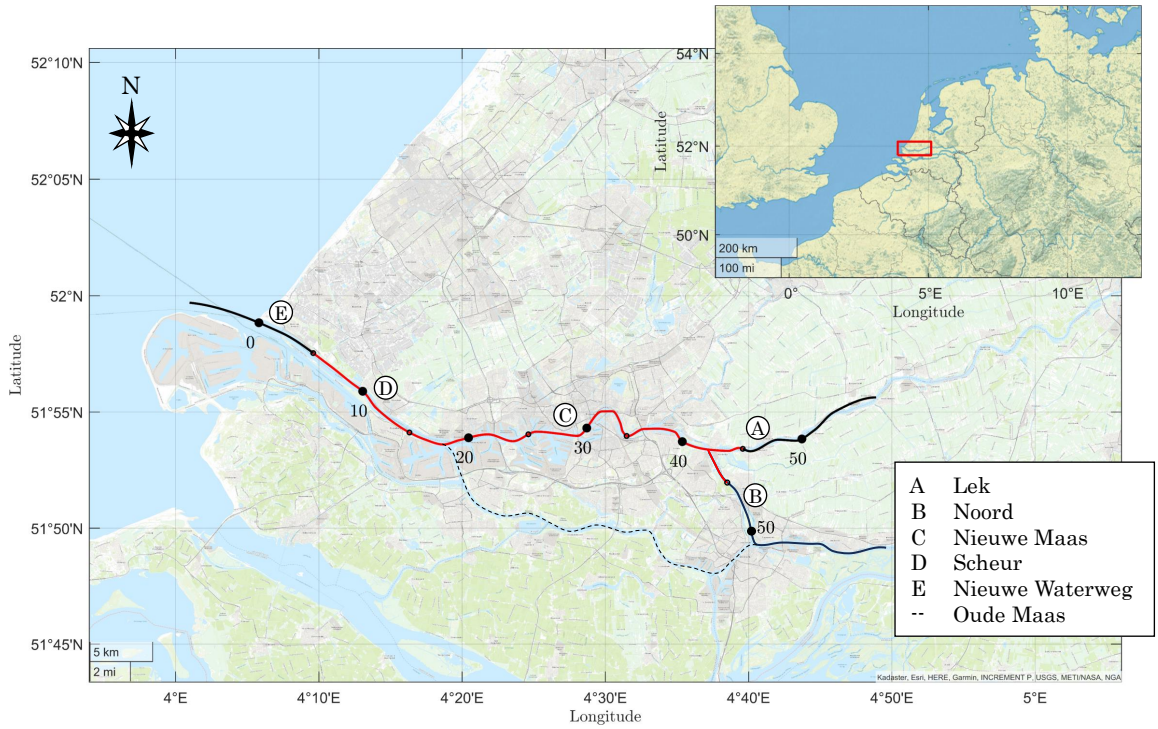

Figure 1.2: The Rotterdam Waterway in the Rhine-Meuse estuary in The Netherlands. Numbers indicate the along-estuary position in kilometres with $x = 0$ km located on the seaward side.

The RWW is an estuary with noticeable tidal activity with various tidal constituents and the tidal propagates relatively far into the system (an amplitude of 65% in the Lek compared to the seaward amplitude) (Rijkswaterstaat, 2023b). The dimensions and characteristics of the RWW vary along its length, but the cross-section is generally quite rectangular in the region of salt intrusion, there are no tidal flats and the estuary can be considered as one channel. The width varies from 265 m at its narrowest point in the Nieuwe Maas to 675 m in the Nieuwe Waterweg (Rijkswaterstaat, 2023a). By recurrent dredging operations, the Nieuwe Waterweg and Scheur are maintained at a depth of -16.20 m NAP, and the depth decreases to -5.2 m NAP at the Eastern side in the Nieuwe Maas as it connects to the Lek.

The degree of salt intrusion depends on factors such as tidal range, river discharge, and seasonal variations, but is most severe during summer time conditions when the discharge of Lobith is less than 1100 m^3/s (Laan et al., 2023). During summer conditions, the estuary is mainly classified as a partially mixed estuary and becomes a salt wedge during higher winter discharges (Dijkstra et al., 2022).

The average discharge at Lobith is around 2900 m^3/s, of which approximately half exits the system through the Nieuwe Waterweg (E). We distinguish high and low flow conditions, which we define as less than 1200 m^3/s and more than 4000 m^3/s at Lobith respectively[3]. During low discharges, the Haringvliet sluices are mostly closed and almost all water exits the system through the Nieuwe Waterweg (E) to eliminate a large salt influx. This flushing strategy is employed throughout the

[3]As a reference, during the extreme drought of 2022 the river discharge at Lobith reached 679 m^3/s. A discharge less than 800 m^3/s is only observed twice between 1901 and 2022 (Ottink et al., 2022)

Netherlands to mitigate salt intrusion. However, as the need for freshwater increases and the available freshwater reserves are under threat due to climate change and extreme events. This flushing strategy is considered unsuitable as a sustainable long-term solution and new mitigation strategies are necessary (Kennisprogramma Zeespiegelstijging, 2023).

Salt transport processes during high flow conditions

Flow and salinity measurements by de Boer and Radersma (2011) in the RWW in 2006 show significant salt intrusion, even during high Rhine discharges (varying from 4000 to 5800 m^3/s). Relative to Hook of Holland ($x = 0$ km in Figure 1.2), the minimum near-bed saltwater intrusion lengths were 11 km at low tide and 20 km at high tide. These measurements show the stable existence of a salt wedge during the entire measurement period. The processes influencing the along-channel current structure and the excursion of the salt wedge show that the combination of barotropic and baroclinic forcing, in conjunction with the suppression of turbulence at the interface results in tidal dependence and mean structure of the flow in the RWW. The displacement and structure of the salt wedge are governed by advection since turbulent mixing is suppressed through the pycnocline. Furthermore, they show that turbulence production is correlated to the tide, with flood creating additional eddy diffusivity. Lastly, these measurements are laterally relatively consistent, and the system can be evaluated by a longitudinal cross-section.

Salt transport processes during low flow conditions

During summer conditions, with discharge values below 1200 m^3/s at Lobith, the gravitational circulation is found to be the dominant salt import mechanism in the RWW (Kranenburg & van der Kaaij, 2019). Further upstream, this influence is diminished and the tidally correlated flux, the advective transport mechanism correlated to the tidal cycle, is dominant most of the time. Dijkstra et al. (2022) have shown that the processes determining the salt intrusion in the RWW can be classified locally by separate fluxes. Downstream, up to 26 to 30 km from the seaward boundary, salt transport is characterised as a Chatwin regime. Here, salt transport is governed by a balance due to subtidal shear by gravitational circulation and river-induced flushing. Further upstream, near the freshwater boundary, gravitational circulation becomes less important and a balance between transport due to tidally correlated depth-averaged transport and river-induced flushing exists. These results were found for models with relatively low Rhine discharges at Lobith of around 1000 m^3/s. Kranenburg and van der Kaaij (2019) claim that measures that increase vertical mixing will be the key measures to mitigate salt intrusion in the RWW most of the time.

For our model, as formulated in Chapter 3, we idealise this system as a channel with a length of 50 km and uniform width and depth of 500 m and 15 m respectively. We define the point $x = 0$ km as the seaward mouth located at Hoek van Holland, leading to the along-estuary position $x = 50$ km located in the Lek, as visualised in Figure 1.2.

1.5 Estuarine Sand Dunes

Estuarine sand dunes are distinct bed forms occurring within estuaries, exhibiting similarities to river dunes and marine sand waves, albeit with specific characteristics. Hulscher and Dohmen-Janssen (2005) highlight their shared features, such as relatively long wavelengths compared to water depth, amplitudes of approximately 10% of water depth, and their typical two-dimensional nature as their crests are relatively long and uniform. Moreover, these bedforms align perpendicularly to the main current direction (i.e. river flow and tidal flow on coastal shelves respectively) and form near-bed vertical vortices as shown in in Figure 1.3.

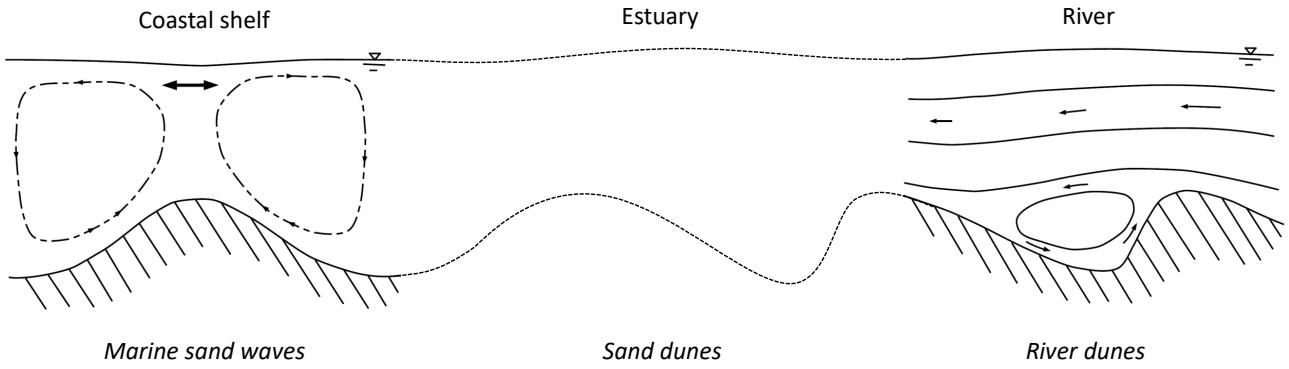

Figure 1.3: Schematic presentation of the tidal flow above sand waves (left) and the flow over river dunes (right). (Figure derived and adapted from Hulscher and Dohmen-Janssen (2005)). Both a background river flow and oscillating tidal flow occur over estuarine sand dunes and a combination of both flow patterns can be present over estuarine sand dunes.

Marine sand waves usually display relatively mild slopes, due to the dominant M2 tide[4] causing sediment transport on both sides. The vertical vortices in Figure 1.3 show tide-averaged residual circulations. The overall magnitude of the circulation flow is small compared to the background current and this flow is not instantaneous at both sides.

River dunes are usually strongly asymmetric, and their geometry mainly depends on the background riverine flow. Field observations in the river Waal show that the dune height decreases, but the dune length decreases during lower summer river discharges (Lokin et al., 2022). Furthermore, the lee side angle was relatively small, ranging from 1° to 3°. However, an increase in dune height and asymmetry can result in large lee-side slope angles that may introduce a flow separation zone and recirculation cell on the steep lee side as shown by the solid line (Lefebvre, 2019). This introduces energy losses and significantly alters flow resistance, potentially leading to higher water levels and intensified vertical mixing (Paarlberg et al., 2009). The precise conditions under which this occurs are not yet fully known (Best, 2005). Using experiments, Best and Kostaschuk (2002) show that intermittent flow separation occurs over dunes with maximum lower lee side slopes of 14°. Some modelling studies assume flow separation already takes place at a critical angle of 10°, but the equilibrium dune dimensions are independent of this value (Paarlberg et al., 2009). Overall, these flow separation effects are non-hydrostatic and can not be captured by a hydrostatic model.

Turbulence

In estuaries, these general characteristics are also observed in bedforms and we refer to these as estuarine sand dunes (Zorndt et al., 2011). They are subject to both tidal- and river forcing and the stratification results in additional forming mechanisms (van der Sande et al., 2021, 2023). Reversely, the influence of estuarine sand dunes on the flow is not fully understood. Field measurements show that sand dunes induce roughness on the flow, which can be attributed to both vortex shedding and wake flapping, related to high and low frequencies respectively (Kostaschuk, 2000). This increase in roughness results in lower horizontal flow velocities and higher mean water levels. According to Best et al. (2001), sand dunes are responsible for the generation of large-scale vortices shedding of the crest, often referred to as macroturbulence, which may advect through the water column and break through the surface in upwelling. Previously, it was thought that this was the consequence of permanent flow separation on a steep dune lee side. The authors show that this also occurs intermittently for low-angle

[4]The principal lunar semi-diurnal tidal constituent

dunes with an angle of 14° where no consistent flow separation takes place for dunes in the Fraser River Estuary, Canada. This leads to a series of cascading diagonal wakes over a rhythmic dune pattern. In this estuary, the location of a salt wedge is correlated to the tidal cycle. Kostaschuk et al. (2010) showed that large internal waves form over the sand dunes, in phase with the bathymetry. This causes water from a highly stratified salt wedge to reach the free surface. Over a flat bed, this did not occur and mixing was restricted to the lower part of the water column. It is suggested that all the above mechanisms are enhanced by the asymmetry of the dune shapes (Bradley et al., 2013).

Internal waves can develop due to density stratification (Pietrzak et al., 1990). Estuarine sand dunes may cause resonance of these internal waves as the background flow increases. When the amplitude grows, internal waves may break and induce additional vertical mixing of the stratified water column which is shown using nonlinear non-hydrostatic models as in Wegman (2021). These internal waves are found in the RWW where they could reach amplitudes of 3 to 4 m (Pietrzak & Labeur, 2004). These non-hydrostatic processes can only be resolved on a small scale and can also not be modelled by a non-hydrostatic model. A laboratory study by Kranenburg and Pietrzak (1989) of a turbulent two-layer fluid, representing conditions of the RWW, found that near the pycnocline and regions of high stratification, there was a significant reduction in turbulence. They also demonstrated that, although internal waves can contribute to turbulence production in the lower layer, negligible mixing was observed between the layers.

Geometric characteristics

We characterise estuarine sand dunes mainly by their dimensions and direction of orientation. A conceptual diagram of estuarine sand dunes is shown in Figure 1.4 where we define a single sand dune from one trough to the next. The total dune length λ_d is defined as the length between subsequent dune troughs. The dune height H_d is defined as the difference between the trough and crest elevation. We distinguish between the lee side and stoss side of the dunes, where the stoss side faces the background river flow (upstream slope) and the lee side faces the sea (downstream slope), indicated by the arrow in Figure 1.4. Subsequently, we can separate the dune length λ_d into the stoss side length λ_s and lee side length λ_l. When $\lambda_s \geq \lambda_l$, we refer to this as ebb-oriented sand dunes, which is the case for the example shown in Figure 1.4.

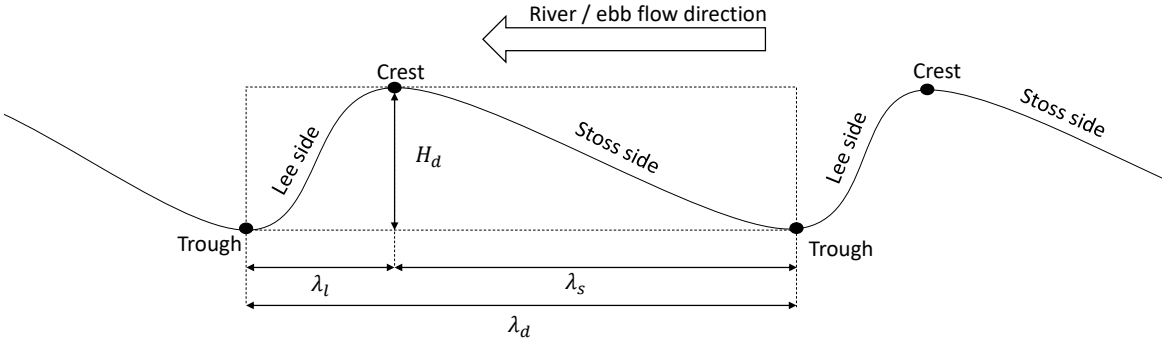

Figure 1.4: Schematisation of dune dimensions, showing dune height H_d, dune length λ_d and the lengths λ_l, λ_s of the lee and stoss side respectively.

Many empirical relations estimating river dune dimensions exist based on the water depth. For a mean depth of $h = 15$ m, this gives rise to the river dune length of $\lambda_d = 5h = 75$ m by Yalin (1964) and river dune height $H_d = h/6 = 2.5$ m and $\lambda_d = 1.16h^{1.55} = 77.2$ m by Allen (1978). However, the variation between rivers and within rivers is large (Bradley & Venditti, 2017). In the North Sea, a large variation in sand wave dimensions exists, with heights ranging from 1 to 8 m and lengths in

the order of 100 to 1000 m (Damen et al., 2018). In estuaries, stratification and horizontal density gradients create additional dynamics that change the forming mechanisms for estuarine sand dunes. Pietrzak et al. (1990) showed that the RWW has a topography with sand dunes of typical length 30 to 80 m and heights of 1.0 to 2.0 m. At around longitudinal coordinate $x = 15$ km, Pietrzak et al. (1991) measures permanent ridges with lengths of $\lambda_d = 28$ m to 74 m and heights from $H_d = 1.15$ m to 1.8 m. Slightly further downstream at $x = 8$ km, two adjacent large-scale topographic features were found with heights of 2 to 3 m. These dimensions are more in line with river dunes, likely due to the relatively narrow confinement of the RWW and the relatively spatially constant river velocity. In this study, we consider sand dunes ranging from $\lambda_d = 50$ m to $\lambda_d = 250$ m and heights up to $H_d = 4.5$ m.

Chapter 2

Model Formulation and Theoretical Analysis

In this chapter, we introduce the model equations based on the 2DV model assumptions[5]. Next, we describe some techniques necessary for analysis of model output, to ascribe some phenomena to physical processes. Finally, in Section 2.3, we use a theoretical analysis of the model equations to predict the influence of sand dunes on vertical flow, and apply non-dimensionalisation to distinguish the dominant processes of the model.

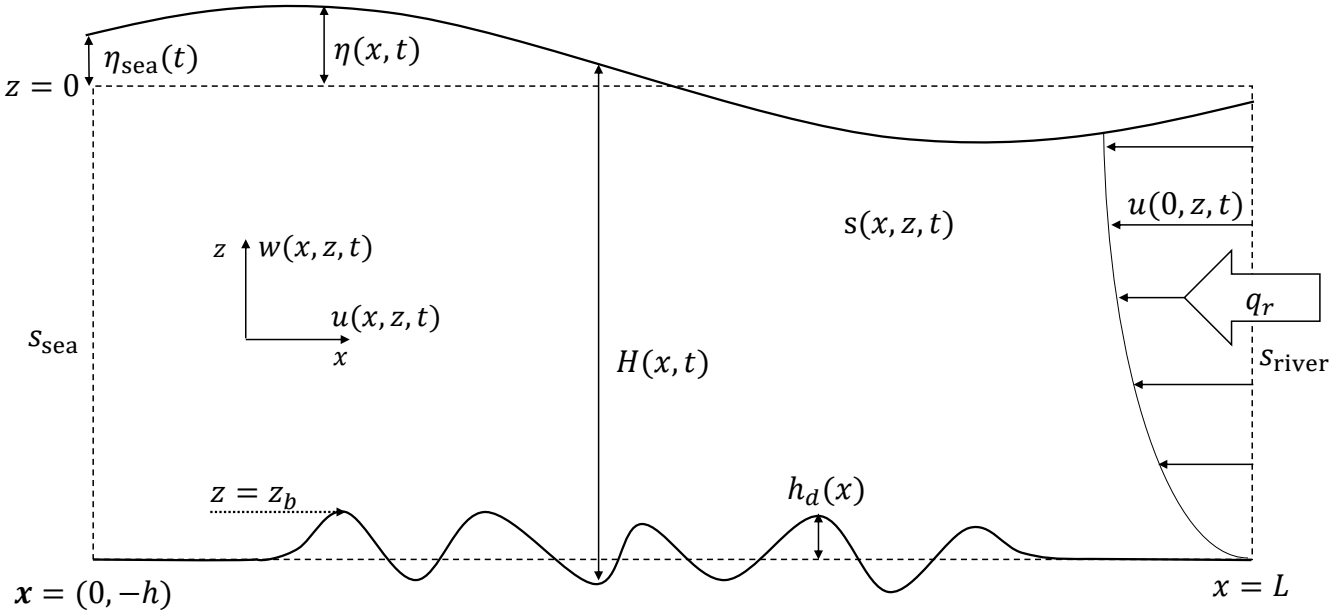

Figure 2.1: Schematisation of the geometry and variables used. The seaward boundary, displaying tidal oscillations, is on the left (at $x = 0$) and the landward boundary, with river inflow, is on the right (at $x = L$).

[5]The abbreviation 2DV means two-dimensional vertical, with one horizontal and one vertical coordinate. The horizontal coordinate is directed along the estuary, which can capture the salt intrusion length.

2.1 Model Geometry and Flow and Transport Equations

The network that comprises the RWW contains multiple channels and harbours but contains a main channel the main outflowing river water with quite uniform dimensions as introduced in Section 1.4. Therefore, to simplify this, lateral variation is neglected and the width-averaged processes of a single-channel estuary will be modelled to focus on the specific interaction of salt dynamics and estuarine sand dunes. The estuary is approximated as a single-channel system of length L, modelled by a 2DV geometry and only evaluating the $\boldsymbol{x} = (x, z)$ components. The seaward side is located at $x = 0$ with the landward (riverine) side at $x = L$. This can be interpreted as a rectangular estuary of constant width B, neglecting any lateral variation in salinity distribution and flow. Moreover, we consider a morphostatic situation without any bed level change and eliminate the influence of a bed slope on the flow by specifying a uniform average bed level h below the reference level $z = 0$. Subsequently, the bed level is defined at $z_b(x) = -h + h_d(x)$ with topography h_d. An overview of the system geometry with accompanying notation is shown in Figure 2.1.

The bed level at both the riverine and seaward sides is set to the mean bed level of $z = -h$ by specifying $h_d(0) = 0 = h_d(L)$. The free surface elevation is specified by variable $\eta(x, t)$. This means the instantaneous water depth is equal to

$$H(x, t) = \eta(x, t) - z_b(x). \tag{2.1}$$

Note that flow over an undulating bottom experiences additional roughness which may increase water levels and hence increase the average water depth. Hence, only without any river flow or tidal flow, the average water depth is guaranteed to equal h. The horizontal and vertical flow components are denoted by $\boldsymbol{u} = (u, w)$ respectively and salinity by s. We consider turbulent effects to be anisotropic, and implement the horizontal and vertical eddy effects separately, as is common within oceanic modelling. The flow and salt transport are modelled by the width-averaged (2DV) hydrostatic shallow-water equations (of which a full derivation is given in Appendix A.1.1)

$$\nabla \cdot \boldsymbol{u} = 0 \tag{2.2a}$$

$$\frac{\partial u}{\partial t} + (\boldsymbol{u} \cdot \nabla)u = \nabla \cdot (A \nabla \boldsymbol{u}) - g\frac{\partial \eta}{\partial x} - g\beta \int_z^{\eta(x)} \frac{\partial s}{\partial x} d\tilde{z} \tag{2.2b}$$

$$\frac{\partial s}{\partial t} + (\boldsymbol{u} \cdot \nabla)s = \nabla \cdot (K \nabla s), \tag{2.2c}$$

where the diagonal matrices A and K contain the horizontal and vertical eddy viscosity and diffusivity respectively, with

$$A := \mathrm{diag}(A_h, A_v), \quad K := \mathrm{diag}(K_h, K_v), \tag{2.2d}$$

in m^2/s. The density of water is denoted by ρ in kg/m^3 and related to salinity by the equation of state ρ_{Eck} (Equation 1.2) with contraction coefficient β in ppt^{-1}. We neglect the influence of a bed slope[6], and gravity acts downward in the vertical dimension z with gravitational acceleration constant g. The term $g\partial\eta/\partial x$ describes the barotropic pressure gradient and $g\beta \int_z^{\eta(x)} \frac{\partial s}{\partial x} d\tilde{z}$ the salinity-induced baroclinic pressure gradient (see derivation in Appendix A.1.1).

Inflowing water has salinity s_{sea} at the seaward side and s_{river} at the riverine side. A width-averaged river discharge $q_r(t)$ (in m^2/s) results in a logarithmic horizontal profile at $x = L$, and the tidal elevation is assumed to be a single harmonic of frequency ω by

$$\eta(0, t) = \eta_{\mathrm{sea}}(t) = A_{\mathrm{sea}} \cos(\omega t), \tag{2.3}$$

[6] Which is representative of the deeper dredged part of the RWW.

at the seaward side for seaward amplitude A_{sea} and angular frequency ω. We choose only the semi-diurnal M2 tide with angular frequency $\omega = 1.4 \cdot 10^{-4}$ rad/s. When the eddy viscosity A and diffusivity K are specified, the problem is well-posed. In Chapter 3, we specify spatially and temporally varying values for A and K using a turbulence closure for a more accurate representation of the flow.

2.2 Quantification of Stratification and Mixing

In this section, the definition of the salt intrusion length is revisited, and we explain the underlying physical processes that govern the transport of salt in estuaries. More background information on the stability of stratification is provided in Appendix A.1.2.

2.2.1 Averaging Operators

First, we introduce some notations used for the various types of averaging needed throughout the report, given for arbitrary variables ψ. For depth-averaged values of ψ, we use an overbar:

$$\overline{\psi}(x,t) = \frac{1}{H(x,t)} \int_{z_b(x)}^{\eta(x,t)} \psi(x,z,t) dz. \tag{2.4}$$

Many processes can be considered subtidal over a tide with period $T = 2\pi/\omega$. Therefore, we define the tidally-averaged (or subtidal) value of any variable ψ to be

$$\langle \psi \rangle(x) = \frac{1}{T} \int_0^T \psi(x,t) dt. \tag{2.5}$$

Note that due to the fluctuating free surface, tidal averaging cannot be done over a vertically varying variable. For example, a hydrodynamic variable only exists for $z > 0$ for part of the tidal cycle. These values can only be given under the rigid lid approximation or after vertical averaging. Finally, some processes show large local fluctuations over the dune field. Therefore, we define the dune-averaged value of ψ to be

$$(\psi * d)(x) = \int_{-\infty}^{\infty} d(x - \tilde{x}) \psi(\tilde{x}) d\tilde{x} = \frac{1}{\lambda_d} \int_{x-\lambda_d/2}^{x+\lambda_d/2} \psi(\tilde{x}) d\tilde{x}, \tag{2.6}$$

for dune convolution filter

$$d(x) = \begin{cases} \frac{1}{\lambda_d}, & |x| \leq \lambda_d/2 \\ 0, & \text{else} \end{cases} \tag{2.7}$$

Some model output is directly proportional to dune slope or depth H, and hence changes sign over a dune, making it unsuitable to determine the global influence. Hence, dune-averaging can be used to filter out this dependence and to determine the global behaviour of highly varying variables.

2.2.2 Salt Intrusion Length and Stratification Quantification

Firstly, we define the main model output we use for investigating the influence of sand dunes on salt intrusion. In line with Dijkstra et al. (2022), we define the **maximum salt intrusion length** $L_s(t)$ as the maximum distance from the seaward side where the maximum salinity over the water column equals the *critical concentration* $s_c = 1$ ppt. More specifically, we define it by

$$L_s(t) := \max\{x \text{ s.t. } \max_z s(x,z,t) \geq s_c\}. \tag{2.8}$$

Usually, it is assumed that this value is attained at the bed, i.e. $\max_z s(x,z,t) = s(x,z_b,t)$. However, this might not necessarily be the case over sand dunes. Since this is a function over time, we usually depict this as the tidally averaged salt intrusion length $\langle L_s \rangle$ with excursion length

$$\Delta L_s := \max(L_s) - \min(L_s) \tag{2.9}$$

over the last tidal cycle. An alternative definition would be the **depth-averaged salt intrusion length** $L_{\overline{s}}(t)$ (Jongbloed et al., 2022; Hendrickx et al., 2023b), which we define as the maximum distance from the seaward side where the depth-averaged salinity $\overline{s}(x)$ is equal to 1 ppt, or

$$L_{\overline{s}}(t) := \max\{x \text{ s.t. } \overline{s}(x,t) \geq s_c\} \tag{2.10}$$

Again, this can be characterised by $\langle L_{\overline{s}} \rangle$ and $\Delta L_{\overline{s}}$. In both measures, a larger salt intrusion length excursion (Δ) implies a larger tidal correlation.

Finally, we characterise the amount of stratification, as in the classification of MacCready and Geyer (2010) of Figure 1.1, by the length of the 1-ppt-isohaline. We assume that the minimum salinity is attained at the surface, and define the **surface salt intrusion length** as

$$L_{s_\eta}(t) := \max\{x \text{ s.t. } s(x,\eta,t) \geq s_c\} \tag{2.11}$$

This results in the horizontal length of the 1-ppt isohaline of $L_i := L_s - L_{s_\eta}$, which we describe by

$$\langle L_i \rangle = \langle L_s - L_{s_\eta} \rangle = \langle L_s \rangle - \langle L_{s_\eta} \rangle, \tag{2.12}$$

$$\Delta L_i = \max(L_i) - \min(L_i) \tag{2.13}$$

With small isohaline length $\langle L_i \rangle$, a system tends to a well-mixed system and becomes more stratified with increasing $\langle L_i \rangle$. Moreover, a large value of ΔL_i implies more tidal variation in classification.

2.2.3 Salt Flux Decomposition

The transport of salt can be quantified using the salt flux. Using the divergence-free condition Equation 2.2a, we can write

$$(\boldsymbol{u}\cdot\nabla)s - \nabla\cdot(K\nabla s) = \nabla\cdot(\boldsymbol{u}s) - s\cancelto{0}{(\nabla\cdot\boldsymbol{u})} - \nabla\cdot(K\nabla s) = \nabla\cdot(\boldsymbol{u}s - K\nabla s).$$

Hence, the overall transport equation Equation 2.2c can be written as

$$\frac{\partial s}{\partial t} + \nabla\cdot\boldsymbol{\Phi} = 0, \tag{2.14}$$

where

$$\boldsymbol{\Phi} = \begin{pmatrix}\Phi_h \\ \Phi_v\end{pmatrix} := \begin{pmatrix} us - K_h\dfrac{\partial s}{\partial x} \\ ws - K_v\dfrac{\partial s}{\partial z}\end{pmatrix}, \tag{2.15}$$

is the overall salt flux in horizontal and vertical direction respectively, containing both an advective and dispersive component.

Horizontal and Vertical Components

As stated in Section 1.3, the salt intrusion length is a result of a balance of inflowing and outflowing fluxes over the estuary. Therefore, we are mainly interested in the horizontal transport of salt over a water column and define horizontal estuarine salt transport as

$$Q_h(x) = \langle H(x,t)\overline{\Phi_h}\rangle = \left\langle \int_{z_b(x)}^{\eta(x,t)} \left(us - K_h \frac{\partial s}{\partial x} \right) dz \right\rangle, \tag{2.16}$$

in ppt m^2/s. We distinguish between the horizontal *advective* and *dispersive transport*[7] components as

$$Q_u = \langle H\overline{us}\rangle, \tag{2.17}$$

$$Q_{K_h} = -\left\langle H\overline{K_h \frac{\partial s}{\partial x}}\right\rangle \tag{2.18}$$

respectively. These values can be interpreted as the horizontal flux through a water column of 1 m width. Furthermore, vertical mixing decreases the salt intrusion length. Therefore, we quantify the amount of vertical transport by the depth-averaged flux through a parcel of unit length and width using

$$T_v(x) = \langle\overline{\Phi_v}\rangle = \left\langle \frac{1}{H(x,t)} \int_{z_b(x)}^{\eta(x,t)} \left(ws - K_v \frac{\partial s}{\partial z} \right) d\tilde{z} \right\rangle \tag{2.19}$$

in ppt m/s. Similarly, we define vertical *advective* and *dispersive transport* as

$$T_w = \langle\overline{ws}\rangle, \tag{2.20}$$

$$T_{K_v} = -\left\langle\overline{K_v \frac{\partial s}{\partial z}}\right\rangle, \tag{2.21}$$

respectively. Note that we refer to both quantities Q_h and T_v as *transport*, even though their physical interpretation differs. A schematic representation of both the horizontal transport Q_h and vertical transport T_v is shown in Figure 2.2.

Decomposition of Advective Terms

To unravel which processes contribute to the overall salt transport in the estuary, we use a salt flux decomposition. Due to the free surface, the averaging operators $\overline{\psi}$ and $\langle\psi\rangle$ are not commutative, and the salt flux decomposition is structured differently than in Dijkstra et al. (2022). First, we write the velocity components and salinity as a depth-averaged $\overline{\psi}$, and depth-varying part ψ', with

$$\begin{aligned} u(x,z,t) &= \overline{u}(x,t) + u'(x,z,t) \\ w(x,z,t) &= \overline{w}(x,t) + w'(x,z,t) \\ s(x,z,t) &= \overline{s}(x,t) + s'(x,z,t) \end{aligned}$$

using Equation 2.4, such that the depth-averaged value of vertical variations equals $\overline{\psi'} = 0$, for ψ both velocities and salinity. Subsequently, the depth-averaged value can be decomposed into a subtidal part

[7] We call it dispersive as the eddy diffusivity depends on the flow and turbulence and is, therefore, a combination of diffusion and turbulent dispersion

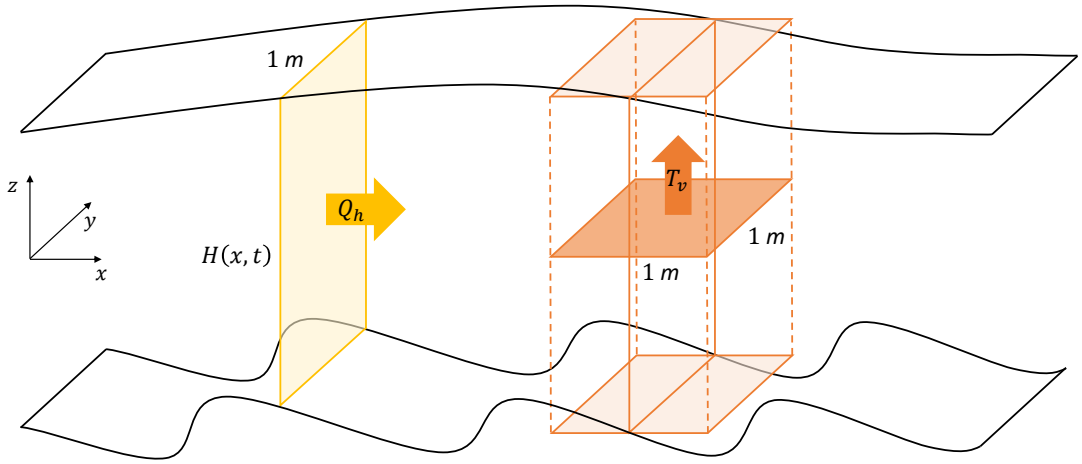

Figure 2.2: Visual representation of the horizontal and vertical transport definition.

and a tidally varying part, resulting in

$$\begin{aligned} u(x,z,t) &= \overline{u}_0(x) + \overline{u}_t(x,t) + u'(x,z,t), \\ w(x,z,t) &= \overline{w}_0(x) + \overline{w}_t(x,t) + w'(x,z,t), \\ s(x,z,t) &= \overline{s}_0(x) + \overline{s}_t(x,t) + s'(x,z,t), \end{aligned}$$

where we use $\overline{\psi}_0 = \langle\overline{\psi}\rangle$ and $\overline{\psi}_t = \overline{\psi} - \overline{\psi}_0$. Equally, we now have that the tidal mean of tidal variations equals $\langle\overline{u}_t\rangle = 0$. In that case, the horizontal salt flux decomposes (of which a full derivation is given in Appendix A.1.4) into

$$Q_u = \underbrace{\overline{u}_0\overline{s}_0\langle H\rangle}_{:=\overline{Q}_{h0}} + \underbrace{\langle H\overline{u}_t\overline{s}_t\rangle}_{:=\overline{Q}_{ht}} + \underbrace{\langle H\overline{u's'}\rangle}_{:=Q'_h} + \underbrace{\overline{u}_0\langle H\overline{s}_t\rangle + \overline{s}_0\langle H\overline{u}_t\rangle}_{:=Q_{h0t}}. \tag{2.22}$$

Here we distinguish the *subtidal depth-averaged transport* $\overline{Q}_{h0}$ (due to river flushing), *tidally-correlated depth-averaged salt transport* $\overline{Q}_{ht}$ (tidal motion, i.e. tidal pumping) and the *shear transport* Q'_h (employing vertical differences in flow velocity, both subtidal and tidal). For the vertical advective transport T_w, an equivalent decomposition to the horizontal is performed, leading to

$$T_w = \underbrace{\overline{w_0}\,\overline{s_0}}_{:=\overline{T}_{v0}} + \underbrace{\langle\overline{w}_t\overline{s}_t\rangle}_{:=\overline{T}_{vt}} + \underbrace{\langle\overline{w's'}\rangle}_{:=T'_v}, \tag{2.23}$$

which we refer to as the *subtidal depth-averaged upward transport* $\overline{T}_{v0}$ (due to a consistent upward or downward velocity), *tidally-correlated depth-averaged salt transport* $\overline{T}_{vt}$ (variations in mean vertical velocity due to tidal activity) and the *shear transport* T'_v (due to vertical variations in flux over the water column). All these individual components can be found by postprocessing of the model outcomes and are normalised by the tidal- and depth-averaged salt concentration $\langle\overline{s}\rangle$, such that the order of magnitude of the components is uniform along the estuary.

The term Q_{h0t} is the residual of the averaging procedure and is usually small unless a large tidal asymmetry is present. In the research of Kranenburg and van der Kaaij (2019) the decomposition is

done by reversing the averaging procedures: first applying tidal averaging $\langle\psi\rangle$ and subsequently applying depth-averaging on the subtidal and tidal components, similar to the theoretical decomposition under the rigid lid approximation of Dijkstra et al. (2022). However, Kranenburg and van der Kaaij (2019) employ a model with surface displacement, and tidal averaging is done on the volume fluxes through grid cells moving vertically with the surface displacement, ignoring the change of vertical coordinates of the cells. The resulting error of this procedure is referred to as Stokes' drift, and the sum of all advective components does not equal the total advective transport. The benefit of this decomposition is the splitting of the advective term into four components, as it allows for the shear transport Q'_h to be decomposed into a subtidal- and tidally-correlated component. The 4-component splitting method has been implemented for our model results and shows that the contribution of the tidally-correlated shear component is rather small, in line with results of Pietrzak and Labeur (2004), Kranenburg and van der Kaaij (2019), and Dijkstra et al. (2022) of the RWW. Therefore, Q'_h denotes the overall shear transport component, which mostly captures the subtidal shear of the subtidal estuarine circulation.

Finally, note that the interpretation of the horizontal and vertical transport components differs and a physical process can be traced back to different components. For example, the estuarine circulation causes vertical variation in the horizontal flow and can be seen in Q'_h, whereas this causes a persistent vertical flow that is seen in $\overline{T}_{v0}$. Hence, similar notation of transport components of Q_h and T_v do not necessarily belong to the same process.

Dune-averaging and Quantification of Vertical Mixing

The flow shows large fluctuations over the sand dunes, both dependent on depth and dune slope. Dune-averaging allows for evaluating the net transport over a single dune as introduced in Subsection 2.2.1. Therefore, when sand dunes are implemented, most horizontal components will be shown as the normalised dune-averaged value, i.e. by

$$\widetilde{Q_\psi} := \frac{Q_\psi * d}{\langle\overline{s}\rangle * d}, \tag{2.24}$$

for each component of horizontal transport $Q_\psi \in \{Q_u, Q_v, Q_{K_h}, \overline{Q_{h0}}, \overline{Q_{ht}}, Q'_h, Q_{h0t}\}$ in m/s. Note that this dune-filtering only applies when dunes are present in the system. Otherwise, we simply normalise with

$$\widetilde{Q_\psi}(x) := \frac{Q_\psi}{\langle\overline{s}\rangle}. \tag{2.25}$$

For filtered vertical components of $T_\psi \in \{T_v, T_w, T_{K_v}, \overline{T_{v0}}, \overline{T_{vt}}, T'_v\}$, we first filter out the correlation to the topography of each component and the cross-correlation of the normalised transport rate to the topography by

$$\widetilde{T_\psi}(x) := \begin{cases} \left(\dfrac{T_\psi * d}{\langle\overline{s}\rangle * d}\right) * d, & H_d > 0 \\ \dfrac{T_\psi}{\langle\overline{s}\rangle}, & H_d = 0 \end{cases} \tag{2.26}$$

in m^2/s. Note that both normalised filtered transport components are now more velocity components and describe the relative transport to the background salinity profile. Furthermore, they are variables along the estuary and we quantify the mean vertical exchange through the estuary using

$$\mathcal{M}_v = \frac{1}{\max(L_s)} \int_0^{\max(L_s)} \widetilde{T_v} dx \tag{2.27}$$

that describes the vertical flux (both advective and dispersive), averaged in the region of significant salinity concentration[8].

The vertical velocity w over a single dune is of relatively equal magnitude but with an opposite sign on each side of the sand dune (see Appendix Subsection A.1.3 for a simple analytic approach). This means the dune-averaged value of the vertical flux ($\widetilde{T_v}$) can tend to zero. Therefore, additionally, we quantify the amount of overall vertical advective transport using the absolute amount of vertical mixing, which we describe using the *stirring variable*

$$\mathcal{S}(x) = \left(\frac{\left\langle \overline{|w|s} \right\rangle * d}{\langle \bar{s} \rangle * d} \right) * d. \tag{2.28}$$

2.3 Classification of Dominant Processes, Estuaries and Regimes

In this section, we show the dominant processes in estuaries and show how estuaries and transport regimes can be classified using a theoretical analysis of the flow and transport equations. These processes are identified on the full estuary scale, and hence, the influence of local sand dunes is not covered. A simple analytic interpretation of flow over sand dunes is provided in Appendix A.1.3.

2.3.1 Non-Dimensionalisation

We analyse the flow and transport equations theoretically using non-dimensionalisation of the system. This shows the relative importance of certain processes and enables a reduction in the apparent total number of free variables. We assume spatially uniform eddy viscosity and -diffusivity, in which case the system (2.2) can be non-dimensionalised using

$$\begin{aligned} \boldsymbol{x} &= (Lx^*, hz^*) & t &= \mathcal{T}t^* \\ \boldsymbol{u} &= (Uu^*, Ww^*) & \eta &= \tfrac{U^2}{g}\eta^* \\ \nabla &= \left(\frac{1}{L}\frac{\partial}{\partial x^*}, \frac{1}{h}\frac{\partial}{\partial z^*} \right) & s &= s_{sea}s^* \end{aligned} \tag{2.29}$$

where variables with an asterisk denote the non-dimensional formulation. Horizontal length scale L is equal to the salt intrusion length, flow landward beyond this point is not considered as salinity concentrations are small. Moreover, we introduce the vertical velocity scale $W = \frac{Uh}{L}$, and the flushing time of the system $\mathcal{T} = L/U$ for background river velocity $U = |U_r| = |-q_r/H|$ (Kranenburg, 1986). Moreover, we assume that the eddy viscosity and diffusivity are uniform and related by the Prandtl-Schmidt number σ_ρ as

$$\frac{A_h}{K_h} = \sigma_\rho = \frac{A_v}{K_v}. \tag{2.30}$$

In that case, the system reduces to

$$\frac{\partial u^*}{\partial t^*} + u^*\frac{\partial u^*}{\partial x^*} + w^*\frac{\partial u^*}{\partial z^*} = \frac{1}{\mathrm{Re}_h}\frac{\partial^2 u^*}{\partial x^{*2}} + \mathrm{St}\frac{\partial^2 u^*}{\partial z^{*2}} - \frac{\partial \eta^*}{\partial x^*} - \frac{1}{\mathrm{Fr}_r^2}\int_{z^*}^{\eta^*}\frac{\partial s^*}{\partial x^*}d\tilde{z}^*, \tag{2.31}$$

$$\frac{\partial s^*}{\partial t^*} + u^*\frac{\partial s^*}{\partial x^*} + w^*\frac{\partial s^*}{\partial z^*} = \frac{1}{\sigma_\rho}\left(\frac{1}{\mathrm{Re}_h}\frac{\partial^2 s^*}{\partial x^{*2}} + \mathrm{St}\frac{\partial^2 s^*}{\partial z^{*2}} \right). \tag{2.32}$$

where we use estuarine non-dimensional numbers relative to the flushing time. For this, we define the

[8] We do not take the mean over the full estuary length L, as large (read: unrealistic) transport rates can appear at regions of low salinity concentrations, a consequence of taking numerical gradients of small numbers and division of small numbers ($1/\langle \bar{s} \rangle$)

Freshwater Froude number: The ratio of the subtidal longitudinal flow velocity $U = |U_r|$ to the celerity c of the fastest internal wave by

$$\mathrm{Fr}_r := \frac{U}{c} \tag{2.33}$$

where $c = \sqrt{g\beta s_{sea} h}$ (MacCready & Geyer, 2010). Note that βs_{sea} is the mass density difference between salt and fresh water.

Estuarine Stokes number: The ratio of the flushing time scale to a time scale for the water column to fully mix by dispersion, equal to

$$\mathrm{St} := \frac{A_v}{h^2}\mathcal{T} = \frac{A_v L}{h^2 U}. \tag{2.34}$$

Horizontal turbulent Reynolds number that describes the ratio of inertial and viscous forces

$$\mathrm{Re}_h := \frac{LU}{A_h}. \tag{2.35}$$

In this case we take turbulent stresses into account by using the the horizontal eddy viscosity A_h.

For the RWW, we approximate the typical values by length $L = 20$ km, eddy viscosities $A_v = 10^{-3}$ m^2/s, and $A_h = 10$ m^2/s and flow velocities $U_r = -0.1$ m/s during summer river discharges (Kranenburg & van der Kaaij, 2019; Dijkstra et al., 2022). For a mean water depth $h = 15$ m, gravitational acceleration $g = 9.81$ m/s^2 and seaward salinity $s_{sea} = 35$ ppt, we have an internal wave celerity of $c = 1.98$ m/s. This results in the non-dimensional quantities $1/\mathrm{Fr}_r^2 = \mathcal{O}(10^2)$, $\mathrm{St} = \mathcal{O}(10^{-1})$, and $1/\mathrm{Re}_h = \mathcal{O}(10^{-2})$, which indicates the strong contribution of the baroclinic pressure gradient and shows how the vertical processes dominate the horizontal.

2.3.2 Estuary Classification of Geyer and MacCready (2014)

Geyer and MacCready (2014) argue that the classification of an estuary can be based on the amount of freshwater flushing, described on the freshwater Froude number $\mathrm{Fr}_r = |U_r|/c$, and the amount of freshwater mixing. The latter is described by a mixing parameter

$$M = \sqrt{\frac{c_D U_t^2}{\omega c h}} \tag{2.36}$$

which captures the tidal dynamics by angular frequency ω and the tidal velocity U_t, with the vertical mixing by non-dimensional roughness coefficient $c_D \approx (1-2.5)\cdot 10^{-3}$ (Geyer & MacCready, 2014) (see Appendix A.1.6 for more information and parameter equations). This classification only uses global estuarine-scale parameters and does not rely on the eddy viscosity and -diffusivity, and can therefore be used to classify estuaries based on global measurements.

The tidal elevation amplitude varies significantly over a spring-neap cycle and there is a large variability in river discharge over the seasons, resulting in variability of M and Fr_r respectively. This variability is estimated and visualised for the RWW in an overview of the seven classified regimes of Geyer and MacCready (2014) in Figure 2.3. During summer conditions in the RWW, the classification parameters equal $\mathrm{Fr}_r = 0.05$ and $M = 0.5$ approximately, making it a strongly stratified estuary. The horizontal border of the black rectangle is a result of a difference in tidal elevation amplitude due to spring-neap variations, and the vertical border results from a changing river velocity between summer and winter.

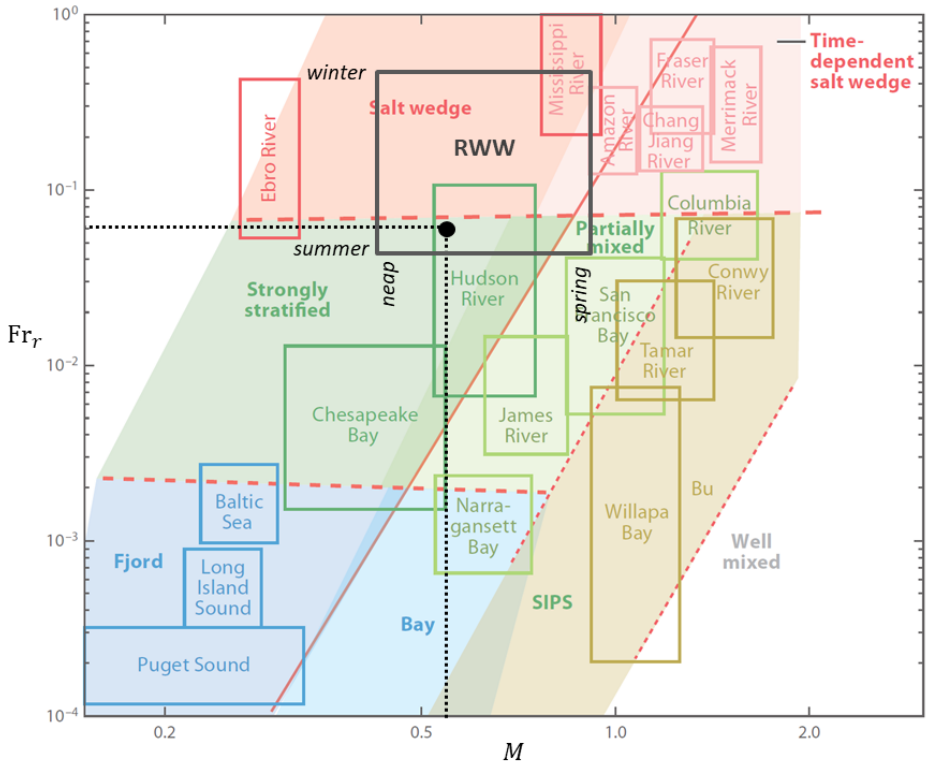

Figure 2.3: Estuary classification of Geyer and MacCready (2014) (adapted), with indicated classification of the RWW by the black dot.

If M would increase by an increase in tidal elevation amplitude or if Fr_r decreases even further, the system would tend to a partially mixed estuary. Increasing the freshwater discharge, as during winter conditions, results in a salt wedge regime, with a strong stratification and a clear saltwater tongue.

The salt intrusion length is related to the parameters M and Fr_r and smaller values increase the salt intrusion length. However, this classification determines the observable stratification structure by the balance of dominant terms in the momentum balance, rather than a prediction of the salt intrusion length. Hendrickx et al. (2023b) investigated the influence of estuarine-scale parameters on the salt intrusion length using 1250 idealised 3D hydrodynamic model runs, covering the M-Fr_r parameter space the classification of Geyer and MacCready (2014) shown in Figure 2.3 almost completely. They show that the salt intrusion length is suppressed for larger values of M and Fr_r and is largely determined by (1) river discharge (2) cross-sectional area (especially water depth); (3) tidal damping/amplification; and (4) tidal asymmetry, where (1,2) relate to Fr_r and the (4) to M. Tidal damping/amplification (3) depends on geomorphology and does not directly relate to Fr_r and M, indicating that more processes play a role in determining $\langle L_s \rangle$, even though the estuary classification remains equal.

2.3.3 Regime Classification of Dijkstra et al. (2022)

Dijkstra et al. (2022) classify narrow estuaries locally based on the dominant transport mechanisms semi-analytically, using internal mixing parameters (such as A_h and K_v). They solve the system of Equation 2.2 under the rigid lid approximation with spatially uniform eddy viscosity and -diffusivity and $A_h = 0$ m^2/s. Their classification is highlighted in this section, as it provides the basis for choosing suitable eddy parameters during model development, but a full derivation is given in Appendix A.1.7. Furthermore, we do not assume $A_h = 0$ m^2/s in line with the system of Equation 2.2. Under the rigid

lid assumption, we have that the depth-averaged flow velocity equals

$$\frac{1}{H}\int_{-H}^{0} u dz = U_r + U_t \cos(\omega t)$$

for tidal velocity amplitude U_t throughout the whole estuary, analogous to the derivation in Subsection A.1.3. In turn, Dijkstra et al. (2022) introduce the **tidal Froude number** Fr_t. Moreover, the characteristic time $\mathcal{T}$ of the system is chosen as the main M2 tidal forcing with angular frequency ω, i.e. $\mathcal{T} = 1/\omega$. Consequently, Dijkstra et al. (2022) define the non-dimensional parameters relative to this time scale and introduce the **tidal Stokes number** as

$$\mathrm{St}_t := \frac{A_v}{h^2}T = \frac{A_v}{\omega h^2} \tag{2.37}$$

which equals the ratio of a time scale for the water column to fully mix and the tidal time scale. Furthermore, they introduce the **estuarine Rayleigh number** as the reciprocal of mixing by

$$\mathrm{Ra} := \frac{h^2 c^2}{A_v K_h}, \tag{2.38}$$

and relates the internal waves through the channel to the vertical eddy viscosity A_v and horizontal eddy diffusivity K_h. Note that the horizontal length scale L is not captured by the non-dimensional numbers anymore. Hence, this scale itself is non-dimensionalised by

$$\mathcal{L} := L\frac{c}{K_h}. \tag{2.39}$$

as the ratio of the dispersive length scale K_h/c of horizontal diffusion and internal wave convection. For spatially uniform eddy viscosity and -diffusivity, with Prandtl-Schmidt number σ_ρ as in Equation 2.30, this results in

$$\begin{aligned}\frac{\partial u^*}{\partial t^*} + \mathrm{Fr}_r\,(\mathrm{St}_t\mathrm{Ra})\,\mathcal{L}^{-1}\left(u^*\frac{\partial u^*}{\partial x^*} + w^*\frac{\partial u^*}{\partial z^*}\right) &= (\mathrm{St}_t\mathrm{Ra})\,\mathcal{L}^{-2}\sigma_\rho\frac{\partial^2 u^*}{\partial x^{*2}} + \mathrm{St}_t\frac{\partial^2 u^*}{\partial z^{*2}} \\ &\quad -\mathrm{Fr}_r\,(\mathrm{St}_t\mathrm{Ra})\,\mathcal{L}^{-1}\frac{\partial \eta^*}{\partial x^*} - \mathrm{Fr}_r^{-1}\,(\mathrm{St}_t\mathrm{Ra})\,\mathcal{L}^{-1}\int_{z^*}^{\eta^*}\frac{\partial s^*}{\partial x^*}d\tilde{z}^*,\end{aligned} \tag{2.40a}$$

$$\frac{\partial s^*}{\partial t^*} + \mathrm{Fr}_r\,(\mathrm{St}_t\mathrm{Ra})\,\mathcal{L}^{-1}\left(u^*\frac{\partial s^*}{\partial x^*} + w^*\frac{\partial s^*}{\partial z^*}\right) = (\mathrm{St}_t\mathrm{Ra})\,\mathcal{L}^{-2}\frac{\partial^2 s^*}{\partial x^{*2}} + \mathrm{St}_t\,\sigma_\rho^{-1}\frac{\partial^2 s^*}{\partial z^{*2}}.. \tag{2.40b}$$

Dijkstra et al. (2022) argue that Fr_r may be interchanged with the tidal Froude number $\mathrm{Fr}_t = U_t/c$ for tidal velocity amplitude U_t everywhere, and changes of these parameters change the inflow boundary condition at $x = 0$ and influence the interior of the domain. Solutions[9] to these equations are approximated with a numerical iteration scheme to find a finite number of eigenfunctions. Subsequently, momentum Equation 2.40a and salt Equation 2.40b are decomposed into four and five processes respectively. For most estuarine systems, Fr_r and Fr_t range from 0 to 1, Ra from 10 to 10^5, and StRa from around 50 to 10^4. The large variability in Ra emanates from the large variability and uncertainty in A_v and K_h. Based on the relative contribution of these parameters, Dijkstra et al. (2022) identify four subtidal transport regimes, and three tidally-correlated transport regimes.

[9]Solutions are equations that are in dynamic equilibrium with the tide, i.e. periodic over a tidal cycle.

Parameters and Characteristic Values of the RWW

In Dijkstra et al. (2022), the authors use a 3D hydrodynamic model of the RWW from Kranenburg and van der Kaaij (2019) with during low-discharge conditions (of $U_r \approx -0.1$ m/s), which is used to identify the dominant local transport processes. The main stratified region of the RWW is governed by the subtidal Chatwin regime, where there is a balance between gravitational circulation and river-induced flushing. Further upstream (at around $x = 22$ km in Figure 1.2), the tidally correlated depth-averaged transport regime dominates. Previously, this was only associated with lateral tidal trapping processes, but the authors show that this can also exist without strong variations in geomorphology.

The model results give $\mathrm{Fr}_r \approx 0.05$, $\mathrm{Ra} \approx 6 \cdot 10^4$, and $\mathrm{St}_t\mathrm{Ra} \approx 1.9 \cdot 10^3$ in the main bulk of the estuary up to the salt intrusion limit. Using a length scale of $L = 20$ km, with these values we obtain

$$\mathrm{Fr}_r\ (\mathrm{St}_t\mathrm{Ra})\ \mathcal{L}^{-1} = 3.52 \cdot 10^{-2} \tag{2.41a}$$

$$(\mathrm{St}_t\mathrm{Ra})\ \mathcal{L}^{-2} = 2.61 \cdot 10^{-4} \tag{2.41b}$$

$$\mathrm{St}_t = 3.17 \cdot 10^{-2} \tag{2.41c}$$

$$\mathrm{Fr}_r^{-1}\ (\mathrm{St}_t\mathrm{Ra})\ \mathcal{L}^{-1} = 14.1 \tag{2.41d}$$

which again shows the huge importance of the baroclinic pressure gradient on flow by many orders. Moreover, advection and the barotropic pressure gradient (both by $\mathrm{Fr}_r\ (\mathrm{St}_t\mathrm{Ra})\ \mathcal{L}^{-1}$) are balanced by vertical viscosity and diffusion (by St) due to an equal order of magnitude. Furthermore, we see that the influence of horizontal viscosity and diffusion is negligible (by $(\mathrm{St}_t\mathrm{Ra})\ \mathcal{L}^{-2}$ being two orders smaller in magnitude). Lastly, the model output shows that the eddy viscosity parameters are approximately equal to $A_h = 10$ m^2/s and $A_v = 10^{-3}$ m^2/s throughout the estuary. These values will be considered for the development of the 2DV model and the transport mechanisms throughout the estuary (longitudinally) as shown in Dijkstra et al. (2022) can be used for verification of the developed model.

Chapter 3

Model Implementation and Development

The model will be implemented in Delft3D-FLOW, which is a commercial software package managed by Deltares that offers a suite of models for simulating hydrodynamics, sediment transport, water quality, and ecology, and is commonly used for coastal and delta management, river engineering, and offshore design (Deltares, 2018). In this chapter, we describe how the flow and transport equations are implemented in the software, and specify the turbulence closure and boundary conditions. Moreover, subsequent model development will be described, showing the spatial convergence of the model and explaining modelling choices.

3.1 Model Formulation in Delft3D-FLOW

In this section, we present the final model equations, including all boundary conditions and turbulence closure. First, we start with the flow and transport equations as already introduced in Chapter 2. Next, we introduce the necessary turbulence closure to determine eddy parameters. Finally, we highlight where salinity interacts with the flow.

Delft3D-FLOW solves the Reynolds-averaged Navier-Stokes equations for an incompressible fluid, neglecting non-hydrostatic effects and applying the shallow water approximation. Moreover, Reynolds stresses are modelled using the eddy viscosity concept, assuming different horizontal and vertical turbulence length scales. This leads to the model equations as in Equation 2.2, where A and K are solved using a turbulence closure. For shallow water flow the stress and diffusion tensor are assumed to be anisotropic. The horizontal eddy viscosity coefficient is much larger than the vertical eddy viscosity ($A_h \gg A_v$). A_h is mostly associated with the contribution of horizontal turbulent motions and forcings that are not resolved by the Reynolds-averaged shallow-water equation on the (usually relatively coarse) horizontal grid. A sub-grid scale (SGS) horizontal eddy viscosity ν_{SGS} model can be introduced to model some of the turbulent effects smaller than the grid size by an additional stress term through a methodology called Horizontal Large Eddy Simulation (HLES), together with a constant horizontal eddy viscosity ν_h^{BACK}. Later, we argue that the SGS model is unsuitable when implementing sand dunes in the topography explicitly, and we only use the constant background values.

3.1.1 Coordinate Transformation

In Delft3D-FLOW version 4, two grid types are available for the vertical direction: the (default) boundary-fitted σ-coordinates and a strictly horizontal grid called the z-grid. The σ-coordinate model

provides an accurate representation of the bathymetry and is therefore well-suited for simulating boundary layer processes. The z-coordinate model is introduced as the σ-grid is not able to reproduce realistic results in highly stratified systems with steep bottom topography. Bijvelds (2001) has shown that differences between the two grids are only observed when modelling regions with steep topography and coarse horizontal grids. To minimise the numerical diffusion, a vertical grid should be used with grid lines coinciding with the direction of anticipated flow fields and density gradients. Moreover, the results of both models should converge for sufficiently high horizontal resolution. This argues for the use of a Cartesian grid, but we hypothesise that near-bed boundary layer modelling is necessary to determine vertical mixing accurately and to implement estuarine sand dunes explicitly. Hence, we desire small vertical grid sizes near the bed. For an undulating topography of large dune height H_d, the computational time needed for the $z-$model would be infeasible if the complete dune field is captured by grid cells sufficiently small in the vertical direction. Therefore, the σ-grid will be used, which allows for small grid cells with small vertical scales above the bed, without drastically increasing the total number of grid cells. Moreover, this is likely to directly align the grid with vertical density gradients, as no global bed slope will be implemented.

The implementation of this vertical transformation results in different model equations. Using the water depth $H = \eta - z_b$, the σ-coordinate system is introduced with

$$\xi = x, \quad \sigma = \frac{z-\eta}{H}, \quad \tau = t \tag{3.1a}$$

such that the vertical dimension is always resolved in the constant domain from $\sigma = -1$ at the bed $z = z_b$ to $\sigma = 0$ at $z = \eta$. The time and space derivatives in the Cartesian coordinate system are subsequently expressed in σ-coordinates as

$$\frac{\partial}{\partial t} = \frac{\partial}{\partial \tau} + \frac{\partial \sigma}{\partial t}\frac{\partial}{\partial \sigma}, \tag{3.1b}$$

$$\frac{\partial}{\partial x} = \frac{\partial}{\partial \xi} + \frac{\partial \sigma}{\partial x}\frac{\partial}{\partial \sigma}, \tag{3.1c}$$

$$\frac{\partial}{\partial z} = \frac{\partial \sigma}{\partial z}\frac{\partial}{\partial \sigma} = \frac{1}{H}\frac{\partial}{\partial \sigma}. \tag{3.1d}$$

The horizontal velocity u remains strictly horizontal in the new coordinate system. We will therefore use the same notation in subsequent equations. The Cartesian vertical velocity equates to $w = Dz/Dt$, in the σ-plane this vertical velocity is denoted by ω and can be obtained similarly by

$$\omega = H\frac{D\sigma}{DT} = w - \left(\frac{\partial \eta}{\partial t} + u\frac{\partial \eta}{\partial x}\right) - \sigma\left(\frac{\partial H}{\partial t} + u\frac{\partial H}{\partial x}\right) \tag{3.2}$$

The full set of equations for $\sigma-$coordinates is given in the user manual of Delft3D-FLOW. The model equations are simplified in the 2DV setting and reiterated in this section. The interaction of salinity and flow is highlighted in parts of the equations in red, which is summarised in Subsection 3.2.4. The complete set of equations is given in Appendix A.2.1.

3.1.2 Flow Equations

Continuity Equation

Integration of the continuity equation over the water depth leads to an evolution equation for the free surface η by

$$\frac{\partial \eta}{\partial \tau} + \frac{\partial H\overline{u}}{\partial \xi} = 0 \tag{3.3}$$

where $\overline{u}$ is the depth-averaged horizontal velocity, defined as

$$\overline{u} = \int_{-1}^{0} u d\sigma.$$

Momentum Equation

In $\sigma-$coordinates, the vertical momentum equation equals

$$\frac{\partial p}{\partial \sigma} = -g\rho,$$

which yields a formulation for the hydrostatic horizontal pressure gradient after integration. Subsequently, the horizontal momentum equation reads

$$\frac{\partial u}{\partial \tau} + u\frac{\partial u}{\partial \xi} + \frac{\omega}{H}\frac{\partial u}{\partial \sigma} = \frac{\partial}{\partial \xi}\left(A_h \frac{\partial u}{\partial \xi}\right) + \frac{1}{H^2}\frac{\partial}{\partial \sigma}\left(A_v \frac{\partial u}{\partial \sigma}\right) - g\frac{\partial \eta}{\partial \xi} - \frac{gH}{\rho_0}\int_{\sigma}^{0} \frac{\partial \rho}{\partial \xi} + \frac{\partial \rho}{\partial \sigma}\frac{\partial \sigma}{\partial x} d\sigma'. \tag{3.4a}$$

Note that the horizontal coordinate transformation term $\partial\sigma/\partial x$ of Equation 3.1c is only implemented in the barotropic pressure contribution and is neglected in the viscous term. This is done following the work of Mellor and Blumberg (1985), to prevent an unphysically large net flux component normal to the bottom (Bijvelds, 2001). However, not taking into account the full set of transformed terms for the diffusive fluxes leads to artificial vertical mixing in flow over steep sloping beds. Inclusion of all terms reduces these mixing effects but does not eliminate them (Cornelissen, 2004). We assume that this numerical influence will be relatively small as no sloping bed is present and due to the small contribution of the overall horizontal viscous terms as shown in the non-dimensionalisation.

Again, the total horizontal and vertical eddy viscosity are represented by A_h and A_v respectively. However, as opposed to the theoretical analysis, these are not constant but are given by the turbulence closure and given by

$$A_v = \nu_{mol} + \max(\nu_{3D}, \nu_v^{BACK}) \tag{3.4b}$$

$$A_h = A_v + \nu_{SGS} + \nu_h^{BACK} \tag{3.4c}$$

respectively. This includes the molecular kinematic viscosity of water ν_{mol}, and the turbulence part ν_{3D} as defined by the turbulence closure model for the vertical direction. In the horizontal direction, the sub-grid viscosity ν_{SGS} from the HLES turbulence model is included (see next section). Background eddy viscosities ν^{BACK} are available in Delft3D-FLOW that provide a lower bound for the eddy viscosity and are user-specified.

3.1.3 Transport Equation for Salt

The salt transport equation in conservative form for the σ-grid is specified by

$$\frac{\partial (Hs)}{\partial \tau} + \frac{\partial (Hus)}{\partial \xi} + \frac{\partial (\omega s)}{\partial \sigma} = \frac{\partial}{\partial \xi}\left(HK_h \frac{\partial s}{\partial \xi}\right) + \frac{1}{H}\frac{\partial}{\partial \sigma}\left(K_v \frac{\partial s}{\partial \sigma}\right), \tag{3.5a}$$

where again the horizontal grid transformation is neglected. The total horizontal and vertical eddy viscosity K_h, K_v are not constant and are determined by the turbulence closure. Similar to the eddy viscosity, the eddy diffusivity is implemented by

$$K_v = \frac{\nu_{mol}}{\sigma_{mol}} + \max(D_{3D}, D_v^{BACK}) \tag{3.5b}$$

$$K_h = K_v + D_{SGS} + D_h^{BACK} \tag{3.5c}$$

with equivalent meaning for subscripts and for the molecular Prandtl-Schmidt number $\sigma_{mol} = 700$ for the molecular mixing of salt. The turbulent eddy diffusivity components are computed relative to the eddy viscosity by

$$D_{3D} = \frac{\nu_{3D}}{\sigma_\rho}, \tag{3.5d}$$

$$D_{SGS} = \frac{\nu_{SGS}}{\sigma_\rho}, \tag{3.5e}$$

with the Prandtl-Schmidt number $\sigma_\rho = 0.7$. Finally, salt changes the density ρ by the equation of state. In Delft3D-FLOW, two different formulations are possible[10] and we employ the default setting of the Eckart formulation $\rho = \rho_{\text{Eck}}(s)$ (Equation 1.2) as already described in Section 1.2.

3.1.4 Turbulence Closure

Four turbulence models are available within Delft3D-FLOW, which are in increasing order of complexity the 1) constant coefficient model, 2) Algebraic Eddy viscosity closure model, 3) k-L turbulence closure model, and 4) k-ϵ turbulence closure model. Of these, the k-ϵ model is most suitable for highly-stratified systems (Warner et al., 2005; Deltares, 2018) and has been implemented successfully for both salt wedge and partially mixed estuaries (Li et al., 2005; Ralston et al., 2017). The eddy viscosity is determined by the turbulent kinetic energy k and the dissipation ϵ by

$$\nu_{3D} = c_\mu \frac{k^2}{\epsilon},$$

for empirical constant $c_\mu = 0.09$. The values of k and ϵ are found by solving two non-linearly coupled transport equations given by

$$\frac{\partial k}{\partial \tau} + u\frac{\partial k}{\partial \xi} + \frac{\omega}{H}\frac{\partial k}{\partial \sigma} = \frac{1}{H^2}\frac{\partial}{\partial \sigma}\left(D_k \frac{\partial k}{\partial \sigma}\right) + P_k + B_k - \epsilon \tag{3.6a}$$

$$\frac{\partial \epsilon}{\partial \tau} + u\frac{\partial \epsilon}{\partial \xi} + \frac{\omega}{H}\frac{\partial \epsilon}{\partial \sigma} = \frac{1}{H^2}\frac{\partial}{\partial \sigma}\left(D_\epsilon \frac{\partial \epsilon}{\partial \sigma}\right) + c_{1\epsilon}\frac{\epsilon}{k}\left(P_k + (1 - c_{3\epsilon})B_k - \frac{c_{2\epsilon}}{c_{1\epsilon}}\epsilon\right). \tag{3.6b}$$

It is argued that the conservation of the turbulent quantities is less important and the transport equations are implemented in a non-conservative form (Deltares, 2018). Again, the curvature of the σ-grid has been neglected. These equations are coupled by means of their eddy diffusivity D_k and D_ϵ, defined by

$$D_k = \frac{\nu_{mol}}{\sigma_{mol}} + \frac{\nu_{3D}}{\sigma_k} \quad \text{and} \quad D_\epsilon = \frac{\nu_{3D}}{\sigma_\epsilon}, \tag{3.6c}$$

using the turbulence Prandtl-Schmidt numbers $\sigma_k = 1.00$ and $\sigma_\epsilon = 1.30$. The production P_k of turbulent kinetic energy is prescribed by changes in horizontal velocity over the water column, with

$$P_k = \frac{\nu_{3D}}{H^2}\left(\frac{\partial u}{\partial \sigma}\right)^2. \tag{3.6d}$$

The horizontal gradient of u and gradient of ω are neglected as they are considered small compared to the vertical gradient of u (Deltares, 2018). The buoyancy flux models the influence of stratification on turbulence by

$$B_k = \frac{g}{H\rho}\frac{\nu_{3D}}{\sigma_\rho}\frac{\partial \rho}{\partial \sigma}. \tag{3.6e}$$

[10] See Appendix A.2.2.

The relative influence of the production and energy dissipation is implemented using the constants $c_{1\epsilon} = 1.44$ and $c_{2\epsilon} = 1.92$. The buoyancy constant $c_{3\epsilon}$ is a boolean variable and equals zero in case of unstable stratification, in Delft3D-FLOW implemented by

$$c_{3\epsilon} = \mathbb{1}\left(-\frac{\partial \rho}{\partial \sigma}\right),$$

with Heaviside step function $\mathbb{1}$, representing stability of stratification by means of Ri_g. For estuarine systems where vertical stratification is present, we generally have $B_k \leq 0$, meaning that vertical salinity gradients lead to a reduction in the increase of k. Stable stratification leads to damping of turbulent mixing while unstable stratification leads to higher mixing

3.1.5 Boundary Conditions

Vertical Boundary Conditions

At the bed and free surface, the kinematic boundary condition imposes no flow through the vertical boundaries by

$$\omega = 0, \qquad \sigma = -1 \tag{3.7}$$

$$\omega = 0, \qquad \sigma = 0 \tag{3.8}$$

Moreover, as wind effects are neglected, the dynamic boundary condition for the momentum equations at the free surface is equal to

$$\frac{\partial u}{\partial \sigma} = 0, \qquad \sigma = 0. \tag{3.9}$$

For the dynamic boundary condition at the bed, we assume a logarithmic flow profile and the contribution of the vertical velocity w above the bed is neglected. A bed roughness height z_0 is specified, at which the horizontal velocity equals zero. For the k-ϵ model to function properly, it is required that the closest grid point to the bed Δz_b is located within the logarithmic boundary layer. In that case, the shear velocity is approximated by

$$u_* = \frac{\kappa}{\ln(1 + \frac{\Delta z_b}{2 z_0})} u_b \tag{3.10}$$

in which u_b is the flow velocity in the first layer just above the bed. It is assumed that the bed shear stress is related quadratically to the shear current just above the bed u_* by $\tau_b = \rho_0 u_* |u_*|$. Hence, the bed shear stress, and subsequently the bed boundary condition is equal to

$$\frac{A_v}{H}\frac{\partial u}{\partial \sigma} = \frac{\tau_b}{\rho_0} = \left(\frac{\kappa}{\ln(1 + \frac{\Delta z_b}{2 z_0})}\right)^2 u_b |u_b|, \qquad \sigma = -1 \tag{3.11a}$$

For salt transport at the vertical boundaries, no vertical-flux conditions $\Phi_v = 0$ are imposed. Using the boundary condition of ω above, this simplifies to

$$\frac{K_v}{H}\frac{\partial s}{\partial \sigma} = 0, \qquad \sigma = -1, \tag{3.11b}$$

$$\frac{K_v}{H}\frac{\partial s}{\partial \sigma} = 0, \qquad \sigma = 0. \tag{3.11c}$$

Open Boundary Conditions

At open boundaries, we either specify the horizontal flow velocity, or the free surface elevation. At the seaward boundary $x = 0 = \xi$, we use a single harmonic time series for the free surface elevation

$$\eta(0,\tau) = \eta_{\text{sea}}(\tau) = A_{\text{sea}} \cos(\omega\tau + \phi). \tag{3.12a}$$

with tidal elevation amplitude A_{sea}, frequency ω and phase difference $\phi = 0$ without loss of generality. As the free surface elevation is specified, the relative vertical velocity ω is assumed to equal zero over the water column, and the horizontal velocity is free and solved by Equation 3.4a under the assumption of zero momentum flux $\partial u/\partial\xi = 0$, resulting in

$$\omega = 0 \tag{3.12b}$$

$$\frac{\partial u}{\partial \tau} = \frac{1}{H^2}\frac{\partial}{\partial \sigma}\left(A_v \frac{\partial u}{\partial \sigma}\right) - g\frac{\partial \eta}{\partial \xi} - \frac{gH}{\rho_0}\int_\sigma^0 \frac{\partial \rho}{\partial \xi} + \frac{\partial \rho}{\partial \sigma}\frac{\partial \sigma}{\partial x} d\sigma' \tag{3.12c}$$

at $\eta = 0$. Similarly, in case of outflow ($u < 0$), the salinity is free and solved by the transport Equation 3.5a, salinity is uniform over depth and equal to the salinity s_{sea} at sea in case of inflow:

$$\begin{cases} \dfrac{\partial Hs}{\partial \tau} + \dfrac{\partial Hus}{\partial \xi} = \dfrac{\partial}{\partial \xi}\left(HK_h \dfrac{\partial s}{\partial \xi}\right) + \dfrac{1}{H}\dfrac{\partial}{\partial \sigma}\left(K_v \dfrac{\partial s}{\partial \sigma}\right) & u < 0 \\ s = s_{\text{sea}} & u > 0 \end{cases} \tag{3.12d}$$

At the riverine side $x = L = \xi$, we impose a freshwater inflow through a discharge definition. The flow velocity on this boundary is given by the logarithmic law of the wall profile proportional to the water depth at any moment (in Cartesian coordinates), and the vertical velocity is set to zero. Hence, the flow velocity is always positive and salinity can be given by a Dirichlet boundary condition:

$$\omega = 0. \tag{3.13a}$$

$$u = \frac{u_*}{\kappa} \ln\left(\frac{H+z}{H+z_0}\right), \tag{3.13b}$$

$$s = s_{\text{river}} \tag{3.13c}$$

where $\kappa = 0.41$ denotes the vón Karman constant and $z_0 = 0.001$ m (see Subsection 3.2.3) is the height at which the flow velocity equals 0 m/s theoretically. This value is related to the bed roughness and determines the steepness of the logarithmic profile. Here, we solve for u_*, such that the logarithmic profile ensures the depth-averaged velocity with

$$\int_{-1}^0 u d\sigma = -\frac{q_r}{H}. \tag{3.14}$$

Turbulence Boundary Conditions

Dirichlet boundary conditions are imposed at the bed and free surface, for the turbulent kinetic energy we prescribe

$$k = 0, \qquad \sigma = 0, \tag{3.15a}$$

$$k = \frac{u_*^2}{\sqrt{c_\mu}}, \qquad \sigma = -1. \tag{3.15b}$$

and for the dissipation ϵ,

$$\epsilon = 0, \qquad \sigma = 0, \tag{3.15c}$$

$$\epsilon = \frac{u_*^3}{\kappa z_0}, \qquad \sigma = -1. \tag{3.15d}$$

Here again, u_* denotes the friction velocity just above the bed as in Equation 3.10. In case of outflow ($u < 0$) at the seaward side $\xi = 0$, the turbulent quantities are computed by their respective transport equations without horizontal advection by

$$\frac{\partial k}{\partial \tau} = \frac{1}{H^2}\frac{\partial}{\partial \sigma}\left(D_k \frac{\partial k}{\partial \sigma}\right) + P_k + B_k - \epsilon \tag{3.16a}$$

$$\frac{\partial \epsilon}{\partial \tau} = \frac{1}{H^2}\frac{\partial}{\partial \sigma}\left(D_\epsilon \frac{\partial \epsilon}{\partial \sigma}\right) + c_{1\epsilon}\frac{\epsilon}{k}\left(P_k + (1 - c_{3\epsilon})B_k - \frac{c_{2\epsilon}}{c_{1\epsilon}}\epsilon\right). \tag{3.16b}$$

In case of flow into the domain at the seaward side ($\xi = 0, u > 0$), and at the riverine side ($\xi = L$), a Dirichlet vertical distribution over z is imposed with

$$k(z) = \frac{u_*^2}{\sqrt{c_\mu}}\left(1 - \frac{z + h}{H}\right), \tag{3.16c}$$

$$\epsilon(z) = \frac{|u_*|^3}{\kappa(z + h)}, \tag{3.16d}$$

This is a linear profile in turbulent kinetic energy from the bed to the free surface and a hyperbolic distribution for the dissipation with infinitely large dissipation at the bed.

3.1.6 Initial Condition

At the start of the simulation, boundary conditions do not necessarily align with the initial condition. Therefore, a smoothing period of 1 hour is defined in which a linear interpolation is applied between the actual field value and the boundary condition to reduce spin-up time. However, this does not apply to salinity and the boundaries should match the initial value. The precise construction of an initial condition over the full grid, for model settings in the RWW is described in Subsection 3.2.5.

3.2 Model Settings, Geometry and Parameter Values

In this section, we describe the geometry and topography we use to schematically represent the RWW in Delft3D-FLOW. Moreover, we describe the interaction of salinity and flow in Delft3D-FLOW, which ultimately leads to further specification of the turbulence model.

3.2.1 Geometry and Boundary Values

Corresponding to the RWW, the average water depth is set to $h = 15$ m and an estuary length of $L = 50$ km is sufficient to capture the expected salt intrusion lengths. We only use the semi-diurnal lunar tidal constituent M2 with period $T = 12.42$ h and angular frequency $\omega = 2\pi/T$, and tidal elevation amplitude $A_{\text{sea}} = 1$; realistic at Hoek van Holland (Rijkswaterstaat, 2023b). In the case of inflowing horizontal velocities, a vertically uniform seaward salinity of $s_{\text{sea}} = 35$ ppt is prescribed. A width-averaged river discharge of $q_r = 1.5$ m^2/s introduces an average river flow velocity of $U_r = -q_r/h = -0.1$ m/s with no salinity ($s_{\text{river}} = 0$ ppt). For a uniform rectangular estuary of depth $h = 15$ m and width $B = 500$ m, this corresponds to a discharge of 750 m^3/s. For the RWW these flow velocities are approximately in line with a discharge of 1,000 m^3/s at Lobith (Dijkstra et al., 2022).

3.2.2 Topography

We define sand dunes relative to $z = -h$ such that the mean bed level remains at this level when no human interventions are in place. The local bed level is defined at $z_b(x) = -h + h_d(x)$ for dune function[11] h_d, for which we use a product of functions, with

$$h_d(x) = \frac{H_d}{2} b_d(x) \Lambda_d(x), \tag{3.17}$$

where H_d is the overall height of the dunes, $b_d(x) \in [0, 1]$ an envelope function used to impose dunes on the interior of the domain (such that they are not too close to the boundaries) and the dune shape function $\Lambda_d(x)$, describing the geometry of the dunes. Human interventions such as dredging and dumping can be implemented by changing the definition of the bed level z_b, as will be discussed Subsection 5.2.1. To limit the interaction of boundary conditions effects on sand dunes, we restrict the topography to the middle of the domain. A typical envelope function would be the logistic function, symmetric over the estuary with

$$b_d(x) = \frac{1}{1 + \exp\left(-\frac{4(x-L_0)}{\Delta L_0}\right)} + \frac{1}{1 + \exp\left(-\frac{4(L-x-L_0)}{\Delta L_0}\right)} - 1. \tag{3.18}$$

which ensures that sand dunes are mainly located between $L_0 \leq x \leq L - L_0$ with $b(L_0) = \frac{1}{2}$, as long as L_0 is not close to $L/2$. Parameter ΔL_0 is the characteristic length in which the spatial smooth start-up of the sand dunes is located with $b(L_0 - \Delta L_0) = 0.018$ and $b(L_0 + \Delta L_0) = 0.982$. An example for $L = 50$ km can be seen in Figure 3.1. However, local adaptations of this function are possible and regional dune height changes can also be implemented with this function (also discussed in Subsection 5.2.1).

As described in Section 1.5 and shown in Figure 1.4, the landward facing slope is referred to as the stoss side with length λ_s and the seaward facing slope is the lee side with length λ_l. In line with Knaapen (2005), we characterise the asymmetry of the dunes by the difference between the stoss and lee side, relative to the overall length of the dune, i.e. by

$$\mathcal{A}_d = \frac{\lambda_s - \lambda_l}{\lambda_d} \quad \in [-1, 1]. \tag{3.19}$$

A positive value of $\mathcal{A}_d > 0$ means $\lambda_s > \lambda_l$, i.e. ebb-oriented estuarine sand dunes (as in Figure 1.4). Note that we can find the length of each side by

$$\lambda_l = \frac{1 - \mathcal{A}_d}{2} \lambda_d, \tag{3.20}$$

$$\lambda_s = \frac{1 + \mathcal{A}_d}{2} \lambda_d. \tag{3.21}$$

Subsequently, for the dune geometry, we use the shape formulation

$$\Lambda_d(x) = \begin{cases} \sin\left(\frac{2\pi x}{\lambda_d}\right) & \mathcal{A}_d = 0 \\ \frac{2}{\pi \mathcal{A}_d} \arctan\left(\frac{\sin(\frac{\pi}{2}\mathcal{A}_d)\sin\left(\frac{2\pi x}{\lambda_d}\right)}{1 - \sin(\frac{\pi}{2}\mathcal{A}_d)\cos\left(\frac{2\pi x}{\lambda_d}\right)}\right) & \mathcal{A}_d \in [-1, 1] \setminus \{0\} \end{cases} \tag{3.22}$$

which leads to an asymmetrical periodic function with dune length λ_d and amplitude 1. A visualisation of the shape function $\Lambda_d(x)$ as given in Equation 3.22 for positive $\mathcal{A}_d$ is shown in Figure 3.2.

[11] The dune function h_d has mean zero along the estuary.

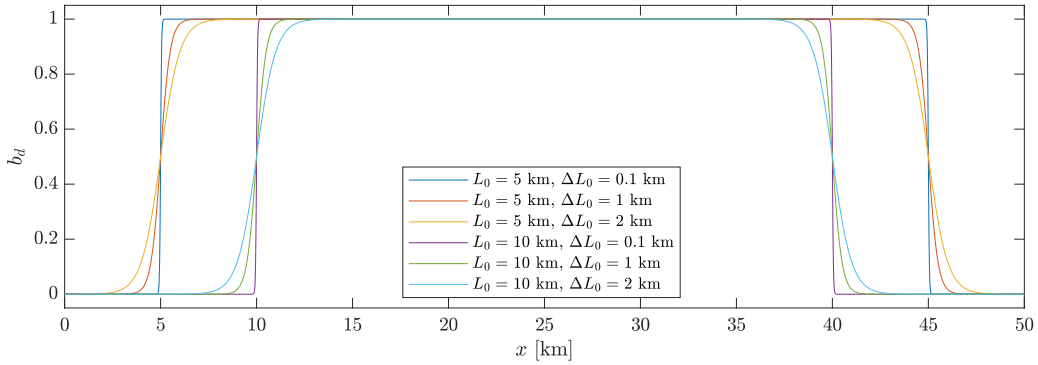

Figure 3.1: Visualisation of envelope function $b_d(x)$ on a domain of length $L = 50$ km for various envelope function parameters L_0, ΔL_0.

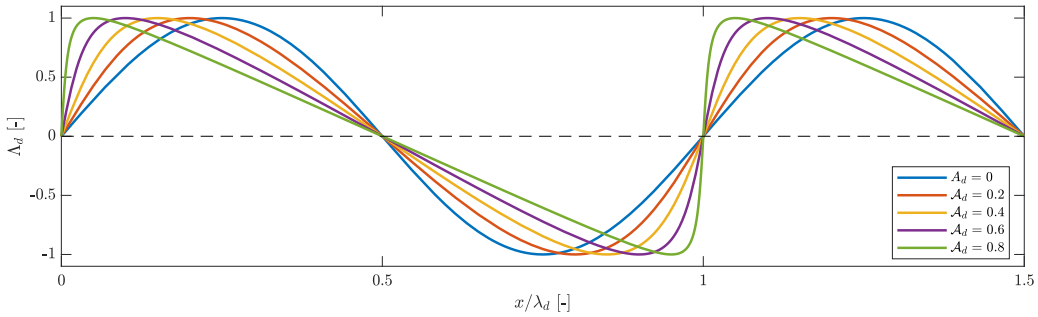

Figure 3.2: Visualisation of shape function $\Lambda_d(x)$ for increasing value of dune asymmetry $\mathcal{A}_d$.

Lee Side Dune Angle

When increasing dune asymmetry, the dune angle increases which may lead to flow separation as described in Section 1.5, which can not be modelled by Delft3D-FLOW. Therefore, we evaluate what dune angles are imposed with changing shape parameters. The largest positive and largest negative slopes are attained at $x = 0$ and $x = \lambda_d/2$ respectively, i.e. in the middle of each respective slope. With the dune shape formulation Λ_d, we can determine the dune angle analytically. Without loss of generality, we assume that $\mathcal{A}_d > 0$ and $\lambda_l < \lambda_s$ such that the largest dune angle is achieved at the lee side. Then, the mean angle of the lee side equals

$$\phi_{d,\text{mean}} = \arctan\left(\frac{H_d}{\lambda_l}\right) = \arctan\left(\frac{H_d}{\lambda_d}\frac{2}{1-\mathcal{A}_d}\right). \tag{3.23}$$

The maximum local negative slope is achieved at the point $x = 0$, where

$$\left.\frac{\partial}{\partial x}\Lambda_d(x)\right|_{x=0} = \frac{4\sin(\frac{\pi}{2}\mathcal{A}_d)}{\mathcal{A}_d\lambda_d(1-\sin(\frac{\pi}{2}\mathcal{A}_d))},$$

which means the lee side has a maximum slope angle of

$$\phi_{d,\text{max}} = \arctan\left(\frac{H_d}{\lambda_d}\frac{2\sin(\frac{\pi}{2}\mathcal{A}_d)}{\mathcal{A}_d(1-\sin(\frac{\pi}{2}\mathcal{A}_d))}\right). \tag{3.24}$$

Hence, both the mean and maximum dune angle are functions of the dune's aspect ratio H_d/λ_d, and the asymmetry parameter $\mathcal{A}_d$, which is visualised in Figure 3.3.

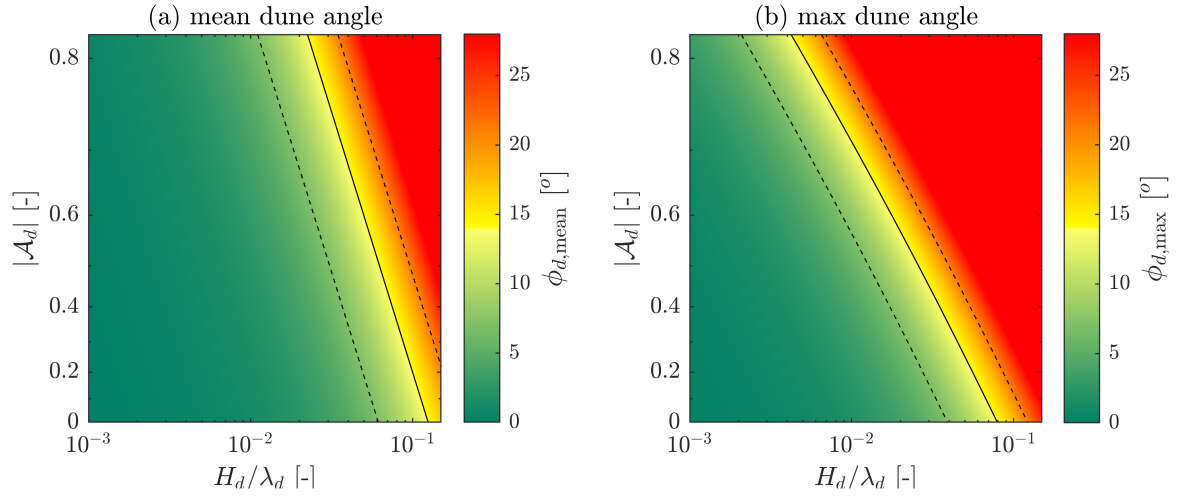

Figure 3.3: (a) Mean angle of the lee side from trough to crest, (b) maximum angle of the lee side. Both as a function of dune aspect ratio H_d/λ_d and dune asymmetry $\mathcal{A}_d$. Solid black lines indicate an angle of 14°, and dashed lines of 7° and 21° respectively.

3.2.3 Value of Roughness Height

In Delft3D-FLOW, a bed roughness should be defined that determines the shear velocity and in turn the dynamic boundary condition (3.11a). We do so by a uniform roughness height z_0 that does not depend on the instantaneous water depth H and is thus independent of sand dune topography. This roughness height can be interpreted as the distance above the bed where the tangential flow velocity is zero. To determine the value of z_0, we consider all alternative roughness definitions to find a suitable roughness length. In most coastal engineering applications, roughness formulations revolve around the Chezy parameter where

$$\frac{\tau_b}{\rho_0} = \frac{g u_b |u_b|}{C^2}, \tag{3.25}$$

for Chézy coefficient C. This parameter ranges from $C = 30$ m$^{1/2}$/s for very rough systems to $C = 90$ m$^{1/2}$/s for smooth systems. Other roughness definitions in Delft3D-FLOW are the Manning's formulation with $C = h^{1/6}/n$ for Manning's coefficient n and White-Colebrook's formulation with $C = 18\log_{10}(12h/k_s)$ for Nikuradse coefficient k_s. For sandy beds in relatively slow-flowing channels without vegetation, Manning's coefficient is empirically validated around 0.023 to 0.025 m$^{-1/3}$ s and Nikuradse roughness length ranges from 0.01 m to 0.1 m, motivating our choice $C = 65$ m$^{1/2}$/s. In turn, we will use a spatially uniform roughness height of

$$z_0 = \frac{h}{e(e^{\kappa C/\sqrt{g}} - 1)} \approx 0.001 \text{ m} \tag{3.26}$$

for mean water depth $h = 15$ m and Von Kárman constant $\kappa = 0.41$.

3.2.4 Turbulence Modelling and the Interaction of Salinity and Flow

The transport of salt within estuarine systems is primarily governed by fluid properties, including advection and diffusion, but also turbulence. In this subsection, we describe the implementation of this interaction with flow and turbulence in more detail, such that a model choice can be made on the turbulence models and model parameters.

Estuarine flow is inherently turbulent, and capturing this turbulence accurately in our model is crucial. Initial model development revealed that even minor fluctuations in turbulence parameters

significantly affect salt intrusion length. Initially, we developed a model without a turbulence closure model, leading to large oscillations and instabilities. Moreover, for partly mixed and strongly satisfied systems, implementation of the k-ϵ turbulence model is always recommended to introduce local and temporal variability in the turbulent effects (Deltares, 2018). Therefore, the k-ϵ model was employed to introduce additional viscosity and diffusion via ν_{3D}, effectively modelling turbulent estuarine behaviour.

The interaction of salinity and flow in Delft3D-FLOW are highlighted in the equations above, especially those with variable density. Note that the boundary conditions merely use constant reference density ρ_0 and not the variable density ρ, following the Boussinesq assumption. The same applies to the baroclinic pressure term $\frac{\partial \eta}{\partial \xi}$ in the horizontal momentum equation. Horizontal density gradients mainly affect the horizontal velocity through the baroclinic density gradient in the momentum equation, giving rise to gravitational circulation. The influence of vertical density gradients (stratification) is much smaller and is only applied due to the coordinate transformation.

Turbulent diffusion of salt is taken into account by an increase in the diffusivity parameter. Conversely, literature indicates that stratification also greatly reduces turbulent production. In Delft3D-FLOW this is reproduced by the buoyancy flux term B_k in the turbulence closure Equation 3.6e. Greater stratification reduces turbulent kinetic energy k, subsequently decreasing turbulent eddy viscosity ν_{dD} and significantly suppressing turbulent salinity dispersion.

In estuaries, horizontal scales are usually assumed to be much larger than vertical scales, and the same applies to turbulent scales. Therefore, Delft3D-FLOW allows for separate specifications of turbulent processes in both directions. The user manual recommends modelling 2D horizontal turbulence in simulations with vertical layers (hence also 2DV) either using the HLES model or spatially uniform horizontal eddy viscosity (Deltares, 2018). A vertical background viscosity $\nu_v^{BACK} = 10^{-4}$ m^2/s is applied to limit short oscillations, to model the influence of internal waves unaccounted for by the turbulence closure and, more importantly, to obtain physical model results representative for the RWW (see Appendix A.2.4 for more information). All other background values are set to zero to limit the influence of user-defined parameter values while emphasizing intrinsic model processes, and the influence of the HLES model and performance of the k-ϵ model for basic settings is evaluated, which yields the following conclusions.

HLES model:
The SGS model directly introduces additional horizontal viscosity (by means of ν_{SGS}) as a function of depth H and horizontal flow gradients $\partial u/\partial x$, both of which are directly related to sand dunes (see Subsection A.1.3). This implies that the HLES model is unsuitable for modelling horizontal eddy effects over sand dunes and is more useful for bathymetry changes on a larger scale. We consider the background parameter ν_h^{BACK} more suitable, as it models the subgrid horizontal turbulence uniformly over the domain, rather than the large variability over the sand dunes locally.

k-ϵ model:
The k-ϵ model, employing the model settings outlined in Table 3.1, results in an eddy viscosity ν_{3D} in the order of 10^{-2}. Literature suggests that magnitudes of $A_v \geq 10^{-4}$ and $A_h \geq 10^{0}$ m^2/s are to be expected, more specifically, we estimate the order of individual components as

$$\underset{\mathcal{O}(10^{-4})}{A_v} = \underset{\mathcal{O}(10^{-6})}{\nu_{mol}} + \max(\underset{\mathcal{O}(10^{-2})}{\nu_{3D}}, \nu_v^{BACK}), \tag{3.27}$$

$$\underset{\mathcal{O}(10^{0}-10^{2})}{A_h} = \underset{\mathcal{O}(10^{-4})}{A_v} + \nu_{SGS} + \nu_h^{BACK}. \tag{3.28}$$

Consequently, the k-ϵ model can model vertical eddy effects, but it does not capture horizontal structures. Background values are essential for an accurate study of salt dispersion, especially in scenarios where the HLES model cannot be employed. This implies that the k-ϵ model captures dune effects

on turbulence primarily in the vertical dimension and background values account for some of the un-modelled dynamics.

All in all, larger background values are necessary for physically representative model results, but should not override all turbulent vertical mixing that can be modelled by the k-ϵ model. Background parameter values are chosen in line with the constant eddy viscosity and diffusivity as in Dijkstra et al. (2022) and described in Subsection 2.3.3, using the salinity Prandtl Schmidt number $\sigma_\rho = 0.7$. These model settings show the expected transport regime of a partially mixed estuary. The value of $\nu_v^{BACK} = 10^{-3}$ m^2/s is increased to obtain a more physically representative result. The initially used value of 10^{-4} m^2/s resulted in a salt wedge with an unphysically large salt intrusion length. A more detailed analysis of the influence of these background values on the salt intrusion length is discussed in Section 4.5.

3.2.5 Initial Condition for the RWW

The initial surface elevation is set to $\eta(x, 0) = 0$, the initial vertical velocity to $w = 0$ m/s and the initial horizontal velocity is imposed by a logarithmic law-of-the-wall function, such that $\overline{u}(x, 0) = -q_r/H(x, 0)$ over the whole domain, similar to the river inflow boundary Equation 3.13b. During initial model development, a linearly decreasing salinity profile from the sea to the river is specified, uniform over depth, i.e. by

$$s(x, z, 0) = s_{\text{sea}} \left(1 - \frac{x}{L}\right), \quad \forall z.$$

After around five days of simulation time, most models almost reached dynamic equilibrium. It turns out that the system attains dynamic equilibrium more quickly by flushing the system (i.e. imposing too much landward salinity initially), than by letting the salt intrusion naturally develop from the seaward side (i.e. flow in). Furthermore, the stratification occurred even more quickly. Most model runs ended up with a horizontal salt profile $\langle \overline{s} \rangle$ that can be approximated by a third-order polynomial from $x = 0$ km to $x = \langle L_s \rangle$.

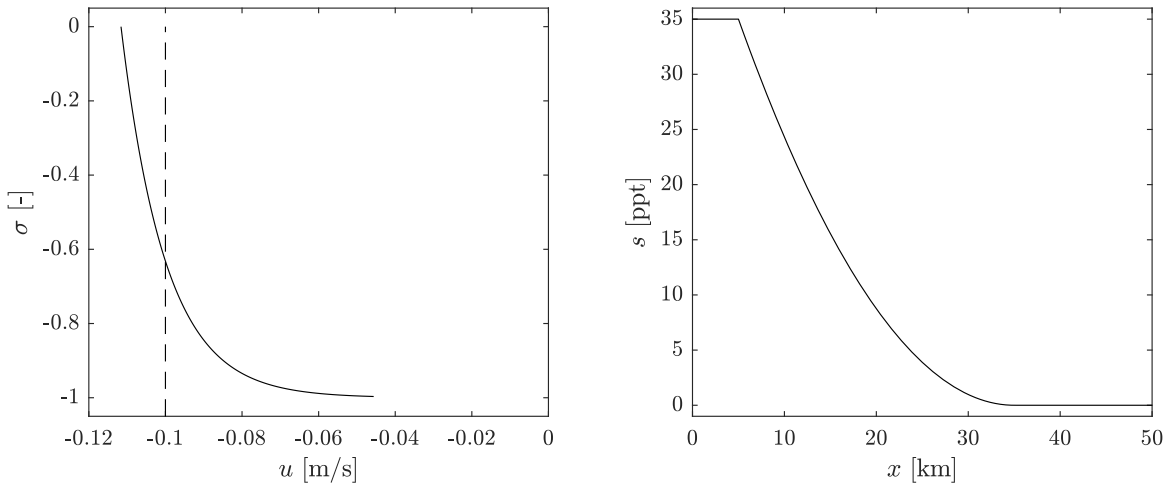

Figure 3.4: Initial conditions for horizontal flow velocity u (left) and initial longitudinal salinity profile s, uniform over depth (right).

Considering the timescale of flushing, the relatively fast presence of stratification, and the eventual longitudinal distribution, the initial salinity profile in subsequent models was given by a quadratic polynomial from $x_{0,\text{sea}} = 5$ km to $x_{0,\text{river}} = 35$ km (slightly further than the expected salt intrusion

length). A function is defined that specifies the salinity uniform over depth and only introduces longitudinal variation by

$$s(x,z,0) = \begin{cases} s_{\text{sea}}, & x \in [0, x_{0,\text{sea}}] \\ s_{\text{sea}} \left(\frac{x - x_{0,\text{river}}}{x_{0,\text{river}} - x_{0,\text{sea}}} \right)^2, & x \in [x_{0,\text{sea}}, x_{0,\text{river}}] \\ s_{\text{river}}, & x \in [x_{0,\text{river}}, L]. \end{cases} \tag{3.29}$$

These initial condition equations for u and s are described analytically (as shown in Figure 3.4), mapped to the discretised grid, and written to a `.ini` file using a MATLAB script. Model output can be used as an initial condition for new model runs which do not differ significantly in topography and boundary conditions, which gives even faster convergence and reduces computational time significantly.

3.3 Numerical Methods and Discretisation

In this section, we describe the discretisation of the system, highlight the attention required for defining vertical layers, and present the numerical method and timestep restrictions.

3.3.1 Horizontal Discretisation

The horizontal length L is discretised by a pre-determined uniform grid size Δx, creating $N = L/\Delta x$ horizontal grid cells. The influence of longer boundaries with larger grid cell sizes near the boundaries has been tested but showed a negligible impact on model output. The bathymetry is implemented using Equation 3.17 on the cell edges $x_{i-1/2} = (i - \frac{1}{2})\Delta x$. As Λ_d is an analytic expression for all x, the maximum height at $z = -h + H_d/2$ might not be reached on the cell edges with the used discretisation. Therefore, to ensure that sand dunes also have height H_d in the discretised space, the discretised topography is re-normalised with $\max_i \Lambda_d(x_{i-1/2})$. Hence, the bathymetry in discrete space equals

$$z_b(x_{i-1/2}) = -h + \frac{H_d}{2} b_d(x_{i-1/2}) \frac{\Lambda_d(x_{i-1/2})}{\max_i \Lambda_d(x_{i-1/2})}, \tag{3.30}$$

such that model results do not depend on the used horizontal discretisation but on varying H_d only.

3.3.2 Vertical Discretisation

The σ-layers are defined from the bed layer $k = 1$ to the top layer[12] $k = K$ by means of fractions f_k of the total water depth[13], with $\sum_{k=1}^{K} f_k = 100\%$. Subsequently, layer heights are equal to $\Delta z_{i,k} = f_k H_i$ for horizontal grid cell i for any moment in time (and $\Delta z_{i+1/2,k} = f_k H_{i+1/2}$ at the cell faces).

Initial model development has shown the importance of implementing small layers near the bed for accurate flow and turbulence modelling, as well as top layers small enough for accurate modelling of salt transport. Taking both into account, we propose a linear increase in thickness layer of Δf per layer in the bottom $K/2$ layers ($f_k = f_{k-1} + \Delta f$ for $k = 1, \ldots K/2$), and a uniform thickness for the top half ($f_k = f_{k-1}$ for $k = K/2 + 1, \ldots K$), or

$$f_k = \begin{cases} f_1 + (k-1)\Delta f, & k = 1, \ldots K/2 \\ f_1 + \frac{K}{2}\Delta f, & k = K/2 + 1, \ldots K. \end{cases} \tag{3.31}$$

[12] The symbol K is also used for the eddy diffusivity in Equation 2.2d. Note that here we describe an integer (scalar) value, as opposed to the matrix in Equation 2.2d. We clearly distinguish the two in the text, but can also be retrieved from mathematical use (scalar or matrix).

[13] The unit of these fractions is given in percentages as this forms the unit of implementation in Delft3D-FLOW

The layer thickness increase parameter Δf can be found by

$$100\% = \sum_{k=1}^{K} f_k = K f_1 + \Delta f \left(\frac{3K^2}{8} - \frac{K}{4} \right)$$
$$\implies \Delta f = \left(\frac{3K^2}{8} - \frac{K}{4} \right)^{-1} (100\% - K f_1), \tag{3.32}$$

which defines the complete layer definition if the bottom layer fraction f_1 is known. An example of this discretisation for $K = 20$ layers (such that layers are nicely visible) with bottom layer thickness $f_1 = 0.1\%$ is shown in Figure 3.5.

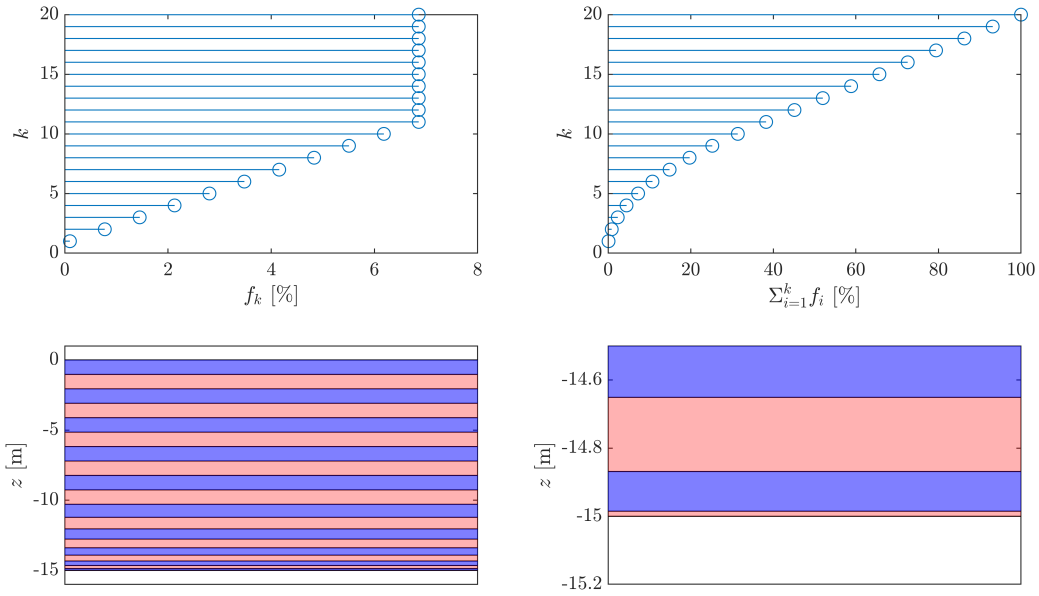

Figure 3.5: Visualisation of the vertical discretisation with $K = 20$ vertical layers and bottom layer thickness $f_1 = 0.1$ %. Top: individual layer thickness f_k (left) and cumulative sum from $k = 1$ to K (right). Bottom: visualisation of grid layer height from $z = -15$ m to $z = 0$ m.

The Dirichlet bed boundary conditions produce values proportional to the bed grid height $\Delta z_b = \Delta z_1$, and errors made by an unsuitably chosen bottom cell height will propagate through the water column. This means a convergence study in K will solely show numerical convergence if the bottom cell height is chosen independently of K. Moreover, the k-ϵ-model only works properly when the grid point closest to the wall is in the log-law layer near the wall. This is done using the nondimensional length

$$y^+ = \frac{y u_*}{\nu}, \quad \text{with } u_* = \frac{\sqrt{|\tau_b|}}{\rho}, \tag{3.33}$$

where y is the distance from the wall, or in our model, the distance from the bed. A value of $30 < y^+ < 300$ in the centre of the bottom grid cell is necessary for accurate performance of the wall function. In Delft3D-FLOW, the bed shear stress τ_b is given as output and allows us to evaluate y^+. Initial model development shows a bed layer thickness of $f_1 = 0.1\%$ to produce suitable values of y^+ for most points in the estuary during the tidal cycle. Furthermore, Equation 3.11a requires $\frac{\Delta z_b}{2 z_0} \gg 0$ to ensure that the bed shear stress formulation does not diverge. With a value of $\Delta z_b \approx 0.015$ m and $z_0 = 0.001$ m this is satisfied. It is acknowledged that a suitable value of y^+ is not attained throughout the complete tidal cycle as $y^+ < 30$ when the shear velocity goes to zero during flow reversal. This is accepted, as during this period there is a negligible production of turbulence to begin with.

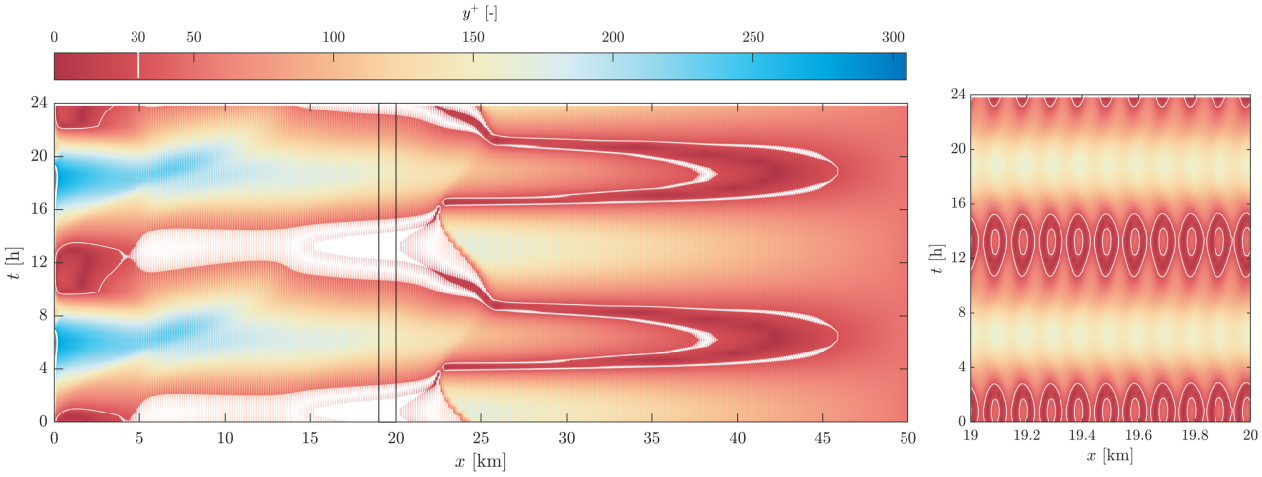

Figure 3.6: Value of y^+ over a tidal cycle during a simulation when $f_1 = 0.1\%$. The right panel shows a zoom of the sand dunes in the boxed area. White lines indicate where $y^+ < 30$.

3.3.3 Numerical Solution Procedure

The system is discretised using a staggered Arakawa C-grid, using N grid cells in the horizontal direction and K in the vertical direction. Discrete salinity, density and turbulent quantities are computed in the grid centres and thus denoted by $\psi^n_{i,k}$ for horizontal index $i = 1, \dots N$, vertical index $k = 1, \dots K$ and time index n. Flow velocities are defined on the cell edges and are denoted by $u^n_{i-\frac{1}{2},k}$ for $i = 1, \dots N$ and $w^n_{i,k-\frac{1}{2}}$ for $k = 1, \dots K$ respectively. The surface elevation is computed in the centre of the top cell. Therefore, the grid cell height is given at the cell faces by $\Delta z_{i+1/2,k}$.

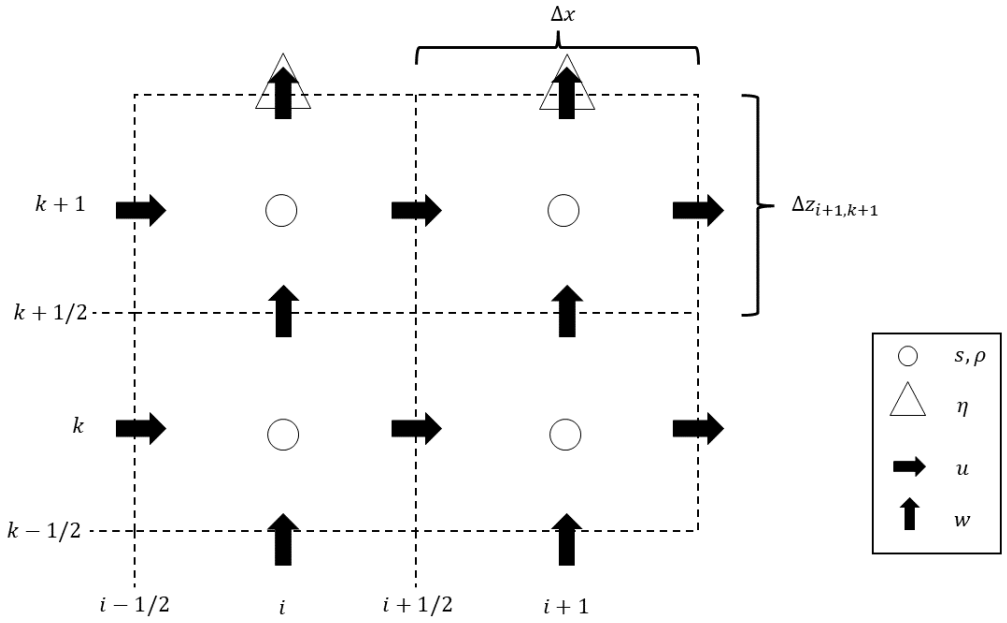

Figure 3.7: Visualisation of the Arakawa C-grid discretisation method, where flow velocities are computed through the cell interfaces and salinity and density in the cell centres (i, k), allowing for a cell-centred finite difference method.

For pressure calculation, the depth at grid cell faces is computed using the mean of the nearest edges. For the horizontal advection of momentum, we use the cyclic scheme[14], which shows the best convergence behaviour (Deltares, 2018). It is a two-stage upwind finite difference scheme for the spatial derivative of third-order, while time is integrated implicitly. A fully implicit time integration is used for the vertical exchange terms to prevent instabilities and to prevent a small upper bound on the time step. The advection terms are discretised using a second-order central difference and the vertical viscosity term by applying the central difference twice.

In the transport equation, the cyclic method is also used. This uses a second-order central scheme of the flux terms, which in turn are constructed using a third-order upwind scheme. To limit negative salinity concentrations, the Forester filter is applied, which increases the salinity in the given cell using a mass-conserving iterative process. Lastly, the use of σ-coordinates creates artificial flow and unphysical transport when cells become steep, which especially occurs when large sand dunes are modelled using coarse horizontal discretisations. This causes hydrostatic inconsistency and, when not dealt with properly, results in unphysical transport as salt is only transported through equal layers of k (Bijvelds, 2001). Therefore, a correction algorithm is implemented based on the work of Stelling and van Kester (1994), which has been extended to a nonlinear algorithm that is consistent and assures the maximum principle (Deltares, 2018).

3.3.4 Time Step Restrictions and Output Generation

The semi-explicit solution method for the advection equation introduces a time-step restriction based on the CFL criterion:

$$\mathrm{CFL} = |u|\frac{\Delta t}{\Delta x} \leq 1. \tag{3.34}$$

The viscous terms in the momentum equation and vertical terms are solved implicitly to eliminate severe timestep restrictions. However, the horizontal background eddy diffusivity still indirectly poses a timestep restriction for numerical stability of the diffusion equation, as

$$\Delta t \leq \frac{\Delta x^2}{2K_h} < \frac{\Delta x^2}{2D_h^{BACK}}. \tag{3.35}$$

where K_h can be approximated by D_h^{BACK}. Flow velocity magnitudes in the order of $|u| = 1$ m/s are expected, resulting in

$$\Delta t \leq \min\left\{\frac{\Delta x^2}{2D_H^{BACK}}, \frac{\Delta x}{1\ \mathrm{m/s}}\right\}. \tag{3.36}$$

A full day of 24 hours is discretised by 32,000 timesteps of $\Delta t = 2.7$ s $= 0.045$ min. Model output is generated every 690 timesteps with an interval of 31.05 min, such that every tidal cycle of duration $T = 12.42$ h $= 44712$ s (or $31.05 \cdot 24 = 745.2$ min) can be evaluated with 24 model outputs.

3.4 Numerical Model Convergence

3.4.1 Horizontal Convergence

An initial horizontal spatial convergence study is performed by varying the horizontal grid cell width $\Delta x = 80 \cdot \left(\frac{1}{2}\right)^i$ for $i = 0, 1, \ldots 4$. The vertical discretisation is fixed with $K = 20$ layers. Sand dunes are implemented with a symmetric ($\mathcal{A}_d = 0$) sinusoidal topography with length $\lambda_d = 125$ m and height

[14] More options are available, such as the WAQUA scheme, see Deltares (2018) for more information

$H_d = 0.8$ m. We acknowledge that a horizontal resolution of $\Delta x > 20$ m can not accurately represent dune lengths of 125 m. However, this specific dune length of 125 m is chosen such that larger grid cells are not a divisor of the dune length, such that the global behaviour in the estuary may still be captured by coarser grid cells. For the finest simulation with $\Delta x = 5$ m, the horizontal stability criterion of $\Delta t \leq \Delta x^2 / 2 D_h^{BACK}$ is violated when using $\Delta t = 2.7$ s. Therefore, the time step is reduced to $\Delta t = 2.7/4$ s, which dramatically increases computation time.

Convergence of Salt Intrusion Length

The left plot of Figure 3.8 shows the temporal evolution of the salt intrusion length L_s over time, which are qualitatively, over the tide, relatively similar for different horizontal grid sizes. The difference of L_s over time after grid refinement is shown in the middle. The relatively consistent difference over two tidal cycles indicates the results will not diverge further. The largest increase in accuracy is achieved from $\Delta x = 40$ m to $\Delta x = 20$ m, which likely results from a more accurate sand dune representation. The difference between the models with $\Delta x = 10$ m and $\Delta x = 5$ is relatively minor, with a difference in $\langle L_s \rangle$ of around 50 m. The dependence of $\langle L_s \rangle$ on the horizontal grid is shown in the right of Figure 3.8, and appears to converge for smaller Δx. The difference with the final grid refinement is relatively small, suggesting that a horizontal resolution of $\Delta x = 10$ m is sufficient to accurately model salt intrusion.

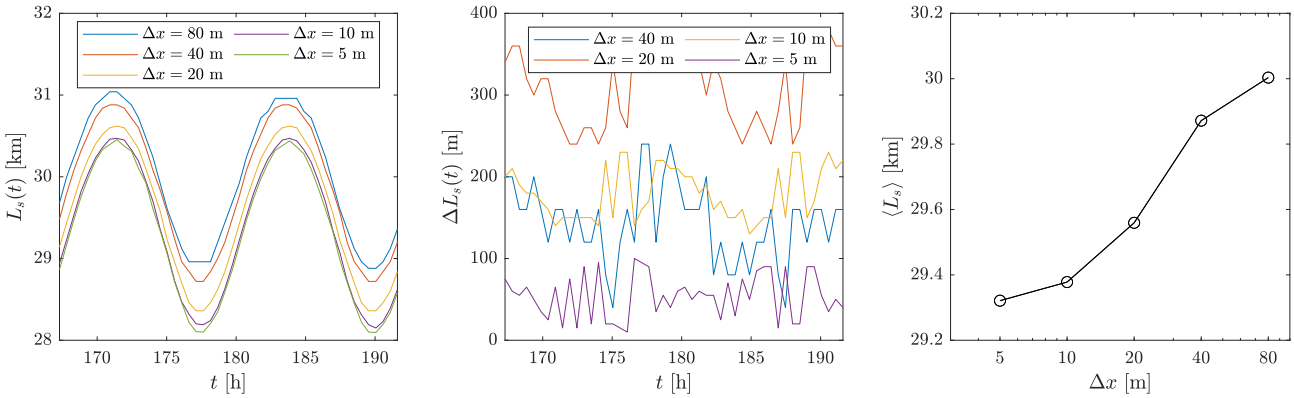

Figure 3.8: Salt intrusion lengths $\langle L_s \rangle$ for various horizontal discretisations and temporal evolution of L_s after grid refinements.

Flow Convergence

The horizontal velocities through σ-layers are averaged over the last tidal cycle time is shown in Figure 3.9 and the difference after horizontal grid refinement by $\Delta\langle u \rangle(\Delta x) = \langle u \rangle(\Delta x) - \langle u \rangle(2\Delta x)$ is shown in Figure 3.10. Even though coarse horizontal grids cannot model the dunes of $\lambda_d = 125$ m accurately, the horizontal flow can still be captured relatively accurately. The largest qualitative differences occur near the salt intrusion length, which likely results from the dependence of $\langle L_s \rangle$ on Δx.

Overall, it appears that differences in modelled flow velocities are relatively small in the order of cm/s for different grids. Although small, Qualitative differences are observed for all grid refinements for $\Delta x > 10$, i.e. structural differences occur in the horizontal velocity over depth. However, when comparing $\Delta x = 10$ m and $\Delta x = 5$ m, the flow difference is in the order mm/s and is almost uniform over depth, i.e. no additional vertical variations are introduced by refining. Hence, we conclude that a horizontal grid resolution of $\Delta x = 10$ m is sufficient to capture the overall flow characteristics and salt intrusion, which still is computationally feasible (contrary to $\Delta x = 5$ m).

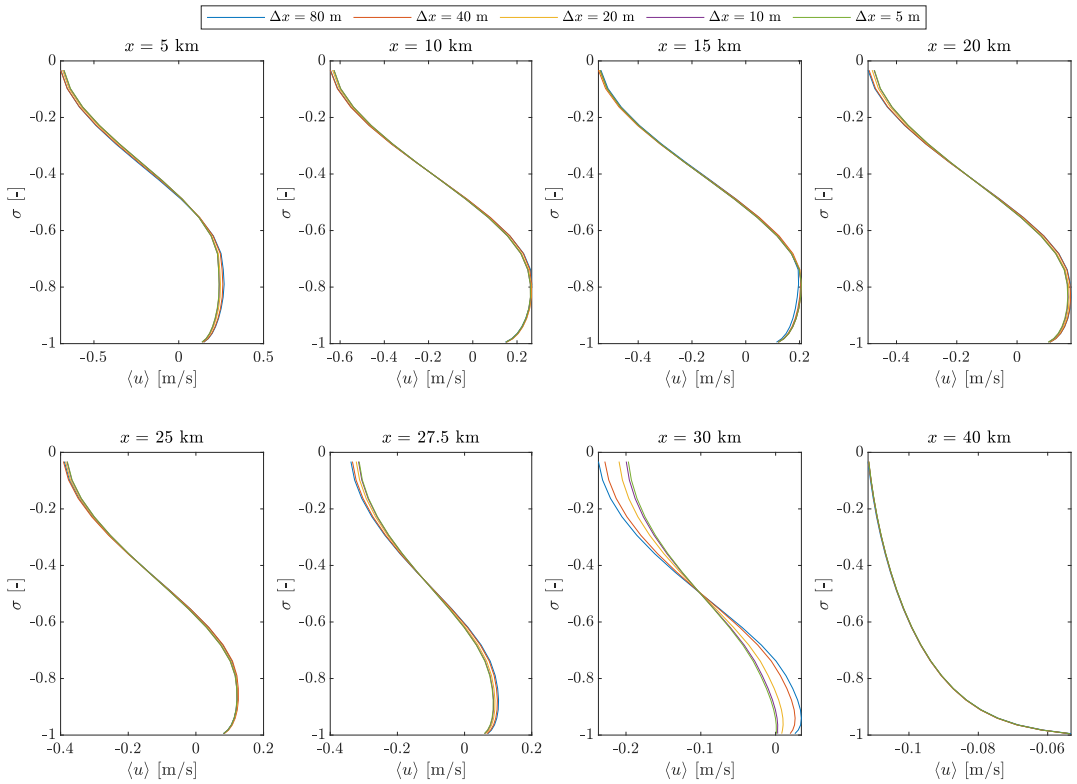

Figure 3.9: Tidally averaged flow velocity $\langle u \rangle$ over $\sigma-$coordinates for various horizontal discretisations for several locations in the estuary.

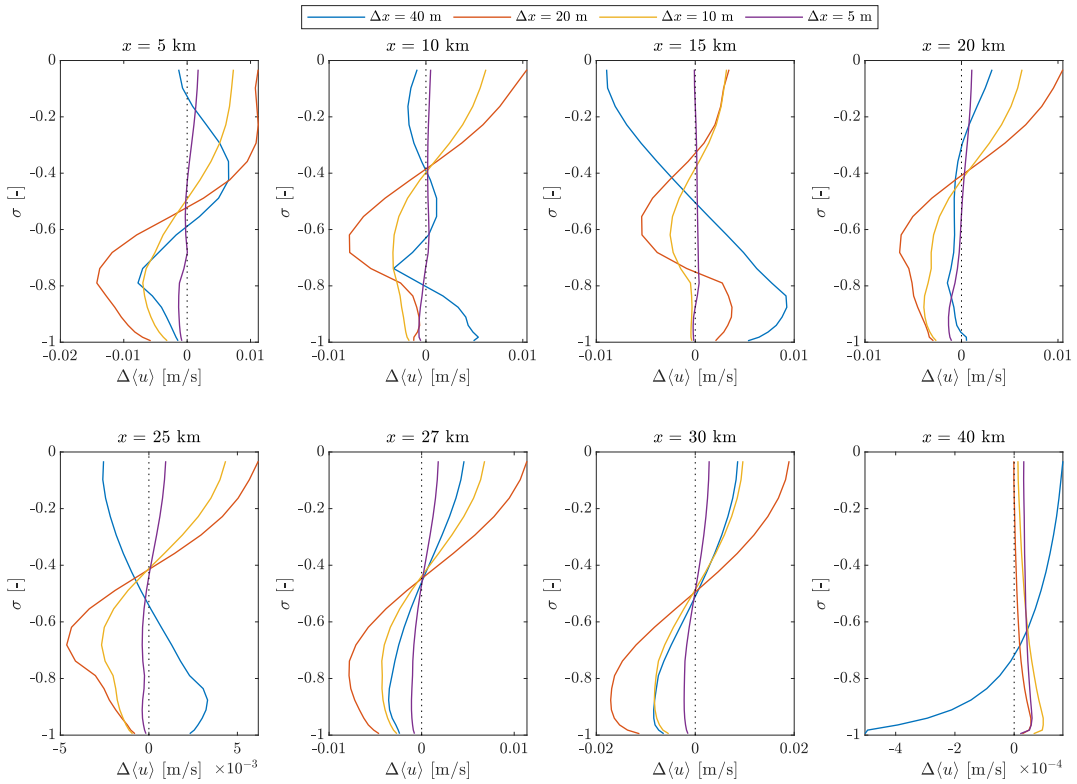

Figure 3.10: Difference in $\langle u \rangle$ over $\sigma-$coordinates for subsequent horizontal grid refinements for several locations in the estuary.

3.4.2 Vertical Convergence

The vertical spatial convergence of the flow is examined by analysing the flow properties for an increasing number of vertical layers with $K = 10, 20, 40, 80$ with a horizontal grid cell size of $\Delta x = 10$ m. The model is run for 3 days with equal model settings and initial conditions (as described in Subsection 3.2.5). Symmetric dunes are implemented in the interior of the domain ($L_0 = 5$ km, and $\Delta L_0 = 1$ km) with length $\lambda_d = 100$ m and height $H_d = 1.0$ m.

Flow Convergence

The tidally-averaged horizontal flow velocities through each vertical grid cell (i.e. over $\sigma-$coordinates) for several locations along the estuary are shown in Figure 3.11. A precise measure of convergence based on the flow profiles cannot be given due to the use of σ-layers, which changes the location of the vertical coordinates throughout the simulation and between model refinements. In the upper part of the estuary ($x = 40$ and 48 km), with mostly riverine flow, results are almost equal for all discretisations. In the region of stratification, there is barely any quantitative difference in mean velocity between the model runs of $K = 40$ and $K = 80$. The largest qualitative difference in terms of flow structure is seen near the salt intrusion length. The coarse discretisation of $K = 10$ underestimates the salt intrusion and therefore shows a logarithmic riverine flow profile for a larger region of the estuary, whereas finer grids show more salt intrusion and a larger estuarine circulation. Overall, we see a convergence of the mean flow profile at these locations, with $K = 40$ and $K = 80$ generating identical results.

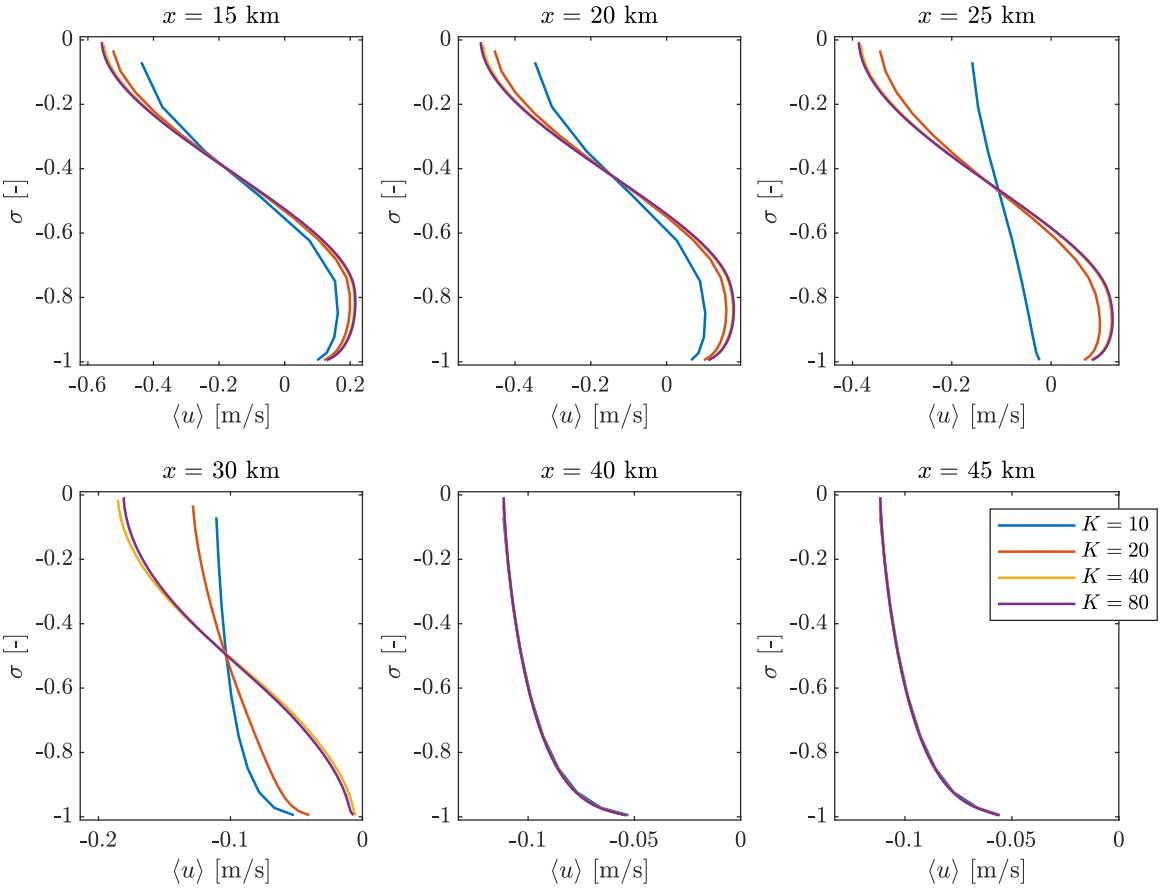

Figure 3.11: Tidally-averaged horizontal flow velocity $\langle u \rangle$ at several locations along the estuary for subsequent vertical grid refinements.

Energy Convergence

Instead of looking at flow profiles at certain locations, we can characterise the system using a global energy measure of the system. We only do so in the internal domain Ω with $x \in \Gamma = [1\text{ km}, 49\text{ km}]$, characterised by horizontal grid cells I_{min} to I_{max} to eliminate influences of errors near the boundaries.

With a variable density over the water column, the mass m over a water column approximates to $m = \int_{z_b}^{\eta} \rho dz \approx \sum_{k=1}^{K} \Delta z_{i,k}\rho_{i,k}$ for every water column at cell i. Therefore, the width-averaged potential energy E_p (in J/m or kg·m/s^2) at time step n, in terms of deviation from the still water level (using height η) is approximated by

$$E_p^n(K) = \int_\Gamma mg\eta dx \approx g\Delta x \sum_{i=I_{\min}}^{I_{\max}} \eta_i \sum_{k=1}^{K} \Delta z_{i,k}\rho_{i,k}. \tag{3.37}$$

where $\Delta z_{i,k} = \frac{1}{2}\left(\Delta z_{i-1/2,k} + \Delta z_{i+1/2,k}\right)$ is approximated by the average of the nearest cell face heights. The width-averaged kinetic energy is determined by

$$E_k^n(K) = \frac{1}{2}\iint_\Omega \rho|\boldsymbol{u}|^2 d\Omega \approx \frac{1}{2}\Delta x \sum_{i=I_{\min}}^{I_{\max}} \sum_{k=1}^{K} \Delta z_{i,k}\rho_{i,k}((u_{i,k}^n)^2 + (w_{i,k}^n)^2). \tag{3.38}$$

where the flow velocities at the centre of the cell are approximated by

$$u_{i,k}^n = \frac{1}{2}(u_{i-\frac{1}{2},k}^n + u_{i+\frac{1}{2},k}^n), \tag{3.39}$$

$$w_{i,k}^n = \frac{1}{2}(w_{i,k-\frac{1}{2}}^n + w_{i,k+\frac{1}{2}}^n). \tag{3.40}$$

Finally, the total turbulent kinetic energy in the flow domain equals

$$E_t^n(K) = \iint_\Omega \rho k d\Omega \approx \Delta x \sum_{i=I_{\min}}^{I_{\max}} \sum_{k=1}^{K} \Delta z_{i,k}\rho_{i,k}k_{i,k}. \tag{3.41}$$

The evolution of these energies over time is shown in Figures 3.12. The error over time after grid refinements is evaluated by differences in energy, i.e. for potential energy by

$$e_p^n(K) = E_p^n(K) - E_p^n(K/2), \tag{3.42}$$

at timestep n, similarly for other energy components. This is shown in Figure 3.13. Potential energy clearly shows the largest magnitude, as there is a large change in total mass in the system due to tidal activity. Also, a clear convergence is visible with differences in subsequent model energy values converging to zero for increasing K. However, for potential energy, the differences are around 1% and relatively accurate for $K = 10$ already. The most relative improvement can be seen in the kinetic energy as the quotient is rather large, but the improvement of $K = 40$ to $K = 80$ is negligible and $K = 40$ already seems to capture all kinetic energy.

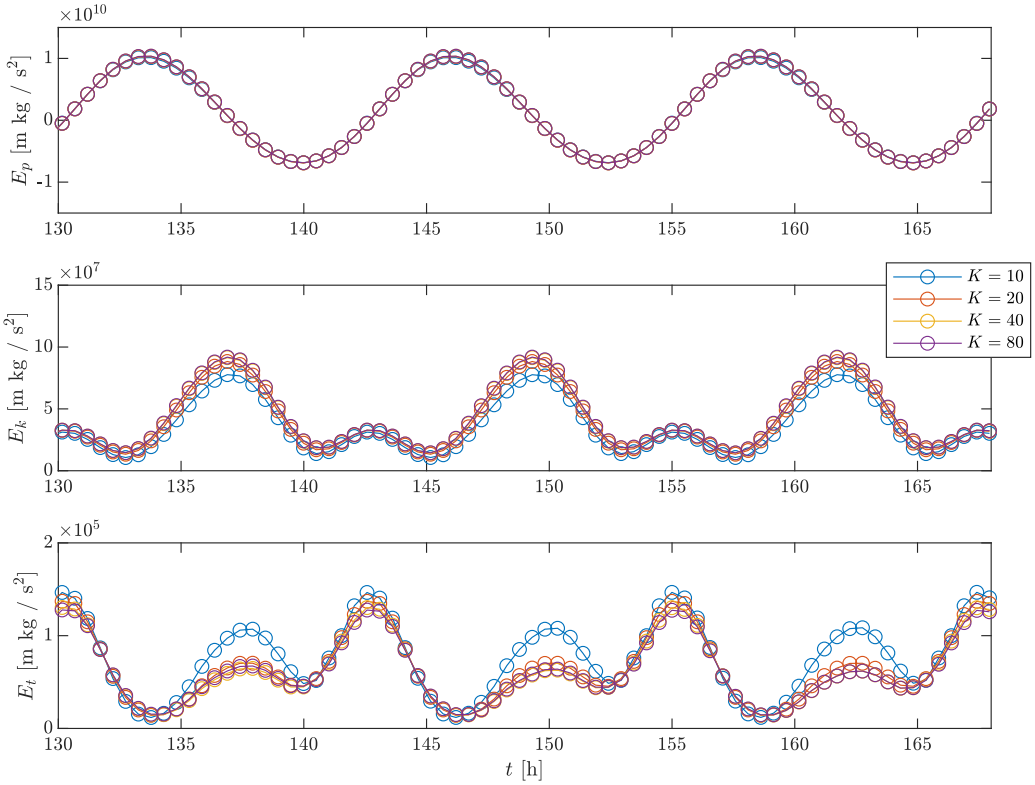

Figure 3.12: Evolution of the potential, kinetic and total turbulent kinetic energy over time for various vertical discretisations

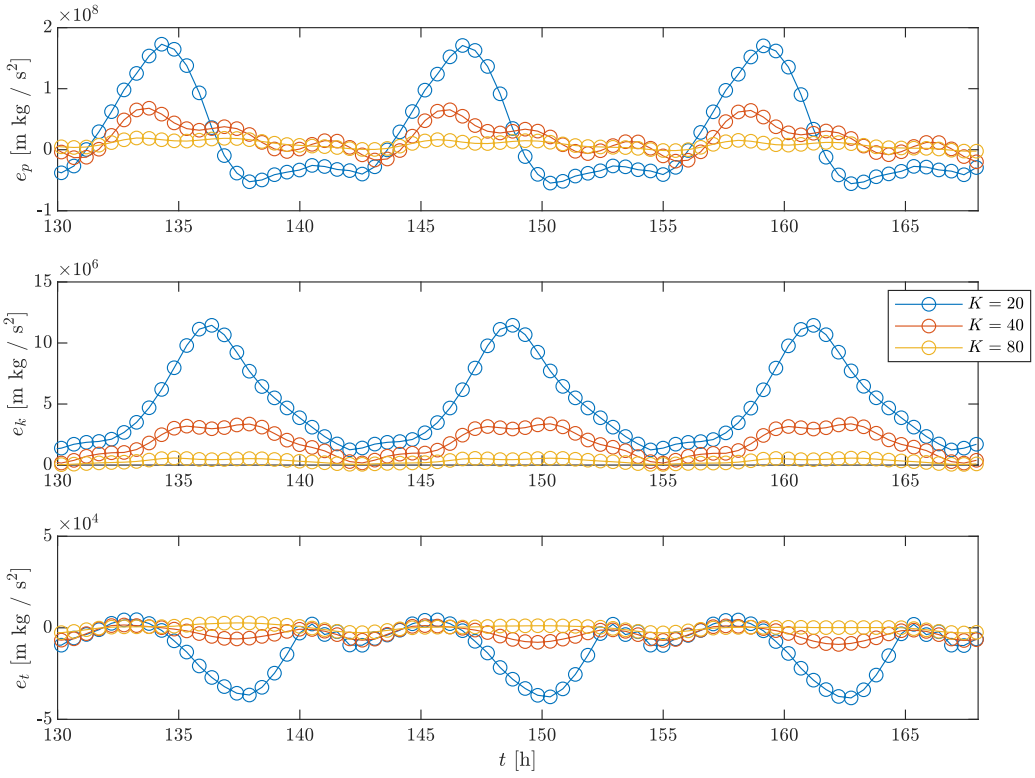

Figure 3.13: Difference of the potential, kinetic and total turbulent kinetic energy over time for subsequent vertical discretisations

Salt Convergence

Finally, as salt intrusion forms the main model output that will be investigated, we can determine the final state of the average longitude salt profile $\langle \overline{s} \rangle$, and numerical convergence of $L_s(t)$, which is shown for various K in Figure 3.14. Again, results are equivalent for $K = 40$ and $K = 80$. The depth-averaged salinity decreases with fewer layers, and the salt intrusion length decreases. The difference between grids is only visible for $x > L_0$, where sand dunes are located and hence stems from inaccurate modelling of flow over dunes in coarse vertical grids.

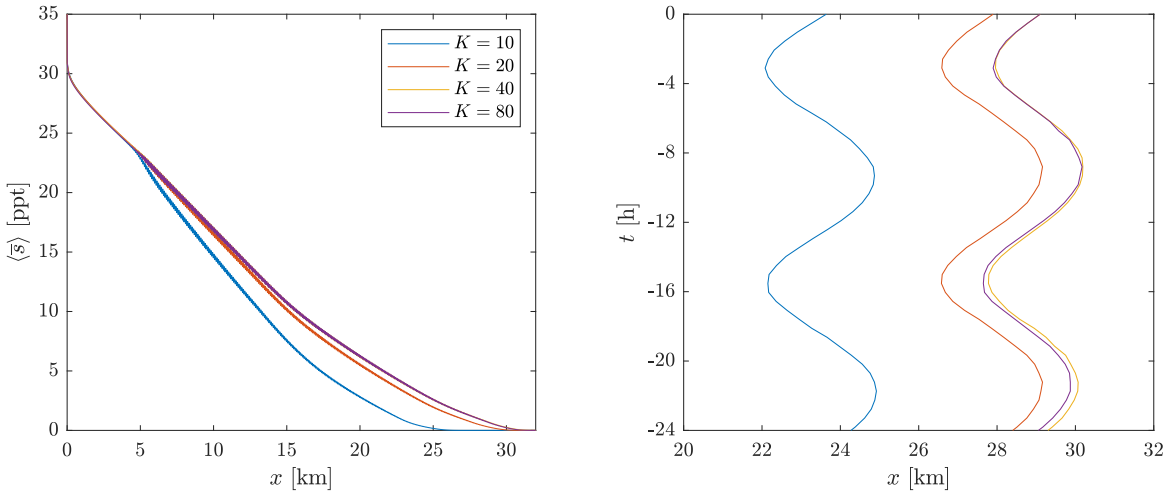

Figure 3.14: Left: Tidally- and depth-averaged salinity $\langle \overline{s} \rangle$ over the last tidal cycle for different vertical discretisations. Right: Evolution of $L_s(t)$ for the final stages of the simulation for various number of vertical layers.

3.5 Summary of Final Model Discretisation and Parameters

All in all, we conclude that using $K = 40$ vertical layers is sufficient to capture most of the tidal, flow and turbulent dynamics in the system and this resolution is sufficient to capture the salt intrusion accurately. A visualisation of the grid for symmetric dunes with length $\lambda_d = 100$ m, and $H_d = 2.0$ m for $\Delta x = 10$ m and $K = 40$, when $\eta = 0$ is shown in Figure A.2 in Appendix A.2.3. Furthermore, the model geometry, turbulence parameters, and discretisation settings are shown in Table 3.1.

Table 3.1: Final model settings and parameters.

Parameter	Value	Setting / Parameter	Value	Parameter	Value
L	50 km	Turbulence model	k-ϵ	Δx	10 m
h	15 m	HLES	Off	K	40
s_{river}	0 ppt	ν_h^{BACK}	10 m^2/s	f_1	0.1%
q_r	1.5 m^2/s	ν_v^{BACK}	10^{-3} m^2/s	z_0	0.001 m
s_{sea}	35 ppt	D_h^{BACK}	$10/\sigma_\rho$ m^2/s	Δt	2.7 s
ω	$1.406 \cdot 10^{-4}$ rad/s	D_v^{BACK}	$10^{-3}/\sigma_\rho$ m^2/s	L_0	5 km
A_{sea}	1 m			ΔL_0	1 km
g	9.81 m^2/s				
σ_ρ	0.7				

Chapter 4

Model Validation and Verification

In this chapter, we validate the model output of two reference models by comparison with field measurements in the RWW and verify the transport mechanisms with model results of a different study, which shows that model settings represent the RWW relatively accurately. We highlight the influence of the definition of the salt intrusion length and show how different definitions change the interpretation of model output marginally. The two reference models show the potential influence of a natural dune field on salt dynamics and intrusion. We show the influence of the background eddy parameters on model output and salt transport and argue that these values can be used to model different estuaries.

4.1 Validation and General Model Analysis

Firstly, we describe the results for two general model settings; a flat bathymetry model B-0 (where $H_d = 0$ m) and uniform symmetric sinusoidal bathymetry model B-1 where $(\lambda_d, H_d, \alpha_d) = (100\text{ m},\ 2\text{ m},\ 0)$. Snapshot flow velocities of u and w and of salinity s for model B-1 throughout the tidal cycle have been shown in Appendix A.4. We validate the model results based on the flow and salinity measurements of de Nijs et al. (2010) and verify it against the 3D Delft3D-FLOW model results of the Operationeel Stromingsmodel Rotterdam (OSR-model[15]) of Kranenburg and van der Kaaij (2019) and the regime determination of the RWW based on the OSR-model by Dijkstra et al. (2022).

4.1.1 Free Surface Elevation

Fourier analysis of water levels at Hook of Holland from Rijkswaterstaat (2023b) shows multiple significant (high-frequency) tidal components, of which the principal solar semidiurnal S2 (with elevation amplitude $A_{\mathrm{S2}} = 0.3$ m), the principal lunar diurnal ($A_{\mathrm{O1}} = 0.2$ m), lunar semi-diurnal tide ($A_{\mathrm{M2}} = 0.8$) and shallow water overtide ($A_{\mathrm{M4}} = 0.2$ m) are dominant, but many more exist. Moreover, visual inspection shows a spring-neap difference of around 0.5 m (a combination of the M2 and S2 components). Figure 4.1 shows the tidal elevation for several locations along the estuary in September 2023 (Rijkswaterstaat, 2023b). This shows some lag in the flood wave, but in general, the time of the peak seems relatively uniform in the interior. Moreover, the peak tidal elevation at $x = 32$ km (in the city centre of Rotterdam) is about equal to the elevation at the seaward side.

In our model, the tide is strongly schematised with only one tidal constituent. Hence, we do not expect to obtain realistic tides that compare with the RWW, but merely look for realistic tidal propagation. The free surface elevation of B-1 is shown in Figure 4.2. The overall high- and low-water heights are realistic values compared to Figure 4.1. The negligible phase difference across the estuary

[15] See Kranenburg et al. (2014) for model construction

and the tidal amplification of the flood wave do not match with field data. Changing the roughness height z_0 only influences the amplification slightly, but greatly influences the salt intrusion length. Therefore, as the tidal wave shows no clear resonance or unphysical amplification, we neglect the influence of the (relatively small) amplification. Moreover, the missing phase difference likely results from the 2DV setting and a simplified tidal boundary condition with a single frequency.

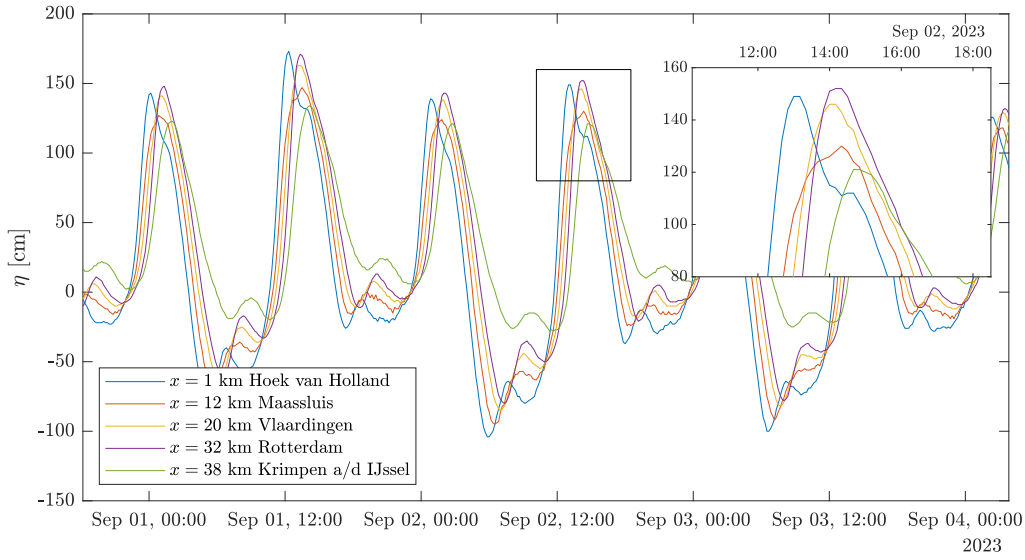

Figure 4.1: Free surface elevation from Rijkswaterstaat (2023b).

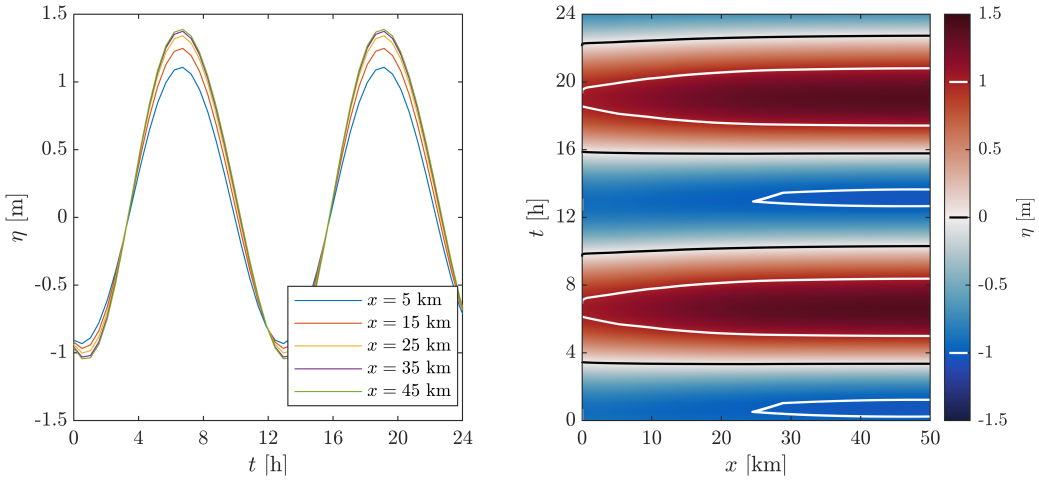

Figure 4.2: Free surface elevation for model B-1 over a single day. Left: Timeseries of η for five locations along the estuary. Right: Surface plot of tidal elevation, black and white lines indicating contours of constant free surface elevation of $\eta = 0$ m and $\eta = \pm 1$ m respectively.

4.1.2 Flow Velocities

The horizontal velocity u at the surface (layer $k = K = 40$) and near the bed (in layer $k = 10$, resulting in $h \sum_{k=1}^{10} f_k = 8.3\% h \approx 1.25$ m from the bed) are shown in Figure 4.3. The surface velocity is directed seaward for a major part of the tidal cycle. Flow reversal occurs during a small part of the tidal cycle, but is especially present above the dune field of $x \in [5, 45] = [L_0, L - L_0]$ km (which could be a coincidence). We find a relatively sharp boundary (on the estuary scale) of different horizontal flow structures, just landward of $\langle L_s \rangle$. This can also be seen in the horizontal flow velocity u in

Figures A.5 and A.9 in Appendix Section A.4. This is not necessarily unphysical, there are no lateral processes to smooth this transition due to the 2DV setting. Furthermore, turbulence differs greatly in the two respective regions due to the dampening effect of the stratification (see Subsection 4.1.3). In the incoming river flow, wherever the salinity concentration and stratification are small, a smooth logarithmic flow develops over the bed. As a salinity gradient is formed, the turbulent kinetic energy is dampened by the buoyancy flux, the eddy viscosity is halved and the gravitational circulation can be observed. Since we are interested in the structure within the region of stratification, and since $\langle L_s \rangle$ is located within the region of stratification, we can neglect this sharp boundary.

Modelled low velocities and salt concentrations for four locations are shown in Figure 4.4, besides the measurements of de Boer and Radersma (2011) in Figure 4.5. Even though the model is highly idealised, the flow patterns and velocity magnitude are relatively similar to the measurements of de Nijs et al. (2010) in the RWW, with velocities at the surface reaching over 1.2 m/s during ebb. During flood, both the model and measurements show landward-directed flow. However, in the model, these largest negative velocities are attained in the middle of the water column, as opposed to the surface. Moreover, at $x = 8$ km in our model, there is always a negative horizontal flow velocity near the bed, whereas measurements show that the near-bed velocity changes sign over the tidal period.

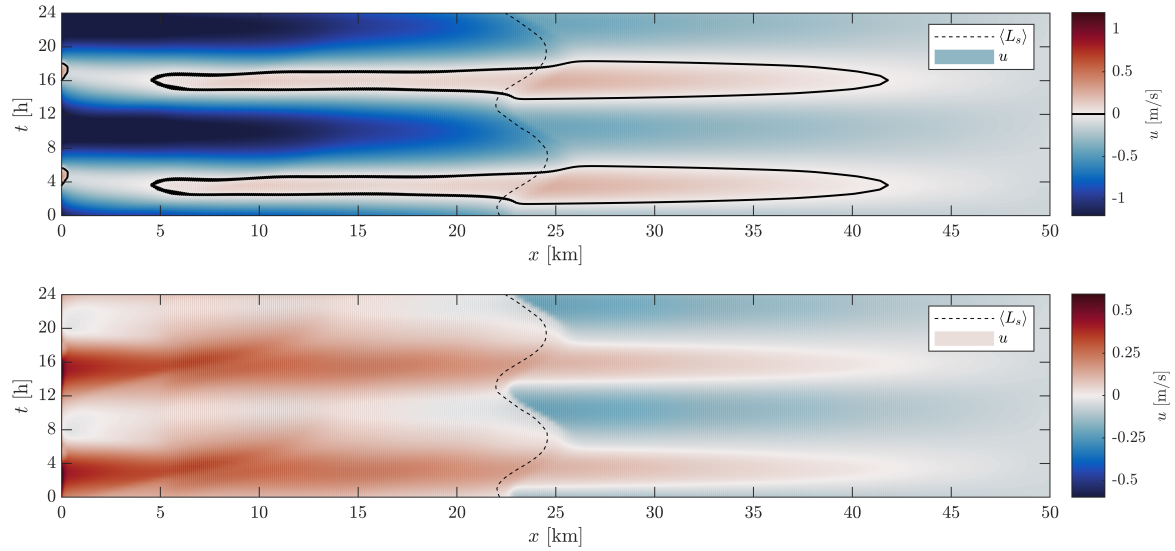

Figure 4.3: Horizontal velocity u at the surface (top) and at the 10th layer from the bed (bottom) for the base case over a single day.

Under the rigid lid approximation, the depth-averaged depth-averaged flow velocity $\overline{u}$ is uniform over the estuary (details of this are provided in Appendix A.1.3). Hence, when assuming that the seaward tidal elevation results in a tidal flow component of velocity magnitude U_t, Dijkstra et al. (2022) have shown that $\overline{u}$ then equals

$$\overline{u} = U_r + U_t \cos(\omega t). \tag{4.1}$$

In our model, the free surface moves freely and (almost) uniformly over the domain. Moreover, at the riverine boundary $x = L$, we have a constant inflowing river discharge of $q_r = 1.5$ m^2/s, resulting in a depth-averaged velocity of $\overline{u} = U_r = -0.1$ m/s. As a consequence, we find from model results that the tidal velocity component decreases linearly over the estuary, and the depth-averaged horizontal velocity is approximately equal to

$$\overline{u} = U_r + \frac{L - x}{L} U_t \cos(\omega t), \tag{4.2}$$

with $U_t \approx 0.55$ m/s. This shows that the implementation of a free surface does change along-estuary flow characteristics, and shows the physical influence of the estuary length L, which will be discussed further in the discussion in Section 6.1.

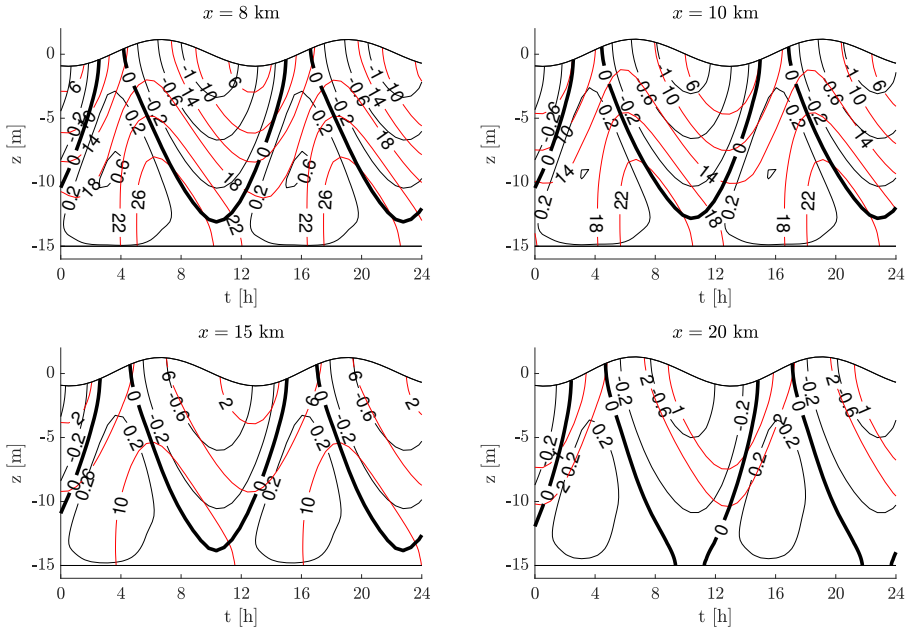

Figure 4.4: Model results of B-1: Evolution of velocity and salinity over time for some fixed locations, velocity contour lines in black and isohalines in red.

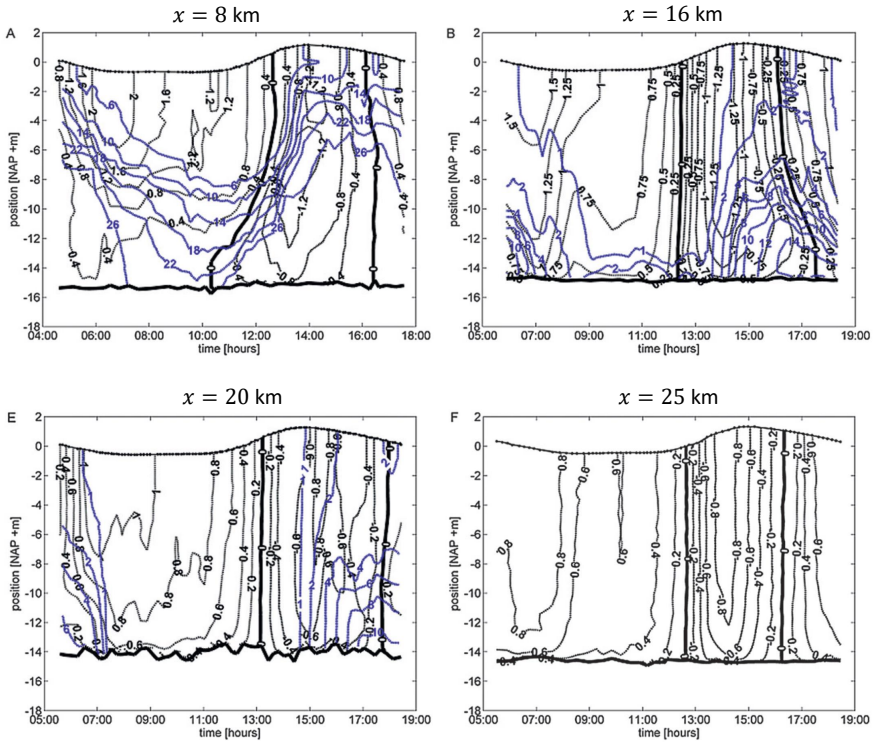

Figure 4.5: Measurements of velocity and salinity over time for some fixed locations, velocity contour lines in black and isohalines in blue. Retrieved and adapted from de Boer and Radersma (2011).

4.1.3 Turbulence

The eddy diffusivity through the water column is estimated by de Nijs et al. (2010) based on the Reynolds' stresses and shown over a tidal cycle in Figure 4.6. These measurements show turbulent diffusivity is mainly located in the bottom half of the water column and that turbulence is more suppressed in the upper half near the sea in a region of high stratification.

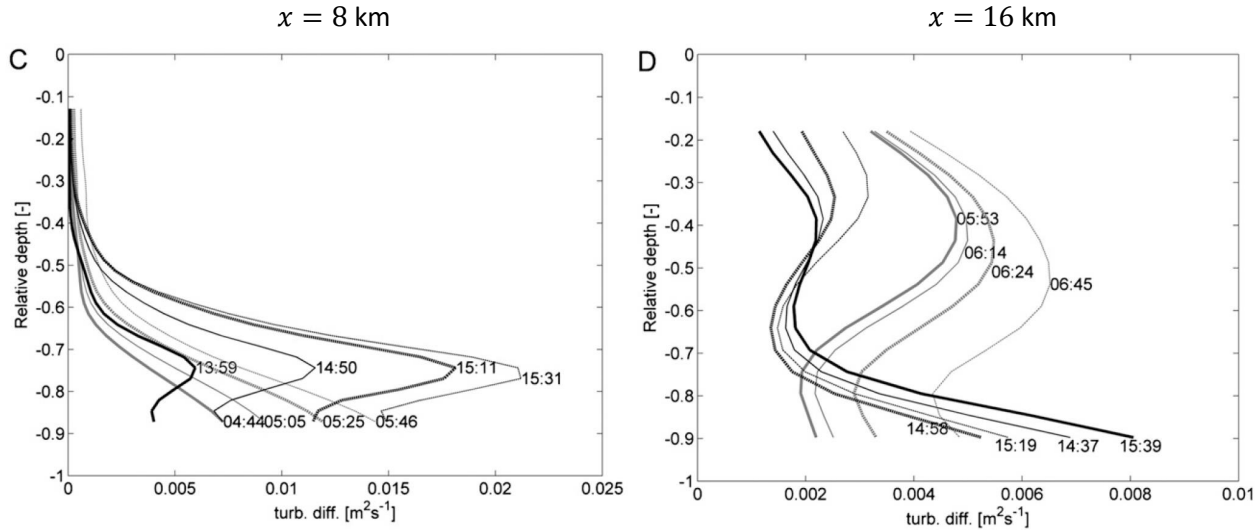

Figure 4.6: Prediction of eddy viscosity K_v, based on estimates of Reynold's stresses. Retrieved and adapted from de Boer and Radersma (2011). Times indicated align with the time and free surface shown in Figure 4.5.

The value of K_v throughout a tidal cycle in the model is shown in the stratified region in Figure 4.7. Again, results are relatively similar as the largest values are attained about 2 meters above the bed. Moreover, the order of magnitude is relatively similar and the largest values are attained during flood.

The main difference is that the model shows almost no additional turbulent diffusivity in the top half of the water column, and eddy diffusivity reduces to the background eddy diffusivity D_v^{BACK}. Furthermore, in the model, the turbulent component D_{3D} reduces to zero over the complete water column during ebb. Measurements indicate also more turbulent diffusion during ebb in the upper part of the water column, especially further from the seaward end (See $x = 16$ km in Figure 4.6). This might originate from the riverine turbulence, and therefore, we show the eddy diffusivity further upstream in Figure 4.8. The riverine region shows way larger values of K_V than the stratified region, which indicates the large influence of the buoyancy flux on the turbulence closure. In line with Figure 4.6, the eddy diffusivity is larger during ebb than flood.

All in all, we conclude that the magnitude of all flow, salinity and turbulence properties in the stratified region of the RWW are well represented by the numerical model. Furthermore, qualitative patterns in model runs and measurements are similar.

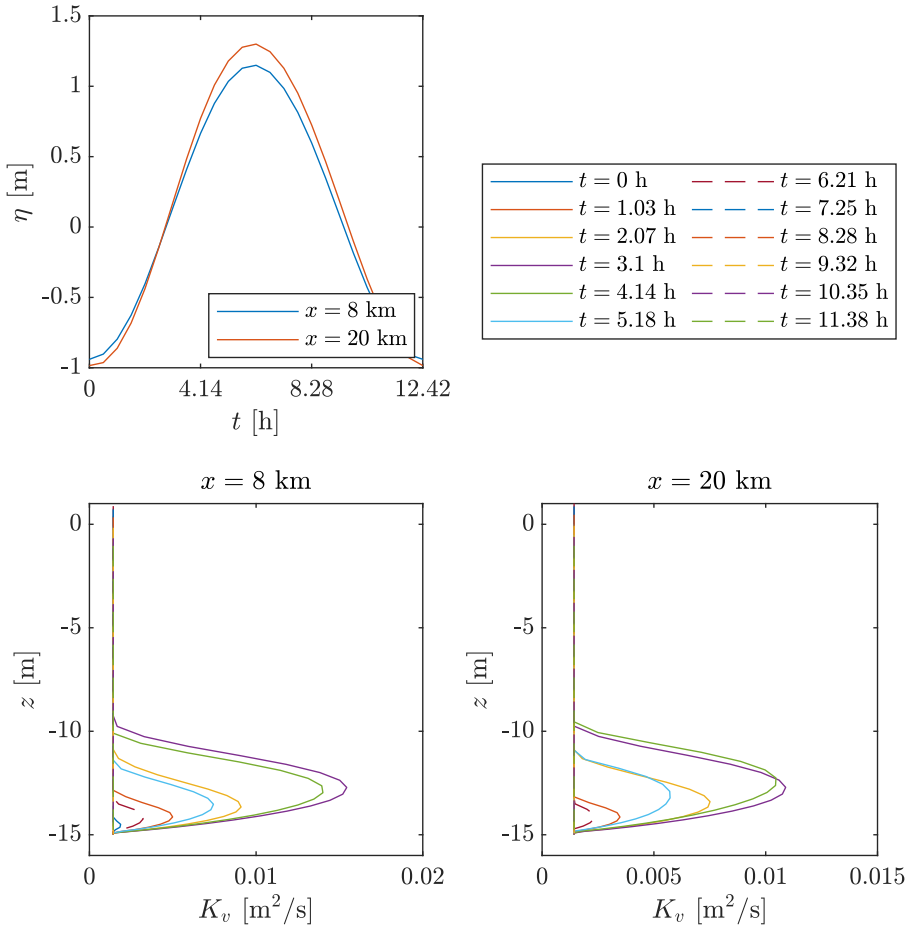

Figure 4.7: Vertical eddy diffusivity at several moments during the tidal cycle within the region of stratification, note that the eddy viscosity is especially large during flood (dotted lines) when water levels increase.

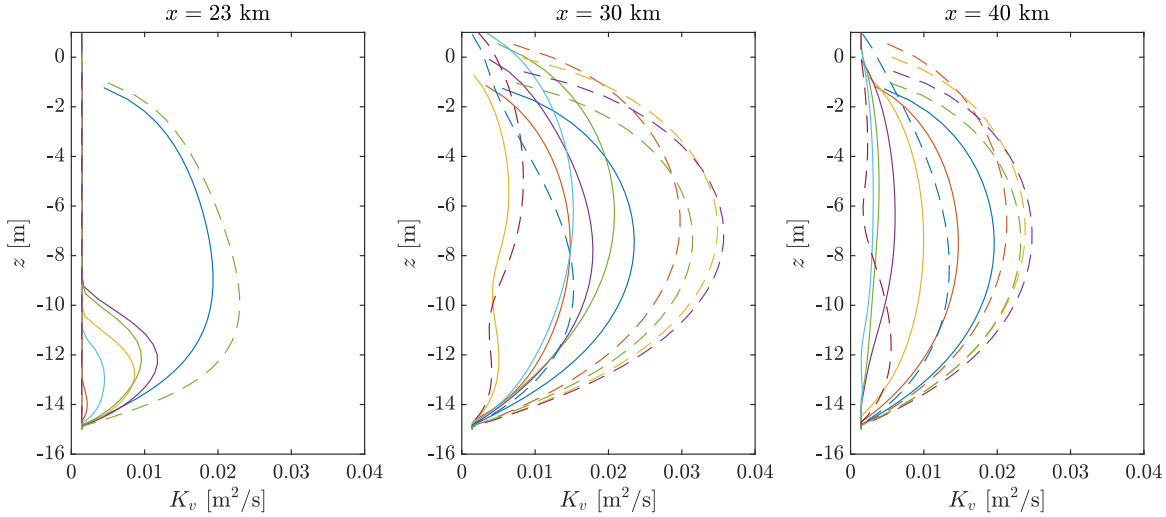

Figure 4.8: Vertical eddy diffusivity at several moments during the tidal cycle in freshwater river flow. Colours are the same as in Figure 4.7. Note that the eddy viscosity is larger during ebb.

4.2 Influence of Definition of Salt Intrusion Length on Results

The influence of topography changes on salt intrusion is quantified by the salt intrusion length, which we can define by L_s, $L_{\overline{s}}$ and L_{s_η} as given in Subsection 2.2.2. The choice of mainly using L_s for analysis and the critical concentration of $s_c = 1$ ppt for each definition is quite arbitrary and other quantifiers could be made, for example, the concentration 5 meters below the free surface as often measured by field campaigns. In any case, the chosen quantifier should not qualitatively influence the analysis of the results. Therefore, we highlight the influence of the quantifier choice on the relative influence of salt intrusion length and show the independence of results on the quantifier.

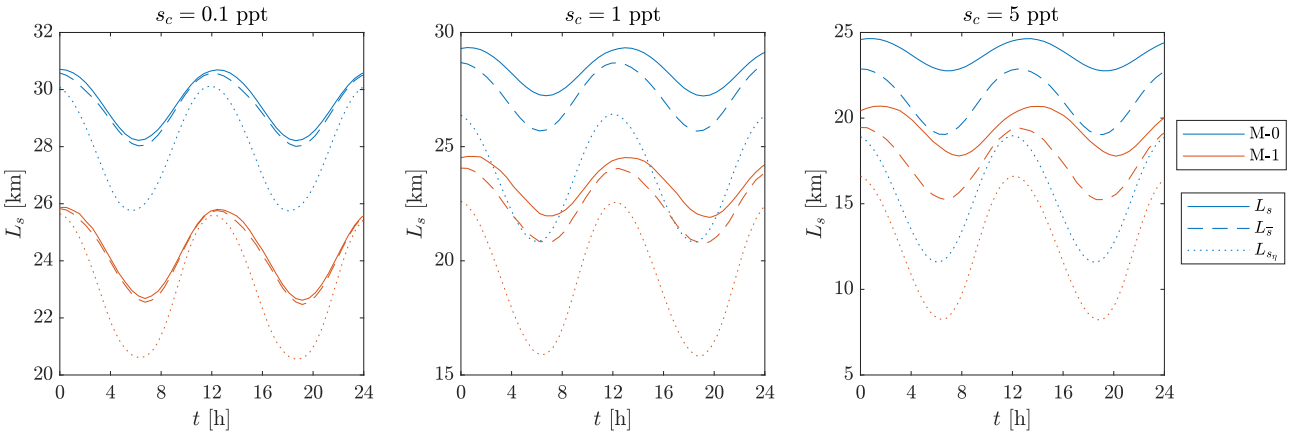

Figure 4.9: Comparison of the tidal excursion of salt intrusion quantifiers L_s, $L_{\overline{s}}$, L_{s_η} for both B-0 and B-1 for three different critical salinity concentrations s_c.

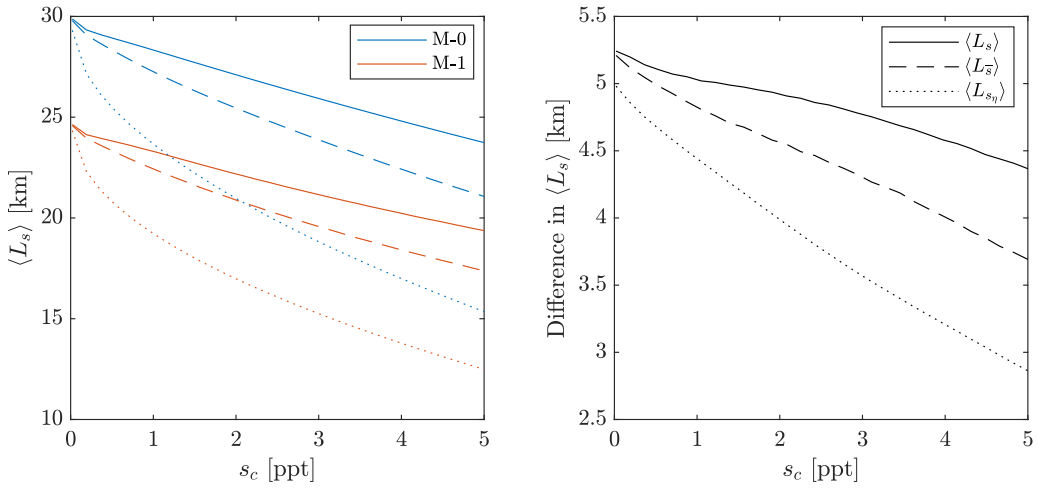

Figure 4.10: Left: Comparison of subtidal salt intrusion length of L_s, $L_{\overline{s}}$, L_{s_η} for both B-0 and B-1 for different critical salinity concentrations s_c. Right: Comparison of relative improvement of salt intrusion length from B-0 to B-1 for different quantifiers and critical salinity concentrations s_c.

In Figure 4.9 we show the evolution of all three quantifiers over time for B-0 and B-1, using three critical concentrations of $s_c = 0.1$, 1.0 and 5.0 ppt respectively. A lower critical salinity decreases the difference between the quantifiers, which argues for a lower value of s_c. Figure 4.10 shows that when the s_c goes to 0 ppt, all quantifiers converge to the same salt intrusion length. Furthermore, the right plot of Figure 4.10 shows that the observable model differences increase with lower critical salinity concentration. The model improvement from B-0 to B-1 is similar when using $\langle L_s \rangle$ or $\langle L_{\overline{s}} \rangle$, with 5.05

and 4.85 km respectively at $s_c = 1$ ppt, which still allows for a significant difference of L_s and L_{s_η}, allowing for evaluation of the stratification measure L_i.

All in all, a change in salt intrusion length between two bathymetries can be measured using all quantifiers and critical concentrations and results are independent of the choice. We see that L_s provides a good choice of quantifier as model improvements after topography changes are least dependent on the critical concentration. Moreover, the critical concentration of $s_c = 1$ ppt seems to be low enough to provide significant model improvement, while not being influenced by numerical inaccuracy for small concentrations and still distinguishing a significant isohaline length L_i.

4.3 Verification of Transport Mechanisms

The main transport mechanisms and the value of the non-dimensional parameters Ra, StRa, Fr_r and Fr_t are estimated locally for the RWW by Dijkstra et al. (2022). Using the salt flux decomposition, we identify the individual processes and estimate the value of these parameters based on their depth-averaged value. The results are shown in Figure 4.11.

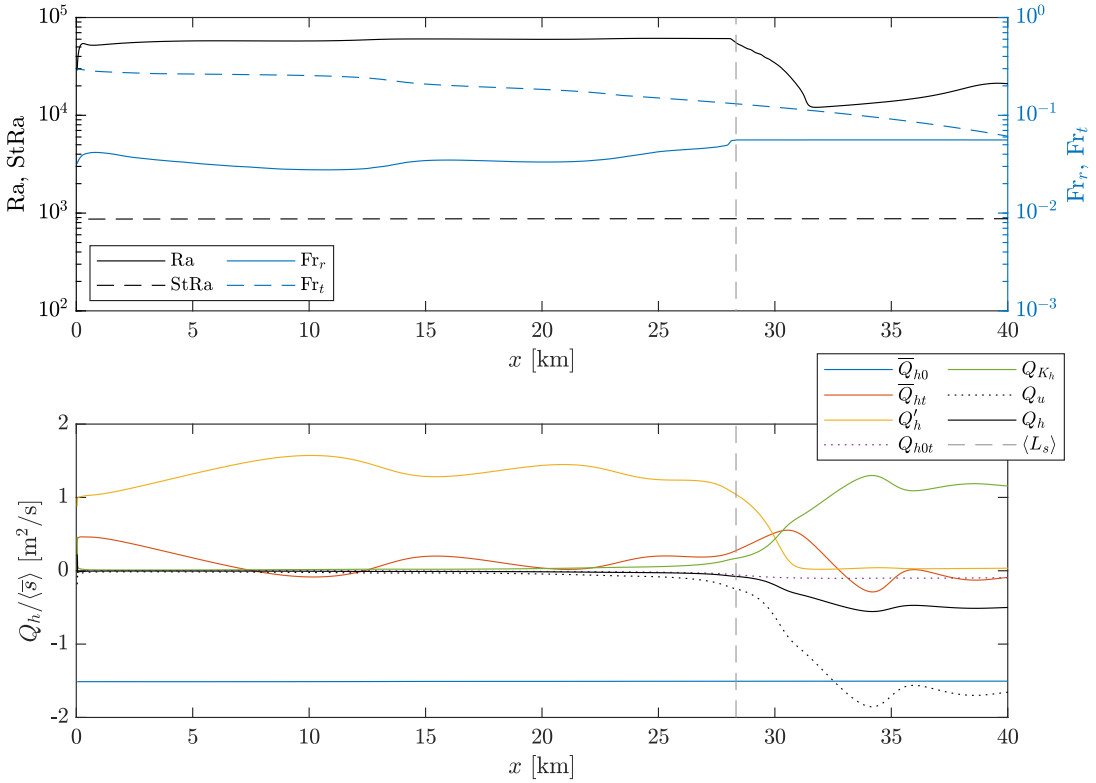

Figure 4.11: Top: Non-dimensional numbers along the estuary in line with Dijkstra et al. (2022). Bottom: Horizontal flux decomposition from B-0 in dynamic equilibrium. The black line indicates the sum of all processes Q_h, the dotted line is the sum of all advective processes Q_u and the dashed vertical line is the salt intrusion length.

In terms of non-dimensional parameters, we observe that the order of magnitude is equivalent and that the value of Ra decreases upstream of $\langle L_s \rangle$. Our model shows relatively little variation in the Froude numbers as there is no lateral variation. Both models show a similar balance between the subtidal depth-averaged transport of river flushing ($\overline{Q}_{h0}$) and the subtidal shear by estuarine circulation (Q'_h). The contribution of this shear decreases upstream of the salt intrusion length. The tidal depth-averaged contribution $\overline{Q}_{ht}$ is nearly the same, it is directed seaward (negative) near the mouth and of

relatively low order, and the magnitude increases just upstream of $x = \langle L_s \rangle$. The order of magnitude of all transport components is of the same order of magnitude, when multiplying our result for Q_h with the mean estuary width 500 m, we also obtain transport rates of around $-1.0 \cdot 10^3$ m^3/s. The main observable difference is the larger fluctuations in Dijkstra et al. (2022), especially due to river flushing. This results from the variable width, and in turn, varying river velocity for equal discharge.

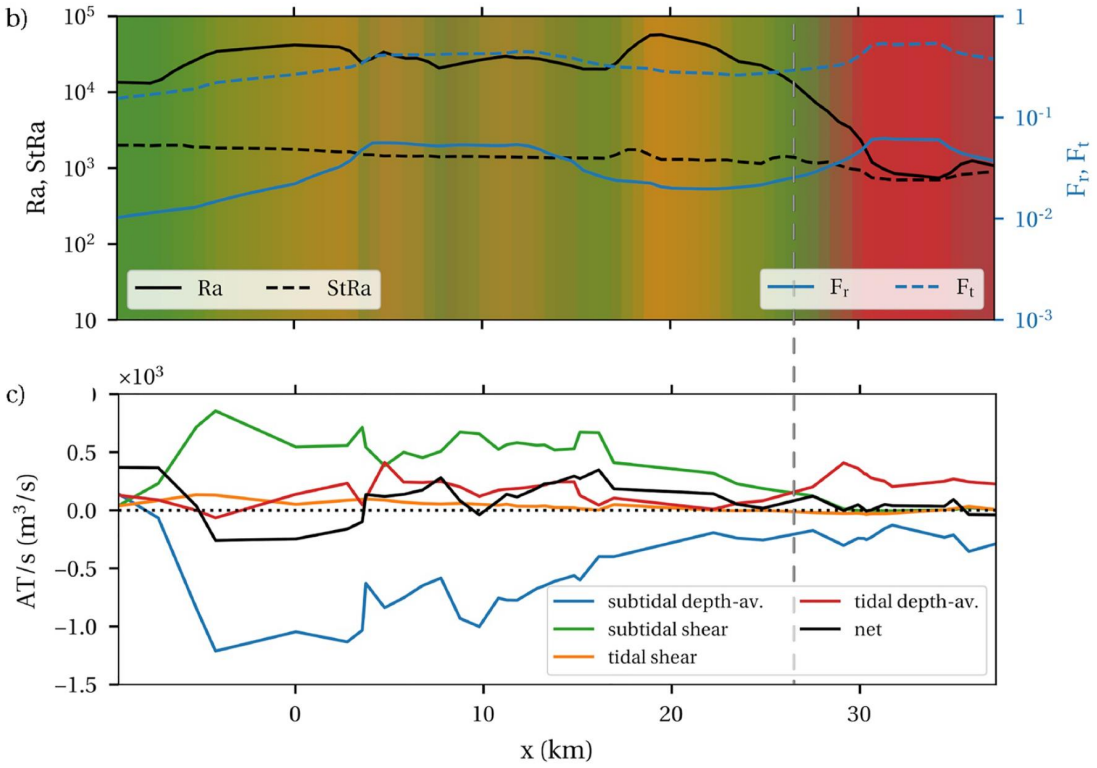

Figure 4.12: Retrieved and adapted (the x-axis is shifted) from Dijkstra et al. (2022). Non-dimensional numbers and horizontal flux decomposition throughout the RWW.

4.4 Comparison of Reference Models

Next, we show the influence of sand dunes on the transport mechanisms by comparing reference models B-0 and B-1. The horizontal transport components for both B-0 and B-1 are shown in Figure 4.13, where dune-averaging is applied to the transport components of B-1 as in Equation 2.24. Both systems are in dynamic equilibrium with the tide[16], and the salt intrusion length is smaller when sand dunes are present, but the relative contributions of all transport mechanisms are relatively equal; subtidal depth-averaged transport $\overline{Q}_{h0}$ is uniform over the estuary, the estuarine circulation induces a shear transport Q'_h directed landward and the tidally-correlated depth-averaged transport $\overline{Q}_{ht}$ is largest just landward of the 1 ppt isohaline and locally directed landward near $x = 10$ km. Lastly, the averaging residual Q_{h0t} is negligibly small along the estuary.

As expected, the contribution of dispersive transport Q_{K_h} is negligible. Landward of $\langle L_s \rangle$, where salinity concentrations are small, we see an increase in dispersive transport, balanced by the outflowing river flow. However, this is likely a numerical artefact of numerical gradients of small concentrations.

[16] see Appendix A.3 for more information on how this is determined.

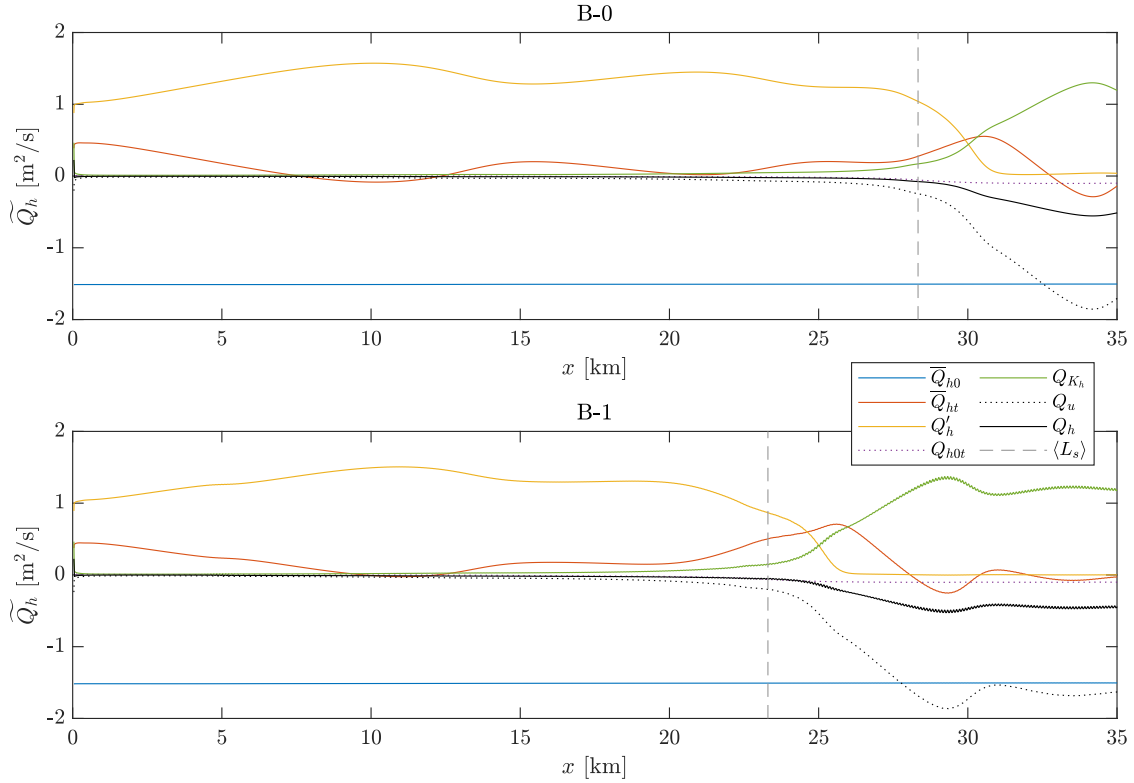

Figure 4.13: Horizontal flux decomposition, total amount of transport and salt intrusion length for reference models B-0 and B-1.

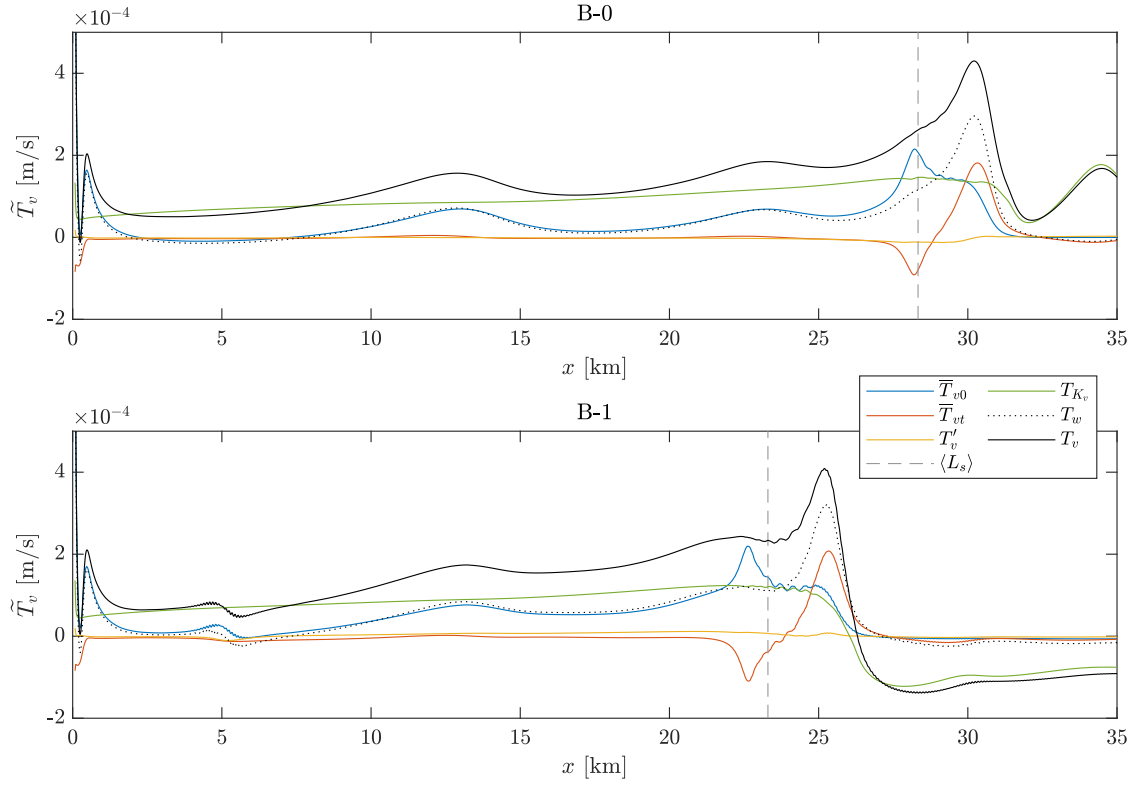

Figure 4.14: Vertical flux decomposition, total amount of transport and salt intrusion length for reference models B-0 and B-1.

For the vertical flux components, we apply the dune-averaging to each component as in Equation 2.26. The results for models B-0 and B-1 are shown in Figure 4.14. Quite surprisingly, the along-estuary dune-averaged vertical transport is relatively similar between both models, both qualitatively and quantitatively. The advective transport of model B-0 can only be attributed to the overall estuarine circulation. Still, the magnitude of advective and dispersive transport are relatively equal, especially near the salt intrusion limit.

The main advective transport component is the subtidal depth-averaged transport $\overline{T}_{v0}$, i.e. a persistent net upward transport over the dunes. Only near the salt intrusion limit, which moves back and forth during the tidal cycle, there is a tidally-correlated depth-averaged transport through the water column $\overline{T}_{vt}$, downward seaward of $\langle L_s \rangle$ and upward landward of $\langle L_s \rangle$. This can be explained by the change in near-bottom horizontal velocity u on the landward and seaward side of this limit, causing different vertical transport on either side as shown in by the vertical velocity in Figure A.7 in Appendix A.4.2. This effect is more pronounced when sand dunes are present, as the overall magnitude of advective transport increases. Within the region of significant salt concentration ($0 < x < \max(L_s)$), there is more net upward transport in B-0 compared to B-1. Later, in Subsection 5.1.1, we quantify this exactly using $\mathcal{M}_v$ of Equation 2.27.

The dispersive transport T_{K_v} is relatively equal between both models. Furthermore, this transport is relatively uniform along the estuary (when dune-averaged) and drops in magnitude landward of $\langle L_s \rangle$. However, we do not consider these values as they are again likely artefacts of taking numerical gradients of small numbers over small distances.

The net vertical transport as in Figure 4.14 is relatively small and almost equal between B-0 and B-1, due to the relative symmetry with opposite signs of vertical transport on each side of a sand dune (downward and upward respectively). We characterise the overall amount of vertical stirring with $\mathcal{S}$ of Equation 2.28 to determine the vertical advective activity, which is shown in Figure 4.15. Note that the magnitude[17] increases by a factor of 20 between B-0 and B-1. This shows the large impact sand dunes have on the overall stirring through the water column by vertical advective processes.

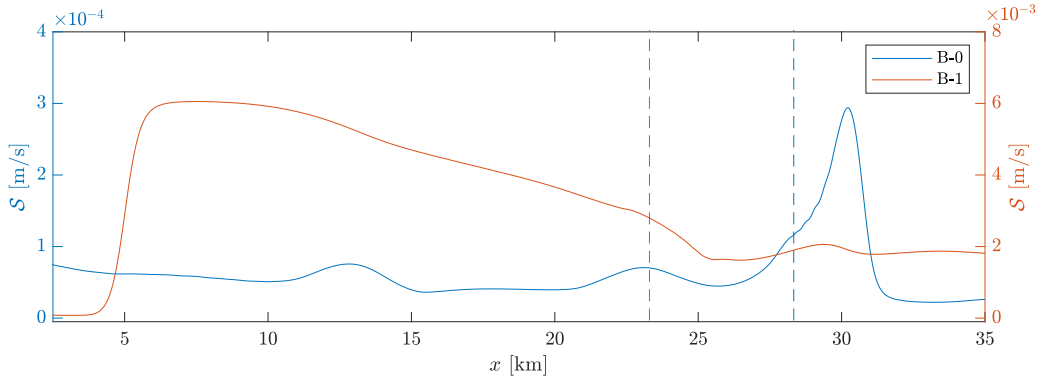

Figure 4.15: Vertical stirring parameter $\mathcal{S}(x)$ of Equation 2.28 for models B-0 (blue) and B-1 (red), dashed lines indicate salt intrusion length.

Generally speaking, we observe that sand dunes do change the salt intrusion length significantly. However, the horizontal transport mechanisms and net vertical transport in dynamic equilibrium do not change, hence the estuarine and transport classification is not altered by sand dunes. The change in salt intrusion is likely a result of overall vertical mixing, characterised by $\mathcal{S}$, which in turn changes the salt intrusion length.

[17] y-axes use different scales for B-0 and B-1

4.5 Influence of Background Eddy Parameters

The background eddy parameter values were chosen based on research of Dijkstra et al. (2022). However, their results showed local variability while our model uses estuarine uniform parameter values. Therefore, in this section, we investigate the influence of these model parameters on model output. We vary every parameter independently from the baseline values as presented in Table 3.1 by multiplication $\cdot(1/2)^i$ for $i = -1, 1, 2$ (i.e. relative parameter values of 2, 1/2 and 1/4 respectively) for model geometry B-1.

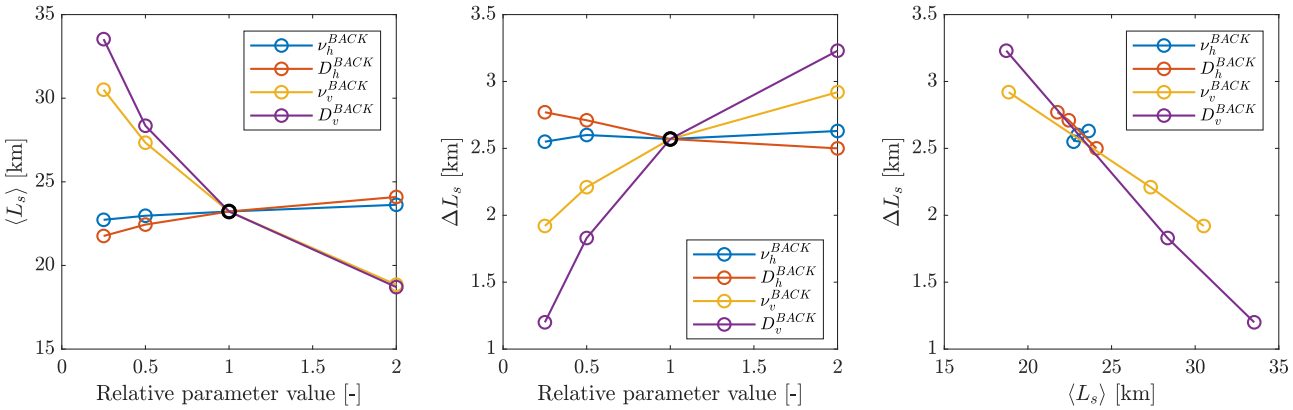

Figure 4.16: Influence on background eddy parameters, relative to the values as in Table 3.1, on salt intrusion length. Left: Salt intrusion length $\langle L_s \rangle$ for different relative background parameter values. Middle: Influence of background parameters on tidal excursion length ΔL_s. Right: Relation of tidal excursion ΔL_s to salt intrusion length $\langle L_s \rangle$.

The influence on the salt intrusion length $\langle L_s \rangle$ and tidal excursion ΔL_s can be seen in Figure 4.16. We show the absolute length of L_s, rather than the relative change, as the magnitude and physical interpretation now remains. Overall, vertical background values influence the salt intrusion length significantly more than horizontal parameters, in line with theoretical non-dimensionalisation. Moreover, as expected, larger horizontal values increase horizontal dispersion and increase $\langle L_s \rangle$, whereas larger vertical values increase vertical mixing and decrease $\langle L_s \rangle$. Moreover, the tidal excursion of the salt intrusion limit changes with model background parameters, which turns out to be inversely proportional to the salt intrusion length, except for ν_h^{BACK} (right of Figure 4.16).

When $D_v^{BACK} \to 0$ m^2/s, the salt intrusion length increases further, resulting in large concentrations at the riverine boundary and unphysical model results; there is no coupling of the vertical pycnoclines and horizontal flow velocities persist in landward direction near the bed. This results in large vertical flow velocities just near the boundary. Once these patterns are in place, they persist after increasing background values due to unphysical interaction with the boundary condition.

The influence of model parameters on the horizontal isohaline length is shown in Figure 4.17. Changing horizontal parameters leaves the subtidal length of L_i basically untouched and the stratification remains such that the isohaline is approximately 4 km in length. Reducing the vertical diffusion parameter D_v^{BACK} can increase the length of the isohaline, indicating an increase in the overall amount of stratification. The middle panel of Figure 4.17 shows that a decrease in ν_v^{BACK} decreases the variability of the isohaline length over the tide, i.e. it stabilizes the stratification over time. The right panel indicates that a larger salt intrusion length generally correlates to a larger isohaline length, i.e. more stratification near the salt intrusion limit.

In general, we note that the tidal variability of the isohaline ΔL_i is relatively constant at around 3 to 5 km in length and is approximately equal to the isohaline length itself. This indicates a large

variability in general, and the isohaline can differ from 2 km during high tide, to 6 km at low tide (see Figure A.8).

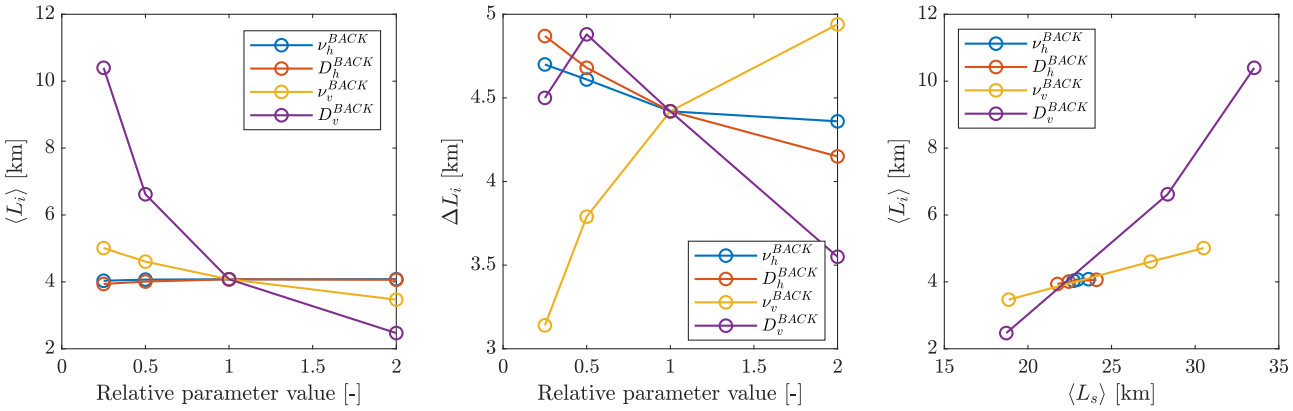

Figure 4.17: Influence on background eddy parameters, relative to the values as in Table 3.1, on the horizontal isohaline length. Left: Isohaline length $\langle L_i \rangle$ for different relative background parameter values. Middle: Influence of background parameters on tidal variability of the isohaline ΔL_i. Right: Relation of the isohaline $\langle L_i \rangle$ to salt intrusion length $\langle L_s \rangle$.

The various transport components are also analysed for various model parameters, and all have a negligible influence on horizontal transport components. In the vertical direction, the following observations are made:

- ν_h^{BACK} has a negligible influence vertical transport components.
- D_h^{BACK} has a significant influence on the vertical components. When decreasing this value, the magnitude of the tidally-correlated depth-averaged transport component $\overline{T}_{vt}$ increases linearly, and the total advective transport increases equally as all other components remain equal.
- ν_v^{BACK} has a significant influence on the vertical components, similarly to D_h^{BACK}. Decreasing the value of ν_v^{BACK} results in an increase of $\overline{T}_{vt}$ just landward of the salt intrusion length. However, contrary to D_h^{BACK}, the salt intrusion length increases.
- D_v^{BACK} has a significant effect on the dispersive transport T_{K_v} as expected. The advective transport components change much less. Furthermore, it can significantly change the isohaline length and determines the amount of stratification.

Overall, the estuary remains partially mixed and does not make a transition into a different regime for these changes in background value. A change in vertical diffusivity can change the stratification, but this is also mostly correlated to the salt intrusion length itself. The fact that the regime of the estuary does not change ensures that the results remain consistent and robust; the model parameters, derived from literature, will not alter the qualitative outcomes. Larger background values will result in different transport and estuary regimes altogether and examining this influence falls outside the scope of this research.

Chapter 5

Model Results: The Influence of Dune Geometry and Human Interventions on Salt Intrusion

In this chapter, we show the influence of dune geometry and dune-related human interventions on salt intrusion. An overview of all dune changes is provided in Figure 5.1, but for detailed explanations, we refer to each respective section.

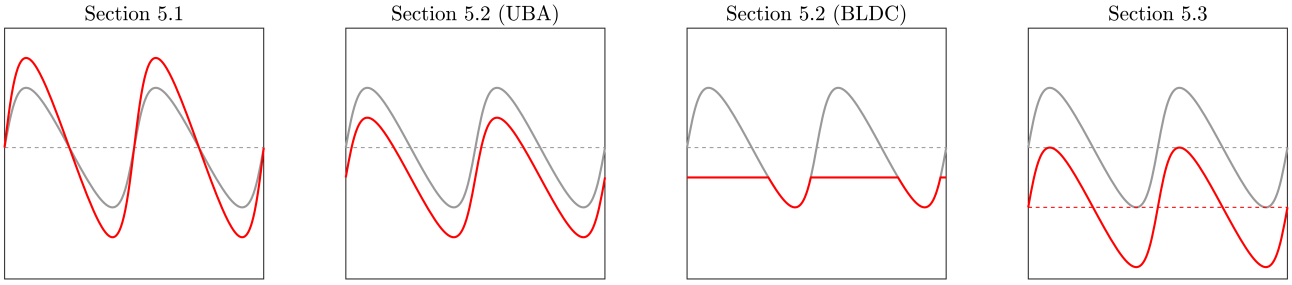

Figure 5.1: Overview of all dune geometry changes and human interventions of Chapter 5. Left (Section 5.1) shows a visualisation of a change in dune height H_d. Middle two figures (Subsection 5.2.1) show visualisations of two dredging techniques of Uniform Bed Alteration (UBA) and Bed-Leveling Depth Control (BLDC). Right (Section 5.3) shows a visualisation of dredging dunes while keeping the maximum bed level equal at $z = -h$. More detailed information on abbreviations is provided in the respective sections.

In Section 5.1, we will use the dune shape parameter space $(\lambda_d, A_d, \mathcal{A}_d)$ to change the shape of bedforms and determine the influence of the dune geometry on salt intrusion. We assume that dunes have formed naturally from a flat bed over the interior of the estuary by a spatial redistribution of sediment, meaning the average estuary depth is kept at $h = 15$ meters. Under this assumption, the navigation depth decreases as sand dunes increase in height. The left panel Figure 5.1 displays a visualisation of changing dune height H_d. In this section, visualisation of changing length λ_d and asymmetry $\mathcal{A}_d$ are given in the respective subsections.

Next, in Section 5.2, we implement interventions on the existing dune field as analysed in Section 5.1, analysing the difference between two dredging and dumping methods when applied to a local intervention interval. The middle panels of Figure 5.1 display these two methods in case of dredging. In Section 5.3, we show the effect of dunes while keeping the same navigable depth, that is, the situa-

tion that could be envisioned when implementing or dredging sand dunes while keeping the navigation depth constant. We show how these artificially created sand dunes in a flat bed may mitigate salt intrusion. The right panel Figure 5.1 visualises this method. Finally, in Section 5.4 we describe the general influence of changing geometry (dune dimensions and channel depth) on the amount of vertical mixing and describe how the amount of vertical mixing is related to the salt intrusion length.

5.1 Influence of Dune Geometry with a Dune Field

In this first section, we specify a dune field over the interior of the dune field, using the envelope function of Equation 3.18 with $L_0 = 5$ km, such that sand dunes are mainly located in $x = [5, 45]$ km. Note that for all these model runs, the total volume of sediment in the system is the same, and the mean bed level remains at $z = -h$. Hence, changes from one dune geometry to the next can be interpreted as a different placement of sediment. This implies that changes in dune height can also be interpreted as changes to an existing dune field employing a swiping dredging strategy, where sediment of the crests is moved into the troughs (Campmans et al., 2021).

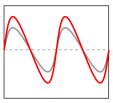

5.1.1 Dune Height

The influence of dune height is investigated for a constant dune length of $\lambda_d = 100$ m, which is representative of the RWW, can be captured well by the discretisation, and is likely to produce significant results as indicated in Chapter 4. All model runs commence from the same initial condition[18], after which we vary the dune height. The model is run until a state of dynamic equilibrium of tide-averaged salt intrusion length $\langle L_s \rangle$ is reached. An explanation of the determination of this state is given in Appendix A.3.

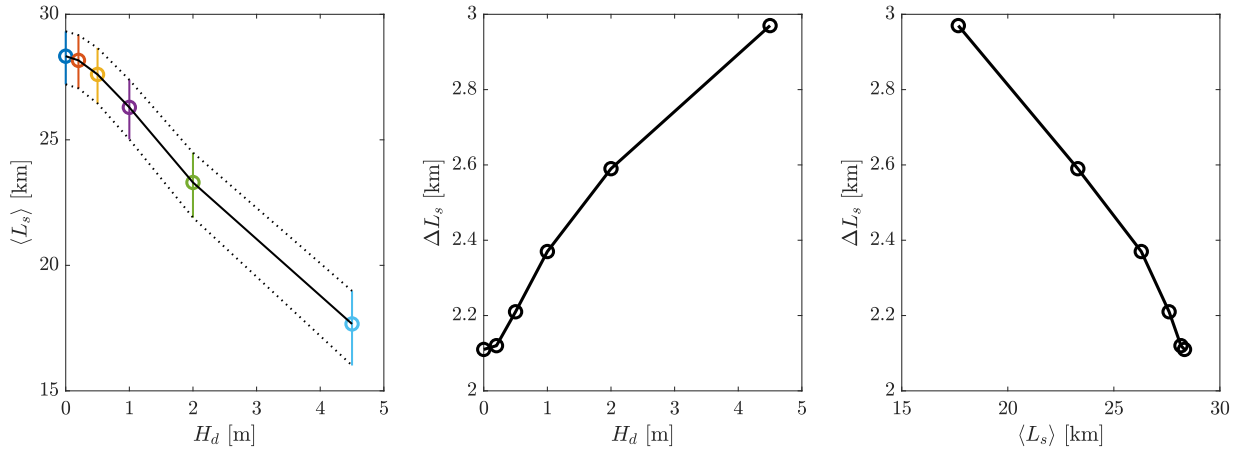

Figure 5.2: Influence of dune height H_d on salt intrusion for $\lambda_d = 100$ m. Left: Mean salt intrusion length as a function of dune height, coloured vertical lines indicating spread over the last tidal cycle. Middle: Tidal excursion length of L_s as a function of dune height. Right: Inverse correlation of tidal excursion to salt intrusion length.

The results can be seen in Figure 5.2, which shows a large influence of dune height on the salt intrusion length with changes in the order of several kilometres. The mean salt intrusion length exceeds 28.3 km for a flat bed and decreases to $\langle L_s \rangle = 23.2$ km for dunes with height $H_d = 2.0$ m. The excursion over the tidal cycle ΔL_s increases with increasing dune height. This relationship is

[18] The initial condition is derived from a different model run with dune height $H_d = 1.0$ m that nearly reached dynamic equilibrium for L_s. This approach ensures model run times remain manageable when both decreasing and increasing H_d.

inversely proportional to $\langle L_s \rangle$ itself, similar to the results shown for varying background parameters in Figure 4.16. This suggests this is a result of the overall salt balance, salt intrusion length and estuary dimensions, rather than local flow characteristics introduced by eddy effects or dunes.

The horizontal transport components remain the same for changing topography, similar to the results of Figure 4.13. The relative location change of horizontal fluxes is merely a consequence of the movement of the salt distribution. However, the transport patterns are similar within the region of stratification, the governing processes remain equal and the estuary does not enter a different regime. The vertical flux controls the salt intrusion length and an increase in dune height increases the advective vertical mixing, while dispersive vertical transport remains relatively equal as shown in Figure 5.3. Moreover, the peak of the advective transport is reached just landward of the subtidal salt intrusion length. The magnitude of this peak increases only slightly with increased dune height. In dynamic equilibrium, the largest vertical flux occurs just landward of $\langle L_s \rangle$ and decreases in magnitude, but the magnitude of vertical advective transport increases throughout the estuary with an increase in H_d.

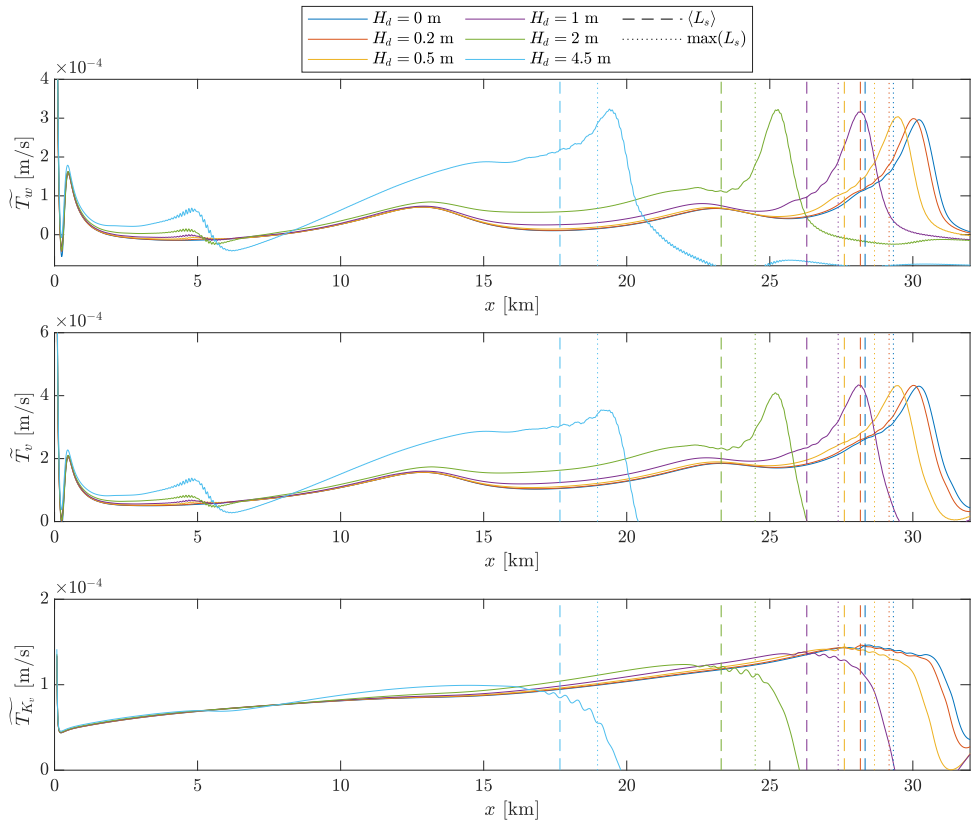

Figure 5.3: Changes in normalised dune-averaged vertical flux componentsfor various dune heights H_d, dashed lines indicating salt intrusion length $\langle L_s \rangle$ in all figures. Top: vertical advective flux $\widetilde{T_w}$. Middle: vertical dispersive flux $\widetilde{T_{K_v}}$. Bottom: total vertical flux $\widetilde{T_v}$

The largest difference is observed in the absolute vertical stirring parameter $\mathcal{S}$, and especially the magnitude of the peak attained near $x = 6$ km, referred to as max($\mathcal{S}$), which turns out to be proportional to H_d. This increase in vertical exchange likely reduces the salt intrusion length. In summary, sand dunes do not induce a transport and estuary regime change. Qualitatively, the net vertical flux stays relatively similar in the stratified region. but increases with an increase in dune height. The shift in salt intrusion length results from the comprehensive mixing occurring throughout the water column.

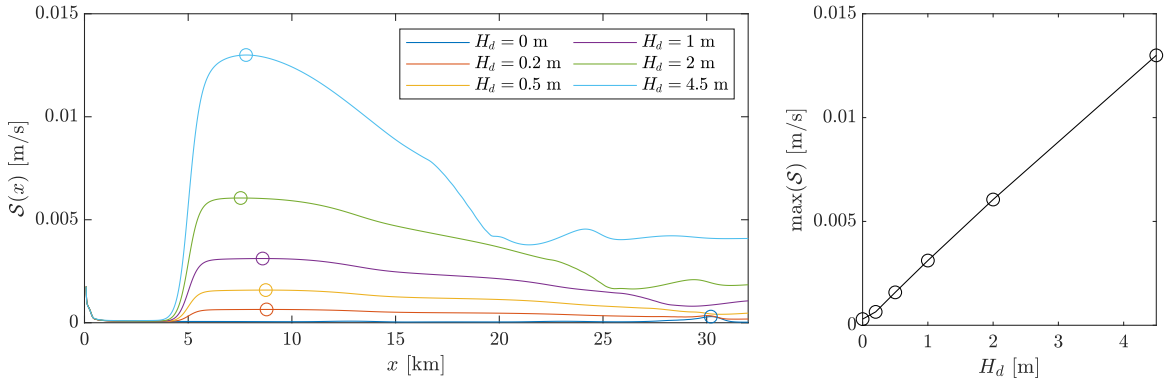

Figure 5.4: Left: Changes in stirring parameter $\mathcal{S}$ over the estuary for different dune heights with attained maximum max($\mathcal{S}$) indicated by the circle. Right: Relation of max($\mathcal{S}$) to dune height H_d.

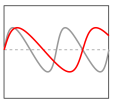

5.1.2 Dune Length

The influence of dune length is investigated by varying λ_d from 50 to 250 m, for a fixed dune height of $H_d = 1.0$ m. Again all model runs start from the same initial condition, and the simulation continues until a dynamic equilibrium is reached. Shorter dunes of less than $\lambda_d < 50$ m have not been modelled to eliminate inaccurate parameterisations with $\Delta x = 10$ m. Again, the model is run for 120 hours (5 days), resulting in temporal convergence of the subtidal salt intrusion length, and model output is generated for the last 48 hours. The results can be seen in Figure 5.5. The flux components show no visual difference and are not shown.

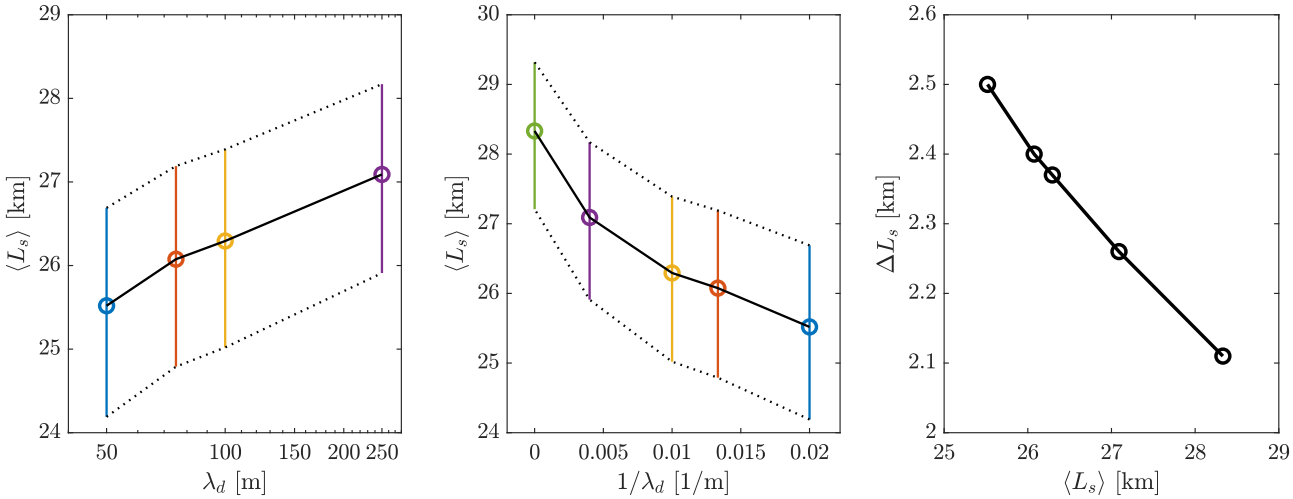

Figure 5.5: Influence of dune length λ_d on salt intrusion length for $H_d = 1.0$ m. Left: Salt intrusion length $\langle L_s \rangle$ as a function of dune length λ_d, coloured vertical lines indicating spread over the last tidal cycle. Middle: Salt intrusion length $\langle L_s \rangle$ as a function of dune wave number $1/\lambda_d$, including B-0 in green. Right: Inverse correlation of tidal excursion to salt intrusion length.

The influence of dune length is significant, albeit smaller than the influence of dune height as in the previous subsection. Shorter dunes decrease the salt intrusion length, likely due to an increase in vertical mixing by steeper dune slopes. As dunes increase in length ($\lambda_d \to \infty$), dune slopes become small and the overall bed is approximately flat. This is shown in the middle panel of Figure 5.5, which includes the model run with a flat bed, approximated by $1/\lambda_d = 0$ m^{-1}. This plot shows an inverse-root relationship of $\langle L_s \rangle \propto 1/\sqrt{\lambda_d}$ for the investigated range of $\lambda_d \geq 50$ m.

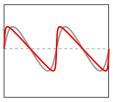

5.1.3 Dune Asymmetry

The influence of dune asymmetry is investigated for a fixed dune length of $\lambda_d = 100$ m with two different dune heights of $H_d = 1.0$ m and $H_d = 4.5$ m respectively. All model runs for both cases start from the same initial condition from a model run with $\mathcal{A}_d = 0$, after which the dune asymmetry is increased in both positive and negative $\mathcal{A}_d$, resulting in 9 model runs[19] for each dune height. Models are run with sand dunes that exceed the critical slope angle of $\phi_{d,\max} > \phi_c = 14°$ where flow separation is likely to occur, and where non-hydrostatic phenomena that cannot be resolved become important. These are two and six model runs for $H_d = 1.0$ m and $H_d = 4.5$ m respectively. The model runs with larger dune angles are still analysed to evaluate the hydrostatic effects, but note that many physical processes are not captured.

The results are shown in Figure 5.6, where the left shows the maximum dune angle that is achieved. For both $H_d = 1.0$ m and $H_d = 4.5$ m, the influence of dune asymmetry is relatively small. The horizontal and vertical salt transport components also show no meaningful difference. Interestingly, model outputs are almost equal between a given $\mathcal{A}_d$ and $-\mathcal{A}_d$, with the negative value (flood-oriented sand dunes) consistently showing slightly less salt intrusion when $H_d = 1.0$ m. However, this difference is in the order of single grid cells (10 m) and is not significant. We expected that an increase in dune asymmetry (increasing $|\mathcal{A}_d|$) would result in more vertical mixing and less salt intrusion. However, under the hydrostatic assumption, we conclude that the influence of dune asymmetry is negligible for salt intrusion. Results are likely different when non-hydrostatic effects are implemented.

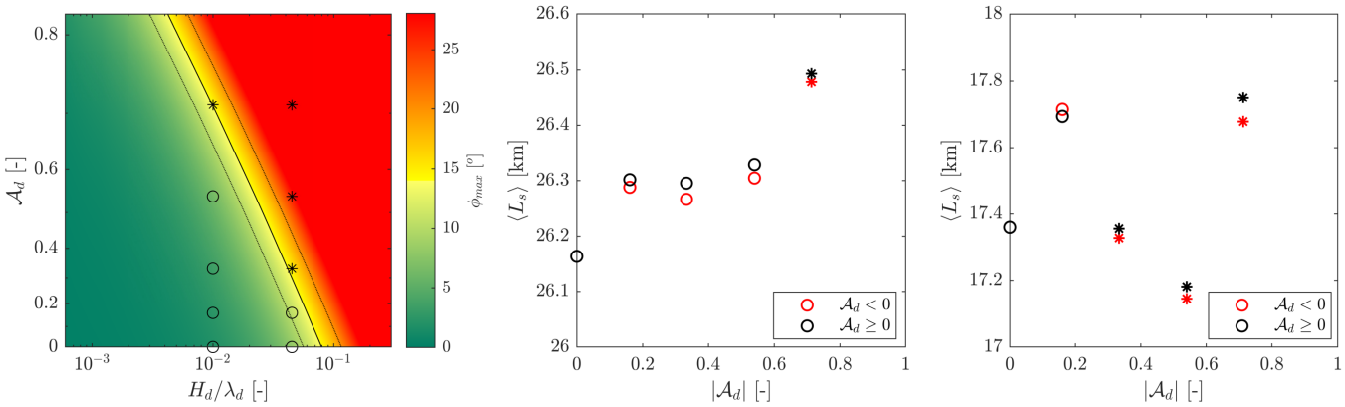

Figure 5.6: Lee side dune angle as a function of dune aspect ratio and dune asymmetry, with indicated runs for $H_d/\lambda_d = 1/100$ and $H_d/\lambda_d = 4.5/100$ (left). Influence of dune asymmetry $\mathcal{A}_d$ on salt intrusion lengths with $\lambda_d = 100$ m for $H_d = 1.0$ m (middle) and $H_d = 4.5$ m (right)

[19] More specifically, we use values for $\mathcal{A}_d \in (-1, 1)$ such that the term $\sin(\frac{\pi}{2}\mathcal{A}_d) = \pm 0.25,\ \pm 0.5,\ \pm 0.75,\ \pm 0.9$. This term appears in the dune shape formulation Λ_d as given in Equation 3.22.

5.2 Dredging and Dumping on Existing Dune Fields

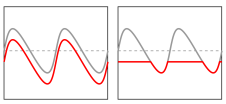

In this section, we investigate the influence of bed manipulations on an existing dune field of model B-1 using a new bed-level formulation z_b. We explore two distinct strategies and hypothesize a better performance for one over another. Due to computational constraints, we do not cover the complete parameter space for each strategy. Instead, we perform explorative research to shed light on which interventions perform better than others and identify potential regions where an optimal strategy is located.

5.2.1 Types of Interventions

We introduce two types of human interventions, which we refer to as **Uniform Bed Alteration** (UBA) and **Bed-Leveling Depth Control** (BLDC). Both interventions are placed in an interval $x \in [x_{int} - L_{int}, x_{int}]$ for most landward location x_{int} and intervention length L_{int}, using a similar envelope function b_{int} defined as

$$b_{int}(x) = \frac{1}{1+\exp\left(-\frac{4(L_{int}+(x-x_{int}))}{\Delta_{int}}\right)} + \frac{1}{1+\exp\left(\frac{4(x-x_{int})}{\Delta_{int}}\right)} - 1. \tag{5.1}$$

for envelope smoothing parameter $\Delta_{int} = 200$ m. Uniform Bed Alteration (UBA) can be performed by changing the bed level *uniformly* over x using

$$z_b(x) = -h + h_d(x) + h_{int} b_{int}(x). \tag{5.2}$$

which adds or subtracts sand uniformly over the *intervention interval*, except for the tapering at the ends of the envelop function b_{int}. See Figure 5.7 for an example. In practice, this means dredging and dumping of sediment over any (unknown initial) topography. Bed-Leveling Depth Control (BLDC) means dredging or dumping a section to ensure a minimum or maximum depth over the region of intervention $b_{\text{int}}(x)$ is attained, and the existing vertical variation by sand dune topography is always reduced (hence bed-levelling). This can be done using dredging, resulting in

$$z_b(x) = \min(-h + h_d(x), (-h + h_{\text{dredge}}) b_{int}(x)) \tag{5.3a}$$

for a pre-determined dredging height h_{dredge} relative to reference level $z = -h$. Note that this method is equivalent to the *topping strategy* as described by Campmans et al. (2021). Dumping using this method is specified by

$$z_b(x) = \max(-h + h_d(x), (-h + h_{\text{dump}})(2 - b_{int}(x))) \tag{5.3b}$$

for a pre-determined dumping height h_{dump} relative to reference level $z = -h$. Examples of both dredging and dumping with BLDC are shown in Figure 5.8. In practice, this means dredging to guarantee a minimal depth, or a dumping strategy which first fills the troughs of an existing dune pattern.

We analyse the influence of both UBA and BLDC on the salt intrusion length. In this analysis, we refer to the navigation depth as the minimum depth introduced by the interventions w.r.t. the reference level of the free surface $z = 0$. Without measures, this means the navigation depth is equal to $h - H_d/2$. With UBA, the overall dune topography is conserved, and hence, the changed vertical velocities are mainly a result of changing water depth and not the shape itself. In this method, the navigation depth is always changed, together with the average water depth. This is in contrast to BLDC, where the shape and vertical variation of the bed are always reduced. Similar to UBA, when dredging is done using BLDC, the navigation depth directly increases. However, dumping of sediment does not directly change the navigation depth as long as $h_{\text{dump}} < H_d/2$.

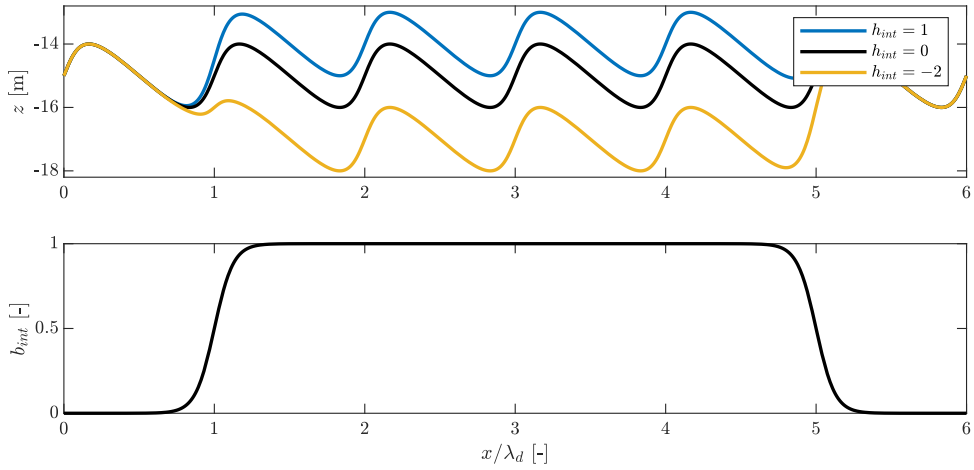

Figure 5.7: Example of **Uniform Bed Alteration** for various h_{int} (top) for an example of interval envelope function b_{int} (bottom).

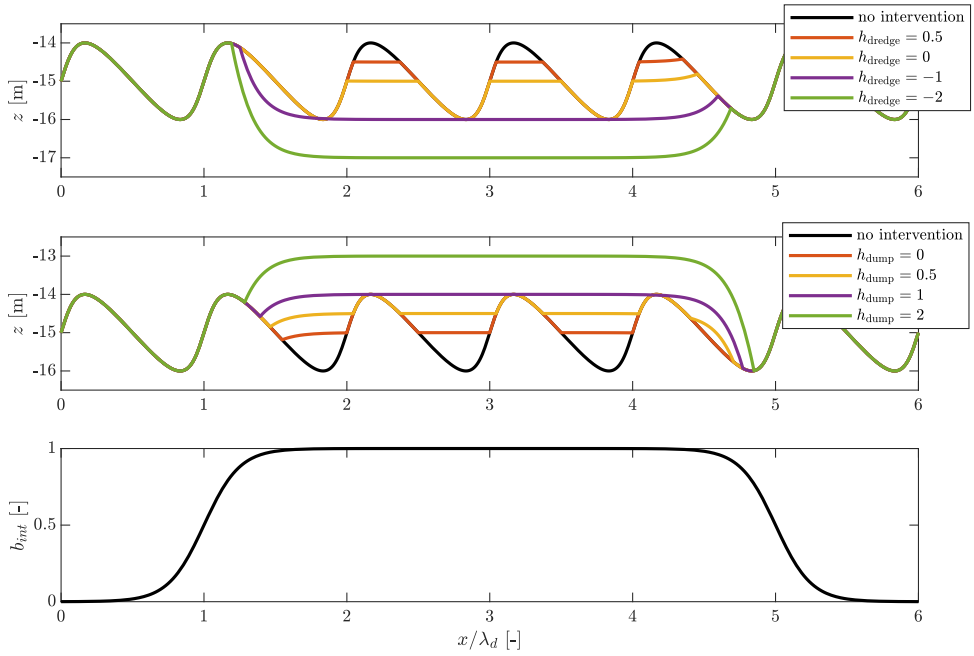

Figure 5.8: Example of **Bed-Leveling Depth Control** with both dredging (top) and dumping (middle) or various depths and an example of interval envelope function b_{int} (bottom).

A decrease in average water depth decreases the salt intrusion length by enhanced vertical mixing and increases background river flow (Hendrickx et al., 2023b; Siemes et al., 2023). Hence, both methods likely aid in reducing the salt intrusion length when sediment is dumped in an intervention interval as the water depth is decreased locally. However, this is likely done more efficiently in the shape-preserving UBA method, as vertical advective mixing by the existing topography is retained. Furthermore, when sediment is dumped in these methods, the navigability of the channel decreases, similar to an increase in dune height, which can have a large impact on shipping (Hendrickx et al., 2023a).

5.2.2 Influence of Uniform Bed Alteration (UBA)

We investigate the influence of UBA for various intervention locations and intensities (length and height) when interventions are placed on the existing sand dune field of model B-1 ($\lambda_d = 100$ m, $H_d = 2.0$ m, $\mathcal{A}_d = 0$). The efficiency of the intervention is examined by evaluating the salt intrusion length $\langle L_s \rangle$ and comparing it to the results of the B-1 model without interventions.

Location and Horizontal Extent of Dumping

Firstly, we investigate the influence of dumping only, more specifically, we investigate the dumping location x_{int} by implementing interventions of fixed height $h_{int} = 1.0$ m with different lengths and at various locations. The results are shown in Figure 5.9, which directly indicates that dumping of sediment always decreases the salt intrusion length, regardless of location. However, it indicates that both the location and length of the intervention can change the effectiveness of a measure. An increase in intervention length generally decreases the salt intrusion length (Figure 5.9, right panel), however, a significantly shorter intervention length of $L_{int} = 1$ km can be more effective when placed at the right location. Moreover, for an intervention length of $L_{int} = 5$ km, there seems to be an optimal location at around $x = 20$ km.

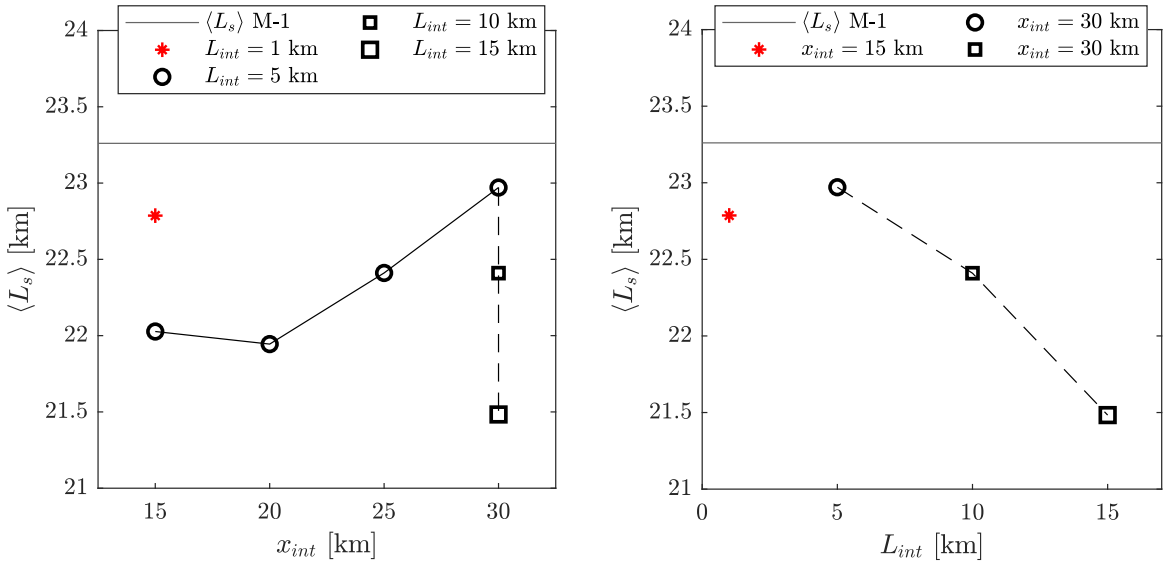

Figure 5.9: Influence of location and length of intervention for $h_{int} = 1$ m, grey line indicating the value of $\langle L_s \rangle$ for the reference model B-1 without interventions.

Intervention Height

The influence of intervention height is investigated by varying h_{int} for two different intervention lengths. Results are shown in Figure 5.10. For a given intervention length, a linear relationship of h_{int} to the salt intrusion length is found. Remarkable is the fact that for some dredging activities over a small domain of $L_{int} = 1$ km, the salt intrusion length also decreases, this is likely a result of the rapid change from one average depth to the next (due to an increase in b_{int}). This strengthens the idea that periodic interventions over the estuary can be used to create multiple changes in water depth and, as such, create additional vertical mixing, this idea is explored in Section 5.3.

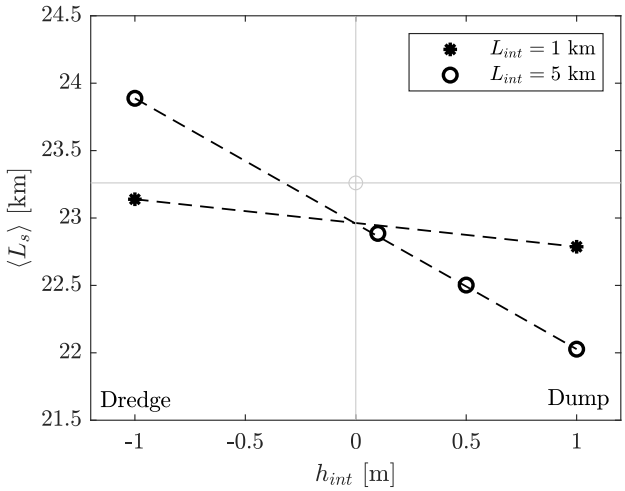

Figure 5.10: Influence of changing intervention height with $x_{int} = 15$ km for $L_{int} = 1$ and $L_{int} = 5$ km respectively. Grey lines indicating the value of $\langle L_s \rangle$ for the reference model B-1 without interventions ($h_{int} = 0$).

Intervention Volume

The previous analysis indicates that a combination of both the length and height of the intervention can be used to describe the salt intrusion length. We do so using the intervention volume, equal to $V_{int} = h_{int}L_{int}$ in the case of the UBA method. The relation of V_{int} to $\langle L_s \rangle$ is investigated for multiple configurations, where a maximum intervention height of $h_{int} = 2$ m is used. Intrusion reduction is largest near the seaward side and interventions are mainly located here. Figure 5.11 shows that the volume of intervention is the main predictor of change in salt intrusion length, with a linear relationship. The right of Figure 5.11 again shows the influence of location for an intervention of $h_{int} = 1$ m, $L_{int} = 5$ km. The measure is most effective when centred around $x = 17$ km. However, the overall magnitude of change is relatively small. The subtidal salt intrusion length decreases by around 1 km. Significantly larger sand volumes are necessary for a significant reduction.

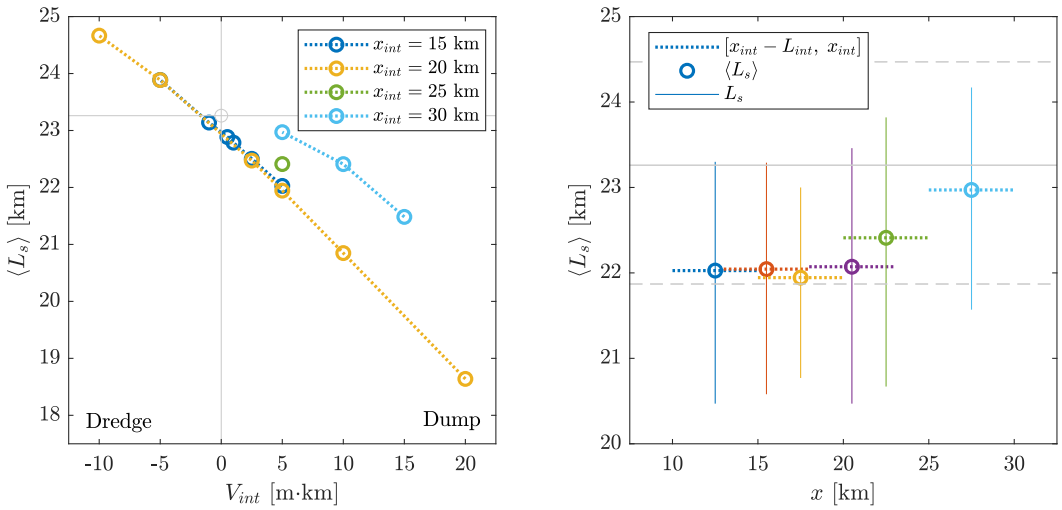

Figure 5.11: Grey lines indicating reference B-1 value. Left: Influence of changing intervention volume at various locations. Right: Influence of location of intervention for constant $h_{int} = 1$ m, $L_{int} = 5$ km. Dotted lines indicate the region of intervention, the marker indicates subtidal salt intrusion length $\langle L_s \rangle$ and the solid line is the excursion over the tide (with magnitude ΔL_s).

Influence of Interventions on Transport Components

The horizontal and vertical transport components of Q_h and T_v for several cases are shown in Figure 5.12 and Figure 5.13 respectively, ordered from largest to smallest (most negative) volume V_{int}. The grey area in the figures shows the location and length of intervention, with the height of the intervention h_{int} given in the title. Different cases with various lengths and heights (but not all model runs) are shown to shed light on how local interventions change salt transport.

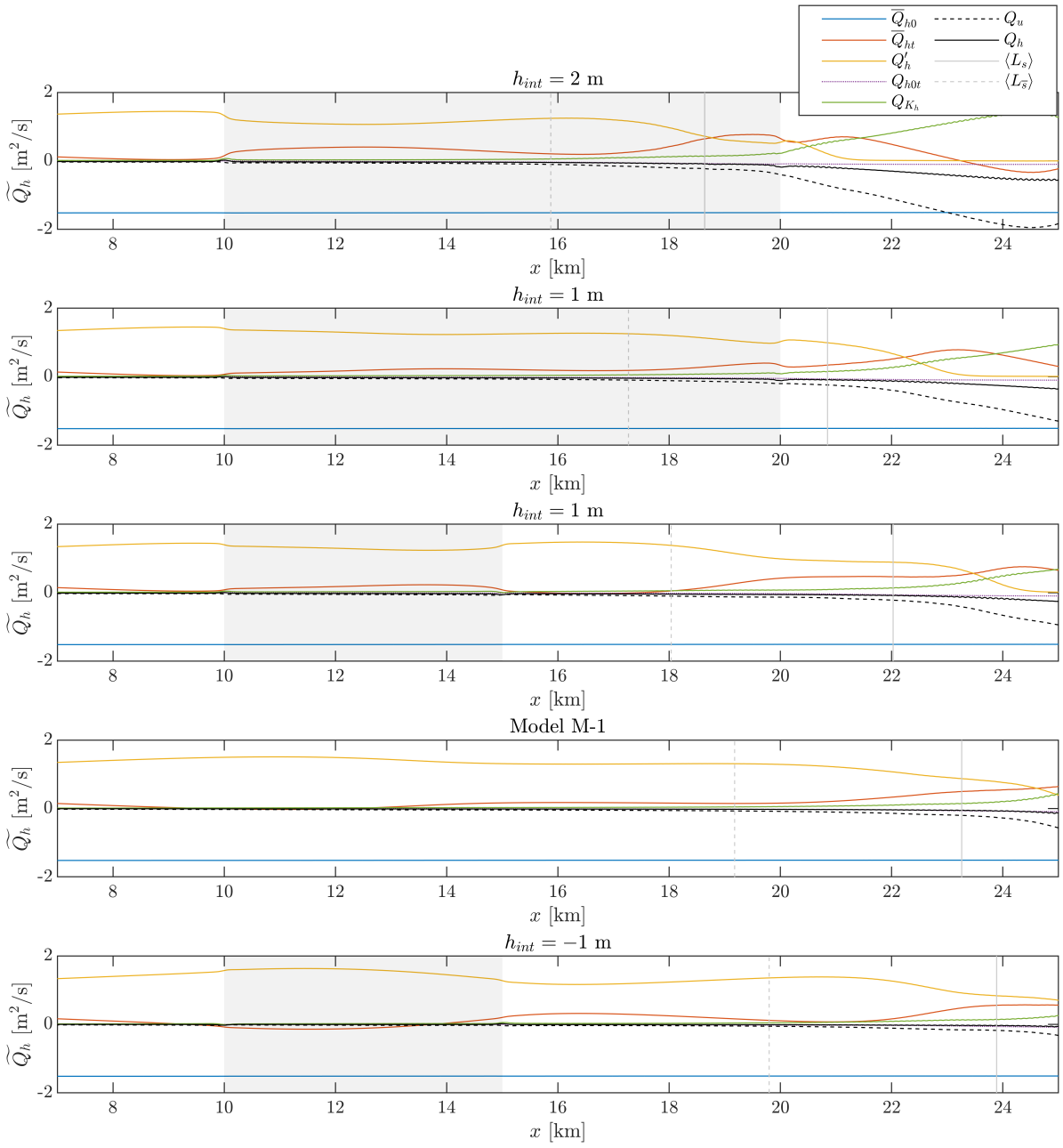

Figure 5.12: Horizontal fluxes for various bed manipulations, grey area indicating the interval of intervention.

The horizontal component shows total transport over a water column and, hence, is independent of the changing water depth, most noticeable for the subtidal depth-averaged transport $\overline{Q}_{h0}$. Freshwater flushing remains equal between simulations, even though the water depth changes. Positive intervention

heights (dumping of sediment) reduce the landward-directed shear transport Q'_h by reducing vertical variations in the flow; the estuarine circulation. This magnitude of this component is correlated to subtidal depth-averaged longitudinal salinity gradient $\partial\langle\overline{s}\rangle/\partial x$. Simultaneously, the tidally-correlated depth-averaged transport component $\overline{Q}_{ht}$ is increased over the intervention, likely a result of accelerated tidal flow over the increased bed level height.

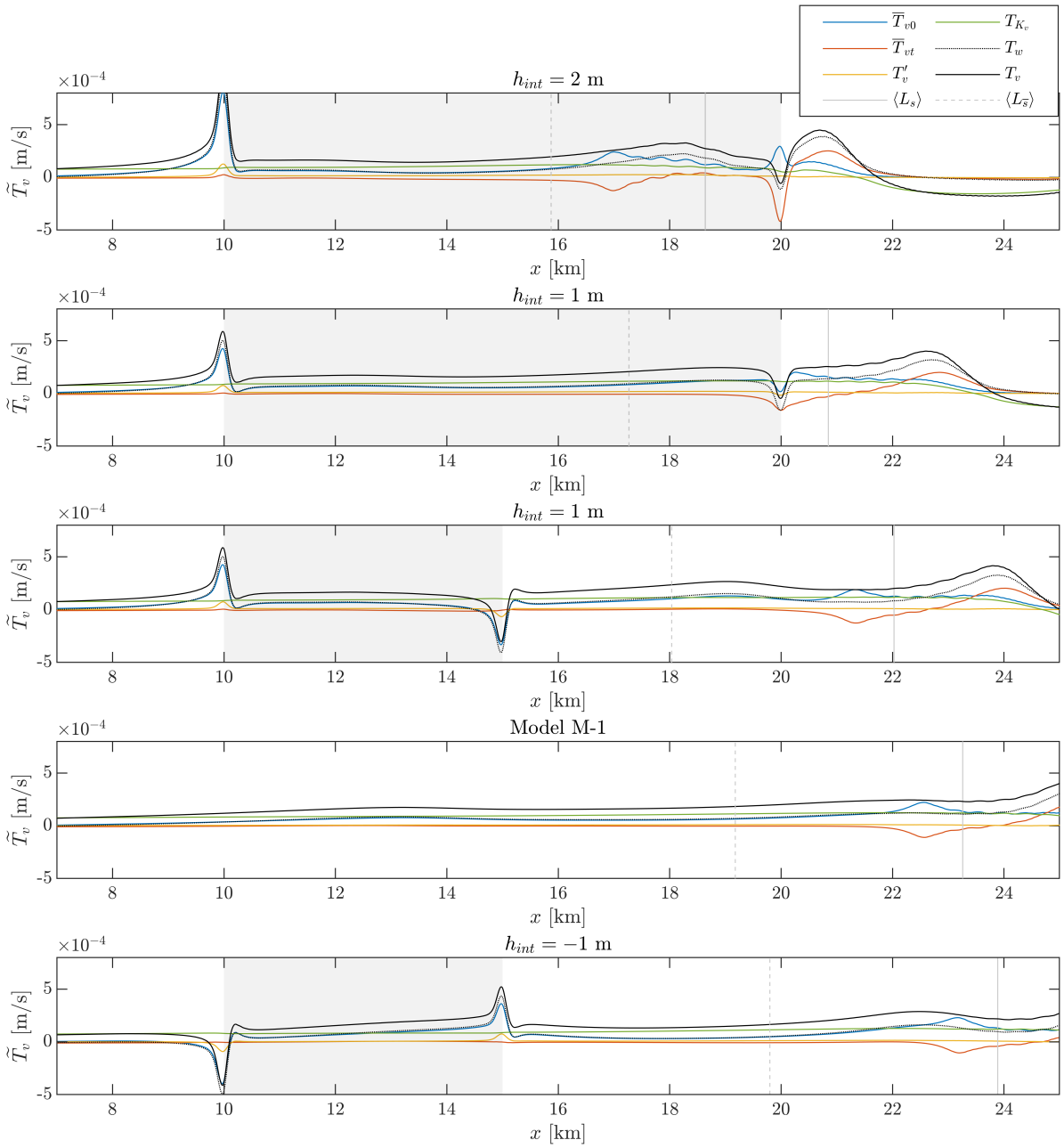

Figure 5.13: Horizontal fluxes for various bed manipulations, grey area indicating the interval of intervention.

In the vertical component, we mainly see changes at the boundaries of the intervention intervals where changes in mean water depth occur, indicating that maybe the transition introduced by the intervention causes additional net vertical mixing and a shift in salt intrusion length, rather than the vertical transport in the region of the intervention itself.

The right panel of Figure 5.11 shows how a given intervention can best be placed centred around $x = 17$ km. Differences are very minor, but analysis of the transport components of this intervention indicates that this likely results from a relatively larger decrease of Q'_h than the increase of $\overline{Q}_{ht}$. Moreover, the peak in upward transport at the start of the intervention ($x_{int} - L_{int}$) is in line with a decrease in landward-directed transport $\overline{Q}_{ht}$, meaning that salt transport upwards by a change in water depth is less transport inland by the estuarine circulation.

5.2.3 Influence of Bed-Leveling Depth Control (BLDC)

Next, we investigate the influence of BLDC by dredging and dumping sediment at $x = 10$ km to 15 km in the estuary in model B-1. This is performed for various dredging heights (h_{dredge} of 0.5, 0, -1 and -2 m) and dumping heights (h_{dump} of 0, 0.5, 1 and 2 m) as illustrated in Figure 5.8.

The results are shown in Figure 5.14, where for the right panel the intervention volume V_{int} is determined by the difference in bed level in the discredited models to B-1. The left panel shows that dredging always increases the salt intrusion length. This effect becomes larger as the sand dunes are completely dredged away in the B-1 model ($h_{\text{dredge}} < -1$ m), and the average water depth increases while the vertical mixing previously induced by dunes is removed. A similar argument holds for dumping; dumping of sediment where the height of the dune crests is not increased (i.e. $h_{\text{dump}} < 1$ m) increases salt intrusion even further as vertical mixing is reduced. This again highlights the importance of estuarine sand dunes. Furthermore, similar to the transport component analysis of the UBA, this indicates that interventions mainly affect the salt intrusion length by mean depth changes, rather than local topography changes.

Overall, using dumping with BLDC is less effective in mitigating salt intrusion than dumping in UBA for the same volume of sediment at the same location. Moreover, when this dredging strategy is applied, the effects on salt intrusion are even more detrimental than the bed manipulation technique as shown in the right panel of Figure 5.14 which overlays the BLDC method on the UBA method of Figure 5.11 (now in grey).

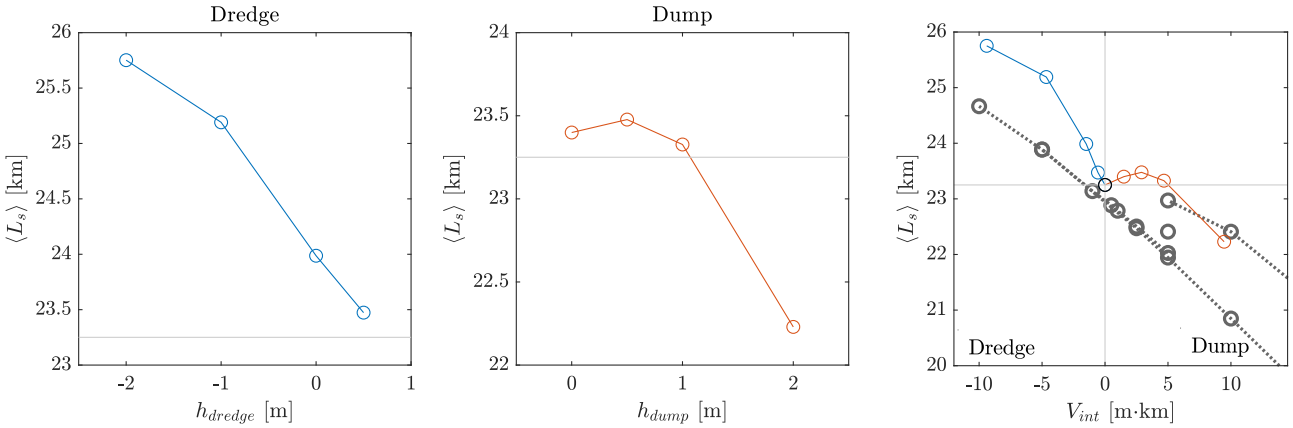

Figure 5.14: Bed-Levelling Depth Control between 10 and 15 km with eight different intervention heights, the horizontal grey lines indicate the reference salt intrusion length from the B-1 model. Left: Influence of dredging height. Middle: Influence of dumping height. Right: Total volume used for interventions V_{int} and compared to the bed manipulation results of Figure 5.9 in grey.

5.3 Creating Sand Dunes in a Flat Bed

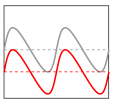

Previous sections indicate that dunes are important for generating vertical velocities that induce vertical mixing, potentially counteracting the effect of average water depth. Therefore, we investigate whether the salt intrusion length can be reduced by dredging artificial dunes in the flat bed of model B-0. Hence, we repeat the study of dune height on salt intrusion, using the bed level function

$$z_b(x) = -h + \frac{H_d}{2} b(x)(\Lambda_d(x) - 1) \tag{5.4}$$

such that crests of the dunes and hence, the navigation depth are maintained at $z = -h$; the troughs are located at at $z = -h - H_d$, see Figure 5.15 for a visualisation. We now refer to the variable H_d as the dredged dune depth, rather than height. Note that this method removes sediment from the system, similar to the analysis of Section 5.2. For the envelope function b, both the global estuary dune function b_d (Equation 3.18) and the local intervention function b_{int} (Equation 5.1) can be used.

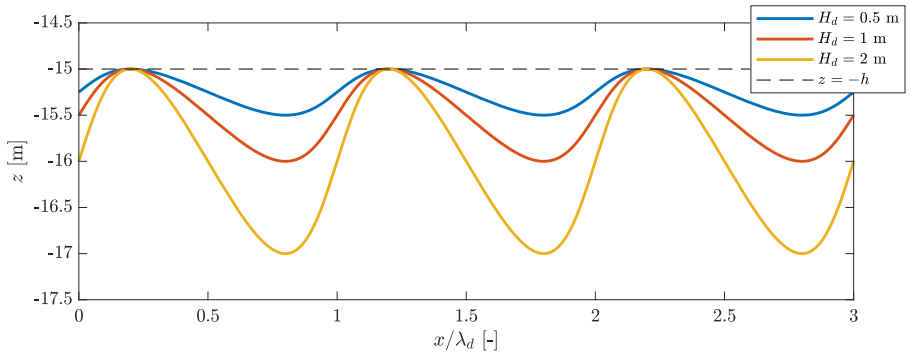

Figure 5.15: Example of dunes below the reference level for various dune heights H_d.

5.3.1 Influence of Dredged Dune Depth

We investigate the influence of the dredged dune depth H_d on the salt intrusion length, as we assume that the influence of dune length λ_d and asymmetry $\mathcal{A}_d$ on the salt intrusion length is relatively similar to the results of Section 5.1 and that dune height is the predominant predictor. Therefore, we only vary the dredged dune depth H_d, and use constant $\lambda_d = 100$ m and $\mathcal{A}_d = 0$. Dunes are generated over the full estuary with $b = b_d$ using Equation 5.4. Where $b > 0$, the average water depth increases, and subsequently, the depth-average seaward-directed river flushing will decrease. To determine the influence of this channel-deepening that is embedded in Equation 5.4, we also run simulations with channel deepening only, i.e. with

$$z_b(x) = -h - \frac{H_d}{2} b(x) \tag{5.5}$$

for the same values of H_d to determine the influence of increased water depth.

The results are shown in Figure 5.16 and compared to the salt intrusion length of model B-0 (a flat bed) and a close-up of the middle and right panel is provided in Figure 5.17. The left panel of Figure 5.16 shows that for small dredged dune height $H_d < 1.2$ m, the salt intrusion is increased. The middle panel indicates that results from the increased water depth, which decreases riverine flushing while relatively little vertical mixing is generated by the dunes. For small $H_d = 0.2$ m, the salt intrusion length follows the trend of channel deepening only. Moreover, analysis of the transport components Q_h and T_v shows a significant increase in estuarine circulation Q'_h, whereas the vertical transport remains relatively similar (this figure is not shown). Increasing dredged dune depth further,

sufficient vertical transport is generated by the dredged dunes and the change of salt intrusion length follows the decreasing trend shown earlier in Figure 5.2. The estuarine circulation Q'_h and tidally-correlated depth-averaged transport $\overline{Q}_{ht}$ are both decreased, resulting in a decrease of the salt intrusion length. The transition where $\langle L_s \rangle$ is less than the baseline value of model B-0 occurs at approximately $H_d = 1.2$ m.

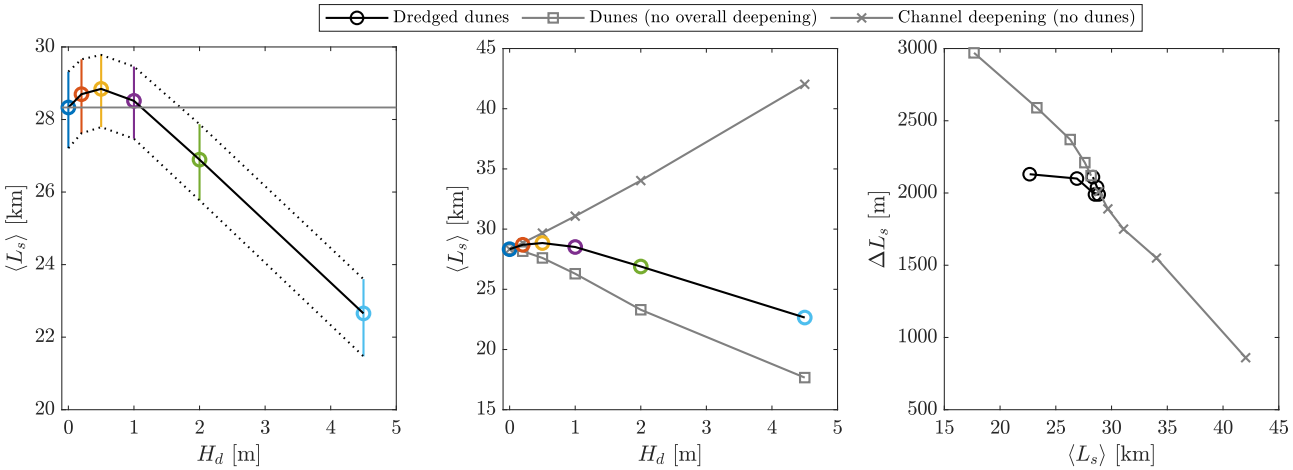

Figure 5.16: Influence of dredging depth of artificial dunes with $\lambda_d = 100$ m and $\mathcal{A}_d = 0$ on the salt intrusion length $\langle L_s \rangle$ (left), comparison with the data from the dune field of Figure 5.2 and channel deepening only (middle) and relation of $\langle L_s \rangle$ to ΔL_s for all model runs (right).

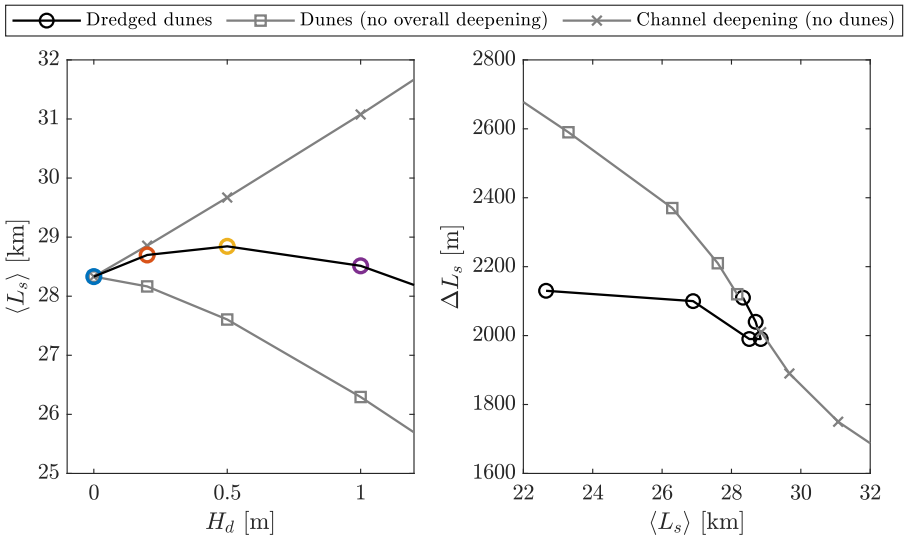

Figure 5.17: (Zoom of Figure 5.16) Influence of dredging depth of artificial dunes with $\lambda_d = 100$ m and $\mathcal{A}_d = 0$ on the salt intrusion length $\langle L_s \rangle$ with comparison with the data from the dune field of Figure 5.2 and channel deepening only (left) and relation of $\langle L_s \rangle$ to ΔL_s for all model runs (right).

The right panels of Figure 5.16 and Figure 5.17 show that for dunes and channel deepening without dunes, the tidal excursion length ΔL_s is inversely proportional to the salt intrusion length $\langle L_s \rangle$. This likely results from a linearly decreasing tidal flow velocity relative to the distance of the seaward end $x = 0$ km. However, the dynamics are slightly difference for the dredged dunes simulations, where the tidal excursion does not change significantly between model runs.

5.3.2 Influence of Dredging Location

We have shown that dredging dunes in a flat bed of bathymetry B-0 can decrease the salt intrusion length when performed over the full estuary. In this final subsection, we dredge dune shapes in a specific location using $b = b_{int}$, to determine whether this mitigation strategy is also effective in a smaller interval. We do so similar to the analysis of UBA. Symmetric ($\mathcal{A}_d = 0$) sand dunes are dredged with depth $H_d = 2.0$ m and length $\lambda_d = 100$ m over a horizontal extent $L_{int} = 5$ km at various locations, which is expected to reduce the salt intrusion length.

The results are shown in Figure 5.18, relative to the result of model B-0. The overall effect is relatively small but significant with a reduction of the salt intrusion length of around 1 km. The excursion over the tidal cycle ΔL_s remains equal, and the dredging activities are best located around $x = 5$ to 10 km.

Overall, this indicates that dredging dunes in a flat bathymetry, while keeping navigability equal, can decrease the salt intrusion length significantly. Digging larger sand dunes with a larger aspect ratio H_d/λ_d is likely more efficient in achieving a reduction of the salt intrusion length. Furthermore, results are more significant when the measure is performed in a larger region of the estuary, and the influence of relatively small dunes ($H_d = 2$ m) over a small region ($L_{int} = 5$ km) is relatively minor.

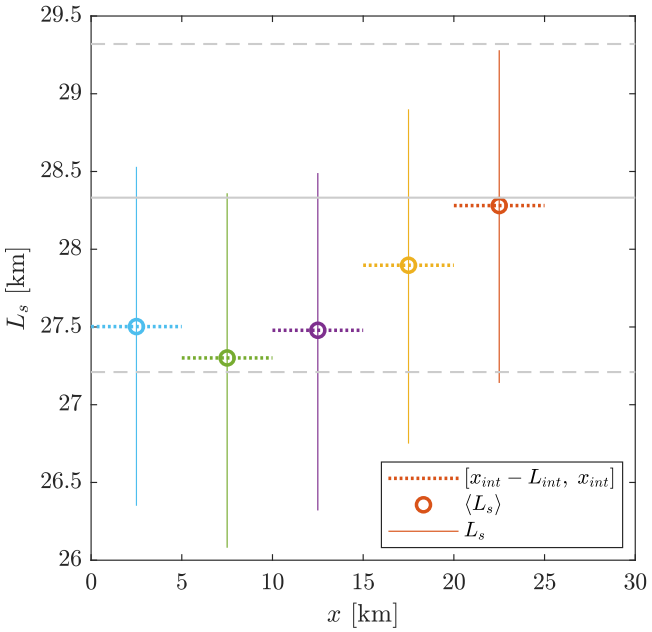

Figure 5.18: Influence of location of digging $H_d = 2$ m on the salt intrusion length $\langle L_s \rangle$. Grey lines indicate the reference value of B-0, with minimum and maximum over the tide by dashed grey lines.

5.4 Influence of Geometry on Vertical Transport and Relation to Salt Intrusion Length

In this last section, we generalise the above findings to characterise the influence of sand dune characteristics on vertical transport. We do so using data from Subsection 5.1.1, Subsection 5.1.2 and Subsection 5.3.1, i.e. variations in dune length λ_d, dune height, and dredged dune depth (both characterised by H_d over the whole estuary (using b_d). This results in an analysis comprised of 19 model simulation runs in total. We only focus on changes over the whole estuary and variation in asymmetry is neglected as the influence turns out to be negligible. To quantify the amount of vertical activity

and transport, we evaluate the overall stirring parameter $\mathcal{S}$ as in Equation 2.28 and the mean vertical transport $\mathcal{M}_v$ as in Equation 2.27.

Figure 5.19 shows the relation of $\max(\mathcal{S})$ to the salt intrusion length in the left panel, and the influence of changing dune aspect ratio H_d/λ_d on this stirring parameter in the right panel. This is done both for dunes where the mean depth is maintained (Subsection 5.1.1 and Subsection 5.1.2) and dredged dunes where the depth increases with H_d (Subsection 5.3.1). Changes in channel depth only are not taken into account (as $H_d = 0$ m).

The peak of $\max(\mathcal{S})$ is always attained around $x = 6$ km as shown in Figure 5.4 and the magnitude of the peak is linearly related to the aspect ratio. The left panel shows that this stirring parameter $\max(\mathcal{S})$ also does not correlate to the salt intrusion length $\langle L_s \rangle$ and highlights that the influence of estuarine sand dunes should always be evaluated in relation to the overall geometry such as channel depth. Hence, this parameter only quantifies the overall amount of vertical mixing induced by a change in topography (just landward of L_0), where a sudden increase in vertical mixing occurs.

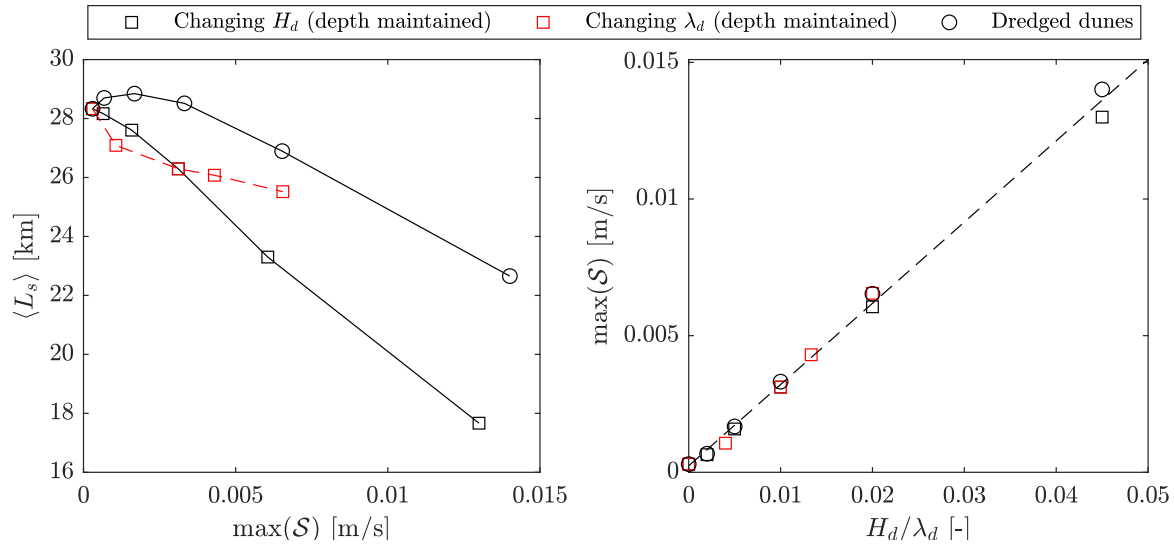

Figure 5.19: Left: Relation of the maximum absolute stirring parameter $\max(\mathcal{S})$ to the salt intrusion length $\langle L_s \rangle$. Right: Relation of aspect ratio H_d/λ_d to $\max(\mathcal{S})$. Symbols are the same as in Figure 5.16.

The relation of the salt intrusion length $\langle L_s \rangle$ to the mean amount of vertical transport $\mathcal{M}_v$ in the region of stratification and geometry is shown in Figure 5.20. The dashed line in the left panel is the found correlation of the two variables that can be described by

$$\langle L_s \rangle = (p_1 \mathcal{M}_v + p_0)^{-1}, \tag{5.6}$$

for $p_1 = 0.437$ s/m^2 and $p_0 = -1.96 \cdot 10^{-5}$ m^{-2}. Note that both these parameters are derived from model output and this is not a causal relation of one variable of the other, but merely a correlation as the two are highly intertwined. A larger vertical transport will decrease the salt intrusion length. Reversely, when the salt intrusion length decreases, the mean vertical transport must increase to balance the overall salt transport.

The relation of the amount of vertical mixing $\mathcal{M}_v$ to input parameters (dune height, dune length, and change in channel depth) is shown in the middle and right panels of Figure 5.20. As indicated by the right panel, channel deepening alone linearly decreases the mean amount of vertical mixing when dunes are not implemented. Similar to Figure 5.16, the dynamics present with dredged dunes are located between dunes and channel deepening, but an exact quantification of the relative contributions

can not be given. For small dune length $\lambda_d = 50$ m ($H_d/\lambda_d = 0.02$), the red line tends to deviate from the black line (where only H_d is changed). This might be due to the discretisation of $\Delta x = 10$ m that is too coarse for small dunes, but it might also be that this relation is not dependent on H_d/λ_d as currently presented, but on some other relationship.

All in all, this shows that vertical mixing throughout the whole estuary and the salt intrusion length are greatly connected. An increase in vertical mixing decreases salt intrusion, in line with literature (MacCready & Geyer, 2010). Both channel deepening and changing dune geometry can change the amount of vertical mixing. We have shown that also dredged estuarine sand dunes, can reduce the salt intrusion length, solely by generating sufficient vertical mixing to counteract the adverse decline in vertical mixing introduced by channel deepening.

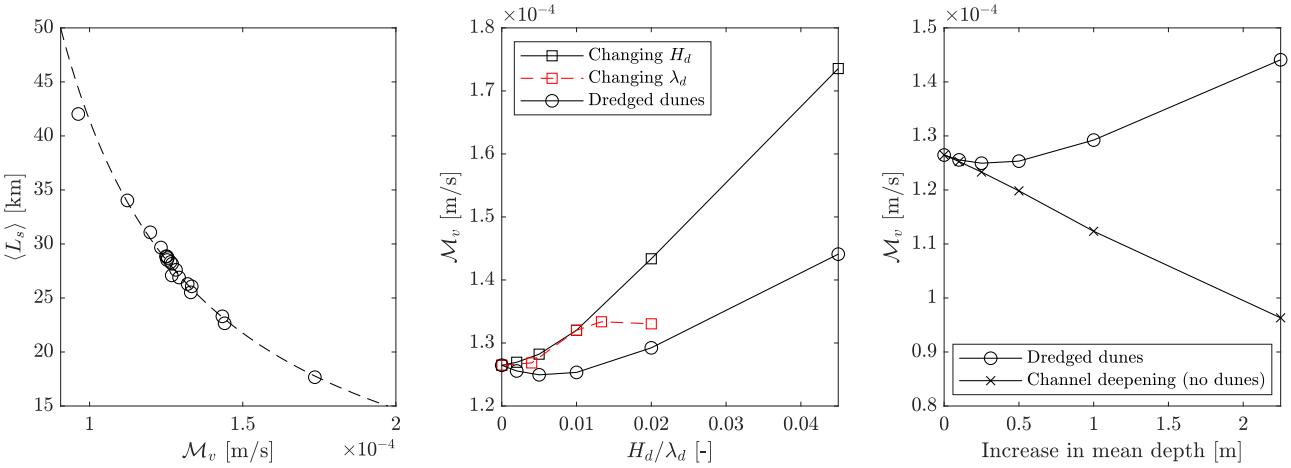

Figure 5.20: Relation of the salt intrusion length $\langle L_s \rangle$, the mean amount of vertical transport $\mathcal{M}_v$ in the region of stratification and geometry. Results are shown from 19 simulations for various dune and depth configurations. Left: relation of $\mathcal{M}_v$ to $\langle L_s \rangle$. Relation of changing dune aspect ratio H_d/λ_d (middle) and mean depth of the estuary (right) to the mean amount of vertical transport $\mathcal{M}_v$ in the region of stratification.

Chapter 6

Discussion and Conclusions

6.1 Model Set-up and Assumptions

The construction of the model relies on specific assumptions aimed at narrowing the free parameter space and concentrating the investigation on sand dune characteristics and potential interventions. These assumptions are revisited here to place the results into context. The idealised setting is fundamental to the research strategy and does not constrain the results but instead enhances the focus on estuarine sand dunes. The strength of this approach is its ability to trace changes in salt intrusion length directly to dune characteristics, without interference from other processes.

6.1.1 Model Geometry

The 2DV model construction allows for evaluating the two most dominant transport mechanisms related to salt intrusion, which results from a balance of in- and outflowing longitudinal transport components, with vertical transport decreasing the stratification. However, the 2DV setting neglects some aspects of salt dynamics in estuaries. Lateral processes, such as tidal trapping and lateral flow in harbours, can change the salt balance and geomorphological characteristics such as meandering are neglected. This has been shown to influence tidal propagation and the salt intrusion length significantly (Hendrickx et al., 2023b). Additionally, the uniform width leads to a constant background river velocity, whereas many estuaries have a funnel-like shape, resulting in variability of the river velocity. By neglecting the variability of lateral processes, we allow ourselves to focus on the longitudinal and vertical transport components, most important for sand dunes.

The average bed level of $-h = -15$ m NAP is a schematisation of the seaward part of the estuary RWW ($0 < x < 30$ km) and the influence of a slight bed slope in the upper part of the estuary is neglected. During the model set-up, the river discharge q_r was identified to be a dominant parameter influencing the salt intrusion length. Similarly, model results are likely sensitive to a model choice of location of a change in bed level. Therefore, to focus on sand dunes, the choice was made to use a uniform mean bed level to prevent a possible interaction of transport mechanisms and a bed slope.

Due to the implementation of boundary conditions, the estuary length L is not an independent, but a physical parameter of the system representing the length over which the tidal influence decays (as indicated in Equation 4.2). The value $L = 50$ km was chosen to be sufficiently large to capture all salt dynamics while avoiding resonance length issues[20], and which produces a tidal flow representative

[20]For a frictionless channel of uniform width, the smallest theoretical resonance length of the M2 tide equals 136 km (Khojasteh et al., 2020), which is significantly larger than the used estuary length.

of the RWW. Lastly, during model development, an increase in estuary length to $L = 200$ km only resulted in a small difference in the salt intrusion length (order of 1 km).

6.1.2 Model Parameters and Validation

The value of the roughness height is representative of sandy beds but results in more tidal amplification than expected for the RWW. This amplification is enhanced further when more tidal constituents are implemented. This amplification might result from neglecting lateral effects and meandering. Usually, the roughness height is used for model calibration, and increasing this value can reduce the amplification. However, our early modelling efforts indicate that while this is effective for calibrating the free surface, it drastically reduces the salt intrusion length, creating salt transport unrepresentative of the RWW. Hence, calibration of the free surface on roughness height in an idealised 2DV model may be unsuitable when evaluating salt intrusion. In our model, the tidally-correlated transport components only play a minor role in the transport of salt, both horizontally and vertically. Therefore, a reduction of amplification of the free surface likely affects salt intrusion to a negligible degree.

The k-ϵ model was selected with constant background eddy parameters. The horizontal SGS model models eddy diffusivity as a function of depth and is considered unsuitable for sand dunes. The values of the background values are chosen based on the modelling study of Dijkstra et al. (2022) to ensure sufficient turbulent diffusion throughout the domain, which results in flow and transport characteristics similar to the RWW. However, the constant background parameters dominate the eddy diffusivity in the horizontal direction, resulting in a longitudinally uniform horizontal turbulence model. This might be unrealistic for the RWW and a more accurate representation of horizontal turbulence might be required, for example, Kranenburg and van der Kaaij (2019) use a spatially varying horizontal eddy viscosity.

The reduction of turbulence in regions of high stratification is likely overestimated in Delft3D-FLOW, as shown by the comparison of vertical diffusivity K_v with field measurements (de Nijs et al., 2010). Stratification results in a large buoyancy flux that greatly reduces the turbulent kinetic energy, and the vertical eddy viscosity and diffusivity reduce to the specified background values in the upper half of the water column. This implies that the remaining dispersion is a result of user-defined dispersion and is not resolved by the model.

6.1.3 Assumptions in Flow and Transport Model

The flow and transport equations are derived from the Navier-Stokes equations, using the Reynolds-averaging approach, the hydrostatic assumption and the Boussinesq approximation. We describe the influence of these assumptions.

The k-ϵ model is applied to close the RANS equations. While the k-ϵ model serves its purpose, more accurate turbulence models exist, especially in stratified and boundary friction-dominated flows (Dijkstra, 2014). In our model, turbulence is modelled and not resolved (i.e. no Direct Numerical Simulation (DNS) or Large Eddy Simulation (LES)), and highly turbulent effects such as vortex shedding and internal wave breaking are not present explicitly but are represented implicitly by the background values. Hence, the current model predominantly captures advective effects. When these processes are resolved accurately by changing from RANS to LES or DNS, the turbulent diffusivity would likely increase and decrease the salt intrusion length.

Similarly, the hydrostatic assumption does not capture internal waves nor flow separation over sand dunes. The idealised estuary resembles low-velocity conditions with relatively low-angled estuarine sand dunes. Hence, the hydrostatic assumption is credible as internal waves mainly form with significant flow, and flow separation mainly occurs over steep dunes. Furthermore, the exclusion of these processes

further contributes to an underestimation of turbulent diffusivity. All in all, the model equations can determine salt intrusion over an undulating topography well. The mitigating effect of sand dunes on salt intrusion is probably even larger than currently predicted.

6.1.4 Delft3D-FLOW Disretisation and Solver

Delft3D-FLOW forms the main standard for most coastal engineering modelling problems in the Netherlands, employed both by industry and research. The used version is calibrated to, and validated for various physical systems, and can also be used in an idealised setting (Hibma et al., 2003; Borsje et al., 2013; Overes, 2021). The σ-grid captures the flow over sand dunes well with relatively low computational cost. It can be implemented well as no global bed slope is present, in which case this discretisation would be unsuitable. Bijvelds (2001) shows that the z-model (that uses a Cartesian discretisation) is more suitable for accurate salt dynamics modelling over steep topography and large bathymetry changes. It is unclear whether this also applies to local topography changes such as sand dunes. This can easily be investigated by modelling the transport of salt over the B-1 model using the z-model. As this requires significantly more vertical layers near the bed and greatly increases computation time this is not investigated in this research but is open for future research.

6.2 Recommendations

6.2.1 Model Improvement

Our convergence study has demonstrated the accuracy of the discretisation, particularly in predicting the influence of sand dunes on salt intrusion with hydrostatic processes. When continuing the current study in Delft3D-FLOW, we recommend lowering the value of D_h^{BACK} to eliminate the dispersive time-step restriction, as the influence on transport and $\langle L_s \rangle$ is relatively small. This allows running the model with a larger timestep and decreases computation time. Furthermore, with dunes of $\lambda_d = 125$ m in length, we have shown a solid numerical convergence using $\Delta x = 10$ m. The results of Section 5.4 seem to indicate that the used discretisation of $\Delta x = 10$ m is suitable for these longer dunes, but that smaller grid cells are required for dunes smaller than $\lambda_d = 75$ m in length.

To further the current study, we advise running more simulations with our model to continue investigating the tidal propagation through the estuary and to determine the influence of multiple tidal constituents on salt intrusion. The interaction of sand dunes with more complex tidal behaviour is not covered by this research.

While the current computational cost is manageable and feasible on a laptop, it is advisable to implement the model on a high-performance cluster for calculations. This allows to cover a larger parameter space to determine the influence of sand dunes on a larger variety of estuaries, rather than the limited partially mixed estuary currently covered (also see Figure 2.3). Unfortunately, attempts to implement the Delft3D-FLOW Version 4.0 on a cluster were unsuccessful in this study, and a careful selection of model runs was needed. While the successor D-FLOW Flexible Mesh has been successfully implemented in a computational cluster, current studies show that this version may yield local instabilities in stratified systems (personal communication with R.W.A. Siemes, September 2023).

The model can mainly be improved by the addition of processes currently not captured, such as non-hydrostatic effects and more advanced turbulence models. Given the limitations of Delft3D-FLOW to account for these processes, it is recommended to implement these processes in more flexible solvers such as OpenFOAM. This allows for the evaluation of intermediate results and calculations and gives more flexibility in adapting the numerical solver and implementation of boundary conditions. Current challenges lie mainly in the implementation of the free surface and boundary conditions.

6.2.2 Future Research

Estuarine sand dunes as a nature-based solution against salt intrusion seems an effective measure, raising questions that merit further research. A first step into a general quantification of the amount of vertical mixing induced by estuarine sand dunes was performed based on the aspect ratio H_d/λ_d of the dunes in Section 5.4. Other parameterisations of dunes might be necessary to quantify this across all estuarine regimes. Furthermore, the influence of non-hydrostatic effects requires more exploration, especially the relation to the salt intrusion length on the estuary scale. Turbulent mixing may be enhanced by internal wave-breaking, and the salt intrusion length might decrease even further when internal waves close to resonance conditions can be generated (Groenenboom et al., 2019; Wegman, 2021).

In this research, the effectiveness of estuarine sand dunes is measured for a single type of estuary with specific conditions, focussing on parameters representative of the RWW during summertime conditions. Research efforts should look at whether this mitigation strategy is also effective in other systems and under different conditions. For example, the effectiveness of estuarine sand dunes might be less effective in systems that are already well-mixed, and the processes might be different for systems where the geometry or external influences like tidal and river velocities differ. Furthermore, salt intrusion is most detrimental during extreme events, in particular, low river discharges and set up of the sea surface elevation, which might be enhanced by estuarine sand dunes. Measures that rely on an increase of vertical mixing are less effective during set-up events and further research should evaluate the effectiveness of estuarine sand dunes during changes in external influences during extreme events (Kranenburg & van der Kaaij, 2019).

This research especially focuses on the influence of a morphostatic bathymetry in terms of sand dunes on salt intrusion and stratification. Research dedicated to understanding how stratification influences sand dune growth and migration should be continued. This is already the topic of current research (van der Sande et al., 2021, 2023), and evaluating what dune shapes are likely to form for specific estuaries is essential. This study has highlighted the potential benefits of artificially dredged sand dune fields in decreasing salt intrusion length. Future work should focus on ensuring that the shape characteristics align close to the system's natural equilibrium (assuming that it exists), minimizing the need for periodic dredging activities. When sand dunes can be implemented as a nature-based solution against salt intrusion, and when this can be done in a minimal-intervention method, biotic influences will alter the dynamics of the bed and flow. For example, research has shown the interaction of worms and benthic organisms on marine sand wave growth (Damveld et al., 2019; Damveld et al., 2020).

6.2.3 Implications

The modelled influence of sand dunes is in the order of kilometres to an overall salt intrusion length of 30 km. Other external estuarine-scale factors, such as tidal amplitude and river flushing, influence the salt intrusion length to a much larger degree but are under limited human control. In the Netherlands, the flow can be diverted over the different branches, but the overall discharge remains. Meandering and decreasing the average water depth can be adapted, but is often unfeasible due to existing infrastructure along the estuary and the required navigation depth for shipping. Sand dunes, as adaptable measures, offer a means of intervention and can serve as a nature-based solution against salt intrusion. An increase in the dune aspect ratio leads to enhanced vertical mixing and a reduced salt intrusion length. The influence of vertical mixing when creating sand dunes in a flat bed, can even counteract the detrimental effect of deepening the estuary. Conversely, we have shown that current dredging activities in the RWW are likely unfavourable in terms of salt intrusion. The bed-leveling procedures reduce vertical mixing and increase the salt intrusion length. Retaining an undulating topography that allows for vertical transport is recommended when dredging and dumping sediment.

6.3 Conclusions

In this section, we will revisit the methodology and argue why results can be trusted. Moreover, we summarise our findings and answer the research questions as presented in Section 1.1. Most importantly, we aim to answer the question: **What is the influence of estuarine sand dunes on salt intrusion?**

6.3.1 Validity of the Model

The problem of salt intrusion is modelled in a highly idealised manner to focus solely on sand dune characteristics, eliminating numerous influencing factors such as lateral effects, multiple channels, bed slope and narrowing of the estuary. Nevertheless, the model shows a good resemblance of flow and salinity distribution of a partially mixed estuary, aligning relatively well with field measurements of the RWW (Subsection 4.1.3). Furthermore, the model shows robust numerical convergence (Section 3.4), and a doubling of the number of grid cells in both vertical and horizontal directions is expected to yield a negligible improvement in model accuracy. A horizontal grid cell size of $\Delta x = 10$ m and $K = 40$ vertical layers effectively captures most of the hydrostatic flow and salt transport behaviour, ensuring the results' robustness and independence of the chosen discretisation.

6.3.2 Methodology and Analysis Tools

We introduced a methodology to quantify and decompose the vertical transport of salt. In combination with dune averaging, this method provides a tool that aids in understanding the overall vertical flux and correlates well to the salt intrusion length. It enables successful evaluation of the advective and dispersive components respectively. Furthermore, it shows how the newly introduced dune-averaging operator works effectively, approximating the net flux over a single dune.

6.3.3 Answers to Research Questions

- What processes govern the salt dynamics and what role do sand dunes play?

In the literature research, we have highlighted the main processes that play a role in salt intrusion. The balance between longitudinal processes determines the salt intrusion length, and an increase in vertical transport decreases stratification. Similarly, sand dunes can be schematised as 2DV bedforms, and we mainly highlight and investigate vertical and longitudinal processes. Research indicates that the outflowing freshwater flushing and the inflowing estuarine circulation are the dominant transport mechanisms for the RWW, which can be identified as a partially-mixed to salt wedge estuary.

Our model results suggest that the presence of sand dunes does not change the type of estuary or transport regime, and the dominant horizontal components are always the outflowing river flushing and estuarine circulation causing a net inward transport. Although the balance between transport components may shift, resulting in different salt intrusion lengths, the dominant processes remain consistent, enabled by a change in salinity structure through the estuary from the seaward end to the salt intrusion limit. Furthermore, in the case of constant mean water depth, we have found an inversely proportional relationship of tidal excursion length ΔL_s to salt intrusion length $\langle L_s \rangle$, which likely arises from the linearly decreasing tidal velocity from the seaward end.

- What is the influence of sand dune characteristics such as height, length and asymmetry, on salt transport and the salt intrusion length?

Changes in dune geometry and characteristics impact the salt intrusion length, which is most sensitive to a change in dune height. An increase in dune height enhances vertical advective transport, bringing more saline water upwards through the water column and reducing stratification. Similarly, decreasing

dune length increases the dune slope and enhances the vertical exchange. Dune asymmetry, however, has a negligible influence on our model results, likely originating from the hydrostatic assumption. With all these changes, the overall horizontal transport components do not change qualitatively. The mean total vertical transport $\mathcal{M}_v$ depends on the dune geometry and is linked to the salt intrusion length. Generally, salt intrusion can be reduced with dunes with a larger dune height.

- How does dredging and dumping of sediment in a sand dune pattern influence the salt intrusion length?

Manipulation of an existing sand dune field changes the salt intrusion length. Dredging of sediment reduces the main outward-flowing river transport and causes an increase in water depth which decreases the amount of vertical mixing, both contributing to an increase in the salt intrusion length. The volume of sediment dredged is roughly proportional to the change in salt intrusion length.

The influence of dumping depends on the strategy employed. Uniform Bed Alteration (UBA) preserves topography and decreases the salt intrusion length proportionally to the volume of sediment dumped by a uniform reduction of the mean water depth over the intervention location. Alternatively, Bed-Levelling Depth Control (BLDC) removes the topography and subsequently, reduces vertical mixing. Dumping of sediment is only effective in mitigating salt intrusion when the volume used is sufficient to exceed the original crest height.

Regardless of the method used, a change in salt intrusion length is similar to the influence of a changing mean water depth where the vertical mixing and freshwater flushing increase. However, the downside of this method is that it decreases navigability. The horizontal transport components change slightly in the region of intervention. The vertical transport only changes near the boundary of the intervention region and the magnitude of the vertical flux over the intervention itself is not altered significantly. These interventions do not change the overall mean vertical flux (as with changing dune height) but rather change the balance of horizontal components. Lastly, the location of dumping sediment matters, the achieved reduction in the salt intrusion length is most effective relatively close to the seaward end. However, it is unclear whether this location also holds for different dumping volumes.

- How can artificially created sand dunes reduce salt intrusion in an estuary previously depth-maintained?

Creating sand dunes by dredging in a flat bed can serve as a mitigation tool against salt intrusion. A sufficiently deep dredged dune height generates sufficient vertical mixing to counteract the adverse effects of deepening the channel, maintaining estuary navigability while enhancing vertical mixing with local topography. This method is most effective when performed on a large scale throughout the estuary. When a smaller extent is used, again an optimal location will exist.

What is the influence of estuarine sand dunes on salt intrusion?

In summary, our findings underscore the necessity of considering estuarine sand dunes in the evaluation of salt intrusion. These dunes have demonstrated a substantial capacity to enhance net vertical advective transport and, thereby, reduce the salt intrusion length. This highlights the importance of preserving these bedforms and indicates the potential adverse effects associated with dredging. Not only by an increase in water depth that reduces freshwater flushing and vertical mixing but also by removing vertical changes in the bed level that facilitate the advective vertical transport. This shows that dredging in the RWW can be performed more efficiently with regards to salt intrusion, by retaining vertical variation of the bed while keeping navigability the same. Finally, given the natural presence of these bedforms in estuarine systems, they can serve as a nature-based solution to effectively mitigate salt intrusion.

Bibliography

Allen, J. R. L. (1978). Computational models for dune time-lag: Calculations using stein's rule for dune height. *Sedimentary Geology*, *20*, 165–216. https://doi.org/10.1016/0037-0738(78)90054-4

Best, J. L., Kostaschuk, R. A., & Villard, P. V. (2001). Quantitative visualization of flow fields associated with alluvial sand dunes: Results from the laboratory and field using ultrasonic and acoustic doppler anemometry. *Journal of Visualization*, *4*(4), 373–381. https://doi.org/10.1007/BF03183900

Best, J. L. (2005). The fluid dynamics of river dunes: A review and some future research directions. *Journal of Geophysical Research: Earth Surface*, *110*(F4). https://doi.org/10.1029/2004JF000218

Best, J. L., & Kostaschuk, R. A. (2002). An experimental study of turbulent flow over a low-angle dune. *Journal of Geophysical Research: Oceans*, *107*(C9), 18–1. https://doi.org/10.1029/2000JC000294

Biemond, B., de Swart, H., & Dijkstra, H. (2023). Mechanisms of salt overspill at estuarine network junctions explained with an idealized model. *Journal of Geophysical Research: Oceans*, *128*. https://doi.org/10.1029/2023JC019630

Bijlage A Drinkwaterbesluit. (2023). Wetten.nl - regeling - drinkwaterbesluit - bwbr0030111 (accessed on 19/11/2023). https://wetten.overheid.nl/jci1.3:c:BWBR0030111&bijlage=A&z=2022-12-21&g=2022-12-21

Bijvelds, M. D. J. P. (2001). *Numerical modelling of estuarine flow over steep topography* (Doctoral dissertation). TU Delft, Delft University of Technology. https://repository.tudelft.nl/islandora/object/uuid:39c0c858-579a-47fa-a911-4a4114949a11/datastream/OBJ/download

Borsje, B. W., van Wesenbeeck, B. K., Dekker, F., Paalvast, P., Bouma, T. J., van Katwijk, M. M., & de Vries, M. B. (2011). How ecological engineering can serve in coastal protection. *Ecological Engineering*, *37*(2), 113–122. https://doi.org/10.1016/j.ecoleng.2010.11.027

Borsje, B. W., Roos, P. C., Kranenburg, W. M., & Hulscher, S. J. M. H. (2013). Modeling tidal sand wave formation in a numerical shallow water model: The role of turbulence formulation. *Continental shelf research*, *60*, 17–27. https://doi.org/10.1016/j.csr.2013.04.023

Bradley, R. W., Venditti, J. G., Kostaschuk, R. A., Church, M., Hendershot, M., & Allison, M. A. (2013). Flow and sediment suspension events over low-angle dunes: Fraser estuary, canada. *Journal of geophysical research: Earth surface*, *118*(3), 1693–1709. https://doi.org/10.1002/jgrf.20118

Bradley, R. W., & Venditti, J. G. (2017). Reevaluating dune scaling relations. *Earth-Science Reviews*, *165*, 356–376. https://doi.org/10.1016/j.earscirev.2016.11.004

Campmans, G. H. P., Roos, P. C., Van der Sleen, N. R., & Hulscher, S. J. M. H. (2021). Modeling tidal sand wave recovery after dredging: Effect of different types of dredging strategies. *Coastal Engineering*, *165*, 103862. https://doi.org/10.1016/j.coastaleng.2021.103862

Caulfield, C. P. (2021). Layering, instabilities, and mixing in turbulent stratified flows. *Annual Review of Fluid Mechanics*, *53*, 113–145. https://doi.org/10.1146/annurev-fluid-042320-100458

Cornelissen, S. C. (2004). *Numerical modelling of stratified flows: Comparison of the sigma and z coordinate systems* (Master's thesis). TU Delft, Faculty of Civil Engineering and Geosciences, Hydraulic Engineering. http://resolver.tudelft.nl/uuid:472f2f06-7d0f-42f2-9865-6d34695a2e18

Damen, J. M., van Dijk, T. A. G. P., & Hulscher, S. J. M. H. (2018). Spatially varying environmental properties controlling observed sand wave morphology. *Journal of Geophysical Research: Earth Surface*, *123*(2), 262–280. https://doi.org/10.1002/2017JF004322

Damveld, J. H., Borsje, B. W., Roos, P. C., & Hulscher, S. J. M. H. (2020). Biogeomorphology in the marine landscape: Modelling the feedbacks between patches of the polychaete worm lanice conchilega and tidal sand waves. *Earth Surface Processes and Landforms*, *45*(11), 2572–2587. https://doi.org/10.1002/esp.4914

Damveld, J. H., Roos, P. C., Borsje, B. W., & Hulscher, S. J. M. H. (2019). Modelling the two-way coupling of tidal sand waves and benthic organisms: A linear stability approach. *Environmental fluid mechanics*, *19*(5), 1073–1103. https://doi.org/10.1007/s10652-019-09673-1

de Boer, H. C., & Radersma, S. (2011). *Verzilting in nederland: Oorzaken en perspectieven* (tech. rep. No. 531). Netherlands, Wageningen UR Livestock Research. https://edepot.wur.nl/186856

de Bruijn, L. (2018). *Maintenance dredging in the port of rotterdam: A research to the increase in maintenance dredging volume at port of rotterdam* (Master's thesis). Delft University of Technology. http://resolver.tudelft.nl/uuid:ef075688-d855-4f99-9de4-c562e4211335

Deltares. (2018). *Delft3d-flow: Simulation of multi-dimensional hydrodynamic flows and transport phenomena, including sediments - user manual*. Version 3.15.

de Nijs, M. A. J., Winterwerp, J. C., & Pietrzak, J. D. (2010). The effects of the internal flow structure on spm entrapment in the rotterdam waterway. *Journal of Physical Oceanography*, *40*(11), 2357–2380. https://doi.org/10.1175/2010JPO4233.1

de Vriend, H. J., van Koningsveld, M., Aarninkhof, S. G., de Vries, M. B., & Baptist, M. J. (2015). Sustainable hydraulic engineering through building with nature. *Journal of Hydro-environment research*, *9*(2), 159–171. https://doi.org/10.1016/j.jher.2014.06.004

Dijkstra, Y. M. (2014). *On the effect of tidal variations of turbulent mixing on flow and salt transport in estuaries* (Master's thesis). Delft University of Technology. http://resolver.tudelft.nl/uuid:d4dba2bf-4a98-45b1-a2e1-78fb345fc8ee

Dijkstra, Y. M., & Schuttelaars, H. M. (2021). A unifying approach to subtidal salt intrusion modeling in tidal estuaries. *Journal of Physical Oceanography*, *51*(1), 147–167. https://doi.org/10.1175/JPO-D-20-0006.1

Dijkstra, Y. M., Schuttelaars, H. M., & Kranenburg, W. M. (2022). Salt transport regimes caused by tidal and subtidal processes in narrow estuaries. *Journal of Geophysical Research: Oceans*, e2021JC018391. https://doi.org/10.1029/2021JC018391

Eckart, C. H. (1958). The equation of state of water and sea water at low temperatures and pressures, part 2 of properties of water. *American Journal of Science*, *256*(4), 225–240. https://doi.org/10.2475/ajs.256.4.225

Galperin, B., Sukoriansky, S., & Anderson, P. S. (2007). On the critical richardson number in stably stratified turbulence. *Atmospheric Science Letters*, *8*(3), 65–69. https://doi.org/10.1002/asl.153

Garcia, A. M. P., Geyer, W. R., & Randall, N. (2022). Exchange flows in tributary creeks enhance dispersion by tidal trapping. *Estuaries and Coasts*, 1–19. https://doi.org/10.1007/s12237-021-00969-4

Geyer, W. R., & MacCready, P. (2014). The estuarine circulation. *Annual review of fluid mechanics*, *46*, 175–197. https://doi.org/10.1146/annurev-fluid-010313-141302

Groenenboom, J., Kranenburg, W., Laan, S., & Kester, J. (2019). *Strategisch Baggeren; Onderdeel van KPP CIP 2019* (1203690-003-BGS-0001). Deltares.

Hamilton, P. (1975). A numerical model of the vertical circulation of tidal estuaries and its application to the rotterdam waterway. *Geophysical Journal International*, *40*(1), 1–21. https://doi.org/10.1111/j.1365-246X.1975.tb01601.x

Hansen, D. V., & Rattray Jr., M. (1966). New dimensions in estuary classification1. *Limnology and Oceanography*, *11*(3), 319–326. https://doi.org/10.4319/lo.1966.11.3.0319

Hendrickx, G. G., Antolínez, J. A. ., Herman, P. M. J., & Aarninkhof, S. G. J. (2023a). Estuarine sensitivity to nature-based salt intrusion mitigation measures. *Coastal Engineering Proceedings*, (37), management.146. https://doi.org/10.9753/icce.v37.management.146

Hendrickx, G. G., Kranenburg, W. M., Antolínez, J. A. A., Huismans, Y., Aarninkhof, S. G. J., & Herman, P. M. J. (2023b). Sensitivity of salt intrusion to estuary-scale changes: A systematic modelling study towards nature-based mitigation measures. *Estuarine, Coastal and Shelf Science*, *295*, 108564. https://doi.org/10.1016/j.ecss.2023.108564

Hibma, A., Schuttelaars, H. M., & Wang, Z. B. (2003). Comparison of longitudinal equilibrium profiles of estuaries in idealized and process-based models. *Ocean Dynamics*, *53*, 252–269. https://doi.org/10.1007/s10236-003-0046-7

Hulscher, S. J. M. H., & Dohmen-Janssen, C. M. (2005). Introduction to special section on marine sand wave and river dune dynamics. *Journal of Geophysical Research: Earth Surface*, *110*(F4). https://doi.org/10.1029/2005JF000404

IAPSO. (1985). The International System of Units (SI) in Oceanography. IAPSO Pulication Scientifique No 32 (UNESCO Technical Papers in Marine Science No 45. https://doi.org/10.25607/OBP-666

Jongbloed, H., Schuttelaars, H. M., Dijkstra, Y. M., Donkers, P. B., & Hoitink, A. J. F. (2022). Influence of wind on subtidal salt intrusion and stratification in well-mixed and partially stratified estuaries. *Journal of Physical Oceanography*, *52*(12), 3139–3158. https://doi.org/10.1175/JPO-D-21-0291.1

Kennisprogramma Zeespiegelstijging. (2023). Tussenbalans van het kennisprogramma zeespiegelstijging. *Ministerie van Infrastructuur en Waterstaat, Staf deltacommissaris and Rijkswaterstaat*. https://www.deltaprogramma.nl/deltaprogramma/documenten/publicaties/2023/11/09/20231107-9525_tussenbalans-kennisprogramma-zeespiegelstijging_06-webversie

Khojasteh, D., Hottinger, S., Felder, S., de Cesare, G., Heimhuber, V., Hanslow, D. J., & Glamore, W. (2020). Estuarine tidal response to sea level rise: The significance of entrance restriction. *Estuarine, Coastal and Shelf Science*, *244*, 106941. https://doi.org/10.1016/j.ecss.2020.106941

Kirichek, A., Rutgers, R., Wensween, M., & van Hassent, A. (2018). Sediment management in the port of rotterdam. *Baggern - Unterbringen - Aufbereiten - Verwerten: 10. Rostocker Baggergutseminar, Kompetenztreffpunkt Nassbaggergut*. https://pure.tudelft.nl/ws/portalfiles/portal/99008340/Kirichek2018SedimentmanagementinthePortofRotterdam.pdf

Knaapen, M. A. F. (2005). Sandwave migration predictor based on shape information. *Journal of Geophysical Research: Earth Surface*, *110*(F4).

Kostaschuk, R. A., Best, J. L., & Villard, P. V. (2010). The influence of dunes on mixing in a migrating salt-wedge: Fraser river estuary, canada. *Earth Surface Processes and Landforms*, *35*(4), 460–465.

Kostaschuk, R. A. (2000). A field study of turbulence and sediment dynamics over subaqueous dunes with flow separation. *Sedimentology*, *47*, 519–531. https://doi.org/10.1046/J.1365-3091.2000.00303.X

Kranenburg, C. (1986). A time scale for long-term salt intrusion in well-mixed estuaries. *Journal of Physical Oceanography*, *16*(7), 1329–1331. https://doi.org/10.1175/1520-0485(1986)016<1329:ATSFLT>2.0.CO;2

Kranenburg, C., & Pietrzak, J. D. (1989). Internal lee waves in turbulent two-layer flow. *Journal of Hydraulic Engineering*, *115*(10), 1352–1370.

Kranenburg, W., & van der Kaaij, T. (2019). *Dispersiemechanismen in de Rijn-Maasmonding; Verkenning van de verhouding tussen zouttransportprocessen middels zoutfluxdecompositie* (1203735-004-ZWS-0006). Deltares. https://publications.deltares.nl/11203735_004.pdf

Kranenburg, W., van der Kaaij, T., & Nolte, A. J. (2014). *Evaluatie van het OSR-model voor zoutindringing in de Rijn-Maasmonding (I)* (1209459-000-ZKS-0028). Deltares. https://publications.deltares.nl/1209459_000_0028.pdf

Laan, S., Huismans, Y., Rodrigo, S., Leummens, L., & Kranenburg, W. (2023). *Effect bodemligging op verzilting Nieuwe Waterweg, Nieuwe Maas en Lek* (11208075-010-ZWS-0001). Deltares.

Lefebvre, A. (2019). Three-dimensional flow above river bedforms: Insights from numerical modeling of a natural dune field (río paraná, argentina). *Journal of Geophysical Research: Earth Surface*, *124*(8), 2241–2264. https://doi.org/10.1029/2018JF004928

Lerczak, J. A., Geyer, W. R., & Ralston, D. K. (2009). The temporal response of the length of a partially stratified estuary to changes in river flow and tidal amplitude. *Journal of Physical Oceanography*, *39*(4), 915–933. https://doi.org/10.1175/2008JPO3933.1

Li, M., Zhong, L., & Boicourt, W. C. (2005). Simulations of chesapeake bay estuary: Sensitivity to turbulence mixing parameterizations and comparison with observations. *Journal of Geophysical Research: Oceans*, *110*(C12). https://doi.org/10.1029/2004JC002585

Limburg, K. E. (1999). Estuaries, ecology, and economic decisions: An example of perceptual barriers and challenges to understanding. *Ecological Economics*, *30*(1), 185–188. https://doi.org/10.1016/S0921-8009(99)00045-2

Lokin, L. R., Warmink, J. J., Bomers, A., & Hulscher, S. J. M. H. (2022). River dune dynamics during low flows [e2021GL097127 2021GL097127]. *Geophysical Research Letters*, *49*(8), e2021GL097127. https://doi.org/10.1029/2021GL097127

Lotze, H. K. (2010). Historical reconstruction of human-induced changes in us estuaries. *Oceanography and marine biology: an annual review*, *48*, 267–338.

MacCready, P., & Geyer, W. R. (2010). Advances in estuarine physics [PMID: 21141657]. *Annual Review of Marine Science*, *2*(1), 35–58. https://doi.org/10.1146/annurev-marine-120308-081015

MacDonald, D. G., & Horner-Devine, A. R. (2008). Temporal and spatial variability of vertical salt flux in a highly stratified estuary. *Journal of Geophysical Research: Oceans*, *113*(C9). https://doi.org/10.1029/2007JC004620

Maddux, T. B., Nelson, J. M., & McLean, S. R. (2003). Turbulent flow over three-dimensional dunes: 1. free surface and flow response. *Journal of Geophysical Research: Earth Surface*, *108*(F1). https://doi.org/10.1029/2003JF000017

Mellor, G. L., & Blumberg, A. F. (1985). Modeling vertical and horizontal diffusivities with the sigma coordinate system. *Monthly weather review*, *113*(8), 1379–1383. https://doi.org/10.1175/1520-0493(1985)113<1379:MVAHDW>2.0.CO;2

Miah, M. Y., Kamal, M. Z. U., Salam, M. A., & Islam, M. S. (2020). Impact of salinity intrusion on agriculture of southwest bangladesh - a review. *International Journal of Agricultural Policy and Research*. https://doi.org/10.15739/IJAPR.20.005

Millero, F. J., Feistel, R., Wright, D. G., & McDougall, T. J. (2008). The composition of standard seawater and the definition of the reference-composition salinity scale. *Deep Sea Research Part I: Oceanographic Research Papers*, *55*(1), 50–72. https://doi.org/10.1016/j.dsr.2007.10.001

Ottink, R., Sibma, M., & Zaanen, I. v. (2022). *Droogteseizoen 2022 : Terugblik wmcn-lcw* (No. 22i380). Rijkswaterstaat. https://open.rijkswaterstaat.nl/zoeken/@253589/droogteseizoen-2022-terugblik-wmcn-lcw/#highlight=droogte

Overes, P. (2021). *Modeling sand wave field dynamics in the north sea using delft3d flexible mesh* (Master's thesis). Delft University of Technology. http://resolver.tudelft.nl/uuid:492ee814-9821-4943-aa16-6299fcf7533e

Paarlberg, A. J., Dohmen-Janssen, C. M., Hulscher, S. J. M. H., & Termes, P. (2009). Modeling river dune evolution using a parameterization of flow separation. *Journal of Geophysical Research: Earth Surface*, *114*(F1). https://doi.org/10.1029/2007JF000910

Paturej, E. (2008). Estuaries-types, role and impact on human life. *Baltic Coastal Zone. Journal of Ecology and Protection of the Coastline*, (12). https://www.researchgate.net/publication/228488312

Pietrzak, J. D., Kranenburg, C., & Abraham, G. (1990). Resonant internal waves in fluid flow. *Nature*, *344*(6269), 844–847. https://doi.org/10.1038/344844a0

Pietrzak, J. D., Kranenburg, C., Abraham, G., Kranenborg, B., & van der Wekken, A. (1991). Internal wave activity in rotterdam waterway. *Journal of Hydraulic Engineering*, *117*(6), 738–757. https://doi.org/10.1061/(ASCE)0733-9429(1991)117:6(738)

Pietrzak, J., & Labeur, R. J. (2004). Trapped internal waves over undular topography in a partially mixed estuary. *Ocean Dynamics*, *54*, 315–323. https://doi.org/10.1007/s10236-003-0081-4

Pritchard, D. W. (1952). Salinity distribution and circulation in the chesapeake bay estuarine system. 1. *Mar. Res*, *11*, 106–123.

Ralston, D. K., Cowles, G. W., Geyer, W. R., & Holleman, R. C. (2017). Turbulent and numerical mixing in a salt wedge estuary: Dependence on grid resolution, bottom roughness, and turbulence closure. *Journal of Geophysical Research: Oceans*, *122*(1), 692–712. https://doi.org/10.1002/2016JC011738

Rijkswaterstaat. (2023a). https://www.rijkswaterstaat.nl/water/vaarwegenoverzicht

Rijkswaterstaat. (2023b). *Waterinfo database*. https://waterinfo.rws.nl/#/expert/Waterhoogten/Hoek-van-Holland%28HOEK%29/details?parameters=Waterhoogte___20Oppervlaktewater___20t.o.v.___20Normaal___20Amsterdams___20Peil___20in___20cm

Siemes, R. W. A., Duong, T. M., Willemsen, P. W. J. M., Borsje, B. W., & Hulscher, S. J. M. H. (2023). Morphological response of a highly engineered estuary to altering channel depth and restoring wetlands. *Journal of Marine Science and Engineering*, *11*(11). https://doi.org/10.3390/jmse11112150

Stelling, G. S., & van Kester, J. A. T. M. (1994). On the approximation of horizontal gradients in sigma co-ordinates for bathymetry with steep bottom slopes. *International Journal for Numerical Methods in Fluids*, *18*(10), 915–935. https://doi.org/10.1002/fld.1650181003

Tully, K., Gedan, K., Epanchin-Niell, R., Strong, A., Bernhardt, E. S., BenDor, T., Mitchell, M., Kominoski, J., Jordan, T. E., Neubauer, S. C., et al. (2019). The invisible flood: The chemistry, ecology, and social implications of coastal saltwater intrusion. *BioScience*, *69*(5), 368–378. https://doi.org/10.1093/biosci/biz027

Valle-Levinson, A. (2010). *Contemporary issues in estuarine physics*. Cambridge University Press. https://doi.org/10.1017/CBO9780511676567

van der Sande, W. M., Roos, P. C., Gerkema, T., & Hulscher, S. J. M. H. (2021). Gravitational circulation as driver of upstream migration of estuarine sand dunes. *Geophysical Research Letters*, *48*. https://doi.org/10.1029/2021GL093337

van der Sande, W. M., Roos, P. C., Gerkema, T., & Hulscher, S. J. M. H. (2023). Shorter estuarine dunes and upstream migration due to intratidal variations in stratification. *Estuarine, Coastal and Shelf Science*, *281*, 108216. https://doi.org/10.1016/j.ecss.2023.108216

Veldkamp, T. I. E., Wada, Y., de Moel, H., Kummu, M., Eisner, S., Aerts, J. C. J. H., & Ward, P. J. (2015). Changing mechanism of global water scarcity events: Impacts of socioeconomic changes and inter-annual hydro-climatic variability. *Global Environmental Change*, *32*, 18–29. https://doi.org/10.1016/j.gloenvcha.2015.02.011

Wada, Y., van Beek, L. P. H., Viviroli, D., Dürr, H. H., Weingartner, R., & Bierkens, M. F. P. (2011). Global monthly water stress: 2. water demand and severity of water stress. *Water Resources Research*, *47*(7). https://doi.org/10.1029/2010WR009792

Warner, J. C., Sherwood, C. R., Arango, H. G., & Signell, R. P. (2005). Performance of four turbulence closure models implemented using a generic length scale method. *Ocean Modelling*, *8*(1-2), 81–113. https://doi.org/10.1016/j.ocemod.2003.12.003

Wegman, T. M. (2021). *Undular bottom topography as a salt intrusion mitigation measure* (Master's thesis). Delft University of Technology. http://resolver.tudelft.nl/uuid:c7516ec1-3698-4127-af4a-096f0b3500f1

Wei, X., Williams, M. E., Brown, J. M., Thorne, P. D., & Amoudry, L. O. (2022). Salt intrusion as a function of estuary length in periodically weakly stratified estuaries. *Geophysical Research Letters*, *49*(15), e2022GL099082.

Wright, D. G. (1997). An equation of state for use in ocean models: Eckart's formula revisited. *Journal of Atmospheric and Oceanic Technology*, *14*(3), 735–740. https://doi.org/10.1175/1520-0426(1997)014<0735:AEOSFU>2.0.CO;2

Yalin, M. S. (1964). Geometrical properties of sand wave. *Journal of the Hydraulics Division*, *90*(5), 105–119. https://doi.org/10.1061/JYCEAJ.0001097

Yu, Q., Wang, Y., Gao, J., Gao, S., & Flemming, B. (2014). Turbidity maximum formation in a well-mixed macrotidal estuary: The role of tidal pumping. *Journal of Geophysical Research: Oceans*, *119*(11), 7705–7724. https://doi.org/10.1002/2014JC010228

Zanke, U., Roland, A., & Wurpts, A. (2022). Roughness effects of subaquaeous ripples and dunes. *Water*, *14*(13), 2024. https://doi.org/10.3390/w14132024

Zorndt, A. C., Wurpts, A., & Schlurmann, T. (2011). The influence of hydrodynamic boundary conditions on characteristics, migration, and associated sand transport of sand dunes in a tidal environment: A long-term study of the elbe estuary. *Ocean Dynamics*, *61*, 1629–1644. https://doi.org/10.1007/S10236-011-0452-1

Appendices

A.1 Appendices to Chapter 2

A.1.1 Derivation of 2DV model equations from 3D Navier Stokes equations

To model both fluid velocities and salinity, we start with the governing equations for fluid flows: the Navier-Stokes equations. A bold notation is used for vectorial quantities. For such objects, the subscript "3" means that it is three-dimensional and without such a subscript the object is two-dimensional. Flow velocities are denoted by $\boldsymbol{u}_3 = (u, v, w)$ in m/s in $\boldsymbol{x}_3 = (x, y, z)$-direction respectively. The nabla operator is defined as $\nabla_3 = (\partial/\partial x, \partial/\partial y, \partial/\partial z)$, with the Laplacian $\Delta_3 = \nabla_3 \cdot \nabla_3$ and unity vector $\boldsymbol{I}_3 = (1, 1, 1)$. The salinity $s(\boldsymbol{x}_3, t)$ is a scalar value in ppt. Under the assumption of a constant temperature of $T = 15$ °C, the basis is formed by the Navier-Stokes equations with a conservation equation for salt, in three dimensions equal to

$$\frac{\partial \rho}{\partial t} + \nabla_3 \cdot (\rho \boldsymbol{u}_3) = 0 \tag{1}$$

$$\frac{\partial \rho \boldsymbol{u}_3^T}{\partial t} + (\boldsymbol{u}_3 \cdot \nabla_3)(\rho \boldsymbol{u}_3^T) = (\mu \Delta_3 \boldsymbol{u}_3)\boldsymbol{I}_3^T - (\nabla_3 p)^T + \rho \boldsymbol{g}^T, \tag{2}$$

$$\frac{\partial s}{\partial t} + \nabla_3 \cdot (s \boldsymbol{u}_3) = \nabla_3 \cdot (D_s \nabla_3 s), \tag{3}$$

$$\rho(s) = \rho_0(1 + \beta s) \tag{4}$$

where we recognise the (1) conservation of mass, (2) conservation of momentum in the three dimensions (transposed notation $\cdot^T$ is used to indicate the three equations) and (3) conservation of total salt. Density is denoted by ρ in kg/m^3, dynamic viscosity μ in kg/m/s and the spatially uniform molecular salt diffusion coefficient D_s in m^2/s. Gravity acts downward in the vertical dimension z with $\boldsymbol{g} = (0, 0, -g)$ with gravitational acceleration constant $g = 9.81$ m/s^2.

Incompressiblity

We assume the flow to be incompressible (but variable-density), meaning that density does not depend on pressure but on salinity only. This incompressibility assumption does not imply that density is constant, only that the material derivative $\frac{D\rho}{Dt} = \frac{\partial \rho}{\partial t} + \boldsymbol{u}_3 \cdot (\nabla_3 \rho)$ is zero. A constant-density flow is a special case of incompressible flow. The **mass conservation equation** (1) now reduces to

$$\frac{\partial \rho}{\partial t} + \nabla_3 \cdot (\rho \boldsymbol{u}_3) = \cancelto{0}{\left(\frac{\partial \rho}{\partial t} + \boldsymbol{u}_3 \cdot (\nabla_3 \rho)\right)} + \rho \nabla_3 \cdot \boldsymbol{u}_3 \tag{5}$$

$$= \rho \nabla_3 \cdot \boldsymbol{u}_3 = 0 \tag{6}$$

Since $\rho > 0$, this simplifies to the divergence-free equation $\nabla_3 \cdot \boldsymbol{u}_3 = 0$. Similarly, for the **momentum conservation equation** (2), the left-hand side equates to

$$\frac{\partial \rho \boldsymbol{u}_3^T}{\partial t} + (\boldsymbol{u}_3 \cdot \nabla_3)(\rho \boldsymbol{u}_3^T) = \boldsymbol{u}_3^T \cancelto{0}{\left(\frac{\partial \rho}{\partial t} + \boldsymbol{u}_3 \cdot \nabla_3 \rho \right)} + \rho \left(\frac{\partial \boldsymbol{u}_3^T}{\partial t} + (\boldsymbol{u}_3 \cdot \nabla_3)\boldsymbol{u}_3^T \right) \tag{7}$$

$$\implies \frac{\partial \boldsymbol{u}_3^T}{\partial t} + (\boldsymbol{u}_3 \cdot \nabla_3)\boldsymbol{u}_3^T = (\nu \Delta_3 \boldsymbol{u}_3)\boldsymbol{I}_3^T - \frac{1}{\rho}(\nabla_3 p)^T + \boldsymbol{g}^T \tag{8}$$

for kinematic viscosity $\nu = \mu/\rho$. Finally, for the **salt transport equation** (3), we see that

$$\frac{\partial s}{\partial t} + \nabla \cdot (s\boldsymbol{u}_3) = \frac{\partial s}{\partial t} + s \cancelto{0}{(\nabla_3 \cdot \boldsymbol{u}_3)} + \boldsymbol{u}_3 \cdot (\nabla_3 s) \tag{9}$$

$$\implies \frac{\partial s}{\partial t} + \boldsymbol{u}_3 \cdot (\nabla_3 s) = \nabla_3 \cdot (D_s \nabla_3 s) \tag{10}$$

such that we end up with

$$\nabla_3 \cdot \boldsymbol{u}_3 = 0 \tag{11}$$

$$\frac{\partial \boldsymbol{u}_3^T}{\partial t} + (\boldsymbol{u}_3 \cdot \nabla_3)\boldsymbol{u}_3^T = (\nu \Delta_3 \boldsymbol{u}_3)\boldsymbol{I}_3^T - \frac{1}{\rho}(\nabla_3 p)^T + \boldsymbol{g}^T, \tag{12}$$

$$\frac{\partial s}{\partial t} + \boldsymbol{u}_3 \cdot (\nabla_3 s) = \nabla_3 \cdot (D_s \nabla_3 s), \tag{13}$$

$$\rho(s) = \rho_0(1 + \beta s) \tag{14}$$

2DV system

Next, we will assume no flow ($v = 0$) and no variation ($\partial/\partial y = 0$) in the lateral direction. This leads to a two-dimensional (2DV) model where we use the definition $\boldsymbol{u} = (u, w)$ in $\boldsymbol{x} = (x, z)$-direction respectively. Also the nabla operator now equals $\nabla = (\partial/\partial x, \partial/\partial z)$, with Laplacian $\Delta = \nabla \cdot \nabla$ and salinity described by $s(\boldsymbol{x}, t)$. This results in the two-dimensional equations

$$\nabla \cdot \boldsymbol{u} = 0 \tag{15a}$$

$$\frac{\partial u}{\partial t} + (\boldsymbol{u} \cdot \nabla)u = \nu \Delta u - \frac{1}{\rho}\frac{\partial p}{\partial x}, \tag{15b}$$

$$\frac{\partial w}{\partial t} + (\boldsymbol{u} \cdot \nabla)w = \nu \Delta w - \frac{1}{\rho}\frac{\partial p}{\partial z} - g \tag{15c}$$

$$\frac{\partial s}{\partial t} + (\boldsymbol{u} \cdot \nabla)s = \nabla \cdot (D_s \nabla s), \tag{15d}$$

$$\rho = \rho(s), \tag{15e}$$

with variables u, w, s, ρ, p now acting in $(\boldsymbol{x}, t)$ only. Instead of fully resolving these equations, we apply Reynolds-averaging, introducing eddy viscosity and -diffusivity in the equations to model the turbulent effects. Next to this, we use the Boussinesq approximation and assume that density differences are only implemented as a buoyancy term and not in viscous effects, and small changes in density (i.e. $\rho/\rho_0 \approx 1$) are neglected. Lastly, we apply the shallow water approximation, meaning that the vertical momentum equation reduces to the pressure equation

$$\frac{1}{\rho}\frac{\partial p}{\partial z} - g = 0,$$

which can be solved explicitly by integrating from the free surface. Here we assume $p(x, \eta, t) = p_{\text{atm}}$, such that

$$p(x, z, t) = p_{\text{atm}} + \int_z^{\eta} g\rho d\tilde{z}.$$

In turn, the pressure gradient in the horizontal momentum equation is equal to

$$\frac{1}{\rho}\frac{\partial p}{\partial x} = \frac{1}{\rho}\frac{\partial}{\partial x}\int_z^{\eta(x)} g\rho d\tilde{z} = g\frac{\rho(\eta)}{\rho}\frac{\partial \eta}{\partial x} + \frac{1}{\rho}\int_z^{\eta(x)} g\frac{\partial \rho}{\partial x}d\tilde{z} = g\frac{\rho(\eta)}{\rho}\frac{\partial \eta}{\partial x} + \frac{\rho_0}{\rho}g\beta\int_z^{\eta(x)}\frac{\partial s}{\partial x}d\tilde{z} \tag{16}$$

$$\approx g\frac{\partial \eta}{\partial x} + g\beta\int_z^{\eta(x)}\frac{\partial s}{\partial x}d\tilde{z} \tag{17}$$

where we use Leibniz's rule of integration, the Boussinesq approximation and the equation of state (Equation 14). Finally, the flow is modelled by the width-averaged (2DV) shallow-water equations

$$\nabla \cdot \boldsymbol{u} = 0 \tag{18}$$

$$\frac{\partial u}{\partial t} + (\boldsymbol{u} \cdot \nabla)u = \nabla \cdot (A\nabla \boldsymbol{u}) - g\frac{\partial \eta}{\partial x} - g\beta\int_z^{\eta(x)}\frac{\partial s}{\partial x}d\tilde{z} \tag{19}$$

$$\frac{\partial s}{\partial t} + (\boldsymbol{u} \cdot \nabla)s = \nabla \cdot (K\nabla s), \tag{20}$$

where the diagonal matrices A and K contain the horizontal and vertical eddy viscosity and -diffusivity respectively, with

$$A := diag(A_h, A_v), \quad K := diag(K_h, K_v).$$

The term $g\partial\eta/\partial x$ describes the barotropic pressure gradient and the salinity-induced baroclinic pressure gradient by $g\beta\int_z^{\eta(x)}\frac{\partial s}{\partial x}d\tilde{z}$. Here, g denotes the gravitational acceleration, and β the contraction coefficient in ppt^{-1}.

A.1.2 Parameters to Characterise Stability of Stratification

Stratification, and the stability of stratification (the resistance for a fluid to mix vertically), can be characterised using several parameters which we will describe in this section. Firstly, the **Brunt-Väisälä frequency** N (also known as the buoyancy frequency or the Brunt-Väisälä parameter) is a measure of the stability of a fluid stratification to vertical displacements such as those caused by advection, and defined as

$$N^2(t) = -\frac{g}{\rho_0}\frac{\partial \rho}{\partial z}.$$

It is referred to as a frequency, as this equals the frequency at which a vertically displaced parcel will oscillate within a statically stable fluid with vertical density profile $\rho(z)$. When it is displaced by a small perturbation $\tilde{z}$ on a background density ρ_0, the additional gravitational force on the parcel equals

$$\rho_0\frac{\partial^2 \tilde{z}}{\partial t^2} = -g(\rho(z) - \rho(z + \tilde{z})).$$

Taking $\tilde{z}$ very small, this approximates to the second-order differential equation

$$\frac{\partial^2 \tilde{z}}{\partial t^2} = \frac{g}{\rho_0}\frac{\partial \rho(z)}{\partial z}\tilde{z}$$

with solution

$$\tilde{z} = \tilde{z}_0 \exp(iNt)$$

For negative vertical density gradients ($N^2 \geq 0$), the displacement solution $\tilde{z}$ will oscillate with frequency N (and eventually stabilize by friction). If instead, density increases with height ($N^2 < 0$), there is exponential growth of displacement $\tilde{z}$ and the stratification in the fluid is unstable.

The previous parameter describes the static fluid situation. Vertical turbulent mixing might break the stable stratification. This dynamic stability of stratification is described by the **gradient Richardson number**, defined as

$$\mathrm{Ri}_g = -\frac{g\dfrac{\partial \rho}{\partial z}}{\rho_0 \left(\dfrac{\partial u}{\partial z}\right)^2} = \frac{N^2}{S^2}.$$

It relates stratification (as a measure of N^2) to the degree of turbulent mixing $S^2 = \left(\frac{\partial u}{\partial z}\right)^2$. The critical gradient Richardson number Ri_c appears in literature as a linear stability threshold of steady, two-dimensional, stably-stratified, horizontal shear flows of an ideal Boussinesq fluid. This analysis suggests that these stratified flows are stable if $\mathrm{Ri} > \mathrm{Ri}_c = 1/4$. However, measurements show that highly turbulent flows can remain stable for increasing Ri above 1. Moreover, hysteresis of the system can alter results, and the value of Ri_c ranges from 0.2 to 1 in literature. Galperin et al. (2007) therefore argue that Ri as a criterion of turbulence extinction is ill-advised and should be avoided. Therefore, we use the Richardson number merely as an indicator of flow stability and not as a strict criterion.

Lastly, the **densimetric Froude number** is often used in the context of the Boussinesq approximation, where

$$\mathrm{Fr}_d = \frac{u}{\sqrt{g'H}}, \quad g' = g\frac{\rho_0 - \rho}{\rho_0},$$

with reduced gravity g' and indicates the relative strength of the exchange flow due to gravity. The leading edge of a gravity current moves with a front Froude number of about unity. Laboratory experiments have shown that the potential for a salt wedge to form increases for a densimetric Froude number less than 1.

All in all, we consider the stratification in the estuary to be stable if $N^2 \geq 0$ with $\mathrm{Ri} > 1/4$ an additional indication that turbulence does not break stability. The relation of stratification and location of $\mathrm{Fr}_d = 1$ will be investigated to determine a possible salt wedge.

A.1.3 Influence of Sand Dunes on Vertical Flow

The influence of sand dunes on the flow can be investigated for a simplified setting without stratification. To do so, we assume the system to be in a steady state with a uniform vertical displacement of the free surface ($\eta(x) = \text{const}$), no bed shear stress ($\tau_b = 0$ free slip) and neglect the influence of salt. In that case, we solve the divergence-free equation (2.2a) with boundary conditions (3.8) and (3.11a) (with $\tau_b = 0$).

Integrating $\nabla \cdot \boldsymbol{u} = 0$ from the bed to height z results in

$$\begin{aligned}
0 &= \int_{z_b}^{z} \nabla \cdot \boldsymbol{u} d\tilde{z} = \int_{z_b}^{z} \frac{\partial u}{\partial x} + \frac{\partial w}{\partial z} d\tilde{z} \\
&= \frac{\partial}{\partial x} \int_{z_b}^{z} u d\tilde{z} + \left[u \frac{\partial(-H)}{\partial x} \right]_{\tilde{z}=z_b} + [w]_{\tilde{z}=z} - [w]_{\tilde{z}=z_b} \\
&= \frac{\partial}{\partial x} \int_{z_b}^{z} u(x,z) d\tilde{z} - \left[w - u \frac{\partial h_d}{\partial x} \right]_{\tilde{z}=z_b} + w(x,z) \\
&= \frac{\partial}{\partial x} \int_{z_b}^{z} u(x,z) d\tilde{z} + w(x,z)
\end{aligned}$$

Now evaluating this at $z = \eta$ shows that we have a horizontal uniform depth-averaged flow of

$$\overline{u} = \frac{1}{H} \int_{z_b}^{\eta} u dz = \frac{q_r}{H}.$$

over the sand dunes. To illustrate the effects of dunes on the vertical flow structure, we actually assume that the horizontal flow is uniform over depth with $u = q_r/H$, which satisfies boundary conditions (3.11a) and (3.9). Using that $z_b(x) = \eta - H(x)$, we obtain

$$w(x,z) = -\frac{\partial}{\partial x} \int_{z_b}^{z} \frac{q_r}{H} d\tilde{z} = -\frac{\partial}{\partial x} q_r \left(\frac{z - z_b(x)}{H(x)} \right) = -\frac{\partial}{\partial x} q_r \left(\frac{z - \eta}{H(x)} + 1 \right) = \frac{q_r}{H} \frac{\partial H}{\partial x} \frac{z - \eta}{H} \tag{21}$$

$$= -\frac{q_r}{H} \frac{\partial h_d}{\partial x} \frac{z - \eta}{H}. \tag{22}$$

This implies that the bathymetry introduces a linear profile from the bed to the free surface, that scales with the depth-averaged longitudinal velocity $\overline{u}$ (proportional to local depth H) and the local bed level slope $\partial h_d/\partial x$. An example of this is shown in Figure A.1.

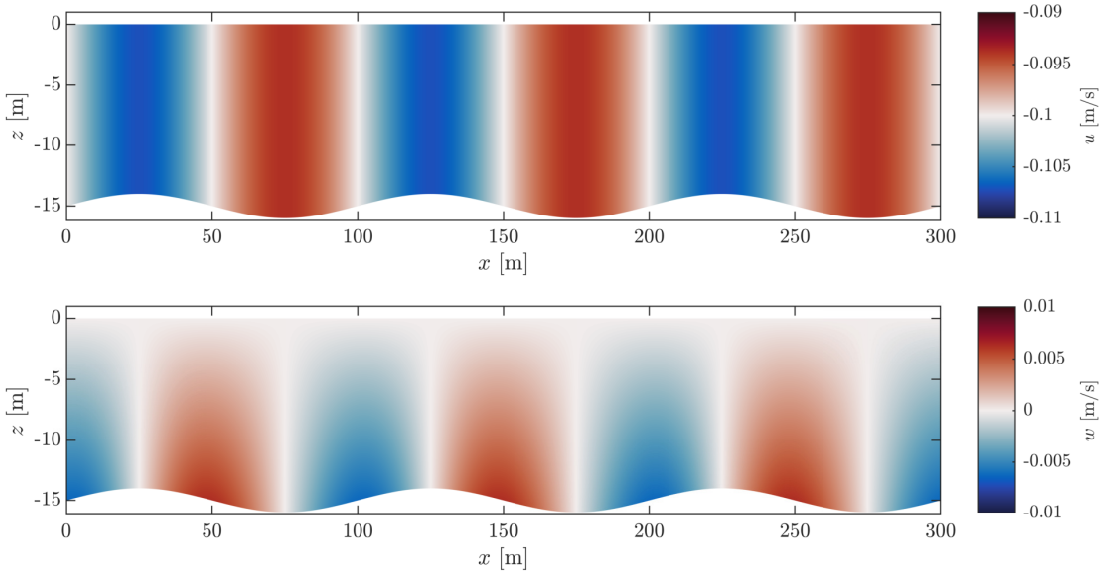

Figure A.1: Example of the vertical flow velocity over a sinusoidal topography with free surface $\eta = 0$ without stratification for a sinusoidal topography with length $\lambda_d = 100$ m and height $H_d = 1.0$ m with a background discharge of $q_r = 1.5$ m^2/s, resulting in a maximum vertical velocity of 0.31 cm/s.

A.1.4 Salt flux decomposition

The transport of salt can be quantified using the salt flux. In the transport equation, we can write

$$(\boldsymbol{u}\cdot\nabla)s - \nabla\cdot(K\nabla s) = \nabla\cdot(\boldsymbol{u}s) - s\cancelto{0}{(\nabla\cdot\boldsymbol{u})} - \nabla\cdot(K\nabla s) = \nabla\cdot(\boldsymbol{u}s - K\nabla s).$$

Hence, the overall transport equation can be written as

$$\frac{\partial s}{\partial t} + \nabla\cdot\boldsymbol{\Phi} = 0, \tag{23}$$

where

$$\boldsymbol{\Phi} = \begin{pmatrix}\Phi_h\\ \Phi_v\end{pmatrix} := \begin{pmatrix} us - K_h\dfrac{\partial s}{\partial x}\\ ws - K_z\dfrac{\partial s}{\partial z}\end{pmatrix}, \tag{24}$$

is the overall salt flux in horizontal and vertical direction respectively, containing both an advective and dispersive component. To unravel which processes contribute to the overall salt transport in the estuary, we can decompose the salt flux. As stated in Section 1.3, the salt intrusion length is a result of a balance of inflowing and outflowing fluxes. Therefore, we are mainly interested in the horizontal transport of salt. Therefore, we define the horizontal estuarine salt transport as

$$Q_h(x) = \langle H(x,t)\overline{\Phi_h}\rangle = \left\langle \int_{z_b}^{\eta} us - K_h\frac{\partial s}{\partial x}dz \right\rangle, \tag{25}$$

This horizontal transport can be decomposed into different contributions. Due to the free surface, the averaging operators $\overline{\psi}$ and $\langle\psi\rangle$ are not commutative, and the salt flux decomposition is structured differently than Dijkstra et al. (2022). First, we write the velocity and salinity as a depth-averaged, and depth-varying part, with

$$u(x,z,t) = \overline{u}(x,t) + u'(x,z,t) \tag{26}$$
$$s(x,z,t) = \overline{s}(x,t) + s'(x,z,t) \tag{27}$$

using Equation 2.4, such that

$$\int_{z_b}^{\eta} u'(x,z,t)dz = \int_{z_b}^{\eta} u(x,z,t) - \overline{u}(x,t)dz = H\frac{1}{H}\int_{z_b}^{\eta} u(x,z,t)dz - H\overline{u}(x,t) = 0 \tag{28}$$

Subsequently, the depth-averaged value can be decomposed into a subtidal part and a tidally varying part, resulting in

$$u(x,z,t) = \overline{u}_0(x) + \overline{u}_t(x,t) + u'(x,z,t), \tag{29}$$
$$s(x,z,t) = \overline{s}_0(x) + \overline{s}_t(x,t) + s'(x,z,t), \tag{30}$$

using $\overline{u}_0 = \langle\overline{u}\rangle$ and $\overline{u}_t = \overline{u} - \overline{u}_0$ and equally $\langle\overline{u}_t\rangle = 0$. In that case, the horizontal depth-averaged advective salt transport (as defined in Subsection 2.2.3) decomposes into

$$Q_u = \left\langle \int_{z_b}^{\eta} (\overline{u}_0(x) + \overline{u}_t(x,t) + u'(x,z,t))(\overline{s}_0(x) + \overline{s}_t(x,t) + s'(x,z,t))dz \right\rangle$$

$$
\begin{aligned}
=&\Big\langle \int_{z_b}^{\eta(t)} \overline{u}_0(x)(\overline{s}_0(x) + \overline{s}_t(x,t) + s'(x,z,t)) \\
&\quad + \overline{u}_t(x,t)(\overline{s}_0(x) + \overline{s}_t(x,t) + s'(x,z,t)) \\
&\quad + u'(x,z,t)(\overline{s}_0(x) + \overline{s}_t(x,t) + s'(x,z,t))dz \Big\rangle \\
=&\Big\langle \overline{u}_0(x) \left(H(x,t)\overline{s}_0(x) + H(x,t)\overline{s}_t(x,t) + \cancelto{0}{\int_{z_b}^{\eta(t)} s'(x,z,t)dz} \right) \\
&\quad + \overline{u}_t(x,t) \left(H(x,t)\overline{s}_0(x) + H(x,t)\overline{s}_t(x,t) + \cancelto{0}{\int_{z_b}^{\eta(t)} s'(x,z,t)dz} \right) \\
&\quad + (H(x,t)\overline{s}_0(x) + H(x,t)\overline{s}_t(x,t)) \cancelto{0}{\int_{z_b}^{\eta(t)} u'(x,z,t)dz} + \int_{z_b}^{\eta(t)} u'(x,z,t)s'(x,z,t)dz \Big\rangle \\
=&\overline{u}_0(x)\Big\langle H(x,t)\overline{s}_0(x) + H(x,t)\overline{s}_t(x,t) \Big\rangle \\
&\quad + \Big\langle \overline{u}_t(x,t)\left(H(x,t)\overline{s}_0(x) + H(x,t)\overline{s}_t(x,t)\right) \\
&\qquad + \int_{z_b}^{\eta(t)} u'(x,z,t)s'(x,z,t)dz \Big\rangle \\
=&\overline{u}_0(x)\overline{s}_0(x)\langle H(x,t)\rangle + \overline{u}_0(x)\langle H(x,t)\overline{s}_t(x,t)\rangle + \overline{s}_0(x)\langle \overline{u}_t(x,t)H(x,t)\rangle + \langle H(x,t)\overline{u}_t(x,t)\overline{s}_t(x,t)\rangle \\
&\quad + \langle H(x,t)\overline{u'(x,z,t)s'(x,z,t)}\rangle \\
=&\overline{u}_0\overline{s}_0\langle H\rangle + (\overline{u}_0\langle H\overline{s}_t\rangle + \overline{s}_0\langle H\overline{u}_t\rangle) + \langle H\overline{u}_t\overline{s}_t\rangle + \langle H\overline{u's'}\rangle,
\end{aligned}
$$

which is the result provided in Subsection 2.2.3. Note that $\overline{u}_0\langle H\overline{s}_t\rangle + \overline{s}_0\langle H\overline{u}_t\rangle$ is usually very small. A similar analysis can be done for the decomposition of the vertical advective term, in which case the instantaneous water depth H is neglected. The decomposition is easily found by replacing u with w and replacing H with 1 in the above derivation, resulting in

$$
\begin{aligned}
T_w &= \overline{w}_0\overline{s}_0 + \overline{w}_0\cancelto{0}{\langle\overline{s}_t\rangle} + \overline{s}_0\cancelto{0}{\langle\overline{w}_t\rangle} + \langle\overline{w}_t\overline{s}_t\rangle + \langle\overline{w's'}\rangle && (31)\\
&= \overline{w}_0\overline{s}_0 + \langle\overline{w}_t\overline{s}_t\rangle + \langle\overline{w's'}\rangle && (32)
\end{aligned}
$$

as given in Equation 2.23

A.1.5 Non-Dimensionalisation of Flow and Transport Equations

We analyse the flow and transport equations theoretically using non-dimensionalisation of the system. This shows the relative importance of certain processes and enables a reduction in the apparent total number of free variables. We assume spatially uniform eddy viscosity and -diffusivity, in which case the system (2.2) can be non-dimensionalised using

$$
\begin{aligned}
\boldsymbol{x} &= (Lx^*, hz^*) & t &= \mathcal{T}t^* \\
\boldsymbol{u} &= (Uu^*, Ww^*) & \eta &= \tfrac{U^2}{g}\eta^* \\
\nabla &= \left(\frac{1}{L}\frac{\partial}{\partial x^*}, \frac{1}{h}\frac{\partial}{\partial z^*}\right) & s &= s_{sea}s^*
\end{aligned}
\qquad (33)
$$

where variables with an asterisk denote the non-dimensional formulation. Applying this to the divergence-free condition (Equation 2.2a) results in

$$\frac{U}{L}\frac{\partial u^*}{\partial x^*}+\frac{W}{h}\frac{\partial w^*}{\partial z^*}=0 \quad \Longrightarrow \quad \frac{\partial u^*}{\partial x^*}+\frac{\partial w^*}{\partial z^*}=0,$$

where we introduce the vertical velocity scale $W=\frac{Uh}{L}$. The horizontal momentum equation and salt transport equation are equal to

$$\frac{1}{\mathcal{T}}\frac{\partial u^*}{\partial t^*}+\frac{U}{L}u^*\frac{\partial u^*}{\partial x^*}+\frac{U}{L}w^*\frac{\partial u^*}{\partial z^*}=\frac{A_h}{L^2}\frac{\partial^2 u^*}{\partial x^{*2}}+\frac{A_v}{g^2}\frac{\partial^2 u^*}{\partial z^{*2}}-\frac{U}{L}\frac{\partial \eta^*}{\partial x^*}-\frac{g\beta s_{sea}h}{LU}\int_{z^*}^{\eta^*}\frac{\partial s^*}{\partial x^*}d\tilde{z}^*, \tag{34}$$

$$\frac{1}{\mathcal{T}}\frac{\partial s^*}{\partial t^*}+\frac{U}{L}u^*\frac{\partial s^*}{\partial x^*}+\frac{U}{L}w^*\frac{\partial s^*}{\partial z^*}=\frac{K_h}{L^2}\frac{\partial^2 s^*}{\partial x^{*2}}+\frac{K_v}{h^2}\frac{\partial^2 s^*}{\partial z^{*2}}. \tag{35}$$

after division of U and s_{sea} respectively. We use the characteristic flushing time of the system $\mathcal{T}=L/U$, for background river flow $U=|U_r|=|-q_r/H|$, resulting in

$$\frac{\partial u^*}{\partial t^*}+u^*\frac{\partial u^*}{\partial x^*}+w^*\frac{\partial u^*}{\partial z^*}=\frac{A_h}{LU}\frac{\partial^2 u^*}{\partial x^{*2}}+\frac{A_vL}{h^2U}\frac{\partial^2 u^*}{\partial z^{*2}}-\frac{\partial \eta^*}{\partial x^*}-\frac{c^2}{U^2}\int_{z^*}^{\eta^*}\frac{\partial s^*}{\partial x^*}d\tilde{z}^*, \tag{36}$$

$$\frac{\partial s^*}{\partial t^*}+u^*\frac{\partial s^*}{\partial x^*}+w^*\frac{\partial s^*}{\partial z^*}=\frac{K_h}{LU}\frac{\partial^2 s^*}{\partial x^{*2}}+\frac{K_vL}{h^2U}\frac{\partial^2 s^*}{\partial z^{*2}}, \tag{37}$$

where $c=\sqrt{g\beta s_{sea}h}$ twice the celerity of the fastest internal wave (MacCready & Geyer, 2010). Here, βs_{sea} is the mass density difference between salt and fresh water. We next define the estuarine non-dimensional numbers relative to the flushing time. The **estuarine Froude number** equals

$$\mathrm{Fr}_r:=\frac{U}{c}, \tag{38}$$

and is the ratio of the cross-sectionally averaged longitudinal flow velocity U and the celerity of the fastest internal wave c. The **estuarine Stokes number** is the ratio of a time scale for the water column to fully mix by dispersion and the flushing time scale, equal to

$$\mathrm{St}:=\frac{A_v}{h^2}\mathcal{T}=\frac{A_vL}{h^2U}. \tag{39}$$

Finally, we define the **horizontal turbulent Reynolds** number as

$$\mathrm{Re}_h:=\frac{LU}{A_h}.$$

Using these non-dimensional quantities, the system reduces to

$$\frac{\partial u^*}{\partial t^*}+u^*\frac{\partial u^*}{\partial x^*}+w^*\frac{\partial u^*}{\partial z^*}=\frac{1}{\mathrm{Re}_h}\frac{\partial^2 u^*}{\partial x^{*2}}+\mathrm{St}\frac{\partial^2 u^*}{\partial z^{*2}}-\frac{\partial \eta^*}{\partial x^*}-\frac{1}{\mathrm{Fr}_r^2}\int_{z^*}^{\eta^*}\frac{\partial s^*}{\partial x^*}d\tilde{z}^*, \tag{40}$$

$$\frac{\partial s^*}{\partial t^*}+u^*\frac{\partial s^*}{\partial x^*}+w^*\frac{\partial s^*}{\partial z^*}=\frac{1}{\sigma_\rho}\left(\frac{1}{\mathrm{Re}_h}\frac{\partial^2 s^*}{\partial x^{*2}}+\mathrm{St}\frac{\partial^2 s^*}{\partial z^{*2}}\right). \tag{41}$$

For the RWW, we approximate the typical values by $L=20$ km, $U=0.1$ m/s, $A_v=10^{-3}$ m^2/s, and $A_h=10$ m^2/s. For a mean water depth of $h=15$ m, $g=9.81$ m/s^2 and $s_{sea}=35$ ppt, we have an internal wave celerity of $c=1.978$ m/s. This results in $1/\mathrm{Fr}_r^2=\mathcal{O}(10^2)$, $\mathrm{St}=\mathcal{O}(10^{-1})$, and $1/\mathrm{Re}_h=\mathcal{O}(10^{-2})$, which indicates the strong contribution of the baroclinic pressure gradient and shows how the vertical processes dominate the horizontal.

A.1.6 Classification of Geyer and MacCready (2014)

Geyer and MacCready (2014) argue that the classification of an estuary can be based on the amount of freshwater flushing and amount of saltwater mixing. This is based on the **freshwater Froude number**

$$\mathrm{Fr}_r = \frac{U_r}{c}$$

for the depth-averaged river velocity U_r, and the **mixing parameter**

$$M = \sqrt{\frac{c_D U_t^2}{\omega N_0 h^2}},$$

which captures the tidal dynamics and the vertical mixing induced by bed roughness by the tidal velocity U_t. This tidal velocity can be approximated by

$$U_t = \frac{1}{2\sqrt{2}}\sqrt{\frac{g}{h}}A_t,$$

for tidal elevation amplitude A_t (Hendrickx et al., 2023b). The buoyancy frequency for maximum top-to-bottom salinity variation equals

$$N_0 = \sqrt{\frac{g\beta s_{\mathrm{sea}}}{h}},$$

and non-dimensional roughness coefficient $c_D \approx (1-2.5)\cdot 10^{-3}$ (Geyer & MacCready, 2014). Hendrickx et al. (2023b) notes that this parameter is related to Mannings' coefficient n by

$$c_D = \frac{gn^2}{h^{1/3}}$$

Subsequently, in Delft3D-FLOW, this Mannings' coefficient is related to the roughness height z_0 by

$$n = \frac{\kappa h^{1/6}}{\sqrt{g}}\left(\ln\left(1+\frac{h}{ez_0}\right)\right)^{-1},$$

such that an estimation of these parameters based on Delft3D-FLOW model development can be given. However, we note that this is provides only a rough estimate, as the analytic expression of U_t is not accurate compared to model output (difference of factor 2).

A.1.7 Non-Dimensionalisation of Dijkstra et al. (2022)

Dijkstra et al. (2022) classify narrow estuaries locally based on the dominant transport mechanisms semi-analytically, using internal mixing parameters (such as A_h and K_v). Their classification is highlighted in this section, as it provides the basis for choosing suitable eddy parameters during model development.

In the non-dimensionalisation as presented before, the characteristic time $\mathcal{T}$ of the system is chosen as the main M_2 tidal forcing with angular frequency ω, i.e. $\mathcal{T} = 1/\omega$. This means, for spatially uniform eddy viscosity and -diffusivity, that the conservation of momentum and salt equal

$$\frac{\partial u^*}{\partial t^*} + \frac{U}{L\omega}u^*\frac{\partial u^*}{\partial x^*} + \frac{U}{L\omega}w^*\frac{\partial u^*}{\partial z^*} = \frac{A_h}{L^2\omega}\frac{\partial^2 u^*}{\partial x^{*2}} + \frac{A_v}{h^2\omega}\frac{\partial^2 u^*}{\partial z^{*2}} - \frac{U}{L\omega}\frac{\partial \eta^*}{\partial x^*} - \frac{g\beta s_{sea}h}{LU\omega}\int_{z^*}^{\eta^*}\frac{\partial s^*}{\partial x^*}d\tilde{z}^*, \tag{42}$$

$$\frac{\partial s^*}{\partial t^*} + \frac{U}{L\omega}u^*\frac{\partial s^*}{\partial x^*} + \frac{U}{L\omega}w^*\frac{\partial s^*}{\partial z^*} = \frac{K_h}{L^2\omega}\frac{\partial^2 s^*}{\partial x^{*2}} + \frac{K_v}{h^2\omega}\frac{\partial^2 s^*}{\partial z^{*2}}. \tag{43}$$

Next to the estuarine Froude number, we introduce the **estuarine Rayleigh number**, which is the reciprocal of mixing by

$$\mathrm{Ra} := \frac{h^2 c^2}{A_v K_h}, \tag{44}$$

and relates the internal waves through the channel to the vertical eddy viscosity A_v and horizontal eddy diffusivity K_h. The **tidal Stokes number** is now the ratio of a time scale for the water column to fully mix and the tidal time scale, and equals

$$\mathrm{St}_t := \frac{A_v}{h^2}\mathcal{T} = \frac{A_v}{\omega h^2} \tag{45}$$

for the angular frequency of the tide ω. In turn, we have that

$$\mathrm{St}_t\ \mathrm{Ra} = \frac{c^2}{K_h \omega}, \tag{46}$$

meaning that St_t Ra is a measure of the horizontal wave convection, tides and horizontal diffusion, i.e. mainly a measure of horizontal effects.

Note that the length L still appears in the equations but not in Equations (44) to (46), meaning it will not disappear. Dijkstra et al. (2022) show how the length scale L can be non-dimensionalised itself, but argue that the quantity used for this is unimportant. Using the dispersive length scale K_h/c of horizontal diffusion and internal wave convection as in Dijkstra and Schuttelaars (2021), we non-dimensionalise by

$$\mathcal{L} := L\frac{c}{K_h}. \tag{47}$$

Note that $\mathcal{L}$ is a non-dimensional measure of the salt intrusion as L is proportional to the salt intrusion length. The non-dimensional quantities now characterise the system with

$$\frac{U}{L\omega} = \frac{U}{c}\frac{c}{L\omega} = \frac{U}{c}\frac{c^2}{K_h\omega}\frac{K_h}{cL} = \mathrm{Fr}\ (\mathrm{St}_t\mathrm{Ra})\ \mathcal{L}^{-1} \tag{48}$$

$$\frac{A_h}{L^2\omega} = \frac{K_h\sigma_\rho}{L^2\omega} = \frac{c^2}{K_h\omega}\frac{K_h^2}{L^2c^2}\sigma_\rho^{-1} = (\mathrm{St}_t\mathrm{Ra})\ \mathcal{L}^{-2}\sigma_\rho \tag{49}$$

$$\frac{A_v}{h^2\omega} = \mathrm{St}_t \tag{50}$$

$$\frac{g\beta s_{sea} h}{LU\omega} = \frac{c^2}{LU\omega} = \frac{c}{U}\frac{c}{L\omega} = \mathrm{Fr}^{-1}\ (\mathrm{St}_t\mathrm{Ra})\ \mathcal{L}^{-1} \tag{51}$$

$$\frac{K_h}{L^2\omega} = \frac{c^2}{K_h\omega}\frac{K_h^2}{L^2c^2} = (\mathrm{St}_t\mathrm{Ra})\ \mathcal{L}^{-2} \tag{52}$$

$$\frac{K_v}{h^2\omega} = \mathrm{St}_t\ \sigma_\rho^{-1}. \tag{53}$$

Here, $\mathrm{Fr} = U/c$ is the tidal or riverine Froude (using U_t or $|U_r|$ respectively), and Dijkstra et al. (2022) argue that the precise choice does not influence qualitative outcomes. This results in the non-

dimensional set of equations

$$\frac{\partial u^*}{\partial t^*} + \mathrm{Fr}\ (\mathrm{St}_t\mathrm{Ra})\ \mathcal{L}^{-1}\left(u^*\frac{\partial u^*}{\partial x^*} + w^*\frac{\partial u^*}{\partial z^*}\right) = (\mathrm{St}_t\mathrm{Ra})\ \mathcal{L}^{-2}\sigma_\rho\frac{\partial^2 u^*}{\partial x^{*2}} + \mathrm{St}_t\frac{\partial^2 u^*}{\partial z^{*2}} - \mathrm{Fr}\ (\mathrm{St}_t\mathrm{Ra})\ \mathcal{L}^{-1}\frac{\partial \eta^*}{\partial x^*} - \mathrm{Fr}^{-1}\ (\mathrm{St}_t\mathrm{Ra})\ \mathcal{L}^{-1}\int_{z^*}^{\eta^*}\frac{\partial s^*}{\partial x^*}d\tilde{z}^*, \tag{54}$$

$$\frac{\partial s^*}{\partial t^*} + \mathrm{Fr}\ (\mathrm{St}_t\mathrm{Ra})\ \mathcal{L}^{-1}\left(u^*\frac{\partial s^*}{\partial x^*} + w^*\frac{\partial s^*}{\partial z^*}\right) = (\mathrm{St}_t\mathrm{Ra})\ \mathcal{L}^{-2}\frac{\partial^2 s^*}{\partial x^{*2}} + \mathrm{St}_t\ \sigma_\rho^{-1}\frac{\partial^2 s^*}{\partial z^{*2}}. \tag{55}$$

Again, with increasing Fr (larger flow velocities), the advective processes and the free surface gradient will dominate the flow behaviour and the transport of salt will be dominated by advection. With decreasing Fr, the influence of horizontal salinity gradients will dominate the flow and diffusion will become more important in the salt transport.

A.2 Appendices to Chapter 3

A.2.1 Final Model Equations

$$\frac{\partial \eta}{\partial \tau} + \frac{\partial H\overline{u}}{\partial \xi} = 0 \tag{56}$$

$$\frac{\partial u}{\partial \tau} + u\frac{\partial u}{\partial \xi} + \frac{\vartheta}{H}\frac{\partial u}{\partial \sigma} = \frac{\partial}{\partial \xi}\left(A_h\frac{\partial u}{\partial \xi}\right) + \frac{1}{H^2}\frac{\partial}{\partial \sigma}\left(A_v\frac{\partial u}{\partial \sigma}\right) - g\frac{\partial \eta}{\partial \xi} - \frac{gH}{\rho_0}\int_\sigma^0\frac{\partial \rho}{\partial \xi} + \frac{\partial \rho}{\partial \sigma}\frac{\partial \sigma}{\partial x}d\sigma' \tag{57}$$

$$\frac{\partial k}{\partial \tau} + u\frac{\partial k}{\partial \xi} + \frac{\vartheta}{H}\frac{\partial k}{\partial \sigma} = \frac{1}{H^2}\frac{\partial}{\partial \sigma}\left(D_k\frac{\partial k}{\partial \sigma}\right) + P_k + B_k - \epsilon \tag{58}$$

$$\frac{\partial \epsilon}{\partial \tau} + u\frac{\partial \epsilon}{\partial \xi} + \frac{\vartheta}{H}\frac{\partial \epsilon}{\partial \sigma} = \frac{1}{H^2}\frac{\partial}{\partial \sigma}\left(D_\epsilon\frac{\partial \epsilon}{\partial \sigma}\right) + c_{1\epsilon}\frac{\epsilon}{k}\left(P_k + (1-c_{3\epsilon})B_k - \frac{c_{2\epsilon}}{c_{1\epsilon}}\epsilon\right) \tag{59}$$

$$\frac{\partial Hs}{\partial \tau} + \frac{\partial Hus}{\partial \xi} + \frac{\partial \vartheta s}{\partial \sigma} = \frac{\partial}{\partial \xi}\left(HK_h\frac{\partial s}{\partial \xi}\right) + \frac{1}{H}\frac{\partial}{\partial \sigma}\left(K_v\frac{\partial s}{\partial \sigma}\right) \tag{60}$$

where

$$\rho = \rho_{\mathrm{Eck}}(s) \tag{61}$$

$$\nu_{3D} = c_\mu\frac{k^2}{\epsilon} \tag{62}$$

$$A_v = \nu_{mol} + \max(\nu_{3D}, \nu_v^{BACK}) \tag{63}$$

$$A_h = \nu_{mol} + \max(\nu_{3D}, \nu_v^{BACK}) + \nu_h^{BACK} \tag{64}$$

$$K_v = \frac{\nu_{mol}}{\sigma_{mol}} + \max\left(\frac{\nu_{3D}}{\sigma_\rho}, D_v^{BACK}\right) \tag{65}$$

$$K_h = \frac{\nu_{mol}}{\sigma_{mol}} + \max\left(\frac{\nu_{3D}}{\sigma_\rho}, D_v^{BACK}\right) + D_h^{BACK} \tag{66}$$

$$D_k = \frac{\nu_{mol}}{\sigma_{mol}} + \frac{\nu_{3D}}{\sigma_k} \tag{67}$$

$$D_\epsilon = \frac{\nu_{3D}}{\sigma_\epsilon} \tag{68}$$

The values of the turbulence model constants, the Prandtl-Schmidt numbers and equations for buoyancy and production terms are given in Table A.1.

Table A.1: Turbulence model constants, the Prandtl-Schmidt numbers and equations for buoyancy and production terms.

Constants	Variables
$\sigma_\rho = 0.7$	$P_k = \frac{\nu_{3D}}{H^2}\left(\frac{\partial u}{\partial \sigma}\right)^2$
$\sigma_{mol} = 700$	$B_k = \frac{g}{H\rho}\frac{\nu_{3D}}{\sigma_\rho}\frac{\partial \rho}{\partial \sigma}$
$\sigma_k = 1.00$	
$\sigma_\epsilon = 1.30$	
$c_{1\epsilon} = 1.44$	
$c_{2\epsilon} = 1.92$	
$c_\mu = 0.09$	

A.2.2 Salinity in Delft3D-FLOW

These are the Eckart formulation and the UNESCO formulation as described in Section 9.3.4. in the User Manual (Deltares, 2018). For constant temperature $T = 15$ °C, the difference of each formulation to the equation of state (Equation 1.2) is negligible, with a maximum difference of 0.085 kg/m^3 for $s =$ 12.9 ppt in the Eckart formulation and -0.048 kg/m^3 for $s = 35$ ppt in the UNESCO formulation. With this minimal difference, we consider the influence of equation choice negligible on model output.

A.2.3 Visualisation of the Grid

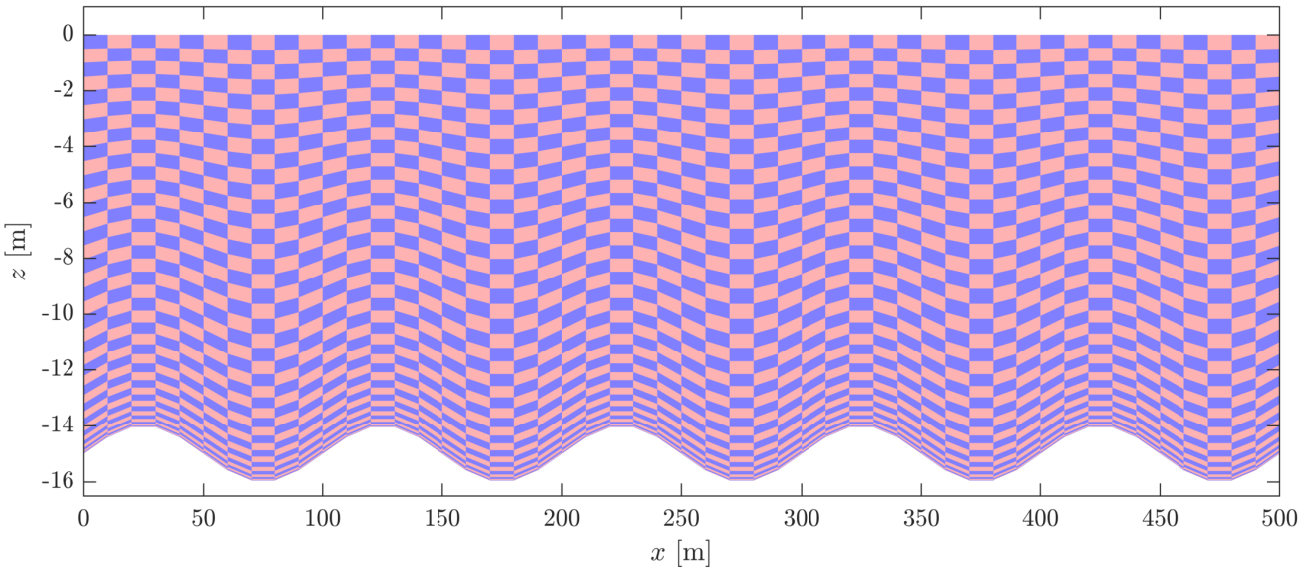

Figure A.2: Visualisation of a grid with $\Delta x = 10$ m and $K = 40$ vertical layers for a topography with symmetric dunes with length $\lambda_d = 100$ m, and $H_d = 2.0$ m.

A.2.4 Motivation of vertical background values

When using the k-ϵ model, the minimum bound ν_v^{BACK} is needed for several reasons:

- To damp out short oscillations generated by boundary conditions. Without it, these short oscillations will only be damped in the bottom layer where turbulence is generated.
- The mixing coefficients computed by turbulence models with shear production reduce to zero in regions of high stratification. In turn, the vertical layers are completely decoupled (frictionless). Disturbances are hardly damped and diffusion is reduced to molecular diffusion only. Background values can aid in keeping separate stratified fluid layers coupled if required.
- In line with the previous point, in regions of high stratification internal waves can form over undulating topography and increase mixing, opposite to the reduction of turbulent mixing. They can transfer potential energy into turbulent kinetic energy and generate vertical mixing of momentum (Wegman, 2021). These internal waves are not modelled by Delft3D-FLOW and require a non-hydrostatic solver (Groenenboom et al., 2019). A background eddy viscosity can model some of the missing dynamics.

Notably, the implementation of vertical background eddy diffusivity and viscosity introduces crucial dynamics into the model. Care must be taken when specifying values for ν_v^{BACK} and D_v^{BACK} in Equations 3.4b and 3.5b, as these parameters can override the impact of salt on turbulent mixing, making ν_{3D} redundant. The value suggested for the background eddy viscosity depends on the application, but must be small compared to the eddy viscosity ν_{3D} calculated by the turbulence closure model. For stratified estuaries and lakes a value of 10^{-4} and 10^{-3} m^2/s is suitable. A value of $\nu_v^{BACK} = 10^{-4}$ m^2/s has been validated for a 3D hydrodynamic model of the Rotterdam Waterway (RWW) and accurately models the vertical exchange of momentum.

A.3 Appendix to Chapter 5: Determining Dynamic Equilibrium of Salt Intrusion Length

In this section, we describe how a state of dynamic equilibrium of L_s with the tide is examined. We do so for simulation runs for the study on dune height in Subsection 5.1.1. In general, it is achieved when $\langle L_s \rangle$ is relatively constant from one tide to the next. More specifically, we evaluate this by

1. determining the salt intrusion length over time $L_s(t)$ using Equation 2.8 (coloured lines in top-left of Figure A.3),
2. determining the tidally-averaged salt intrusion length $\langle L_s \rangle(t)$ over time using equation Equation 2.5 (as a moving mean over multiple tidal cycles, black dashed lines in top-left of Figure A.3),
3. evaluate the change of this length $d\langle L_s \rangle/dt$ numerically (coloured lines in bottom-left of Figure A.3). If $|d\langle L_s \rangle/dt| \leq 2$ m/h, we assume that dynamic equilibrium has been attained.

The above procedure is exemplified in Figure A.3. This figure shows all the steps above, as indicated in the top legend. Dynamic equilibrium has been reached for all instances after 120 hours of simulation time, except for $H_d = 4.5$ m (dashed light-blue line), which is continued for 72 more hours (full light-blue line).

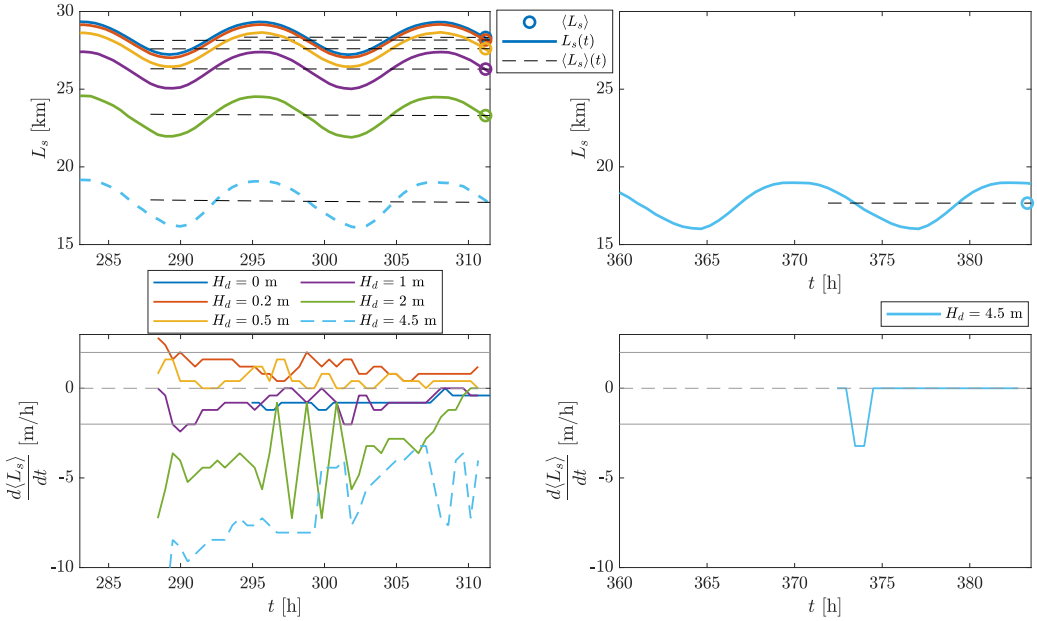

Figure A.3: Top: evolution of salt intrusion length a tidally-averaged value (dotted lines indicating the subtidal value over time, circle marker indicating the final value of $\langle L_s \rangle$ for Figure 5.2). Bottom: Change of tidally averaged salt intrusion length $\langle L_s \rangle$ over the last 20 hours of the simulation. As the simulation of $H_d = 4.5$ m (dotted line) has not reached dynamic equilibrium, and the model to be continued for three more days to generate $\langle L_s \rangle$ for Figure 5.2.

A.4 Snapshots of Model Output

A.4.1 Flood: Salinity and Velocity

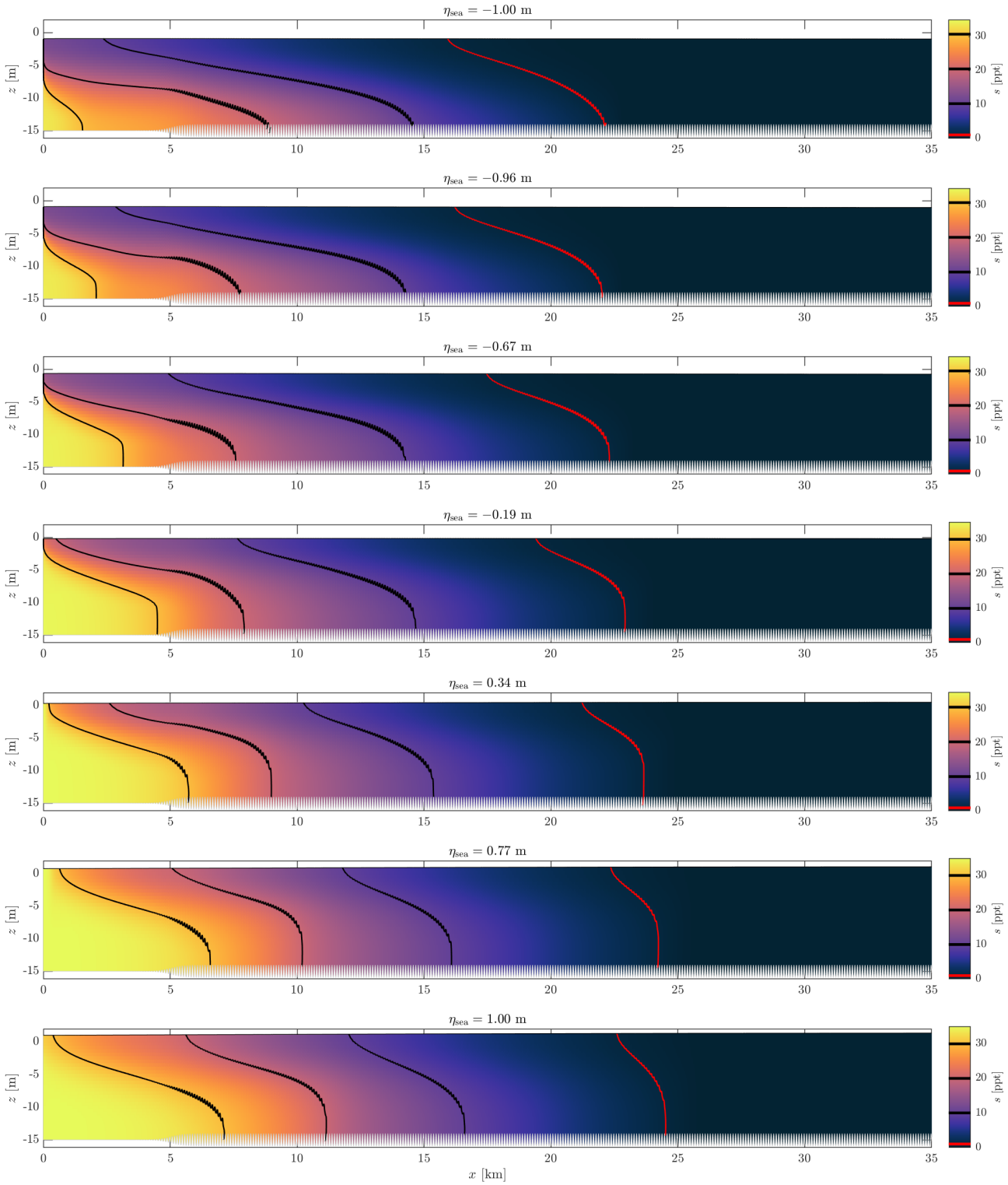

Figure A.4: Snapshots of a simulation of salinity s over the estuary during flood. Red contour indicates critical salinity s_c and black contour lines show increments of 10 ppt.

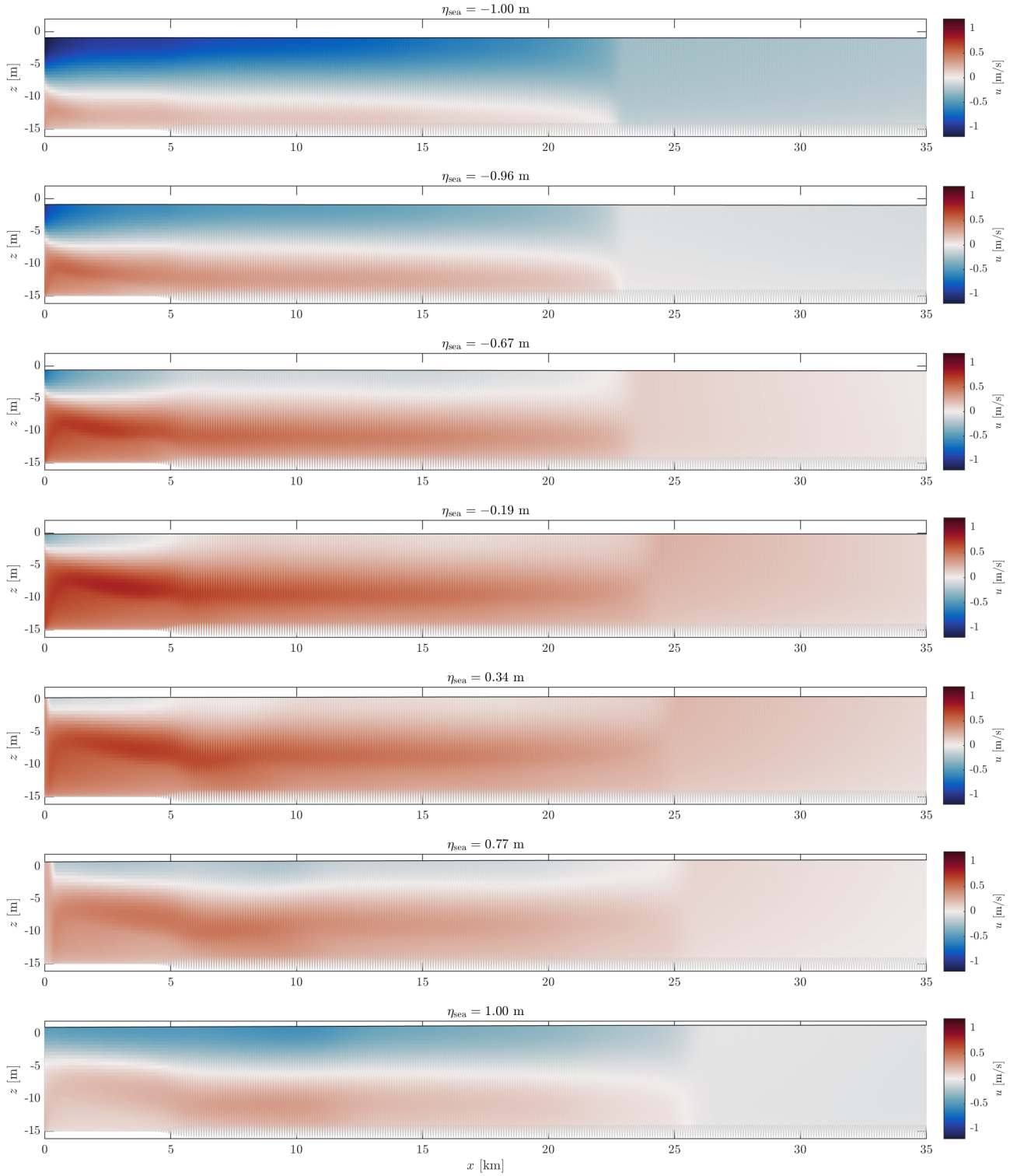

Figure A.5: Snapshots of a simulation of horizontal flow velocity u over the estuary during flood.

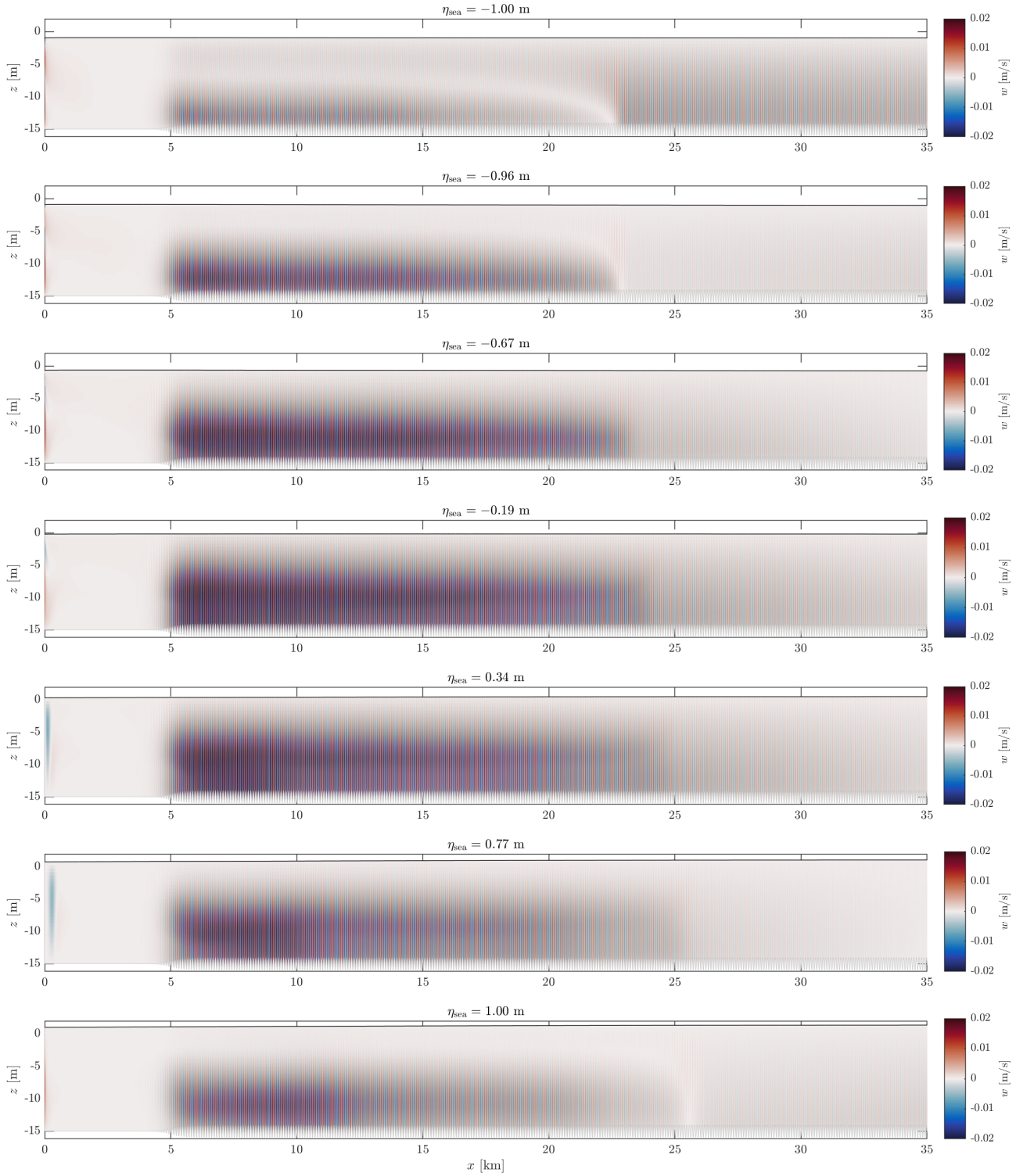

Figure A.6: Snapshots of a simulation of vertical flow velocity w over the estuary during flood.

A.4.2 Flood: Vertical Velocity (Zoomed)

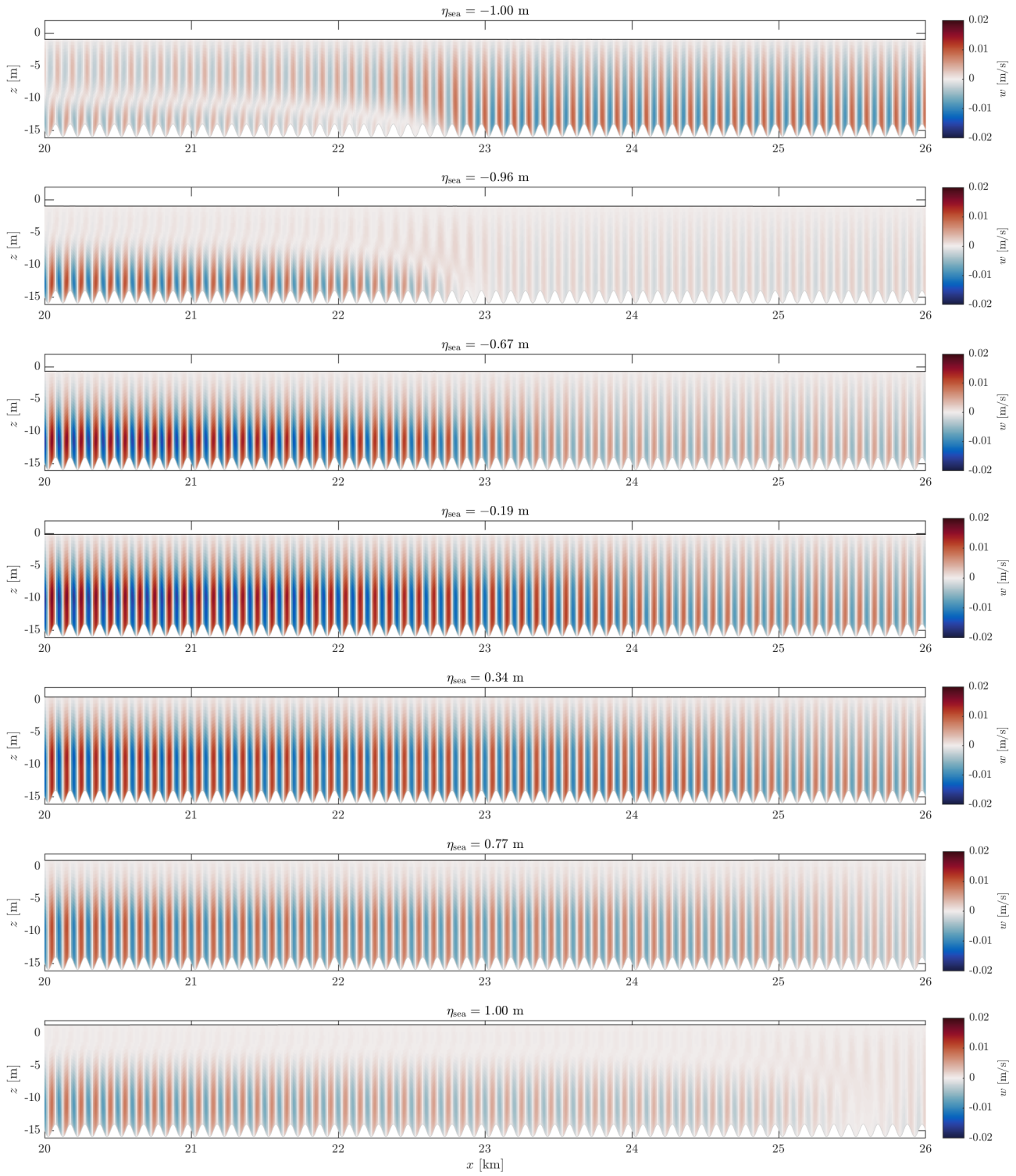

Figure A.7: Snapshots of a simulation of vertical flow velocity w over the estuary during flood, zoomed in.

A.4.3 Ebb: Salinity and Velocity

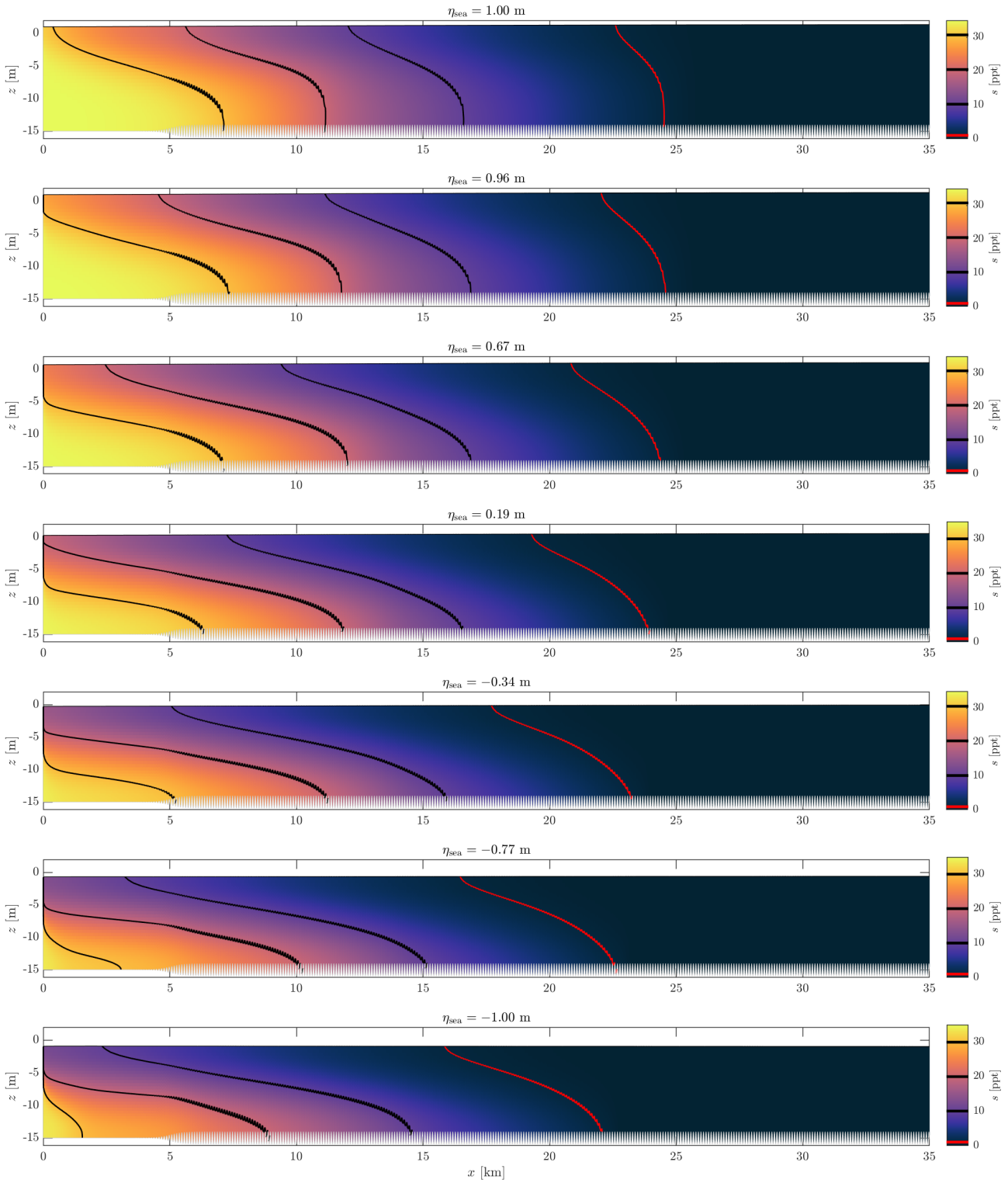

Figure A.8: Snapshots of a simulation of salinity s over the estuary during ebb. Red contour indicates critical salinity s_c and black contour lines show increments of 10 ppt.

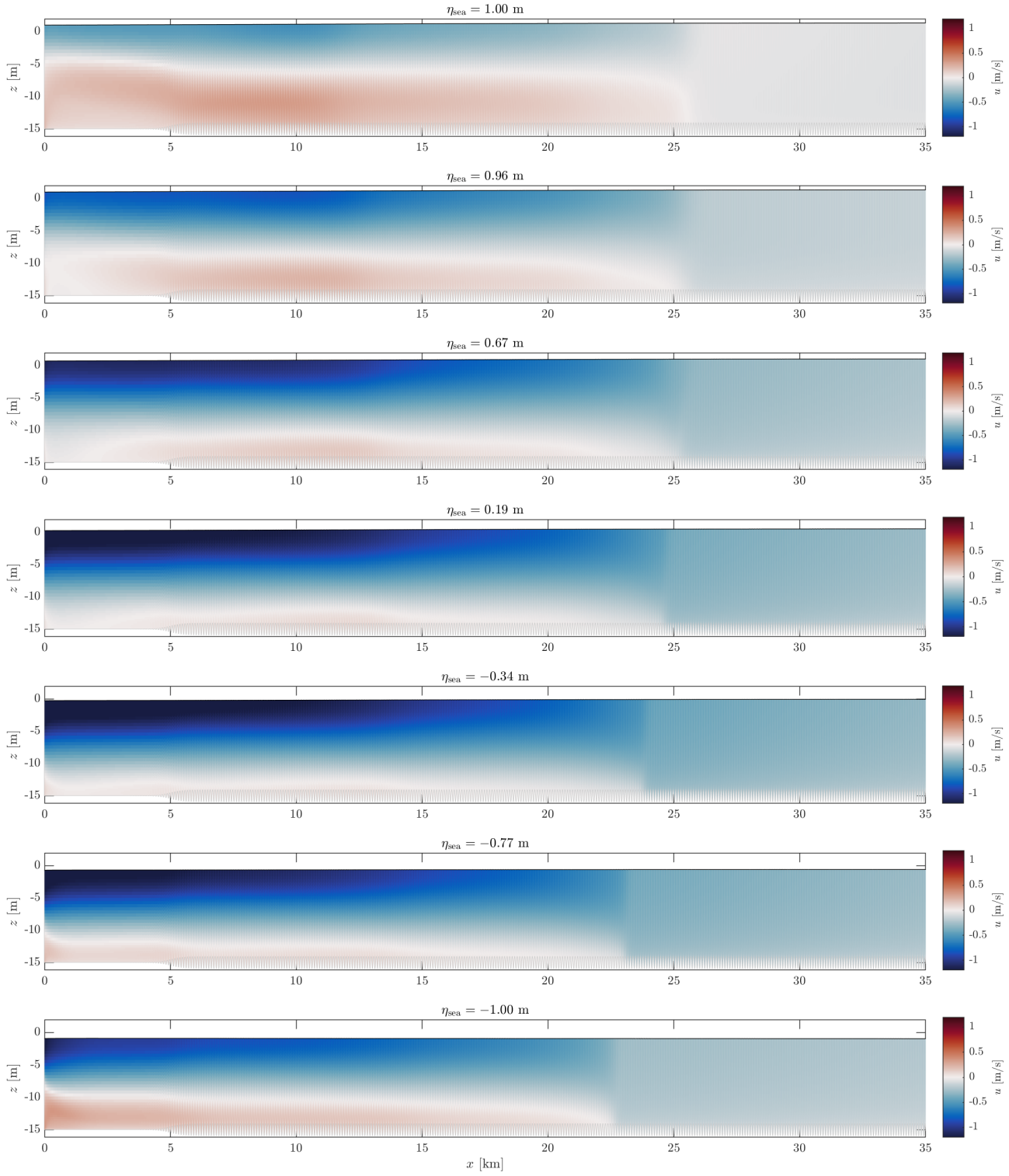

Figure A.9: Snapshots of a simulation of horizontal flow velocity u over the estuary during ebb.

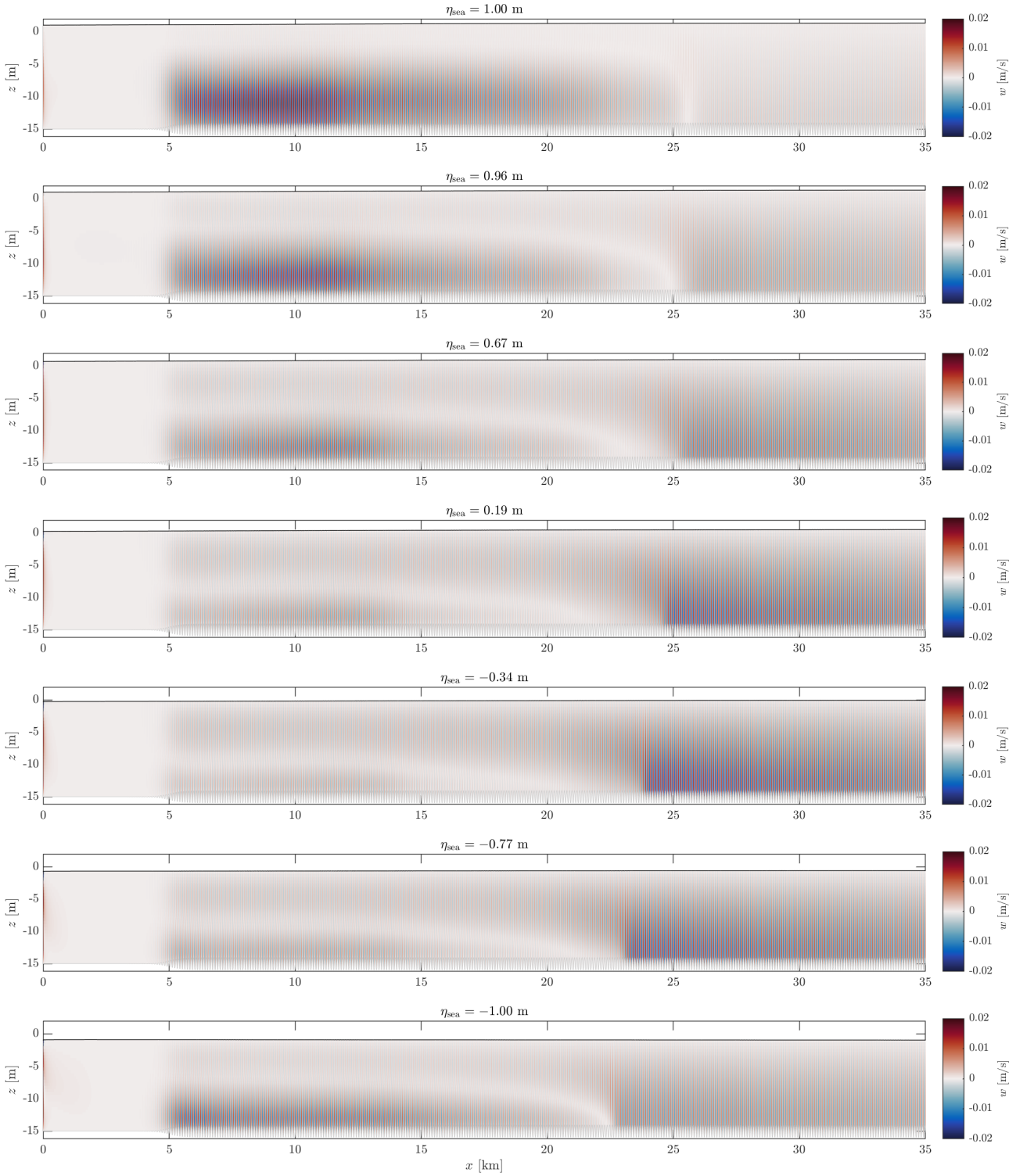

Figure A.10: Snapshots of a simulation of vertical flow velocity w over the estuary during ebb.

List of Figures

List of Abbreviations, Operators and Symbols

L.1 Abbreviations

Abbrevation	Description
B-0	Reference model with a flat bathymetry
B-1	Reference model with a bathymetry of $(\lambda_d, H_d, \mathcal{A}_d) = (100\text{ m},\ 2\text{ m},\ 0)$
BLDC	Bed-Leveling Depth Control
CFL	Courant–Friedrichs–Lewy
HLES	Horizontal Large Eddy Simulation
M2	Principal lunar semi-diurnal tidal constituent
NAP	Normaal Amsterdams Peil
ppt	parts per thousand
psu	practical salinity unit
RWW	Rotterdam Waterway
SGS	SubGrid Scale
UBA	Uniform Bed Alteration

L.2 Operators

Notation	Description
$\overline{\psi}$	Depth-averaged
$\psi * d$	Dune-averaged
$\langle\psi\rangle$	Tide-averaged
ψ'	Deviation from depth-averaged
$\widetilde{Q_\psi}$	Normalised dune-averaged value of horizontal transport component Q_ψ
$\widetilde{T_\psi}$	Normalised dune-averaged value of vertical transport component T_ψ

L.3 Variables and Parameters

Table A.2: Used symbols for physical quantities

Unit	Physical quantity	Quantity
L	Length	m or km
M	Mass	kg
T	Time	s or h
S	Salinity	ppt

Symbol	Description	Default	Unit
A	2x2 matrix of eddy viscosity		$L^2\ T^{-1}$
A_{sea}	Tidal elevation amplitude at the seaward boundary	1 m	L
A_h	Horizontal eddy viscosity		$L^2\ T^{-1}$
A_v	Vertical eddy viscosity		$L^2\ T^{-1}$
b	Envelope function for specifying dunes (b_d) or interventions (b_{int})		-
b_d	Envelope function for specifying dunes		-
b_{int}	Envelope function for specifying interventions		-
B	Width of the estuary		L
c	Celerity of the fastest internal wave		$L\ T^{-1}$
C	Chézy coefficient		$L^{1/2}\ T^{-1}$
D_{3D}	Eddy diffusivity from $k-\epsilon$ model		$L^2\ T^{-1}$
D_h^{BACK}	Horizontal background eddy diffusivity	14.3 m^2/s	$S\ L\ T^{-1}$
D_v^{BACK}	Vertical background eddy diffusivity	$1.43 \cdot 10^{-3}$ m^2/s	$S\ L\ T^{-1}$
e_k	Difference in total kinetic energy after subsequent grid refinement		$M\ L\ T^{-2}$
e_p	Difference in total potential energy after subsequent grid refinement		$M\ L\ T^{-2}$
e_t	Difference in total turbulent kinetic energy after subsequent grid refinement		$M\ L\ T^{-2}$
E_k	Total kinetic energy		$M\ L\ T^{-2}$
E_p	Total potential energy		$M\ L\ T^{-2}$
E_t	Total turbulent kinetic energy		$M\ L\ T^{-2}$
f_k	Relative height of the k^{th} layer as proportion of total water depth		-
Δf	Increase in vertical grid cell height		L
Fr_r	Freshwater / river Froude number		-
Fr_t	Tidal Froude number		-
g	Gravitational acceleration	9.81 m/s^2	$L\ T^{-2}$
h	Reference bed level and average depth below free surface reference level	15 m	L
h_d	Topography formulation, w.r.t reference bed level		L
h_{int}	Height of intervention		L
h_{dredge}	Dredging height, relative to $z=-h$ in the BLDC method		L
h_{dump}	Dumping height, relative to $z=-h$ in the BLDC method		L
H	Instantaneous water depth		L
H_d	Dune height, from crest to trough		L
k	Turbulent kinetic energy		$L^2\ T^{-2}$
K	2x2 matrix of eddy diffusivity		$L^2\ T^{-1}$
K	Number of vertical layers		-
K_h	Horizontal eddy diffusivity		$L^2\ T^{-1}$
K_v	Vertical eddy diffusivity		$L^2\ T^{-1}$
L	Estuary length	50 km	L
L_0	Start location of the dunes		L
ΔL_0	Ramping length for smoothing of b_d		L
L_{int}	Length of intervention		L

L_i	Isohaline length, defined as the distance from the sea to the inland location where the maximum salinity equals 1 ppt		L
$L_{\overline{s}}$	Depth-averaged Salt intrusion length, defined as the distance from the sea to the inland location where the depth-averaged salinity equals 1 ppt		L
L_s	Maximum Salt intrusion length, defined as the distance from the sea to the inland location where the maximum salinity equals 1 ppt		L
ΔL	Excursion of the salt intrusion length over a tidal cycle, can be computed for each L_s $L_{\overline{s}}$, L_i.		L
M	Mixing parameter of (Geyer & MacCready, 2014)		-
n	Manning's roughness coefficient		$\mathrm{T\ L^{-1/3}}$
N	Number of horizontal grid cells		-
q_r	Width-averaged river discharge	1.5 $\mathrm{m^2/s}$	$\mathrm{L^2\ T^{-1}}$
Q_h	Horizontal salt transport		$\mathrm{S\ L^2\ T^{-1}}$
Q_u	Horizontal advective salt transport		$\mathrm{S\ L^2\ T^{-1}}$
Q_{K_h}	Horizontal dispersive salt transport		$\mathrm{S\ L^2\ T^{-1}}$
$\overline{Q}_{h0}$	Horizontal subtidal depth-averaged salt transport		$\mathrm{S\ L^2\ T^{-1}}$
$\overline{Q}_{ht}$	Horizontal tidally-correlated depth-averaged salt transport		$\mathrm{S\ L^2\ T^{-1}}$
Q'_h	Horizontal shear-induced salt transport		$\mathrm{S\ L^2\ T^{-1}}$
Q_{h0t}	Horizontal residual salt transport of averaging procedure (Stokes' transport)		$\mathrm{S\ L^2\ T^{-1}}$
Ra	Estuarine Rayleigh number		-
Re_h	Horizontal turbulent Reynolds number		-
s	Salinity		S
s_c	Critical salinity concentration	1 ppt	S
s_{river}	Riverine salinity	0 ppt	S
s_{sea}	Seaward salinity	35 ppt	S
St	Estuarine Stokes number		-
St_t	Tidal stokes number		-
t	Temporal variable		T
Δt	Timestep	2.7 s	T
T	Tidal period	12.42 h	T
T_v	Vertical salt transport		$\mathrm{S\ L\ T^{-1}}$
T_w	Vertical advective salt transport		$\mathrm{S\ L\ T^{-1}}$
T_{K_v}	Vertical dispersive salt transport		$\mathrm{S\ L\ T^{-1}}$
$\overline{T}_{v0}$	Vertical subtidal depth-averaged salt transport		$\mathrm{S\ L\ T^{-1}}$
$\overline{T}_{vt}$	Vertical tidally-correlated depth-averaged salt transport		$\mathrm{S\ L\ T^{-1}}$
T'_v	Vertical shear-induced salt transport		$\mathrm{S\ L\ T^{-1}}$
u	Horizontal flow velocity		$\mathrm{L\ T^{-1}}$
u_b	Velocity just above the bed		$\mathrm{L\ T^{-1}}$
u_*	Bed shear velocity		$\mathrm{L\ T^{-1}}$
U_r	Background river velocity	0.1 m/s	$\mathrm{L\ T^{-1}}$
U_t	Magnitude of tidal velocity		$\mathrm{L\ T^{-1}}$
w	Vertical flow velocity		$\mathrm{L\ T^{-1}}$
x	Horizontal / longnitudal coordinate		L
Δx	Horizontal length of grid cells	10 m	L

x_{int}	Location of intervention		L
y	Lateral coordinate		L
y^+	Non-dimensional length scale		-
V_{int}	Volume of intervention, negative values indicating dredging		L^2
z	Vertical coordinate		L
z_0	Roughness height	0.001 m	L
z_b	Bed level, including topography		L
Δz_b	Height of the bottom layer		L
$\mathcal{A}_d$	Dune asymmetry		-
β	Contraction coefficient	$7.67 \cdot 10^{-4}$ ppt^{-1}	S^{-1}
ϵ	Dissipation of turbulent kinetic energy		L^2 T^{-3}
η	Instantaneous water level elevation		L
η_{sea}	Seaward water level elevation as boundary condition, function of time		L
κ	Von Kárman constant	0.41	-
λ_d	Dune length		L
λ_l	Lee side length		L
λ_s	Stoss side length		L
Λ_d	Dune shape formulation		-
$\mathcal{L}$	Non-dimensional length scale		-
$\mathcal{M}_v$	Mean vertical exchange of salt over the estuary		L T^{-1}
ν_{3D}	Eddy viscosity from $k-\epsilon$ model		L^2 T^{-1}
ν_{SGS}	Horizontal eddy viscosity produced by the HLES model		S L T^{-1}
ν_h^{BACK}	Horizontal background eddy viscosity	10 m^2/s	S L T^{-1}
ν_v^{BACK}	Vertical background eddy viscosity	10^{-3} m^2/s	S L T^{-1}
ω	Angular frequency of the M2 tide	$1.4 \cdot 10^{-4}$ rad/s	T^{-1}
ω	Vertical velocity w.r.t σ-coordinates		T^{-1}
$\phi_{d,\max}$	Maximum dune angle of the steepest side		
$\phi_{d,\text{mean}}$	Mean dune angle of the steepest side		
Φ_h	Horizontal flux		S L T^{-1}
Φ_v	Vertical flux		S L T^{-1}
$\mathbf{\Phi}$	Two-dimensional flux vector		S L T^{-1}
ψ	General parameter to indicate generality or multiple variables		
ρ	Density		M L^{-3}
ρ_0	Reference density without salinity	999.1 kg/m^3	M L^{-3}
σ	Boundary-fitted vertical coordinate		-
σ_ρ	Salinity eddy Prandtl-Schmidt number	0.7	-
σ_{mol}	Salinity molecular Prandtl-Schmidt number	700	-
$\mathcal{S}$	Absolute vertical advective stirring parameter of salt transport		L T^{-1}
τ	Temporal variable in σ-grid		T
τ_b	Bed shear stress		M L^{-1} T^{-2}
$\mathcal{T}$	Timescale for non-dimensionalisation		T
ξ	Horizontal coordinate in σ-grid		L